

**STUDIES OF PHOTOPHYSICAL PROCESSES IN
SEMICONDUCTOR MATERIALS AND THEIR
APPLICATIONS**

By
KRISHNA MISHRA
CHEM11201704002

**National Institute of Science Education and Research,
Bhubaneswar, Odisha**

*A thesis submitted to the
Board of Studies in Chemical Sciences*

*In partial fulfillment of requirements
for the Degree of*

DOCTOR OF PHILOSOPHY

of

HOMI BHABHA NATIONAL INSTITUTE



April, 2022

Homi Bhabha National Institute¹

Recommendations of the Viva Voce Committee

As members of the Viva Voce Committee, we certify that we have read the dissertation prepared by Krishna Mishra entitled "Studies of Photophysical Processes in Semiconductor Materials and Their Applications" and recommend that it may be accepted as fulfilling the thesis requirement for the award of Degree of Doctor of Philosophy.

Chairman - Dr. Moloy Sarkar	<i>Moloy Sarkar</i>	Date: 17.08.22
Guide / Convener - Dr. Subhadip Ghosh	<i>Subhadip Ghosh</i>	Date 17/08/22
Co-guide -		
Examiner - Prof. Anunay Samanta	<i>Anunay Samanta</i>	Date 17.8.2022
Member 1- Dr. Prasenjit Mal	<i>Prasenjit Mal</i>	Date 17.8.22
Member 2- Dr. Himansu Sekhar Biswal	<i>Himansu Biswal</i>	Date 17-08-2022
Member 3- Prof. Tapobrata Som	<i>Tapobrata Som</i>	Date 17-08-2022

Final approval and acceptance of this thesis is contingent upon the candidate's submission of the final copies of the thesis to HBNI.

I/We hereby certify that I/we have read this thesis prepared under my/our direction and recommend that it may be accepted as fulfilling the thesis requirement.

Date: 17/08/22

Place: NISER, BBSR

Subhadip Ghosh
(Dr. Subhadip Ghosh)
Guide

STATEMENT BY AUTHOR

This dissertation has been submitted in partial fulfillment of requirements for an advanced degree at Homi Bhabha National Institute (HBNI) and is deposited in the Library to be made available to borrowers under rules of the HBNI.

Brief quotations from this dissertation are allowable without special permission, provided that accurate acknowledgement of source is made. Requests for permission for extended quotation from or reproduction of this manuscript in whole or in part may be granted by the Competent Authority of HBNI when in his or her judgment the proposed use of the material is in the interests of scholarship. In all other instances, however, permission must be obtained from the author.

Krishna Mishra
Krishna Mishra

DECLARATION

I, hereby declare that the investigation presented in the thesis has been carried out by me. The work is original and has not been submitted earlier as a whole or in part for a degree / diploma at this or any other Institution / University.

Krishna Mishra -
Krishna Mishra

List of Publications

Journals

- #1. “Ground-State Heterogeneity along with Fluorescent Byproducts Causes Excitation-Dependent Fluorescence and Time-Dependent Spectral Migration in Citric Acid Derived Carbon Dots.” **K. Mishra**, S. Koley, S. Ghosh. *J. Phys. Chem. Lett.* **2019**, *10*, 335–345.
- #2. “Subpicosecond Charge Separation Time Scale at Graphene Quantum Dot Surface.” **K. Mishra**, A. Das, S. Ghosh. *J. Phys. Chem. C* **2020**, *124*, 24115–24125.
- #3. “Ultrafast Interfacial Electron Transfer from Graphene Quantum Dot to 2, 4-Dinitrotoluene.” **K. Mishra**, A. Das, S. Ghosh. *J. Phys. Chem. C* **2021**, *125*, 9638–9645.
- #4. “Femtosecond Upconversion Study of Interfacial Electron Transfer from Photoexcited CsPbBr₃ Perovskite Nanocrystal to Rhodamine 6G.” **K. Mishra**, D. Acharjee, A. Das, S. Ghosh. *J. Phys. Chem. B* **2021**, *125*, 11017-11025.
(Invited Article)
- #5. “Sub-picosecond Hot Hole Transfer in a Graphene Quantum Dot Composite with High Efficiency.” **K. Mishra**, D. Acharjee, A. Das, S. Ghosh. *J. Phys. Chem. Lett.* **2022**, *13*, 606-613.
6. “An Approach to a Model Free Analysis of Excited State Proton Transfer Kinetics in a Reverse Micelle.” S. Singh, S. Koley, **K. Mishra**, S. Ghosh. *J. Phys. Chem. C* **2018**, *122*, 732-740.

7. “Probing of Reorganization Dynamics within the Different Phases of Thermotropic Liquid Crystals.” M. R. Panda, S. Koley, **K. Mishra**, S. Ghosh. *Chem. Select* **2018**, *3*, 1551–1560.
8. “Revealing of Explicit Microsecond Carrier Diffusion from One Emission Center to Other in an all Inorganic Perovskite Nanocrystal.” A. Das, **K. Mishra**, S. Ghosh. *J. Phys. Chem. Lett.* **2021**, *12*, 5413-5422.
9. Synthesis of Cs/Methylammonium/Formamidinium PbBr₃ Perovskite Nanocrystals with Green Emissions: Implications for Display Applications.” S. K. Mahankudo, A. Das, **K. Mishra**, M. Barai, P. Mal, S. Ghosh. *ACS Appl. Nano Mater.* **2022**, *5*, 4360–4366.

Pertaining to Thesis

Conferences

1. Delivered a short talk in National Conference Advances in Materials Chemistry and Applications (**AMCA-2019**) organized by Utkal University, Bhubaneswar, India.
2. Poster presentation titled “Cause of excitation dependent fluorescence in citric acid based carbon dots.” in the international conference Trombay Symposium on Radiation and Photochemistry (**TSRP-2020**) organized by Bhabha Atomic Research Centre (BARC), Mumbai, India.
3. Oral presentation titled “Origin of Excitation Dependent Emission in Carbon Dot” in the International Conference on Chemical and Environmental Sciences (**ICCAES-2020**) organized by IEM Kolkata, India.
4. Poster presentation titled “Ultrafast Photophysical Processes in Graphene Quantum Dots.” at the 7th Theme Meeting on Ultrafast Sciences 2021 (**UFS-**

2021) organized by UM-DAE Centre for Excellence in Basic Sciences, Mumbai, India.

5. Poster presentation titled “Sub-picosecond Hot Hole Transfer in a Graphene Quantum Dot Composite.” in 12th National Workshop on Fluorescence and Raman Spectroscopy (**FCS 2021**) organized by IISER Thiruvanthapuram and RGCB, India.

Krishna Mishra -
Krishna Mishra

Dedicated to.....

My Parents

ACKNOWLEDGEMENTS

This thesis contains an overview of my studies during the last five years, although the foundation was established years ago when I was introduced to the world of science. I would like to express my gratitude and appreciation to everyone who influenced and supported me in this journey. First and foremost I would like to extend my deepest gratitude and respect to my thesis supervisor *Dr. Subhadip Ghosh* for his constant support and guidance. His modern thinking, professionalism, kindness, and insightful suggestions made this work possible and will continue to motivate me in the future. I would like to thank my doctoral committee members *Dr. Moloy Sarkar, Dr. Prasenjit Mal, Dr. Himansu Sekhar Biswal, and Prof. Tapobrata Som* for their suggestions and support throughout this journey. I would like to thank all the faculties, scientific officers, and non-teaching staffs of my department for their cooperation and help. I am grateful to *NISER, HBNI, and DAE* for providing infrastructure, the best research facilities, and financial assistance.

I would like to recognize the invaluable guidance of my senior *Dr. Somnath Koley* during the initial stage of research in learning new techniques and methods. I have been blessed to work in a lab where the atmosphere has always been friendly and enjoyable. I would like to appreciate the cooperation and support of my fellow lab members *Dr. Kiran Bharadwaj, Ms. Ayendrila Das, Mr. Debopam Acharjee, Mr. Manas R. Panda, Ms. Dushali, Mr. Siddharth Singh, Mr. Sanat K. Mohankudo, Mr. Mrinal Kanti Panda, Mr. Akash Sonwane, Dr. Soumitra Hazra, and Dr. Manas Barai.* I thank all my friends *Ms. Namrata Prusty, Mrs. Shalini Pandey, Mr. Sahadev Barik, Mr. Subhrakant Jena, Mr. Rajat K. Tripathy, Ms. Manjari Chakrobarty, Ms. Juhi Dutta, Ms. N. Preeyanka* (and the list continues) for their help and support in NISER.

The accomplishment of my doctoral thesis would not have been possible without the love and support of my family. I would like to extend my heartfelt gratitude to my late grandparents (paternal and maternal) who were always encouraging towards my education and co-curricular activities. My deep and sincere gratitude to my parents (*Mrs. Minati Mishra and Mr. Rasananda Mishra*), my elder brother *Mr. Kisan Kumar Mishra*, and my sister-in-law *Mrs. Debismita Mishra* for their unconditional love, constant encouragement, support, and blessings. I am extremely grateful to my close friends, *Mr. Sunil Kumar Panda, Ms. Bandana Behera, and Ms. Sibani P. Malik* for their constant moral support throughout this journey.

Above all, I thank the Almighty for showing me the right path always.

Krishna Mishra -
Krishna Mishra

CONTENTS

	Page No.
SYNOPSIS	xvi-xxiii
LIST OF SCHEMES	xxiv-xxvii
LIST OF FIGURES	xxviii-xxxviii
LIST OF TABLES	xxxix-xli
CHAPTER 1	1-23
Introduction	
1.1. Quantum Dots	3
1.1.1. General Properties	3
1.1.2. Synthesis Procedure of NCs	4
1.1.2.1. Top-down Approach	4
1.1.2.2. Bottom-up Approach	5
1.1.3. Carbon Dots and Graphene Quantum Dots	5
1.1.3.1. Structure	6
1.1.3.2. Properties	7
1.1.3.3. Applications	8
1.1.4. Perovskite Quantum Dots	9
1.1.4.1. Structure	10
1.1.4.2. Properties	11
1.1.4.3. Applications	12
1.2. Photophysical Processes	12
1.2.1. Fluorescence	13

1.2.2. Excited-state Processes	13
1.2.2.1. Photoinduced Electron Transfer (PET)	14
1.2.2.1.1. Basic Principle	15
1.2.2.1.2. Thermodynamics involved in PET	16
1.2.2.1.3. Importance of PET study	17
1.2.2.1.4. PET involving Quantum Dots	17
1.2.2.2. Solvation Dynamics	20
1.3. Scope of this Thesis	22
CHAPTER-2	24-42
Adopted Methodologies and Instrumentation	
2.1. Steady state absorption and emission spectra	24
2.2. Time-Resolved Fluorescence Measurements	25
2.2.1 Time-Correlated single photon counting (TCSPC)	26
2.2.1.1. Basic concept and working principle	26
2.2.1.2. Instrumentation	27
2.2.2. Fluorescence Upconversion Spectroscopy	28
2.2.2.1 Basic Concept and Working Principle	28
2.2.2.2. Instrumentation	29
2.2.3. Data Analysis	31
2.2.4 Construction of Time-Resolved Emission Spectra (TRES) and Time-Resolved Area normalized Emission Spectra (TRANES)	32
2.2.4.1. TRES	32
2.2.4.2. TRANES	33
2.3. Fluorescence Anisotropy Measurements	34

2.4. Confocal Microscope and Fluorescence correlation spectroscopy (FCS)	36
2.4.1. Basic concepts and Working principle	36
2.4.2. Instrumentation	38
2.5. Isothermal Titration Calorimetry (ITC)	39
2.6. Calculation of fluorescence quantum yield (QY)	40
2.7. Characterizations of Nanomaterials	41
2.8. Calculation of Free energy	41
2.9. Tauc Plot	42
CHAPTER 3	43-66
Understanding The Excitation Dependent Emission In Citric Acid Based Carbon Dots	
3.1. Introduction	43
3.2. Results and Discussion	45
3.2.1. Synthesis of Citric acid-based Carbon dots	45
3.2.2. Purification	46
3.2.3. Characterizations and Spectral Properties	47
3.2.4. Time Dependent spectral Migration and TRES, TRANES analysis	53
3.2.5. Steady state Anisotropy	64
3.3. Conclusion	66
CHAPTER 4	67-92
Subpicosecond Charge Separation At Graphene Quantum Dot Surface: A Combined Femtosecond Upconversion and Fluorescence Correlation Spectroscopic Measurements	
4.1. Introduction	67

4.2. Results and Discussion	68
4.2.1. PET Couple Used	68
4.2.2. GQD Sample Characterization and spectral Properties	69
4.2.3. Steady-State and Time-Resolved Quenching Study and Stern-Volmer (SV) plots Analysis	73
4.2.4. FCS Study of Binding Kinetics, Particle Diffusion, and Mechanism of GQD-DMA Complex Formation.	76
4.2.5. Femtosecond Upconversion Study of Intrinsic Electron Transfer Kinetics of GQD-DMA Complex.	86
4.3. Conclusion	91
CHAPTER 5	93-109
Temperature Dependent Study Of Photoinduced Electron Transfer From Graphene Quantum Dot To 2,4-Dinitrotoluene	
5.1. Introduction	93
5.2. Results and Discussion	94
5. 2.1. Characterization of GQDs	94
5.2.2. Steady state and Time resolved Quenching Study	95
5.2.3. Isothermal Titration Calorimetry Study of GQD–2,4-Dinitrotoluene (DNT) Complex Formation	102
5.2.4. Femtosecond Upconversion Studies of Intrinsic PET at Different Temperatures	104
5.3. Conclusion	108
CHAPTER 6	110-117
Evidence Of Subpicosecond Hot Hole Transfer In A Graphene Quantum Dot Composite	
6.1. Introduction	110
6.2. Results and Discussion	112

6.2.1. Sample Preparation and Characterization	112
6.2.2. Femtosecond Upconversion Study of Hot Carrier Cooling and Extraction	114
6.3. Conclusion	126
CHAPTER 7	128-145
Femtosecond Upconversion Study Of Interfacial Electron Transfer From Photoexcited CsPbBr₃ Perovskite Nanocrystal To Rhodamine 6G	
7.1. Introduction	128
7.2. Results and Discussion	129
7.2.1. Synthesis and Characterization of CsPbBr ₃ NCs	129
7.2.2. Photoluminescence Quenching Study of NCs	131
7.2.3. Rotational Anisotropy Study	137
7.2.4. Femtosecond Upconversion Study of Quenching at Different Temperatures	140
7.3. Conclusion	145
Summary and Future Perspective	146-147
References	148-169

SYNOPSIS

Chapter 1: Introduction

Semiconductor nanocrystals (NCs) have gained much popularity among the scientific community due to their easy tunable optical and electronic properties.¹ The demand for clean energy is increasing day by day for environmental safety. Fluorescent carbon dots (FCDs), graphene quantum dots and halide perovskite nanocrystals are excellent candidates for the building blocks of optical energy conversion devices. Apart from solar cell devices, these materials can be used in LEDs, LASERs, photodetectors and many others.²⁻⁴ All these real applications of semiconductor NCs are fundamentally controlled by a number of photophysical processes like optical absorption, charge separation and recombination, energy relaxation, energy and charge transfer in a sequential manner and with a required timescale. Hence understanding an in-depth photophysical processes will lead to successful utilization of the materials in their respective application fields. This introductory chapter describes about the state-of-the-art of above mentioned materials as well as the fundamentals of associated photophysical processes studied in this thesis.

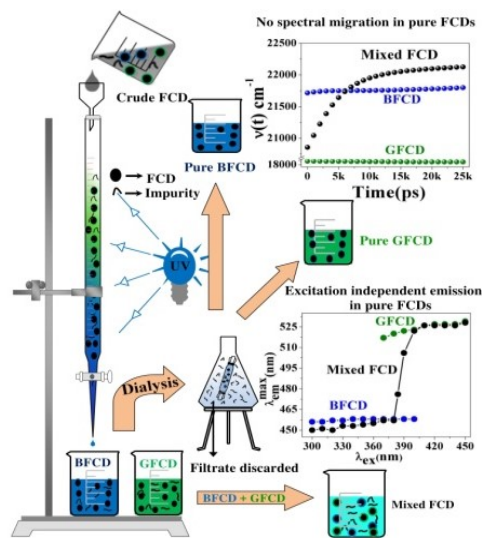
Chapter 2: Adopted Methodologies and Instrumentation

This chapter describes about the instruments used as well as the adopted methods for data analysis. Mostly fluorescence based techniques are employed to carry out this work. The working principle and instrumentation techniques of TCSPC set-up⁵, fluorescence upconversion spectrometer⁶ and fluorescence correlation spectrometer⁷ are discussed in detail due to their extensive use in this work. Other instruments like UV-Vis, Steady state fluorescence, TEM, XRD, ITC are discussed briefly. Besides the

instrumentation, data analysis methods for lifetime measurements, diffusion processes, construction of time resolved emission spectra (TRES)⁸ and time resolved area normalized emission spectra (TRANES)⁹ are also described in detail.

Chapter 3: Understanding the Excitation-Dependent Emission in Citric Acid Based Carbon Dots¹⁰

The origin of excitation dependent emission from fluorescent carbon dots is a matter of debate in the scientific community. In this chapter we have discussed the urgency of sample purification, as molecular impurity has undoubtedly misled carbon dot literature with detrimental claims, misconceptions, and misanalyses. Several controversial

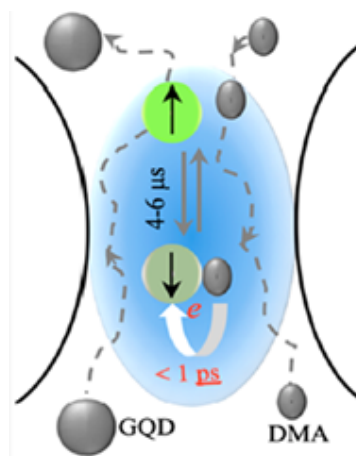


phenomena of FCD fluorescence including excitation-dependent emission, spectral migration with time, and thereby violation of the Kasha–Vavilov rule, which sparked intense debate during recent reports, disappeared when we rigorously purified the citric acid based FCD sample. We have proposed a proper sample purification protocol i.e. column chromatography followed by membrane dialysis to obtain pure FCD samples. From column purification, 2 batches of carbon dots (blue emitting and green emitting) are obtained, membrane dialysis (~15 kDa) confirms the complete removal of molecular fluorophores. Our purified sample barely shows any excitation wavelength dependent emission. TRES analysis confirms the absence of solvent induced spectral migration, TRANES confirms the absence of multiemissive species. We crosschecked our results with the unpurified FCD samples and confirmed the

excitation dependent emission property of carbon dot sample mainly originates from ground state optical heterogeneity. Through this work we are neither contributing to the debate on the actual origin of FCD fluorescence nor proposing the chemical structure of FCD, but our work has substantiated that the actual origin of excitation-dependent emission and spectral migration of FCD fluorescence lies with its ground-state optical heterogeneity.

**Chapter 4: Subpicosecond charge separation at Graphene Quantum dot Surface:
A Combined femtosecond upconversion and fluorescence correlation spectroscopic measurements.¹¹**

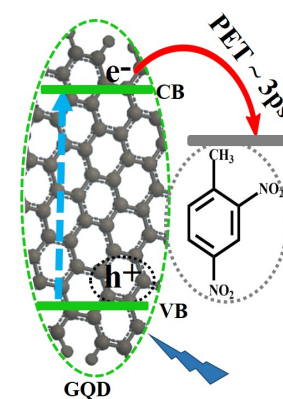
Highly exergonic photoinduced electron transfer (PET) process is studied from electron rich dimethylaniline to the photoexcited graphene quantum dot in water. Steady state as well as lifetime quenching study reveals the presence of both complexation as well as collision induced PET. The collisional quenching rates obtained from the



Stern-Volmer analysis, found to be similar with the diffusion controlled rate of the medium. FCS technique revealed a weak GQD-DMA complex formation with a binding time of 4–6 μs. This few microseconds binding time allowed us to measure the much faster (<1 ps) intrinsic PET time scale in GQD-DMA complex before it dissociates. Intrinsic PET rate was obtained from femtosecond upconversion study. Finding of this work will open paths for plausible use of GQDs as both light absorbing material and electron scavenger, unlike its current use in OPV devices as an electron scavenger only.

Chapter 5: Temperature Dependent Study of Photoinduced Electron Transfer from Graphene Quantum Dot to 2,4-Dinitrotoluene.¹²

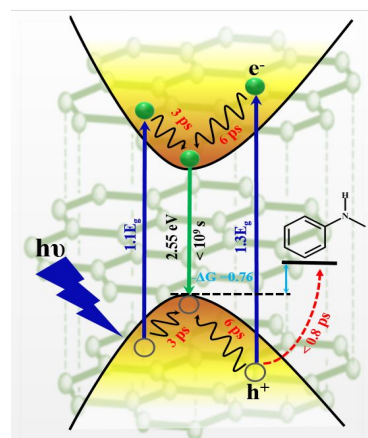
Ultrafast photoinduced electron transfer (PET) from a photoexcited GQD* to an electron-deficient molecule 2,4-dinitrotoluene (DNT) is studied in a water-methanol mixture at different temperatures (5 °C–60 °C). Irrespective of temperature, the collisional PET rate



obtained from the TCSPC lifetime quenching study appears to be diffusion controlled rate of the reaction medium. GQD-DNT complex formation is confirmed from the heat change in the isothermal titration calorimetry (ITC) study. Femtosecond upconversion study reveals the presence of ~3ps intrinsic PET in GQD-DNT complex. Findings of our work would help the researchers in understanding the interfacial charge transfer process of GQD and thereby expand the promises to its real applications, especially in sensing and photovoltaic applications where materials with ultrafast PET are highly desirable.

Chapter 6: Evidence of subpicosecond Hot Hole Transfer in a Graphene quantum Dot Composite.¹³

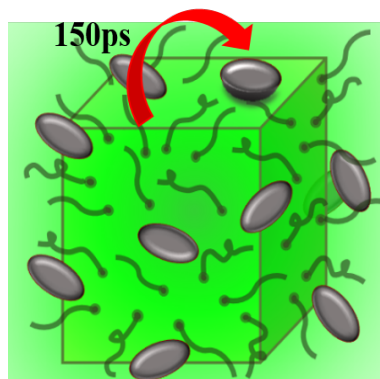
Extraction of hot carriers is important as thermal energy loss limits the efficiency of an optoelectronic device. In this work, using fluorescence upconversion technique we have detected slow hot carrier cooling time and ultrafast sub-picosecond hot hole transfer time in a GQD composite with high efficiency. We excited the sample at two different excitations $1.1E_g$



and $1.3E_g$ (E_g = Band gap energy) and collected the ultrafast fluorescence transients by covering the whole emission spectrum. By doing TRES analysis and plotting a correlation curve we obtained the cooling time scale of 3 ps and 6 ps respectively. We used N-methylaniline as a hole scavenger and < 0.8 ps hole transfer timescale is obtained from the upconversion study. Finding of this study will lead to successful utilization of GQDs in photovoltaic applications for enhancement of their efficiencies with hot carrier extractions.

Chapter 7: Femtosecond Upconversion Study of Interfacial Electron Transfer from photoexcited CsPbBr₃ Perovskite Nanocrystal to Rhodamine 6G.¹⁴

Photoinduced electron transfer (PET) from an excited-state CsPbBr₃ nanocrystal (NC) to rhodamine 6G (r6G) is studied in toluene. Because of weak solubility of r6G in toluene, excess r6G molecules adsorb at NC surface which result in a much slower rotational diffusion time scale of r6G



in the presence of NCs. Study of intrinsic PET benefits from the molecular interactions leading to donor (NC)- acceptor (r6G) complex formation, where solvent diffusion parameters would not play any role in the PET kinetics. Femtosecond transients of NCs are nicely fit to a Poisson expression originally proposed by Tachiya. Conclusive fittings to the temperature dependence quenching data reveal two interesting observations: (1) Even though the average number of surface trap state in a NC does not change with temperature (5–60 °C), the trap-state-induced quenching time scale is accelerated with increase in temperature, pointing towards a more efficient trapping at higher temperature (2) In the presence of r6G, a fast (~ 150 ps per

r6G molecule) interfacial PET time scale is observed, which remains unaffected by temperature (5–60 °C). Our findings demonstrate that even a simple “perovskite NC–electron acceptor” composite like that in the present study can ensure a rapid interfacial charge separation. Such information will help us to realize the actual potential of perovskites NCs in their real applications.

References

1. “Semiconductor Nanocrystals: Structure, Properties, and Band Gap Engineering” A. M. Smith, S. Nie, *Acc. Chem. Res.* **2010**, *43*, 190–200.
2. “All-Inorganic Halide Perovskites for Optoelectronics: Progress and Prospects.” J. Liang, J. Liu, Z. Jin. *Sol. RRL* **2017**, *1*, 1700086.
3. “Luminescent Graphene Quantum Dots for Organic Photovoltaic Devices” V. Gupta, N. Chaudhary, R. Srivastava, G. Datt Sharma, R. Bhardwaj, S. Chand. *J. Am. Chem. Soc.* **2011**, *133*, 9960–9963
4. “Carbon-Based Quantum Dots for Photovoltaic Devices: A Review.” A. Kim, J. K. Dash, P. Kumar, R. Patel. *ACS Appl. Electron. Mater.* **2022**, *4*, 27-58.
5. J. R. Lakowicz, *Principles of Fluorescence Spectroscopy*; Springer science & business media, **2013**.
6. “Ultrafast fluorescence upconversion technique and its applications to proteins” H. Chosrowjan, S. Taniguchi and F. Tanaka, *FEBS J.*, **2015**, *282*, 3003.
7. “Fluorescence correlation spectroscopy: The technique and its applications in soft matter,” A. Gupta, J. Sankaran, and T. Wohland, *Phys. Sci. Rev.* **2019**, *4*, 20170104

8. "Excited state solvation dynamics of 2-anilinoanthracene.", R. P. DeToma, L. Brand, Chem. Phys. Lett., **1977**, *47*, 231.
9. "Time-resolved Area-Normalized Emission Spectroscopy (TRANES): A Novel Method for Confirming Emission from Two Excited States.", A. S. R. Koti, M. M. G. Krishna, N. Periasamy, J. Phys. Chem. A, **2001**, *105*, 1767–1771.
10. "Ground-State Heterogeneity along with Fluorescent Byproducts Causes Excitation-Dependent Fluorescence and Time-Dependent Spectral Migration in Citric Acid Derived Carbon Dots." K. Mishra, S. Koley, S. Ghosh. J. Phys. Chem. Lett. **2019**, *10*, 335–345.
11. "Subpicosecond Charge Separation Time Scale at Graphene Quantum Dot Surface." K. Mishra, A. Das, S. Ghosh. J. Phys. Chem. C **2020**, *124*, 24115–24125.
12. "Ultrafast Interfacial Electron Transfer from Graphene Quantum Dot to 2, 4-Dinitrotoluene." K. Mishra, A. Das, S. Ghosh. J. Phys. Chem. C **2021**, *125*, 9638–9645.
13. "Sub-picosecond Hot Hole Transfer in a Graphene Quantum Dot Composite with High Efficiency." K. Mishra, D. Acharjee, A. Das, S. Ghosh. J. Phys. Chem. Lett. **2022**, *13*, 606-613.
14. "Femtosecond Upconversion Study of Interfacial Electron Transfer from Photoexcited CsPbBr₃ Perovskite Nanocrystal to Rhodamine 6G." K. Mishra, D. Acharjee, A. Das, S. Ghosh. J. Phys. Chem. B **2021**, *125*, 11017-11025.

Annexure

The thesis is divided into seven chapters. The introductory chapter discusses about the properties of materials used and their photophysical processes those have been studied. The second chapter tells about the instrumentation techniques and the data analysis methods. The next five chapters are the working chapters. The third chapter provides an overview of the ground state optical heterogeneity of fluorescent carbon dots. The fourth and fifth chapters describe the photoinduced electron transfer (PET) process in graphene quantum dots composites. The sixth chapter describes the carrier cooling time and ultrafast hot hole extraction in a graphene quantum dot composite. And the last chapter explains the intrinsic PET process in a perovskite nanocrystal and rhodamine 6G complex. We believe the findings of this thesis would help researchers to design next-generation photovoltaic devices.

LIST OF SCHEMES

	Page No.
1. Scheme 1.1. Illustration of size-dependent band gap energy of quantum confined NCs.	4
2. Scheme 1.2. Schematic representation of top-down and bottom-up synthetic approaches used in QD synthesis. The left panel represents the top-down approach whereas the right one represents the bottom-up approach.	5
3. Scheme 1.3. Illustration of CD and GQD structures.	7
4. Scheme 1.4. Pictorial representation of halide lead perovskite. The blue balls represent the A-site cation, the black ball represents the B-site divalent cation and the orange balls represent the monovalent halide anions.	11
5. Scheme 1.5. Jablonski diagram representing absorption of a photon followed by various de-excitation processes.	13
6. Scheme 1.6. Representing various excited state processes and their respective timescales.	14
7. Scheme 1.7. Illustration of PET reaction between donor and acceptor.	16
8. Scheme 1.8. Pictorial representation of charge carrier generation and extraction of carriers through PET process.	19
9. Scheme 1.9. (A) Pictorial representation of the formation of low energy solvated states due to stabilization of the polar excited state of the fluorophore after photoexcitation through interaction between fluorophore and solvent dipoles. (B) Figure showing	21

shifting of emission spectra towards lower energy side with time due to formation of solvated states right after photoexcitation. (C) Represents the wavelength-dependent fluorescence decay measured by the time-resolved fluorescence technique. Here blue and red curve represents the blue end and red end emission wavelength of the steady-state spectrum respectively.

- | | | | |
|-----|--------------------|--|----|
| 10. | Scheme 2.1. | The working principle of TCSPC setup. | 26 |
| 11. | Scheme 2.2. | Scheme representing a basic reverse mode TCSPC setup. | 28 |
| 12. | Scheme 2.3. | Pictorial representation of the basics of fluorescence upconversion. | 29 |
| 13. | Scheme 2.4. | Schematic representation of the upconversion setup, Fluomax from IB photonics. In the scheme, the red line corresponds to the fundamental laser beam and the blue one frequency doubled visible beam. | 30 |
| 14. | Scheme 2.5. | Illustration showing fluorescence depolarization after polarized excitation. | 34 |
| 15. | Scheme 2.6. | Schematic representation of MT-200 provided by PicoQuant. | 38 |
| 16. | Scheme 3.1. | Illustration of Sample purification steps. | 47 |
| 17. | Scheme 3.2. | Illustration of how ground state inhomogeneity can cause spectral migration with time even in the absence of solvation dynamics. (A) Two fluorophores (blue and green-emitting) are present simultaneously, whose excited state energies do not change with time (as solvation dynamics is absent). (B) TRES | 60 |

of the two fluorophores show the decreasing of emission intensity (without changing the emission peak) with time at different rates due to their different fluorescence lifetimes. (C) The actual time t spectrum (solid curves) of the mixed sample (blue + green fluorophore) would be the combination of time t spectra of blue (dotted curves) and green (dashed curves) emitting fluorophores. A faster diminishing rate of the blue emission (dotted curves) would cause the shifting of the overall peak position of TRES of the mixed sample towards the longer wavelengths with time, though individual peak positions do not change. (D) Fluorescence lifetime profiles of the mixed sample at different emission wavelengths. (E) The emission peak position of the mixed sample as a function of time.

- | | | |
|-----|---|----|
| 18. | Scheme 3.3. Coumarin 153 and Coumarin 481. | 61 |
| 19. | Scheme 4.1. Energy Band Diagram of GQD-DMA Pair. | 69 |
| 20. | Scheme 4.2. Path 1 (dynamic/collisional quenching): Collisional quenching takes place by a diffusion-controlled process, following an equilibrium ruled by k_d and k_{-d} rate constants (resulting in structure in cartoon B). Path 2 (static quenching): DMA with a favourable orientation to GQD forms a GQD-DMA static complex in the μs timescale following an equilibrium ruled by k_{asso} and k_{disso} rate constants (resulting in structure in cartoon C). | 79 |

21. **Scheme 5.1.** Energy levels of GQD and DNT involved in the PET reaction. 96
22. **Scheme 6.1.** Schematic representation of carrier cooling (black spiral arrow) and hole transfer (red dotted arrow) in GQD-NMA composite. The blue up-pointed arrows indicate the near band edge excitation (left) and above band edge excitation (right), respectively. The green down pointed arrow shows the band edge emission. 126
23. **Scheme 7.1.** Band Edge and HOMO–LUMO Energy Levels of NC and r6G Participating in the PET Reaction. 134

LIST OF FIGURES

		Page No.
1.	Figure 2.1. A typical ACF curve.	37
2.	Figure 2.2. Tauc Plot generated from GQD absorption.	42
3.	Figure 3.1. (A) Visual silica column separation of as-synthesized FCD under UV illumination (~365 nm). (B) Two subsets, BFCD and GFCD obtained after visual silica column separation. A third beaker containing only water was placed close to the UV lamp for comparison with the other two FCD solutions. (C) HR-TEM image of a BFCD particle and the particle size distribution. GFCD shows a similar TEM image and particle size distribution.	48
4.	Figure 3.2. (A) PXRD spectrum of our FCD sample. Both the FCD samples (BFCD & GFCD) exhibit similar peak position. (B) FTIR spectrum indicates the presence of various groups on the surface of GFCD. C=N (1640 cm ⁻¹), C-N= (1427 cm ⁻¹), C=C (1600 cm ⁻¹) vibrations are also detected. BFCD sample also exhibits similar peak positions. (C) ¹ H NMR Spectrum of GFCD sample very similar to BFCD sample.	48
5.	Figure 3.3. Absorption spectrum of BFCD (A), GFCD (C), Steady-state fluorescence spectra of BFCD (B) and GFCD (D) at different excitation wavelengths.	49
6.	Figure 3.4. TRF of (A) BFCD ($\lambda_{ex} \approx 375$ nm), (B) GFCD ($\lambda_{ex} \approx 405$	51

nm) and (C) mixed FCD ($\lambda_{\text{ex}} \approx 375$ nm), at extreme blue, extreme red, and peak emission wavelengths. In (A) and (B), all three are identical. Very fast IRF (~ 80 ps) is shown by the black curve. The fast decay curves (pink) in (A) ($\lambda_{\text{ex}} \approx 375$ nm) and (B) ($\lambda_{\text{ex}} \approx 405$ nm) depict the TRF (at emission peak) of citrazinic/succinic acid derivatives, probable impurities in crude FCD. (D) Plot of the average fluorescence lifetime (τ_{avg}) as a function of the emission wavelength for all three FCD samples (BFCD, GFCD, and mixed FCD).

7. **Figure 3.5.** Fluorescence quantum yield (Φ_f) as a function of excitation wavelength (λ_{ex}) for citrazinic/succinic acid derivatives (black ball), GFCD (green ball) and BFCD (blue ball). 52
8. **Figure 3.6.** Absorption spectrum of mixed FCD (A), Steady-state fluorescence spectra of mixed FCD (B) at different excitation wavelengths. The inset of (B) shows the same spectra after normalizing with the peak intensity. 53
9. **Figure 3.7.** Emission peak as a function of excitation wavelength for all three samples, mixed FCD (black squares), BFCD (blue triangles) and GFCD (green pentagons). 53
10. **Figure 3.8.** TRES of mixed FCD (A) show spectral migration toward the low-energy side with time, whereas in BFCD (B) and GFCD (C) no shift was observed. (D) Emission peak position of TRES as a function of time for all three 57

- samples.
11. **Figure 3.9.** TRANES (Area Normalized TRES) of mixed FCD (A), BFCD (B) and GFCD (C). A clear iso-emissive point is obtained only in mixed FCD (A) Inset shows the zoomed version for better clarity. 58
 12. **Figure 3.10.** Steady state fluorescence spectra of (A) coumarin 153, (B) coumarin 481, and (C) coumarin mixture (C481 + C153), in ethanol at different excitation wavelengths. Figure (D) shows emission peak position as a function of excitation wavelength for all three samples. The inset of Figure A shows the same spectra shown in Figure A after normalizing with peak intensity. 62
 13. **Figure 3.11.** TRES of (A) C481, (B) C153, (C) C481 and C153 mixture, in ethanol at different times. Inset of C shows the same TRES after area normalization (TRANES). A clear iso-emissive point is obtained only in TRANES of C481 and C153 mixture (insets of Figure C), which is further zoomed for better clarity. (D) Time evolution of the emission peak position of TRES for all three samples. 63
 14. **Figure 3.12.** Steady-state excitation (pink horizontal line) and emission (blue horizontal line) anisotropy values across the fluorescence excitation spectrum (black) and emission spectrum (red) of BFCD (A) and GFCD (B) in glycerol. 65
 15. **Figure 4.1.** (A) HR-TEM image of GQDs. Insets show the FFT 71

patterns and lattice spacings. (B) Size distribution of GQD particles, measured through HR-TEM. (C) Zoomed image (HR-TEM) of GQD surface to the atomic level. (D) Raman spectrum of GQDs.

- | | | | |
|-----|--------------------|---|----|
| 16. | Figure 4.2. | (A) FTIR spectrum of GQDs. (B) Powder XRD spectrum of GQDs. | 71 |
| 17. | Figure 4.3. | High-resolution XPS spectra (black curves) along with splitted curves of C 1s (A), N 1s (B), and O 1s (C), respectively. | 72 |
| 18. | Figure 4.4. | (A) Full range absorption spectrum of GQDs in water. (B) Emission spectra of GQDs in water at different excitation wavelengths. Excitation wavelengths are mentioned in the inset. | 72 |
| 19. | Figure 4.5. | Quenching of steady state emission (A) and PL lifetime (B) of GQDs in water at 20 °C upon addition of DMA at different concentrations. | 73 |
| 20. | Figure 4.6. | Steady-state (I_0/I) and time-resolved (τ_0/τ) Stern–Volmer (SV) plots at 20 °C (A) and 60 °C (B). | 74 |
| 21. | Figure 4.7. | (A) FCS curves of GQDs in water at different DMA concentrations. Inset shows the same but normalized at 10 μ s. The contribution of binding reaction (A_R) appears only after the addition of DMA and increases monotonously with increasing the DMA concentration. (B) Gaussian distribution of diffusion times of GQDs at different DMA | 78 |

- concentrations.
22. **Figure 4.8.** Autocorrelation curves of GQDs in water at different excitation power. Initial amplitude arises only at high excitation power ($>8 \text{ kW/cm}^2$) due to the triplet kinetics. 78
23. **Figure 4.9.** (A) Femtosecond fluorescence transients of GQDs in water at different DMA concentrations ($20 \text{ }^\circ\text{C}$). Inset shows the ratio curves of femtosecond transients ($I_t[\text{Q}]/I_t[0]$), decay of which is due to PET only. (B) Femtosecond transient of GQDs in the presence of 9 mM DMA at two temperatures $20 \text{ }^\circ\text{C}$ (black circle) and $70 \text{ }^\circ\text{C}$ (red ball), respectively. Large contribution of $<1 \text{ ps}$ component at $20 \text{ }^\circ\text{C}$ is due to an ultrafast PET of GQD-DMA complexes, which largely receded at $70 \text{ }^\circ\text{C}$ as most of the complexes dissociate. Interestingly, long decay components, which originate from the collisional quenching, decay at faster rates at $70 \text{ }^\circ\text{C}$ when compared to that at $20 \text{ }^\circ\text{C}$. In the inset, we normalized the counts for both the curves at 10 ps to compare decay rates of long components visually. $\lambda_{\text{ex}} \sim 400 \text{ nm}$ and $\lambda_{\text{em}} \sim 470$ (little blue side of the emission peak). Solid black lines represent the fitted curves. 90
24. **Figure 5.1.** High-resolution TEM (HR-TEM) image of GQDs. Inset shows a lattice spacing of $\sim 0.21 \text{ nm}$ and the hexagonal FFT pattern. (B) Fourier transform infrared spectroscopy (FTIR) image of GQDs.(C) Powder XRD spectrum of 94

- GQDs. (D) Raman spectrum of GQDs showing the G and D bands.
25. **Figure 5.2.** Quenching of PL (A, C), and fluorescence lifetime (B, D) of GQDs in aqueous-methanol at 20 °C (A, B) and 60 °C (C, D) in the presence of DNT at different concentrations. 95
26. **Figure 5.3.** Steady-state SV plot (blue balls) and lifetime SV plot (red balls) at (A) 20 °C and (B) 60 °C, respectively. 98
27. **Figure 5.4.** (A) Figure shows ITC raw data of exothermic binding of DNT with GQD in aqueous methanol. Each peak represents the heat release against each injection of high concentration DNT in aqueous methanol to the cell containing low concentration GQD in the same binary solvent. (B) The figure shows the binding isotherm obtained after processing the raw data and subtracting the heat of dilutions of only DNT and only GQD. The black line is the fitted curve assuming a single binding site. Binding stoichiometry is found to be ~1.2, as shown by the mid-point of the fitted rise curve. 102
28. **Figure 5.5.** (A-B) Femtosecond transients of GQDs in aqueous methanol in the absence and presence of ~9 mM DNT ($\lambda_{\text{ex}} \sim 405$ nm) at 5 °C (A) and 60 °C (B), respectively. Emission was collected at the emission peak position. (C) femtosecond transients of GQDs in the absence (black balls) and presence (green, blue and red balls) of ~9 mM 106

DNT after normalizing with transient of only GQDs [i.e., $I(t,[Q])/I(t); Q=0$ for black balls and ~ 9 mM for others] at different temperatures. Solid lines are the exponential fitting curves. We avoided fitting to the very initial portion (< 0.6 ps) where mostly the lamp scattering contributes.

29. **Figure 6.1.** (A) Particle size distribution of GQDs obtained from HRTEM study. (B) Topological height of the GQDs is measured to be ~ 1.8 nm from AFM study, indicating the presence of $\sim 4-5$ graphene layers. (C) Powder XRD spectrum of GQDs. (D) FTIR spectrum of GQDs showing the presence of different organic functional groups on the surface. 113
30. **Figure 6.2.** Emission spectra of GQDs in toluene at different excitation wavelengths. The excitation wavelengths are mentioned in the figure. 114
31. **Figure 6.3.** Absorption (black solid line), emission (green solid line, $\lambda_{\text{ex}} \sim 400$ nm) and excitation (blue dotted $\lambda_{\text{em}} \sim 510$ nm) spectra of colloidal GQDs dispersed in toluene. Identical absorption and excitation spectra imply the high integrity of the emission state. Above band edge (~ 375 nm) and near band edge (~ 430 nm) excitations are shown by the solid Gaussian pulses and the band edge energy is indicated by the dotted vertical black line (0-0 transition). 115
32. **Figure 6.4.** Femtosecond transients of colloidal GQDs ($\lambda_{\text{ex}} \sim 430$ nm, 116

$\lambda_{em} \sim 505$ nm) dispersed in toluene as a function of photon fluence. We varied the fluence from 0.2×10^{15} (black curve) to $\sim 1 \times 10^{15}$ (purple curve) photons cm^{-2} per pulse. The concentration of GQDs was the same for all the excitations. Inset A shows the long-time amplitude (at ~ 2 ns) of the transient as a function of photon fluence. Inset B shows the same transients as in the main figure but intensity normalized.

33. **Figure 6.5.** Femtosecond transients of colloidal GQDs in toluene at various emission wavelengths (465 nm-570 nm) across the steady state emission spectrum at $\lambda_{ex} \sim 375$ nm (A), and 430 nm (B), respectively. We have recorded lifetimes at 12 different positions across the entire emission spectrum. 118
34. **Figure 6.6.** Intensity normalized time-resolved emission spectra (TRES) of colloidal GQDs in toluene at different times following the excitation at 375 nm (left figure) and 430 nm (right figure), respectively. Emission energy decreases with time as a result of the cooling of hot carriers. 121
35. **Figure 6.7.** Peak position of time-resolved emission spectra (TRES) of GQDs dispersed in toluene as a function of time at $\lambda_{ex} \sim 375$ nm (black balls) and 430 nm (blue balls), respectively. Higher zero time amplitude of ~ 375 nm excitation curve compared to that of ~ 430 nm excitation curve indicating that the former excitation leading exciton to an 122

energetically much higher state compared to the latter. Solid lines show the fittings with a single exponential decay function. Inset showing the same curves as in the main figure but normalized for comparison between their decay timescales.

36. **Figure 6.8.** (A) steady state emission of GQD in the absence (red curve) and presence (blue curve) of ~ 90 mM NMA (B) Femtosecond transients of GQDs dispersed in toluene, in the absence (red curve) and presence (blue curve) of ~ 90 mM NMA. GQDs were excited much above the band-edge states ($\sim 1.3E_g$) and emission was collected at ~ 20 nm red from emission peak position. 124
37. **Figure 7.1.** (A) TEM images of CsPbBr₃ NCs. (B) HR-TEM image of a CsPbBr₃ NC. (C) Particle size distribution of the NCs, the center of mass of which is located at 10 nm. (D) Absorption (black) and emission (green, $\lambda_{ex}=400$ nm) spectra of CsPbBr₃ NCs in toluene. (E) XRD spectrum of CsPbBr₃ NCs, which shows the cubic phase of the crystals. 130
38. **Figure 7.2.** Absorption spectra of ~ 0.14 μ M NCs in toluene at different r6G concentrations. Above ~ 7.4 μ M r6G, the absorption spectrum does not change much. The molar extinction coefficient of NCs at the peak is $\sim 3.5 \times 10^6$ M⁻¹s⁻¹. Inset shows cuvettes containing (i) ~ 0.14 μ M NCs and ~ 7.4 μ M r6G in toluene (left), (ii) saturated solution of r6G in 131

- toluene (middle) and (iii) $\sim 7.4 \mu\text{M}$ r6G in water (right).
39. **Figure 7.3.** Steady-state emission (A, at 25 °C) and TCSPC recorded lifetime profiles (B–D, at 5 °C –60 °C) of NCs in toluene at various r6G concentrations. Excitation pulse (IRF ~ 0.7 ns) is shown by the dotted curves in B–D. 132
40. **Figure 7.4.** (A) Absorption spectrum of r6G in toluene (black) and emission spectrum of CsPbBr₃ NCs in toluene (green, $\lambda_{\text{ex}}=400$ nm). (B) Emission spectra of CsPbBr₃ NCs in toluene at different r6G concentrations ($\lambda_{\text{ex}}=400$ nm). The intensity of NCs is quenched upon the addition of r6G. Absence of r6G peak at 570 nm, even at the highest r6G concentration (red spectrum). 134
41. **Figure 7.5.** Time-resolved (TCSPC) and steady-state Stern-Volmer plots at different temperatures. 137
42. **Figure 7.6.** (A) Absorption (black) and emission (orange, $\lambda_{\text{ex}}=490$ nm) spectra of r6G in toluene. (B) Rotational anisotropy decay of r6G in methanol (black balls) and toluene in the presence of NCs (red balls). Samples were excited at 430 nm, while the emissions were collected at emission peak positions of r6G in free (without NCs) and bound (with NCs) forms. 138
43. **Figure 7.7.** Femtosecond transients of NCs in toluene at different NC-to-r6G ratios at 25 °C (A) and 60 °C (B), respectively. Transients are fit to a stochastic kinetic model, best fitted 141

curves are shown by the black solid lines. We fitted the transients after a few picoseconds following the excitation to avoid any interference from the excitation pulse.

44. **Figure 7.8.** Respectively, Femtosecond and TCSPC transients (A and B) of CsPbBr₃ NCs in toluene at three different temperatures 5 °C (black), 25 °C (blue) and 60 °C (red). 144

LIST OF TABLES

	Page No.
1. Table 4.1. Best fitted parameters of Stern-Volmer (SV) plots at different temperatures (Figure 4.6) Bimolecular diffusion-controlled rates (k_d) of water. $k_d = 8 \times 10^3 RT / 3\eta$ $M^{-1}s^{-1}$; T is the temperature in K, R ($8.3145 J mol^{-1} K^{-1}$) is the gas constant. η , the viscosity coefficient. For water $\eta = 10^{-3} kg m^{-1}s^{-1}$ (20 °C), $0.653 \times 10^{-3} kg m^{-1}s^{-1}$ (40 °C) and $0.466 \times 10^{-3} kg m^{-1}s^{-1}$ (60 °C), respectively.	75
2. Table 4.2. Best fitted parameters (related to the GQD-DMA complexation reaction) of FCS curves using Equation 4.4 (Figure 4.7A).	83
3. Table 4.3. Best fitted parameters (pertaining to $a_i[f(\tau_{Di})]$ histogram; Figure 4.7B) of FCS curves using Equation 4.4. Here translational diffusion parameters are reported. During fitting a total of 30 fixed diffusion times (τ_{Di} ; $i=1$ to 30) were placed linearly in 0.015-0.045 ms time regime. Fitting started from 0.015 ms as the fastest diffusion time to avoid mixing of complexation reaction time (τ_R) with diffusion time.	85
4. Table 4.4. Fitting parameters of femtosecond fluorescence transients ($\lambda_{ex} \sim 400$ nm and $\lambda_{em} \sim 470$ nm) of GQDs at different DMA concentrations. Since femtosecond transients were recorded only up to 100 ps, we fixed	91

long components (post ns, τ_2 and τ_3) from TCSPC fittings.

5. **Table 5.1.** Stern-Volmer fitting parameters and bimolecular diffusion-controlled rate (k_d) in aqueous methanol at different temperatures. 98
6. **Table 5.2.** The fluorescence lifetime of GQDs at different DNT concentrations and temperatures (measured using TCSPC setup) 99
7. **Table 5.3.** Fitting parameters of femtosecond transients of GQDs in the absence and presence of DNT at various temperatures (Figure 5.5 A, B). A lamp like decay component (~ 0.25 ps) is not included in the table, since it is not a real decay component. The long component (τ_2) was fixed as the average TCSPC lifetime (Table 5.2). 108
8. **Table 6.1.** Best fitted parameters of femtosecond transients at different emission wavelengths. The longest component was fixed from its average lifetime measured at the same wavelength using TCSPC (Table 6.2.) 119
9. **Table 6.2.** Fluorescence lifetime components of GQDs in toluene at different excitation and emission wavelengths. 120
10. **Table 6.3** The lifetime of hot Carrier ($\tau_{cooling}$), dynamic Stokes shift ($\Delta\nu = \nu_0 - \nu_\infty$) of TRES due to cooling, and peak positions of hot (ν_0) and cold (ν_∞) emissions of colloidal 122

GQDs for both excitations.

11. **Table 7.1.** Tail fitting parameters of TCSPC measured fluorescence transients of CsPbBr₃ NCs at different NC-to-r6g ratios and temperatures. 136
12. **Table 7.2.** Fitting parameters of femtosecond transients of NCs using Stochastic Kinetic Model at different NC-to-r6G ratios and temperatures 143

Materials having intermediate electrical conductivity values between conductors and insulators are known as semiconductors. Broadly there are two types of semiconductors: (i) elemental semiconductors- these are the single element materials of Si, Ge, Sn, Se, Te, etc. (ii) compound semiconductors- consist of two or more elements.^[1] The latter category is exemplified by GaAs, CdS, CdSe, ZnS, and various allotropes of carbons, among many others. When the size of the semiconductor material is comparable to the Bohr exciton radius, exotic optical properties are observed as a result of tight confinement of exciton, popularly known as the quantum confinement effect.^[2,3] Semiconductor nanocrystals (NCs) are highly desirable in real applications; not only for their exceptional optical properties, but the high surface-to-volume ratio is also very crucial for interfacial charge transfer in light-harvesting devices. High demands of semiconductor NCs in energy and biomedical research have motivated researchers to fabricate different types of NCs [graphene quantum dots (GQDs), carbon dots (CDs), metal chalcogenide quantum dots (QDs), perovskite, etc.] with tunable optical and surface properties following facile synthetic routes. These novel materials are subjected to further explorations from fundamental viewpoints such as carrier trapping, diffusions, and exciton dissociation for their better utilization in various applications like photovoltaic, optoelectronic, photodetector, phototransistors, low threshold lasers, LEDs, and single-photon emitters.^[4-12] In the modern world, with rising awareness of human health and the environment, the demand for clean energy has significantly increased. Solar energy harvesting has evolved as one of the leading techniques for clean energy, where NCs are recognized as a

promising contender. NCs, in light harvesting devices, efficiently convert solar energy to electrical (solar cell) and chemical energies (solar fuel) which have been well documented in literature.^[13-19] Besides photovoltaic and photoelectronic applications, these NCs are also the most promising probes for bioimaging and drug delivery.^[20-25] In this context, metal chalcogenides NCs enwrapped with a lipid/micelle are ideal for bio-imaging and drug delivery in living organisms where the lipid/micelle not only endows surface passivation, but also reduces cytotoxicity.^[25] A step forward in this direction, researchers tried to obtain quantum-confined dots of an element that presents as a major constituent in living organisms, i.e. carbon, for enhanced compatibility with living systems. Their efforts led to, two interesting 3D quantum-confined carbon allotropes, namely a truncated 2D graphene sheet having dimensions comparable to Bohr radius and carbon dots (CDs)- few layers of graphene sheets stacked on x-y facets to form 3D spherical structures with few nm diameters.^[26,27] Besides their appreciable bio-compatibility desirable for imaging applications, excellent material properties such as long carrier diffusion length, high photoluminescence quantum yields (PLQYs.), single photon emission, etc. are other aspects that have huge implications in device applications.^[28,29]

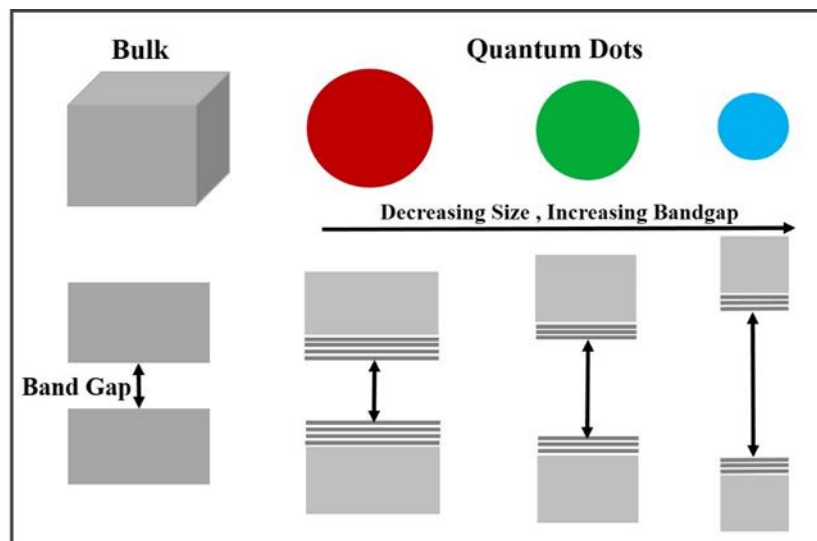
The efficiency of an NC-based device is fundamentally controlled by a series of photophysical processes that need to occur in a sequence with the desired timescale (fs to ps regime). The availability of modern LASERs and ultrafast spectroscopic techniques have revolutionized modern science and enabled the study of ultrafast photophysical processes of NCs which was impossible in the recent past. We have studied several fundamental processes having large implications in device application, using NCs of carbon allotropes and perovskites. Interesting results of our study are discussed in the succeeding chapters that provided a fundamental understanding of carrier kinetics, trapping, de-trapping, charge transfer in NCs, and urgency of sample purifications. The

outcome of our findings would contribute to bridging the gap between fundamental understanding of the photophysical process and its implication in the real application. Thereby the efficiency of a device can be precisely tuned by controlling the photophysical process within the NCs. A brief introduction of NCs used in our study is provided in the subsequent sections.

1.1. Quantum Dots (QDs)

1.1.1. General Properties

Quantum dots are nanostructured quantum confined semiconductor materials.^[2] Their size ranges from ~2-20 nm. They are currently in limelight due to their excellent optical, electrical, and mechanical properties. QDs have unique optoelectronic properties which are in between the bulk and molecular levels due to their quantum confinement effect.^[2] To understand QDs and quantum confinement effects, it is important to understand the concept of the exciton. When a semiconductor material is excited with a suitable wavelength of light the electron in the valence band goes to the conduction band and leaves a hole in the valence band. This electron and hole attract each other by Coulombic force leading to the formation of a bound state known as an exciton. The distance between electron and hole of the exciton is known as exciton Bohr radius which is different for different materials. After sometimes the exciton recombines releasing a photon and the process is known as fluorescence. If the size of an NC falls beyond the exciton Bohr radius the electron gets confined in discrete energy levels from continuous in bulk materials. In QDs electrons are confined in all the 3 dimensions and hence the structures are termed zero-dimensional materials. Further size reduction of quantum confined NCs causes a significant increase in bandgap energy and subsequent blue shift of absorption and emission spectra of the NCs (Scheme 1.1).



Scheme 1.1. Illustration of size-dependent bandgap energy of quantum confined NCs.^[2]

QDs bridge the gap between molecular and bulk levels properties and many exotic phenomena such as size, shape, and composition-dependent bandgap causing the tunable emission, PLQYs, high absorption cross-section, long carrier diffusion lengths, etc are unique in quantum-confined NCs.

Although there are various semiconductor nanomaterials like silicon, gold, silver, and metal chalcogenides-based quantum dots are available, we have mostly studied carbon-based NCs, such as GQDs and CDs for their non-toxic nature. In the subsequent sections, I will discuss the structure, properties, and applications of the NCs I used in my study.

1.1.2. Synthesis Procedure of NCs

Various synthetic approaches are reported in the literature and they are fundamentally categorized into two classes; (i) top-down approach and (ii) bottom-up approach.

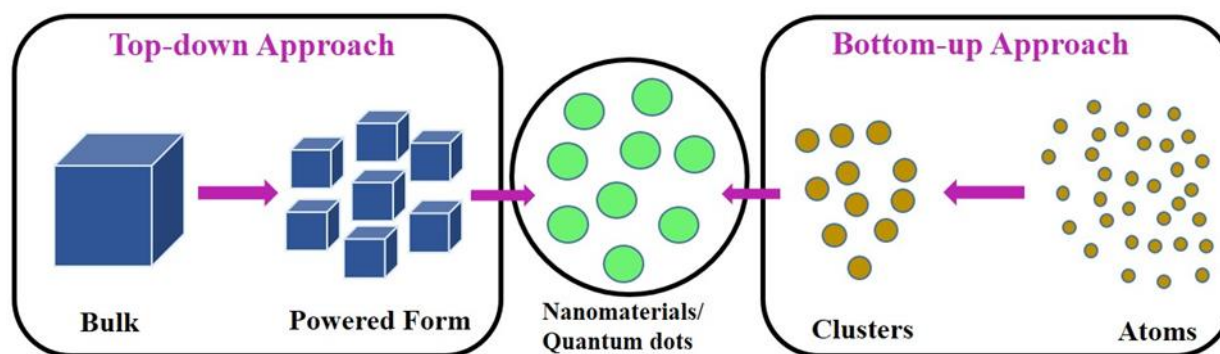
1.1.2.1. Top-down approach

To obtain the QDs, various tools and methods are used to cut down the bulk semiconductor to a

Nanoscale dimension. Milling, grinding, and chemical cutting (oxidation of carbon fibers to GQDs) methods are used to obtain NCs (2-20 nm) from bulk materials.^[30–32] Other methods like optical lithography, laser ablation, arc discharge, chemical etching, exfoliation, etc., are also used in this synthesis route.^[33–36]

1.1.2.2. Bottom-up approach

This approach involves the use of small precursor molecules as the starting material. The organometallic chemical route, colloidal precipitation, hydrothermal synthesis, reverse-micelle route, sol-gel synthesis, template-assisted sol-gel, electrodeposition, hot injection method, precipitation method, ultrasonication, etc., are some of the bottom-up techniques reported for the preparation of QDs.^[37–42]



Scheme 1.2. Schematic representation of top-down and bottom-up synthetic approaches used in QD synthesis. The left panel represents the top-down approach whereas the right one represents the bottom-up approach.

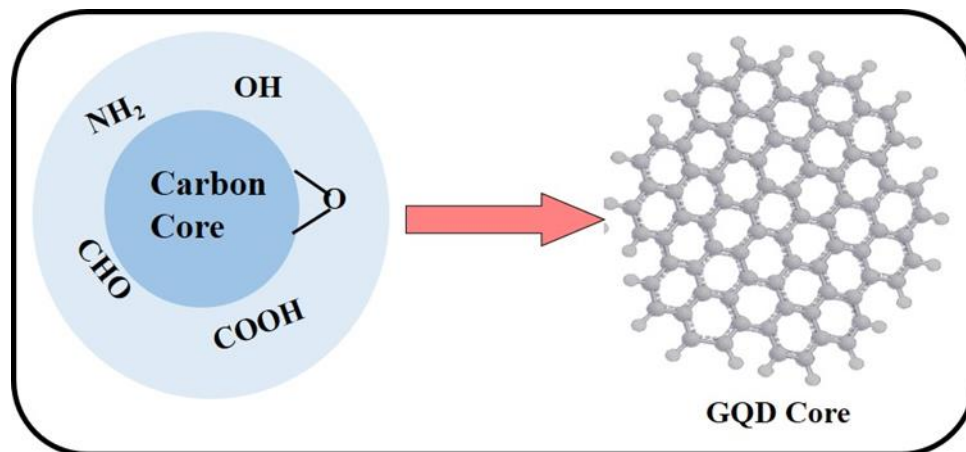
1.1.3. Carbon Dots and Graphene Quantum Dots

CDs and GQDs are carbonaceous materials having an abundant sp^2/sp^3 carbon backbone along with hydrogen, oxygen, and nitrogen.^[43] These are zero-dimensional materials with a size less than

10 nm. Though both CDs and GQDs are considered to be members of the same family, they are structurally different in terms of their optical and material properties. The former was accidentally discovered in the year 2004 by Xu. group, during the purification of single-walled carbon nanotubes,^[44] whereas the latter was fabricated by Ponomarenko and Geim. in 2008 by etching single-layer graphene sheet.^[45] The structural and photo-physical properties of these materials greatly depend upon the synthetic route used, defect state involved, surface groups, and doped heteroatoms.

1.1.3.1. Structure

CDs are quasi-spherical nanomaterials with less than 10 nm in size and have a carbogenic core and various functional groups at the surface. Depending upon the synthesis route, the carbogenic core can be either crystalline or amorphous.^[46] On the other hand, since graphene sheets, and graphene oxides are the starting materials for GQDs, it possesses a graphene lattice core (disc-like structure) with better crystallinity having a size < 20 nm and thickness <10 nm.^[47-50] The core can be made up of single-layer or multi-layer graphene sheets. Also, various functional groups are present on the GQD surface. GQDs when compared with CDs are bigger and exhibit better crystallinity. Although both the materials consist of different core structures, both are passivated with surface groups. Functional groups like carboxyl, hydroxyl, epoxy, and carbonyl contribute to the optical properties of the materials and make them water-dispersible as well^[51,52] Similarly, heteroatoms like oxygen, nitrogen, and sulfur enhance luminescence as well as the electrical conductivity properties to a large extent.



Scheme 1.3. Illustration of CD and GQD structures.

1.1.3.2. Properties

Both CDs and GQDs possess fascinating properties like low cytotoxicity, water-solubility, flexibility to surface modifications, cell permeability, outstanding biocompatibility, excitation-dependent emissions, and many others.^[53–56] However, the optical properties, mainly the origin of excitation-dependent emissions remained a matter of debate for these materials. Different explanations have been provided by different groups for the excitation-dependent emission property of CDs. Some of the explanations are quantum confinement and band edge effect, molecular fluorophore emission, surface state emission, reaction time, slow solvent relaxation, self-trapped exciton emission, and ground-state heterogeneity.^[57–63] Several groups claimed surface states or the heteroatoms present in the surface groups are responsible for the excitation-dependent emission property of CDs.^[51,64–66] Ding group demonstrated that the increase in the degree of oxidation of the surface states of carbon dots is mainly responsible for the fluorescence property of the material.^[66] They claimed the size of the material does not contribute to the emission property. Also by employing silica column chromatography, they have separated 4 types of CDs of the same size, emitting blue, green, yellow, and red lights. Jiang group has explained,

that the presence of different surface groups mainly contributes to the emission property.^[64] They observed; as the electronegativity of the surface heteroatom decreases, the emission wavelength shifted towards the lower energy side. Kumbhakar group explained in an ensemble study, the generation of multiple discrete electronic states leads to excitation-dependent shifting of emission spectra of CD, and these states are generated due to the presence of different types of aggregates even in a very dilute solution.^[57] Nandi group showed slow solvent relaxation around the CDs which competes with the fluorescent lifetime of the material and mostly contributes to the red edge effect of emission properties of the materials.^[59] Yuan group claimed in their synthesized carbon dots different colour emissions were originated from different sized particles.^[67] A quantum-confinement-induced spectral shift of the materials was also claimed by Li group and Peng group independently.^[30,68] Emmanuel group and Feldmann group showed CD emission property mainly depends upon the synthesis time as well as the temperature of the hydrothermal reaction.^[69,70] They observed that low temperature and less reaction time led to the formation of molecular fluorophores with high quantum yields whereas high temperature and large reaction time led to the formation of the carbogenic core with low quantum yield. In this thesis, in chapter three I describe our work on the understanding of the emission properties of CDs where we have emphasized the urgency of sample purification. The literature in the CDs field is full of surprising claims, counterclaims, and controversies on the origin of their exotic optical properties. The exact mechanism for unusual optical properties is still elusive, creating a hurdle to the maturation of their application field.

1.1.3.3. Applications

Despite several controversies about the optical properties of CDs, they still have largescale applications in bio-imaging, drug delivery, sensing, LEDs, solar cell, catalysis, supercapacitors,

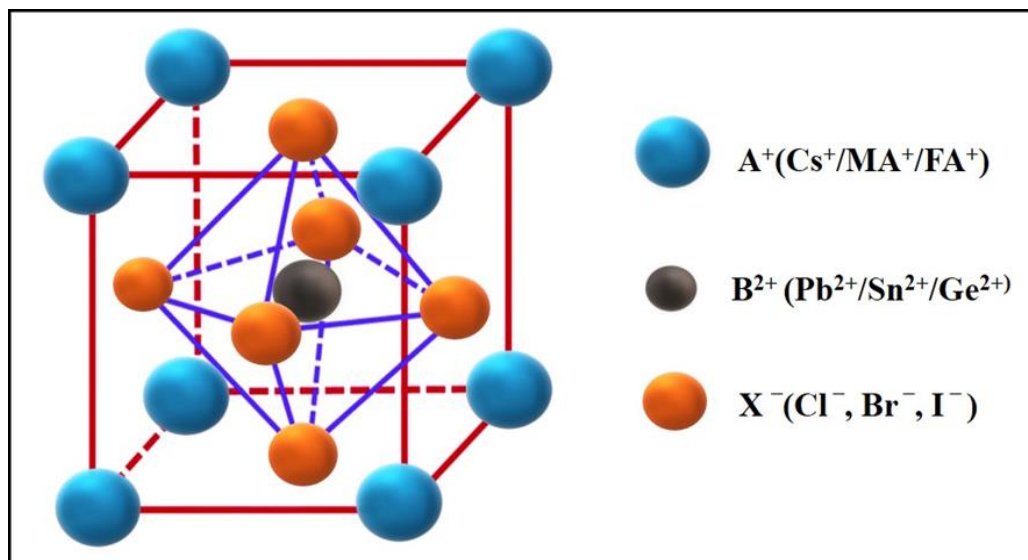
and many others.^[29,71] For example, in cell imaging, for the first time, Sun group showed the potential of CDs as fluorescent markers. In that work, they used PEG1500N-passivated carbon dots to label the E.Coli and Caco cells and took the image through a confocal microscope.^[72] Due to the sensitive electronic property, CDs and GQDs are proven to be potential candidates for sensing biologically relevant ions, metal ions, proteins, etc.^[73,74] Many exploited the emission property of CDs and GQDs in photovoltaic and optoelectronic applications. These materials can be used as building blocks of solar cell devices. They can also be used as light-absorbing species, carrier transporting layers, and sensitizers. For example, Basak group showed that the ZnO-nanowire-GQD composite exhibits an open circuit voltage of 0.8V.^[75] In their work, they have prepared the GQD by hydrazine reduction of Graphene oxide. Titirici group showed biomass-derived CDs can be used as sensitizers for ZnO nanorod based solar cell devices.^[76] Fan group for the first time fabricated CuO/Cu/GQD triaxial nanowires for the Li-ion storage.^[77] There is still a long way to go with their applications and there is a large room for researchers to explore the field.

1.1.4. Perovskite Quantum Dots

Perovskite is a mineral CaTiO_3 , first discovered by Gustav Rose in 1839 in the Ural Mountains of Russia, and named after Russian mineralogist Lev Perovski. Afterward, any material having a crystal structure (ABX_3) similar to the CaTiO_3 structure is known as perovskite. Metal halide perovskites were first reported in the 19th century whereas their true potential in photovoltaic and optoelectronic properties was revealed in the early 21st century i.e. in 2009 when Kojima group have used organometal halide perovskite as visible-light sensitizers in photovoltaic cells for the first time.^[78]

1.1.4.1. Structure

Perovskite nanocrystals (NCs) are obtained with a three-dimensional (3D) structure, formed by three primary ions [monovalent (A) and divalent (B) metal ions and halide anion (X)] with a general formula ABX_3 .^[79] They can be crystallized in tetragonal, orthorhombic, or cubic forms owing to different reaction conditions. They go through phase transitions as reaction temperature changes.^[80] The perovskites used in photovoltaic applications can be classified into two classes; all-inorganic and organic-inorganic halide perovskites depending on their A-site cation. In all-inorganic halide perovskite, A cation can be Cesium or Rubidium, B cation can be lead, tin, or germanium and X anion represents single or mixed halides (chloride, bromide, iodide). However, in organic-inorganic halide perovskites, A cation is either methylammonium (MA) or formamidinium (FA). In both types of NCs B cation coordinates with six X anions and A cation sits in a cavity formed by eight BX_6 octahedra. The ideal structure of perovskite is illustrated in scheme 1.4. The stability of the ideal ABX_3 perovskite structure can be predicted by the Goldschmidt tolerance factor, $t = (r_A + r_X) / \sqrt{2}(r_B + r_X)$, where r is the ionic radii of the A, B, and X ions].^[81] Generally, when the tolerance factor is in the range of ~ 0.76 - 1.13 , stable 3D perovskite structures are formed. Outside this range, other structures are formed.^[81] At the edge of the tolerance factor, the perovskite reorganizes itself to more stable hexagonal or orthorhombic structures at room temperature. Perovskite structure stability also depends upon the octahedral factor $\mu (=r_B/r_X)$ as it defines the stability of the BX_6 octahedron.^[81] The stability range for μ is between 0.442 and 0.895 . The perovskite compounds are held together with ionic bonds, hence perovskite NCs can be formed even at low reaction temperatures.



Scheme 1.4. Pictorial representation of halide lead perovskite. The blue balls represent the A-site cation, the black ball represents the B-site divalent cation and the orange balls represent the monovalent halide anions.

1.1.4.2. Properties

Metal halide perovskite NCs show interesting optical properties like high PLQYs, narrow tunable emission spectrum, and large absorption coefficient. The emission spectrum is tunable in a range from UV to near IR by varying the size, dimensionality, and its constituent elements. Interestingly, modifying the halide composition could tune the emission spectrum in the whole visible region. Using mixed halide composition, Protesescu et al. demonstrated that the emission peak position of CsPbX₃ NCs could be tuned to 410 nm (X = Cl), 512 nm (X = Br), and 685 nm (X = I), or in practice to all intermediate wavelengths fabricating mixed halide NCs with desired halide ratios.^[82]

1.1.4.3. Applications

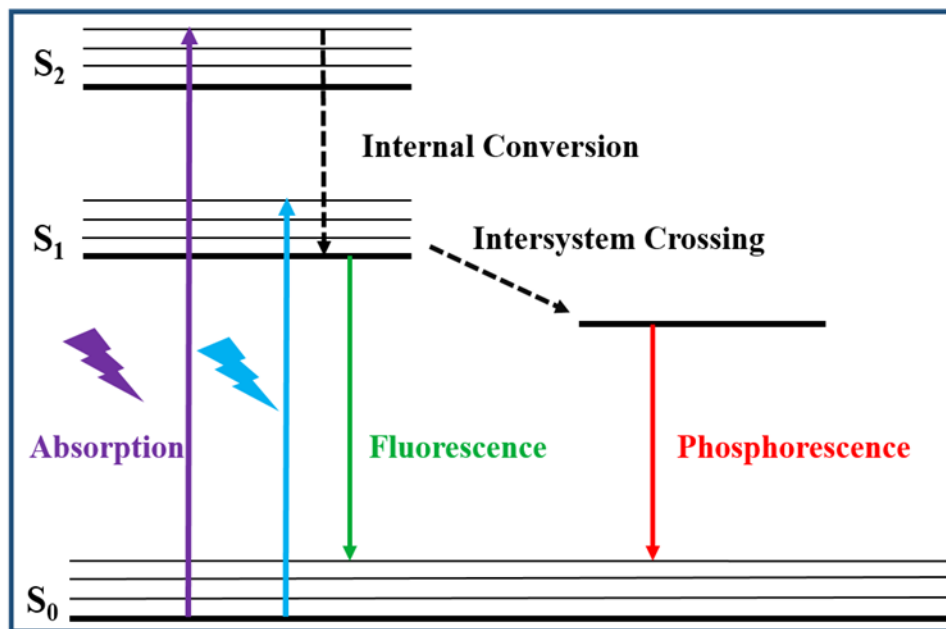
Lead halide perovskites NCs are promising materials in several real applications, like optoelectronics, photovoltaics, low threshold LASERS, LEDs, photodetectors, transistors, and photocatalysis.^[80,83] For example, Zeng group fabricated blue, green, and yellow CsPbX₃ QDs

based LEDs with external quantum efficiencies of 0.07%, 0.12%, and 0.09%, respectively.^[84] Zhu group, demonstrated room-temperature, wavelength-tunable emissions from single-crystal $\text{CH}_3\text{NH}_3\text{PbX}_3$ nanowires with low lasing thresholds.^[85] Su group demonstrated that CsPbBr_3 -Graphene Oxide composite is an efficient photocatalyst for CO_2 conversion.^[86] Volder group fabricated perovskite photo batteries by employing a 2-Dimensional perovskite $((\text{C}_6\text{H}_9\text{C}_2\text{H}_4\text{NH}_3)_2\text{PbX}_4)$ nanocrystal to obtain photo-charging and Li-ion storage, simultaneously. They claimed the efficiency of their photo batteries is comparable to those of electrodes using mixtures of solar cells and batteries as well as they provide storage capacities of 100 mAh/g.^[87]

However, the research on halide perovskites is still at its early stage in terms of its synthesis, stability as well as applications. There is enough room for researchers for further exploration in this field.

1.2. Photophysical Processes

To start with the classical concept, when light with a suitable wavelength interacts with a molecule it is absorbed in a femtosecond timescale (10^{-15} s). As a result, the molecule goes to an electronically excited state from the ground state. Afterward, the molecule comes back to the ground state through various radiative and non-radiative pathways. The non-radiative paths mostly involve internal conversion and intersystem crossing. The radiative paths involve the emission of a photon. Fluorescence and phosphorescence are the two radiative deactivation paths after the photoexcitation of a molecule. The whole process is well explained pictorially through the Jablonski diagram (Scheme 1.5).



Scheme 1.5. Jablonski diagram representing absorption of a photon followed by various de-excitation processes.^[88]

1.2.1. Fluorescence

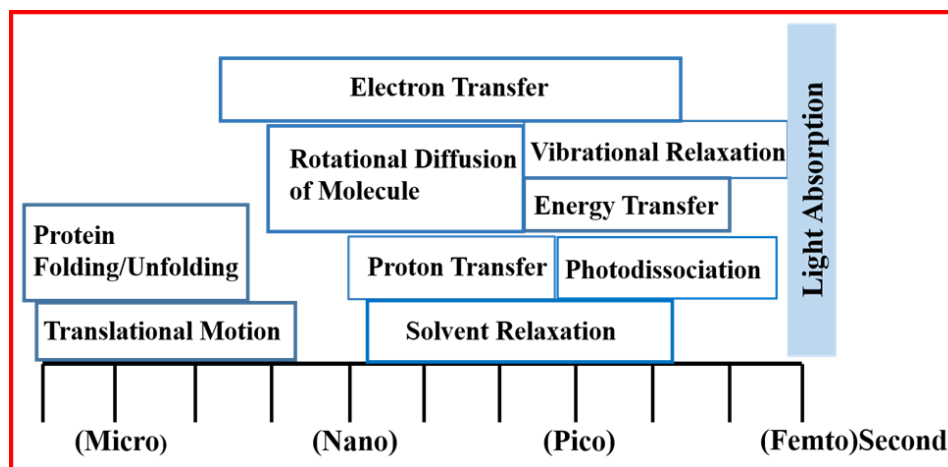
Fluorescence is commonly observed when the singlet excited state is relaxed to the ground state (S_1 to S_0) following a radiative pathway, that involves the emission of photons. This process was observed by Sir John Frederick William Herschel for the first time in 1845, as the colorless solution of quinine sulfate appeared to be blue when exposed to sunlight. Later in 1852, Sir G.G. Stokes demonstrated the phenomenon was an emission of light followed by absorption of light. Also, he coined the term fluorescence. Irrespective of the excitation wavelength, fluorescence is always obtained from the lowest vibrational state of S_1 which is known as Kasha's rule. As a result, fluorescence occurs at lower energies or higher wavelengths when compared to absorption.

1.2.2. Excited-state Processes

After photoexcitation, fluorophores may undergo many excited state processes like electron or hole transfer, proton transfer, photodissociation, energy transfer, molecular motions, solvent

relaxation, relaxation of carriers to band edge state, and conformational change. These processes occur in different timescales as illustrated in scheme 1.6. These processes can be intramolecular or intermolecular in presence of foreign molecules. As these excited state processes are nonradiative and compete with the intrinsic de-excitation processes of fluorophores, we observe a decrease in fluorescence intensity which is known as fluorescence quenching.^[88,89] As molecular fluorescence is highly sensitive and selective to the excited state processes, analytical tools involving molecular fluorescence are much popular among the scientific community. By utilizing and analyzing the time-resolved fluorescence emission of the materials, the timescale, as well as the mechanism of the non-radiative excited state processes, can be explained.

In this thesis, we mostly studied the mechanistic insights of photoinduced electron/hole transfer and associated timescales in the NC composites. In the subsequent section, I provide a discussion on the photoinduced carrier transfer process in GQDs and Perovskite NCs.



Scheme 1.6. Representing various excited state processes and their respective timescales.^[89]

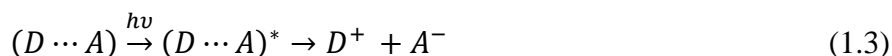
1.2.2.1. Photoinduced Electron Transfer (PET)

PET reaction is one of the widely studied photochemical reactions documented in the literature.^[88,89] PET is indispensable not only in device application but also in biology, for example

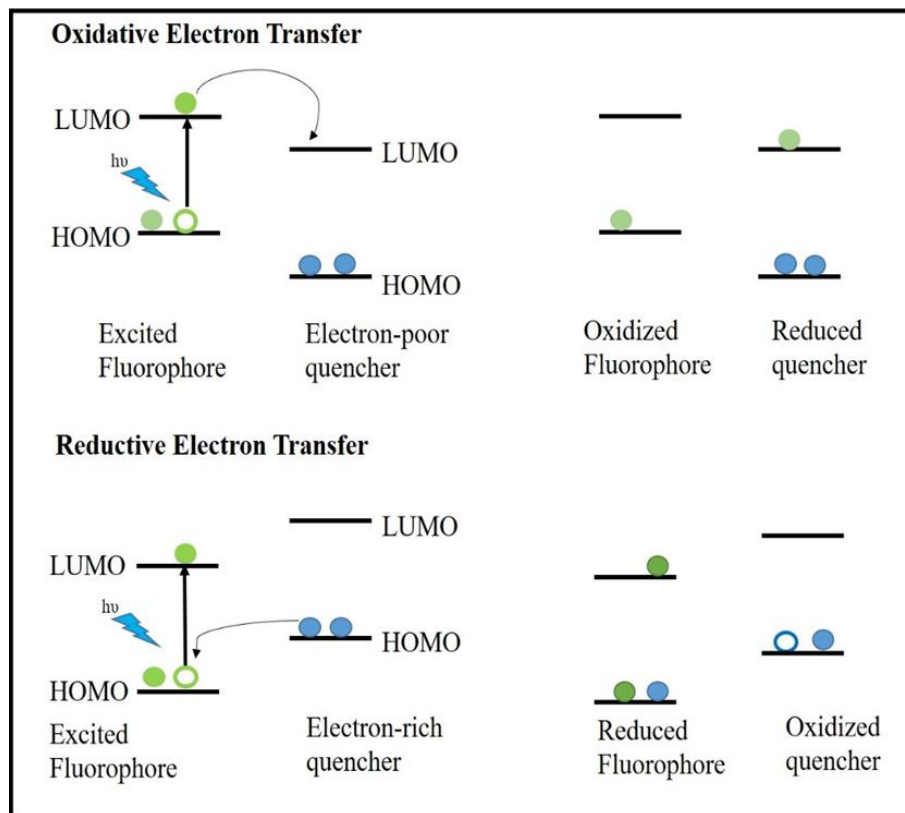
in plant photosynthesis PET plays a crucial role as first observed by Joseph Priestley in the 18th century. Ever since the scientific community has extensively studied PET and charge separation processes to understand their crucial role in photosynthesis as well as in their widespread applications in optoelectronics and photovoltaics. Fluorescence quenching studies can be utilized to get insight into the mechanistic understanding of PET in quantum-confined NC assemblies.^[88]

1.2.2.1.1. Basic Principle

Most simple PET reactions can be explained as the transfer of an electron from one species to another upon photoexcitation. The electron-rich species, from which the electron is transferred is known as the donor (D) and the electron-deficient species that accepts electrons is known as the acceptor (A). In this process, the light-absorbing species can either be the donor (D) or acceptor (A) or a ground-state complex of donor and acceptor (D-A) as shown by the following reaction scheme.



PET involves proper orbital overlap between the participating donor-acceptor pair present at contact distance. An electron donor always has an electron-occupied orbital with higher energy compared to the vacant orbital of the electron acceptor. When the light-absorbing species i.e. fluorophore acts as a donor, it is called an oxidative PET and when the fluorophore acts as an acceptor it is called reductive PET. (Scheme 1.7). The direction of electron transfer is decided by the redox potential of the reacting species.



Scheme 1.7 Illustration of PET reaction between donor and acceptor.^[89]

1.2.2.1.2. Thermodynamics involved in PET^[89]

Photoexcitation leads to the enhancement of redox activity of the material as it promotes an electron from the highest occupied molecular orbital (HOMO) to its lowest unoccupied molecular orbital (LUMO) of the light-absorbing material and generates one electronically excited state. As the excited state possesses lower ionization potential than the ground state and the electron affinity of the ground state is enhanced after photoexcitation due to the generation of a hole, this leads to the possibility of electron or hole transfer. The driving force i.e. change in Gibbs free energy of an electron transfer reaction is estimated by the following equation,

$$\Delta G = E_{red}(A) - E_{ox}(D) - \Delta E_{00} \quad (1.4)$$

Here, ΔG is the chemical driving force i.e the free energy change for PET. $E_{red}(A)$ is the reduction

potential of the acceptor, $E_{ox}(D)$ is the oxidation potential of the donor. ΔE_{00} is the energy difference between the lowest vibrational energy of the excited state and the ground state of the light-absorbing molecule. The above-mentioned equation is known as the Rehm-Weller equation. Another stabilization factor arising from Columbic interaction ($-e^2/\epsilon d$) can be added, where e is the charge of an electron, ϵ is the dielectric constant of the medium and d is the distance between the two charges. The negative ΔG value leads to an efficient PET.

1.2.2.1.3. Importance of PET study

The efficiency of solar cell devices, LEDs, photon detection, phototransistor, sensing, etc. are fundamentally controlled by carrier transfer.^[90–92] Hence, an in-depth analysis of PET kinetics and the associated mechanism is still in demand to understand the factors affecting the electron transfer process. The factors involve chemical driving force, electronic coupling parameter, the structure of the sample, surface traps, etc. Hence, researchers are expected to obtain a mechanistic understanding of PET kinetics and measure the associated timescale in different materials to fundamentally understand this process for their real-time applications.^[93–96]

1.2.2.1.4. PET involving Quantum Dots

As already discussed, QDs when interacting with suitable energy of light ($h\nu$) that matches with the fundamental threshold energy of QDs i.e. the bandgap energy (E_g), generate charge carriers as electrons jump from the valence band to the conduction band. The fast separation of these charge carriers is one of the important parameters in QD sensitized solar cell devices for efficiency enhancement. And this can be achieved by PET in two ways. The electron can be extracted from the conduction band with the help of an electron-deficient molecule, and the hole can be extracted from the valence band with the help of an electron-rich molecule. (Scheme 1.8)

QDs when interacting with light energy ($h\nu$) higher than the bandgap energy (E_g), generate hot carriers by sending carriers to higher energies in valence and conduction bands. These carriers are referred as hot carriers as they are out of equilibrium having excess kinetic energy. And the distribution of excess energies among the carriers can be described by the following equations,

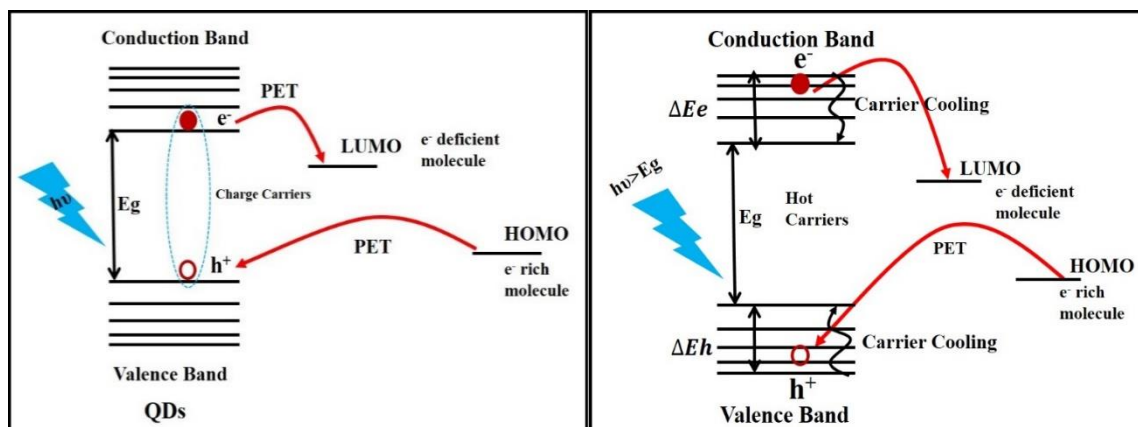
$$\Delta E_e = (h\nu - E_g) \left(1 + \frac{m_e}{m_h}\right)^{-1} \quad (1.5)$$

$$\Delta E_h = (h\nu - E_g) - \Delta E_e \quad (1.6)$$

Where ΔE_e is the difference in energy between the conduction band and the initial energy of the electron in a higher energy level due to photoexcitation (excess kinetic energy of photogenerated electron), similarly ΔE_h is the excess kinetic energy of photogenerated hole, m_h^* and m_e^* are the effective masses of holes and electrons respectively.^[97] These hot carriers come back to the equilibrium state i.e. band-edge state by thermal energy loss through various processes, which is one of the important factors for efficiency loss in solar cell devices.^[98] This carrier cooling timescale varies from femtosecond to nanosecond timescale. This efficiency loss can be stopped by extraction of hot carriers through the ultrafast PET process much before the carrier relaxation.

As a result PET, fundamentally controls the efficiency of a solar cell device. A suitable electron-donor pair design would enable an efficient PET and thereby improve the device's performance.^[99–102] Hence, many researchers have studied the ultrafast PET as well as carrier cooling processes in QD-composites for their successful device applications.

In this context, many groups exploited PET dynamics in GQDs and halide perovskites composites for their real time application in QD sensitized solar cells.



Scheme 1.8. Pictorial representation of charge carrier generation and extraction of carriers through PET process.

Samanta and co-workers have extensively studied the carrier cooling time as well as the rate of hole transfer in halide perovskite nanocrystals.^[103–106] In one of their recent works, their ultrafast pump-probe experiment confirmed that, the efficiency of hole transfer process of CsPbBr₃ nanocrystal depends on the energy content of the hole.^[106] They have also achieved a maximum transfer efficiency of ~43%, for photoexcitation energy of ~1.46 E_g. In another work, they found perovskite nanocrystals to be excellent hole scavengers when complexed with Cadmium chalcogenide quantum dots.^[104]

Patra group also studied the carrier transfer processes with different quantum dots. In one of their recent works, they have shown the hot carrier cooling process of lead halide perovskite nanocrystal as well as the hot hole transfer process from the nanocrystal to 4-pyridyl porphyrin molecule. They have obtained the maximum hot hole transfer efficiency at 370 nm excitation to be 42%.^[100]

Kamat group also studied the PET process in various types of QDs.^[107–109] In one of their recent work, they have studied both hot and cold electron transfer from lead halide perovskite to Au

nanoparticles by employing a femtosecond transient absorption spectroscopy. Through their study they have found out the electron transfer rate constant is much larger for the hot electrons ($(2.43 \pm 0.39) \times 10^{12} \text{ s}^{-1}$) compared to the relaxed electrons ($(1.73 \pm 0.27) \times 10^{10} \text{ s}^{-1}$).^[109]

Prasad group studied the PET between GQDs and aniline as well as six aniline derivatives. They obtained the bimolecular rate constants of the dynamic quenching for all the cases are in the range of $(1.06\text{--}2.68) \times 10^9 \text{ M}^{-1} \text{ s}^{-1}$. The proper band alignment of the GQD-aniline pair, as well as the detection of radical cations of aniline derivatives by a nanosecond laser flash photolysis setup, confirmed the PET from aniline derivatives to the GQD.^[110]

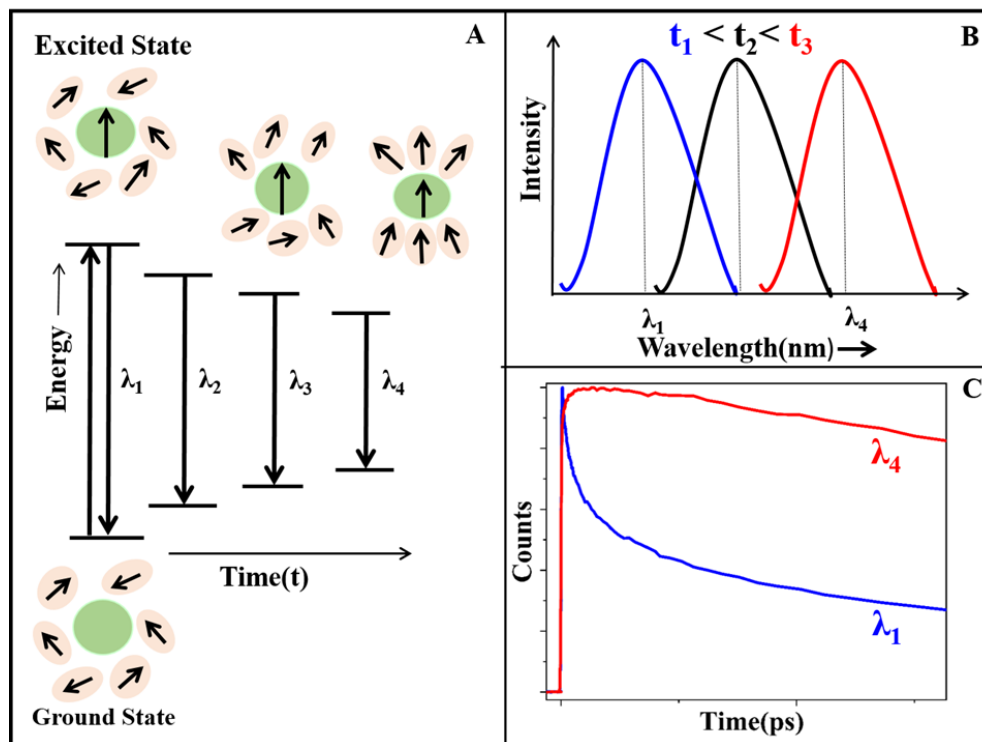
Our group (Ghosh group) studied the PET of different QDs composites.^[95,111–113] Our recent studies on mechanism and timescale of PET studies involving GQD composites and perovskite composites are discussed in this thesis.^[114–117]

1.2.2.2. Solvation Dynamics

Solvation dynamics is an excited state process that tells about the relaxation of solvent dipoles around the generated solute dipole instantly after photoexcitation. In the ground state, the solvent molecules are randomly arranged around the non-polar solute. Instantly after photoexcitation, a large dipole of the solute is created, and the solvent molecules rearrange themselves according to the dipole for the electrostatic stabilization of the solute. Hence, it results in a gradual decrease in the energy of the solute with time. Due to the increase in population of the solvated state a growth phenomenon is observed in the red end of the time resolved spectra. (Red curve scheme 1.9 C) The fluorescence maximum of the solute shows a time-dependent redshift, known as dynamic Stokes shift.(Scheme 1.9 B) This can be observed by constructing time-resolved emission spectra (TRES) using the steady-state emission spectra and fluorescence decays of the emitting solute.

The process is well explained in Scheme 1.9.

As in literature, slowed solvation dynamics which competes with the fluorescence lifetime of the molecule is stated to be one of the reasons for excitation-dependent emission properties in fluorescent carbon dots samples^[59], we have analyzed the TRES spectra carefully to understand the mechanism in the third chapter.



Scheme 1.9. (A) Pictorial representation of the formation of low energy solvated states due to stabilization of the polar excited state of the fluorophore after photoexcitation through interaction between fluorophore and solvent dipoles. (B) Figure showing shifting of emission spectra towards lower energy side with time due to formation of solvated states right after photoexcitation. (C) Represents the wavelength-dependent fluorescence decay measured by the time-resolved fluorescence technique. Here blue and red curve represents the blue end and red end emission wavelength of the steady-state spectrum respectively.

1.3. Scope and Objective of this Thesis

This thesis is divided into seven chapters. The first two chapters are the introduction and instrumentation chapters. The next five chapters are the work chapters. In this introductory chapter, I have given a brief description of the basic concepts and state of the art of semiconductor materials i.e. quantum dots and the photophysical processes studied in this thesis. The second chapter describes the basic instrumentation techniques as well as the data analysis methods used in this thesis work.

The third chapter provides insight into our study to understand the excitation-dependent emission properties of the fluorescent carbon dots. We have studied citric acid-based carbon dots and found out the answer to its emission property lies in its ground state heterogeneity. In this chapter, we have explained the urgency of FCD sample purification before commenting on their spectral properties and also proposed an efficient purification protocol with column chromatography followed by membrane dialysis. The fourth and fifth chapter describes the mechanism and timescale of the PET process in graphene quantum dots composites with small organic molecules, in one case GQD is used as an electron acceptor and in another case as an electron donor. The sixth chapter explains the carrier cooling time and ultrafast hot hole extraction in a GQD-composite by employing a femtosecond upconversion spectrometer. And the last chapter i.e. the seventh chapter explains the intrinsic PET process in a perovskite nanocrystal and rhodamine 6G complex. We have employed Tachiya's stochastic model to analyze the femtosecond transients of the nanocrystals in presence of rhodamine 6G to understand the intrinsic PET.

Hence, this thesis provides an overview of optical heterogeneity of carbon dot samples, electron and hole transfer in graphene quantum dot (GQD)/perovskite NC- molecular system composites, and hot carrier cooling in GQDs. We believe the findings of this thesis would help researchers to

design next-generation photovoltaic devices, as well as the fluorescence quenching of these materials, can be exploited for further sensing applications.

This chapter tells about the experimental and theoretical techniques used for various spectroscopic studies. The experimental techniques describe the basic working principles and key concepts of various instruments used and the theoretical techniques describe the adopted methodologies for an in-depth data analysis.

As this thesis mainly focuses on the various photophysical processes of semiconductor nanomaterials, fluorescence-based experimental techniques like steady state measurements, both picosecond and femtosecond time-resolved fluorescence spectroscopy, and fluorescence correlation spectroscopy methods are extensively used. Other techniques like ITC (isothermal titration calorimetry) for measuring the binding constant of a reaction, HR-TEM, XRD, NMR, FT-IR, and AFM experimental techniques for sample characterization are also used.

To understand the various processes in the material some theoretical methodologies like construction of time-resolved emission spectra (TRES), time-resolved area normalized spectra (TRANES), calculation of chemical driving force for an electron transfer reaction between donor and acceptor, have been adopted.

2.1. Steady state absorption and emission spectra

Steady state electronic absorption spectra were recorded using a Jasco V-730 spectrophotometer with a resolution of 0.17nm in the UV-Vis region and the least detectable optical density of ~0.005. Dilute solutions ($\sim 10^{-5} - 10^{-6} \text{molL}^{-1}$) were used for the measurements.

Steady state fluorescence emission spectra were recorded using a Cary Eclipse fluorescence spectrophotometer with a xenon lamp (Agilent Instruments) as the excitation source. The emitted photons were collected in a perpendicular direction to the excitation with a photomultiplier tube (Hamamatsu; R-928F) photodetector. The lamp stability of the instrument was checked with a stable solution of coumarin dye during all the measurements.

2.2. Time-Resolved Fluorescence Measurements

Time-resolved data provides much more information related to the excited state dynamics of the sample when compared to the steady state data as the latter talks more about the equilibrium state.

After photoexcitation of a sample with a sharp pulse of light, it results in an initial population (n_0) of the fluorophore in the excited state. The excited state population decays as time proceeds. The decay process proceeds through both radiative and non-radiative pathways. The change in the excited state population of molecules ($n(t)$) at any time t , is related to the rate of radiative (k_r) and non-radiative (k_{nr}) decay constant given by the following equation,^[88,118]

$$\frac{dn(t)}{dt} = -(k_r + k_{nr})n(t) \quad (2.1)$$

In a time-resolved fluorescence experiment, we measure the fluorescence intensity ($I(t)$), which is proportional to the number of molecules in the excited state ($n(t)$). The time-dependent fluorescence intensity decays exponentially with time as,

$$I(t) = I_0 \exp(-t/\tau) \quad (2.2)$$

Where I_0 is the intensity at time 0, τ is the fluorescence lifetime of the molecule, and is the reciprocal of the total decay rate,

$$\tau = \frac{1}{(k_r + k_{nr})} \quad (2.3)$$

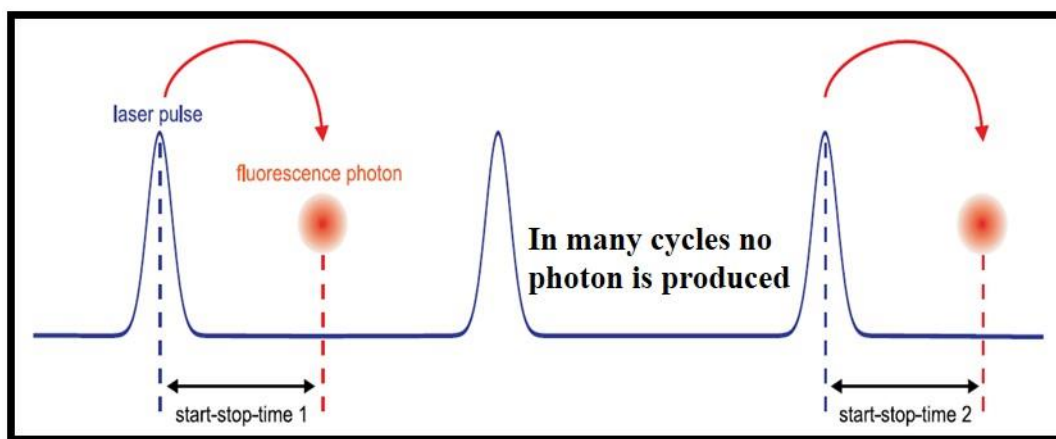
It is important to note here that fluorophores emit randomly throughout the decay, hence lifetime is a statistical average.

2.2.1. Time-Correlated single photon counting (TCSPC)

Time correlated single photon counting (TCSPC) is a very well-established setup to measure the picosecond-nanosecond fluorescence lifetimes of the fluorophores with the help of electronics.

2.2.1.1. Basic concept and working principle

TCSPC technique works like a fast stopwatch with two inputs start and stop. The basic principle of this technique is to measure the time gap between the short excitation pulse and the first detected photon. The TCSPC conditions are adjusted so that less than one photon is detected per hundred laser photons. This condition is maintained to avoid the pile-up effect which describes the photon loss due to the dead time of TCSPC electronics.^[88] These time gaps are stored in a form of a histogram. By repeating this process, the obtained histogram represents the lifetime decay profile. All these are done with the help of electronics.



Scheme 2.1. The working principle of TCSPC setup.^[119]

2.2.1.2. Instrumentation

At first, the sample is excited with picosecond diode lasers. For our experiments mostly 375nm, 405nm, and 445nm diode lasers were used as the excitation sources. One part of the excitation pulse is sent to the constant function discriminator (CFD), which measures the arrival time of the pulse accurately. This signal is then passed to a time-to-amplitude converter (TAC), to generate a voltage ramp. This pulse acts as the start signal. Another part of the excitation pulse is sent through the sample and the arrival time of the single emitted photon is detected by another CFD, which again sends the signal to TAC which stops the voltage ramp started by the laser pulse. The stored voltage information in TAC is proportional to the time delay between the excitation and emission pulses.

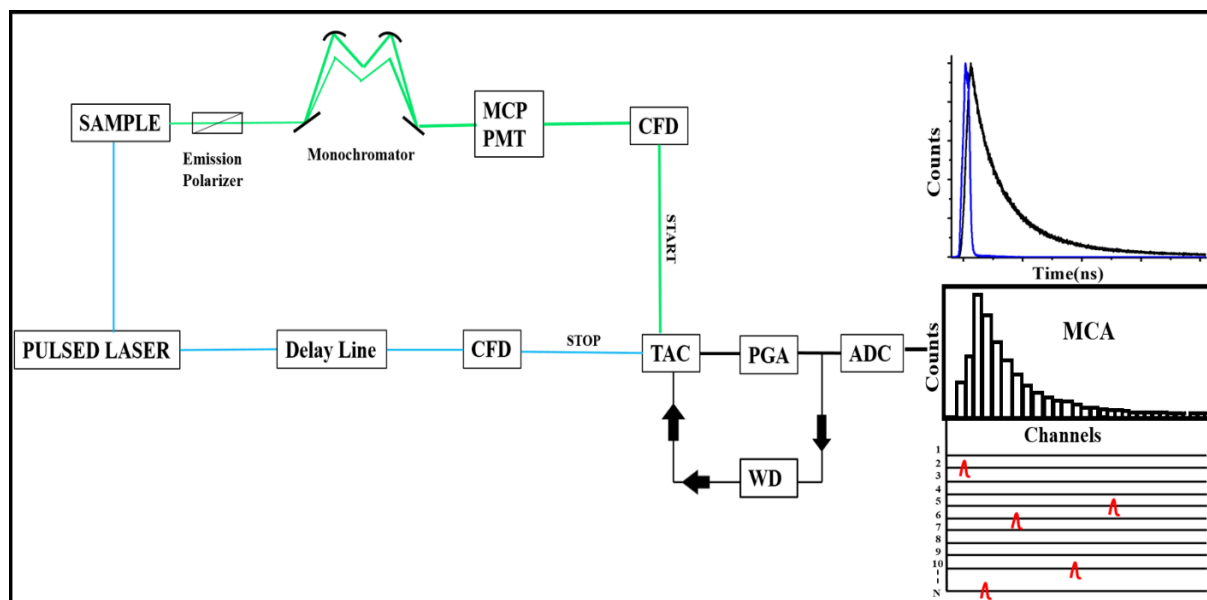
Then the voltage is amplified by a programmable gain amplifier (PGA) to get a better signal, then converted to a numerical value by the analog-to-digital converter (ADC). The rest false signals are suppressed by a window discriminator (WD).

The above process is considered as one event and repeated several times and the data are stored in a multichannel analyzer (MCA) and results in the histogram of decay with the number of photon counts on the y-axis vs time delay in the x-axis.

TCSPC spectrometer can be operated in two different modes. One is forward mode and the other is the reverse mode. The forward mode is discussed in the above section. The working principle of reverse mode TCSPC is the same as the above, the only difference is emission pulse starts the TAC and the excitation pulse stops the TAC.^[88]

In this thesis, the average lifetime of all the samples was measured by using a time correlated single photon counting (TCSPC) technique with a reverse mode Edinburgh OB920 time-resolved

spectrometer. Emissions were collected at the magic angle (54.7°). The full width of the half maxima (FWHM) of the laser pulse was measured by using a scatterer ludox solution. This is known as the IRF (instrument response function) of the instrument which is the lower lifetime detection limit of the instrument. Along with laser pulse width, the characteristics of the detector, monochromator, and timing electronics also contribute to the IRF. The IRF of our instrument is measured to be 90ps.



Scheme 2.2. Scheme representing a basic reverse mode TCSPC setup.

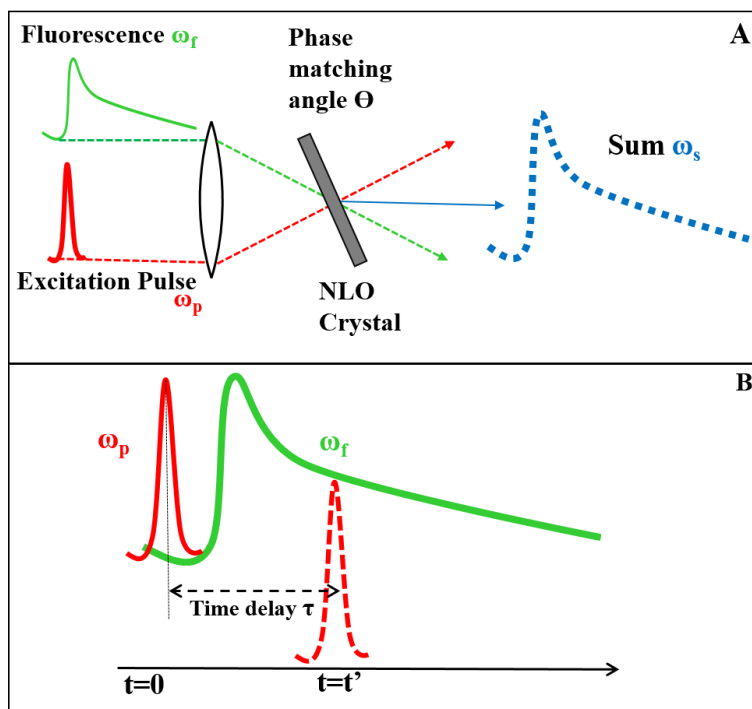
2.2.2. Fluorescence Upconversion Spectroscopy

A fluorescence upconversion spectrometer is used to measure the initial time dynamics (300 fs to 3 ps time window in our case) of any fluorescent material right after photoexcitation.

2.2.2.1. Basic Concept and Working Principle

The working principle of the instrument follows a pump-probe mechanism. If the sample is excited at zero time by an ultrafast laser pulse, then the fluorescence decay curve is obtained by combining the fluorescence from the sample and laser pulse at different time delays is known as upconversion.

The laser pulse is time delayed w.r.t fluorescence (Scheme 2.3) by a delay line. Then both the pulses are focused together on a non-linear optical crystal (BBO in our case) and we obtain an unconverted signal in the UV region. The curve we obtained from this technique is a map of fluorescence from the sample.

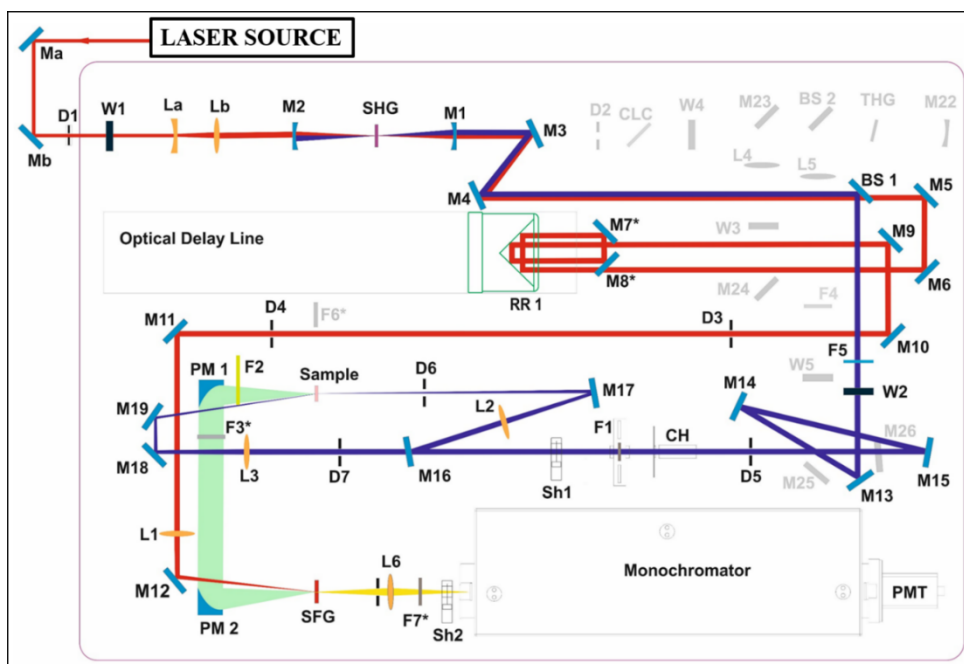


Scheme 2.3. Pictorial representation of the basics of fluorescence upconversion.^[120]

2.2.2.2. Instrumentation

To begin with, the fundamental laser (ω_p) was focused onto a non-linear BBO crystal (SHG), which generates a frequency-doubled visible beam ($2\omega_p$) with the same repetition rate. The fundamental beam (ω_p) and the frequency-doubled beam ($2\omega_p$) were separated through a dichroic mirror called a beam splitter (BS1). BS1 transmits the gate beam (probe, ω_p) and reflects the excitation pulse (pump, $2\omega_p$). The transmitted beam (probe) is guided to the optical delay line through mirrors M1, M6, and M8. Then the reflected beam (pump) goes through a polarizer W2

(35.4°) for collection of a lifetime at a magic angle. To avoid photo degradation, the sample is placed in a rotating cell with a 1 mm path length. Fluorescence from the sample (ω_f) was up-converted using gate pulse (800 nm, ω_p) on a nonlinear BBO crystal (SFG). The gate beam was time-delayed with the fluorescence by using an optical delay line. The up-converted signal is passed through an iris which blocks the fluorescence and the gate beam and up-converted light is focused and guided to a monochromator and finally to the detector (PMT).



Scheme 2.4. Schematic representation of the upconversion setup, Fluomax from IB photonics. In the scheme, the red line corresponds to the fundamental laser beam and the blue one frequency-doubled visible beam.

Femtosecond fluorescence up-conversion data were recorded in a fluorescence up-conversion spectrometer, Fluomax from IB Photonics Ltd. For excitation of the samples, Ti-sapphire laser (Mai Tai HP, Spectra Physics) with a tunable range from 690 nm to 1040 nm was used. Excitation profile and IRF were obtained from the Raman scattering of ethanol i.e. 300fs.

2.2.3. Data Analysis

The fluorescence decay curve that we obtain from time-resolved measurements is a convolution or mixture of the laser pulse and actual fluorescence from the sample. The convolution function can be written as follows,

$$F(t) = \int_0^t P(t)I(t' - t)dt \quad (2.4)$$

Where $F(t)$ is the fluorescence intensity at time t . $P(t)$ is the IRF intensity at time t and $I(t' - t)$ is the response function of the experimental system.

Hence, to extract the actual fluorescence lifetime, the deconvolution method can be applied. But the convolution is much more complicated and during data analysis, direct subtraction of IRF from the decay curve is not possible. Hence an iterative reconvolution method is used in data analysis.

Truly normalized fluorescence lifetime decay can be expressed in mathematical terms as follows,

$$F_n(t) = \int_0^\infty p(\tau)e^{\frac{-t}{\tau_i}}dt \quad (2.5)$$

Where τ is the lifetime of the fluorophore, and $p(\tau)$ is the corresponding probability amplitude. For multi-exponential decay functions, $p(\tau)$ is represented by a weighted sum of n different delta functions positioned at lifetimes τ_i .

$$p(\tau) = \sum_{i=1}^n b_i \delta(\tau - \tau_i) \quad (2.6)$$

Which gives,

$$F_n(t) = \sum_{i=1}^n b_i e^{\frac{-t}{\tau_i}} \quad (2.7)$$

Where b_i is the contribution of i^{th} lifetime component which can be expressed as, $\sum_{i=1}^n b_i = 1$.

So, during data analysis one assumed decay function is obtained by guessing the τ_i value and convoluted with the measured IRF. Fitted parameters, a_i and τ_i are iteratively improved until the

theoretically constructed decay curve matches with the experimentally obtained decay curve and it is judged by minimization of χ^2 value which is known as the goodness of fit and mathematically represented as follows,

$$\chi^2 = \sum_k W_k^2 \frac{F_k - X_k}{n} \quad (2.8)$$

The superscript k represents the individual data point to be fitted and the summation expands over all these data points. W is the weight factor. It depends upon the type of noise specific to the data which is inherited from the measurement method, n is the total number of free parameters. The deviation of points is expressed in the form of χ^2 . The low value of χ^2 between 1.00 and 1.20 represents a good fit. Many iterations are carried out to obtain a good fit.

In this thesis, the collected TCSPC data were fitted by a reconvolution fitting function provided by the Edinburg Instruments, and the femtosecond transients were fitted with a re-convolution fitting function where a Gaussian-shaped lamp profile (FWHM 300 fs), as obtained from Raman scattering experiment, was used.

2.2.4. Construction of Time-Resolved Emission Spectra (TRES) and Time-Resolved Area normalized Emission Spectra (TRANES)

2.2.4.1. TRES

Due to various excited state processes, the energy of the excited state of the fluorophore changes with time. This results change in the fluorescence lifetime of the fluorophore w.r.t emission wavelength. To visualize the changes in the emission profile, right after photoexcitation of fluorophore to the equilibrium state, TRES is constructed by a combination of steady state and time-resolved fluorescence. For the first time, this method was proposed by Maroncelli and Fleming.^[121]

The method is as follows:

Covering the whole steady state emission spectrum, fluorescence lifetime profiles were recorded at 12-14 different emission wavelengths typically at a regular interval of 10 nm. As discussed previously, the real lifetime profiles $[I(t)]$ were extracted using the reconvolution method and fitted with an exponential fitting function, $I(t)=\sum\alpha_i\exp(-t/\tau_i)$; $[i=1,2,3,\dots]$. Here, τ represents the fluorescence lifetime, α represents the contribution of lifetimes, and superscript i represents the number of exponents. Fluorescence intensity $[I(v,t)]$ at emission position (v) and time (t) was derived by the following equation,

$$I(v, t) = I_{SS}(v) \frac{\sum_j \alpha_j(v) \exp(-t/\tau_j(v))}{\sum_j \alpha_j(v) \tau_j(v)} \quad (2.9)$$

Here, $I_{SS}(v)$ is the steady state fluorescence intensity at wavenumber (v). τ_j is the lifetime component and α_j is its contribution. Using the above equation, we obtained the fluorescence intensity for all the wavenumbers at a given time t . Then these intensities were fitted with a lognormal fitting function as follows,

$$f(v) = y_0 \exp \left\{ -\ln 2 \left(\frac{\ln \left[1 + \frac{2b(v-v_0)^2}{\Delta} \right]}{b} \right) \right\} \quad (2.10)$$

Here, y_0 is the peak position, b is the asymmetry parameter, v_0 is the Peak position (Wavenumber), and Δ is the band width. Similarly, we generated TRES, by obtaining a set of fluorescence emission spectra at different times starting from photoexcitation.

2.2.4.2. TRANES

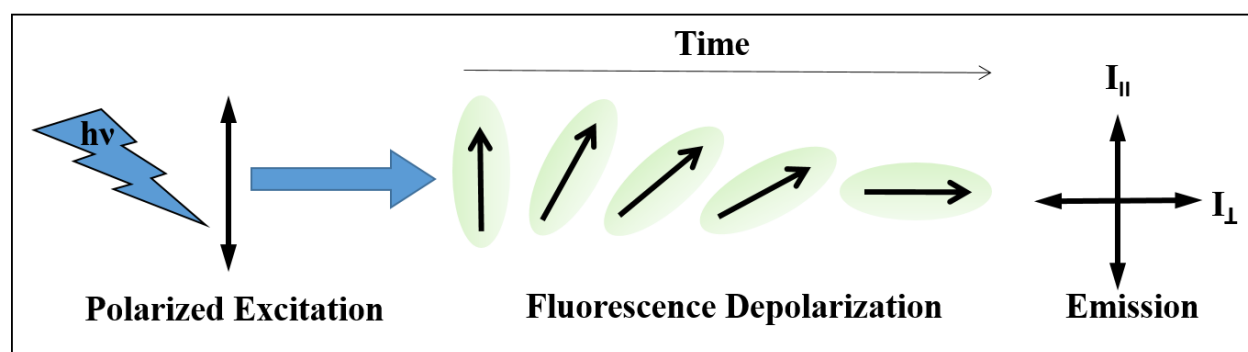
Time-Resolved Area Normalized Emission Spectra (TRANES) is an extension of TRES for understanding the excited-state processes. Though, TRES is an efficient technique to observe the excited-state processes it has some limitations. With time the intensity of TRES decreases due to

the natural excited state decay of the fluorophores. To overcome this limitation TRANES is generated by area normalizing the TRES. This method was proposed by Periasamy and the group for the first time.^[122] In the system, if two emissive species are present in the excited state, irrespective of their origin and kinetics, one isoemissive point is observed in the TRANES. Hence, by analyzing the isoemissive points in TRANES we can comment on the excited-state processes involved in the system.

Construction of TRANES,

$$\text{Time resolved area normalized spectrum (time } t) = \frac{\text{Time resolved Emission Spectrum at time } t}{\text{Area under the emission spectrum at time } t} \quad (2.11)$$

2.3. Fluorescence Anisotropy Measurements



Scheme 2.5. Illustration showing fluorescence depolarization after polarized excitation.

When a set of fluorophores are photoexcited with a plane-polarized light, those fluorophores having transition moment integral close to the electric vector of excitation light, preferentially get excited. As a result, the fluorophores in the excited state becomes partially polarized. As the fluorophores are randomly oriented the emitted fluorescence is anisotropic. But any change in the direction of transition moment during the excited-state lifetime of the fluorophores leads to a decrease in fluorescence anisotropy or fluorescence depolarization. As non-parallel absorption emission transition moment, Brownian motions, torsional vibrations, and energy transfer are some

of the reasons for fluorescence depolarization, hence fluorescence anisotropy analysis can give information regarding size, shape, and mobility, the flexibility of fluorophores as well as the fluidity of the medium, etc.

Hence, fluorescence anisotropy (r) is defined as,

$$r = \frac{I_{||} - I_{\perp}}{I_{||} + 2I_{\perp}} \quad (2.12)$$

Where, $I_{||}$ and I_{\perp} are the emission intensities when emission polarizers are parallel and perpendicular to the excitation polarizer, respectively.^[88]

Experimentally, anisotropy is measured as,

$$r = \frac{I_{VV} - GI_{VH}}{I_{VV} + 2GI_{VH}} \quad (2.13)$$

Where, the first and second subscripts represent the direction of the excitation and emission polarizers respectively (V=Vertical, H=Horizontal). For example, I_{VV} and I_{VH} represent the fluorescence intensity collected at vertical polarizer and horizontal polarizer respectively for vertical excitation polarizer. G is an instrumental factor that is independent of excitation.^[88] It is the sensitivity of the detector in both directions, for horizontally polarized excitation light.

$$G = \frac{I_{HV}}{I_{HH}} \quad (2.14)$$

In time-resolved anisotropy measurements when only one depolarization channel is present then the decay curve can be represented as,

$$r(t) = r_0 \exp(-t/\tau_r) \quad (2.15)$$

Where r_0 is the zero time anisotropy value and τ_r represents the rotational time of fluorophore in specific solvent.

In this thesis, we have studied the CsPbBr₃ complex formation with rhodamine 6G molecule by rotational anisotropy measurements in fluomax upconversion spectrometer mentioned above. We have also used Edinburgh spectrofluorometer for steady state excitation anisotropy measurement of fluorescent carbon dots.

2.4. Confocal Microscope and Fluorescence correlation spectroscopy (FCS)

The FCS technique was used for the first time by Webb and the group to study the DNA binding kinetics with ethidium bromide.^[123] Today the technique has been developed by using a confocal microscope and detectors with very high sensitivity.^[124]

2.4.1. Basic concepts and Working principle

FCS is a single molecule sensitive technique that deals with the temporal fluctuations of fluorescence intensity inside a very tiny reaction volume (~femtoliter in size) created by a focused LASER beam. By utilizing the fluorescence intensity fluctuation property, FCS measures the chemical and physical properties of the molecule like molecular diffusion, chemical reactions, molecular interactions (binding and unbinding kinetics) processes, conformational transitions, photochemical reactions among others, those that control the fluorescence fluctuations.^[125] In principle, any physical or chemical process causing intensity fluctuations at the μ s to ms time scale can be detected by FCS.

The measurement of the frequency of fluctuation and its average duration is obtained by an autocorrelation analysis. The autocorrelation function (ACF) at time τ is given by,^[126]

$$G(\tau) = \frac{\langle \delta F(t) \delta F(t+\tau) \rangle}{\langle F(t) \rangle^2} \quad (2.16)$$

Where $F(t)$ is the fluorescence intensity, $\delta F(t)$ is the fluctuation in the fluorescence intensity at any time t and is given by,

$$\delta F(t) = F(t) - \langle F(t) \rangle \quad (2.17)$$

Where $\langle F(t) \rangle = \frac{1}{T} \int_0^T F(t) dt \quad (2.18)$

Autocorrelation analysis refers to the self-similarity of the signal at different time delays (τ)

This ACF contains two types of information,

- (i) $G(0)$, i.e. the value of the $G(\tau)$ at $\tau=0$, tells about the magnitude of the fluctuation signal and it is inversely proportional to the number of molecules present in the excitation volume. Hence, by decreasing the number of molecules, the sensitivity of FCS increases.
- (ii) The rate and shape of the ACF decay curve contain information about the kinetic aspect of the processes at different timescales. For example, a two-step decay curve refers to two different processes and their two different timescales.

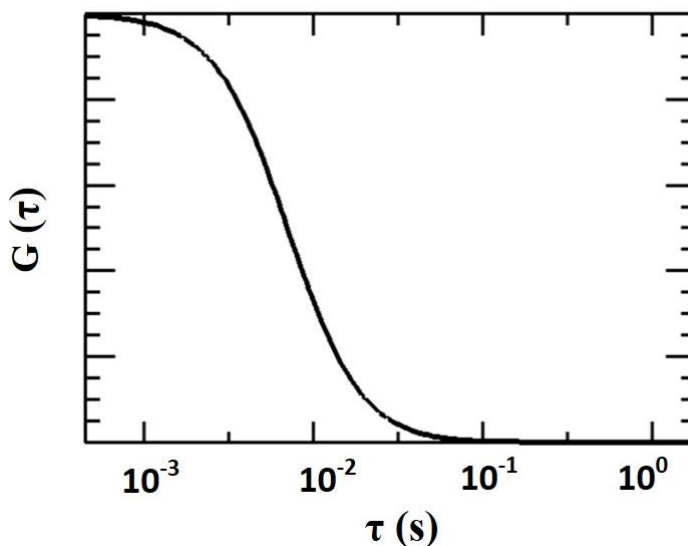
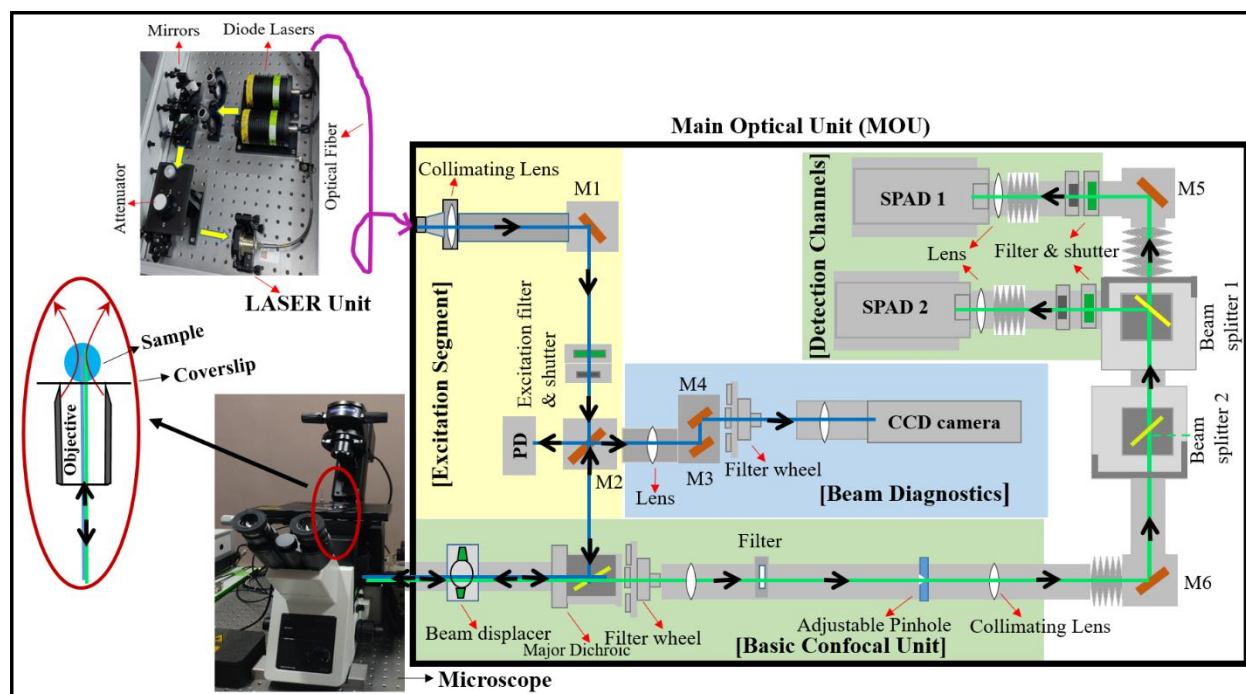


Figure 2.1. A typical ACF Curve.

2.4.2. Instrumentation



Scheme 2.6. Schematic representation of MT-200 provided by PicoQuant.

In this thesis, FCS measurements were performed in a commercially available MicroTime 200 (MT-200) fluorescence lifetime microscope system from Picoquant. Picosecond diode lasers with a base frequency of 40 MHz are used as the excitation source.

In brief, Laser lights are guided to the excitation segment through an optical fiber, then the beam is guided to the excitation shutter through a 100% reflecting mirror (M1). After passing through the excitation shutter the excitation light passes through a 90/10 beam splitter (M2) which directs 10% of the beam to a photodiode to determine the Laser power before the objective. Another 90% of the beam is transmitted to the major dichroic which directs the excitation beam to the right-side port of Olympus IX73, through an adjustable beam displacer. After entering the microscope, the excitation beam is focused on the sample by objective. Then the fluorescence from the sample, as well as the back scattered excitation beam, are guided back to the BS2 by the same microscope

optics and beam displacer. The back scattered excitation beam from BS2 is reflected M2 then focused through a tube lens and guided to a CCD camera which captures the image seen by the objective. The fluorescence signal transmitted through the major dichroic then goes through an optional filter selected by the filter wheel. The beam is then focused by an achromatic tube lens to the pinhole. The pinhole is adjusted in such a way that only the focused beam will pass through it. For our measurements, we used a 50-micron diameter pinhole for a 60x water immersion objective. The beam is then re-collimated by an achromatic lens and directed to a 50/50 beam splitter before entering the detectors (SPADs).

2.5. Isothermal Titration Calorimetry (ITC)

ITC technique is used to obtain the thermodynamic parameters involved in the interactions of solutions. Mostly this is used to study the binding between small molecule/ligand to any macromolecule. The basic principle of this technique involves the measurement of heat change between two cells enclosed in an adiabatic jacket. Heat is either released or absorbed depending upon the nature of the interaction.

In this thesis, I have used the Malvern MicroCal iTC200 calorimeter to obtain the binding interaction between GQD and a small organic molecule. The instrumentation and working principle are as follows,

As mentioned above, this instrument has two identical cells one is the reference cell and the other is the reaction cell. Both the cells are made up of “Hastelloy” a chemically inert material. Through a constant power supply, the temperature difference between these two cells is maintained at zero. The reactant cell is loaded with the GQD sample of volume 200 μL and the reactant syringe is loaded with a syringe of volume 40 μL . Small volumes ($\sim 1 \mu\text{L}$) of the titrant are injected at regular intervals and the heat change is recorded at each injection w.r.t. the mole ratio of the reactant. The

obtained data is used to measure the binding affinity (k_a), enthalpy changes (ΔH), and the binding stoichiometry (n) of the interaction between two or more molecules in solution. For the appropriate measurement of the binding parameters, a sigmoidal curve should be obtained. The shape of the curve is obtained by the c -value which is obtained by the following equation,

$C = n k_a M$ where n , k_a are binding stoichiometry and binding constant and M is the concentration of the molecule in the reactant cell.

2.6. Calculation of fluorescence quantum yield (QY)

Fluorescence quantum yield is the ratio of the number of photons emitted to the number of photons absorbed by a fluorophore. It is a measure of the efficiency of the molecule to fluoresce.

There are two methods for calculation of fluorescence quantum yield,

A) Absolute Method

B) Reference Method

We have adopted the reference method for the calculation of fluorescence quantum yield in our work.

In the reference method, a known reference sample (standard) is used whose quantum yield is already known. The steady-state fluorescence intensity of the sample and the standard were compared while the OD (at excitation wavelengths) of both the samples is the same. For accurate measurements and to avoid the inner filter effect very dilute solutions were used. The following equation is used to calculate the QY of the unknown sample.

$$\Phi_U = \Phi_S \frac{I_U A_S \eta_U^2}{I_S A_U \eta_S^2} \quad (2.19)$$

Here Φ corresponds to fluorescence quantum yields. I is the steady-state fluorescence intensity (area under the curve), A is the optical density and η is the refractive index of the solvent in which

samples are taken. The superscripts U and S correspond to the unknown sample and standard respectively.

2.7. Characterizations of Nanomaterials

High-resolution TEM (HR-TEM) measurements were performed in a JEOL (JEM-2100, 200 kV) electron microscope to measure the size and interplanar distance of the nanomaterials. Carbon-coated Cu grids from Ted Pella are used for sample preparation.

¹H NMR spectra of fluorescent carbon dots were recorded in a Bruker AV-400 MHz spectrometer by using CD₃OD as a solvent.

Powder X-ray diffraction (P-XRD) curves were obtained from a Davinci D8 diffractometer setup from Bruker. (Cu-Kα radiation; λ=1.54 Å).

FT-IR spectra were obtained using a Perkin-Elmer spectrophotometer.

AFM measurement was carried out in a noncontact tapping mode of JPK BioAFM setup (Bruker)

2.8. Calculation of Free energy^[89]

The driving force i.e. change in Gibbs free energy (ΔG) for electron transfer reactions studied in this thesis, is estimated by the following equation,

$$\Delta G = E_{\text{red}}(\text{A}) - E_{\text{ox}}(\text{D}) - \Delta E_{00} \quad (2.20)$$

Where $E_{\text{red}}(\text{A})$ is the reduction potential of the acceptor, $E_{\text{ox}}(\text{D})$ is the oxidation potential of the donor. ΔE_{00} is the energy difference between the lowest vibrational energy of the excited state and the ground state of the light-absorbing molecule (donor or acceptor).

2.9. Tauc Plot

Tauc plot is a derivative of the absorption spectrum, used to estimate the optical bandgap of any semiconductor material and was introduced by John Tauc for the first time.^[127] In this thesis, we have used the Tauc plot to estimate the bandgap of GQD.^[128] The absorption curve of GQD was transformed to an $(\alpha h\nu)^2$ plot as a function of $h\nu$. Where α is the absorption coefficient, h is Planck's constant, and ν is the light frequency. Much better linear fitting with $r=2$ implies our GQD is a direct band gap material. The fitted line was extrapolated to its intersection with the x-axis to determine the bandgap energy.

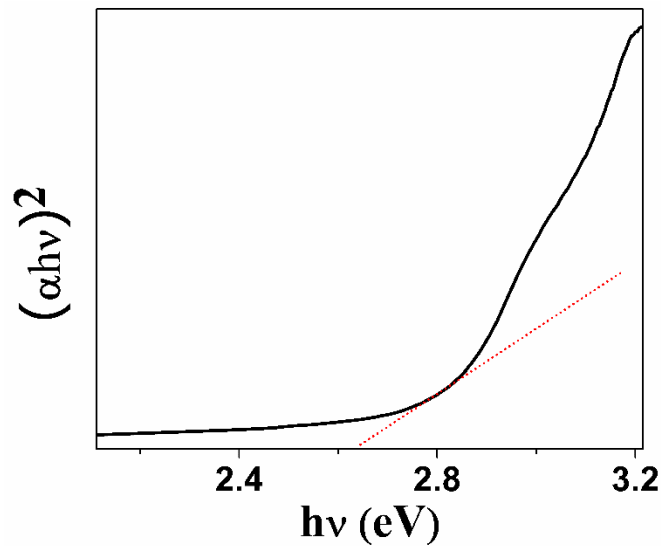


Figure 2.2. Tauc Plot generated from GQD absorption.

3.1. Introduction

As discussed in chapter 1, several attributes of fluorescent carbon dots (FCD) like low cytotoxicity, easy synthesis methods, inexpensive raw materials, and excellent spectral properties have tempted researchers for its burgeoning exploration.^[53,57,58,62,129–131] Recent reports find that FCDs are more promising than other carbon allotropes (nanodiamonds, graphenes, fullerenes, etc.) and conventional inorganic quantum dots (QDs) for bioimaging, drug delivery, biosensing, and light-emitting device applications.^[28,29,43,132,133] It is mainly due to two reasons: (i) unlike QDs, FCDs are mildly cytotoxic and water-soluble, and (ii) harnessing surface state (instead of size) dependent spectral properties of FCD provides easy control over spectral properties. It is not very clear whether the surface state alone or a carbogenic core with a surface state or some other processes control the fluorescence properties of the FCD.^[134,135] An unambiguous answer showing the actual origin of FCD fluorescence with fundamental insights is highly warranted for further exploration of FCD applications. Among the tentative origins, two phenomena are widely accepted: (i) surface energy traps that turn emissive upon surface passivation and (ii) bandgap transitions involved in π -conjugations of FCD.^[72,136–138] Apart from these, there have been other reports claiming quantum confinement effects that attribute the fluorescence property to FCD particles. However, recently many groups have already alluded that molecular fluorophores, produced alongside FCD during the hydrothermal reaction, mostly contribute to the FCD fluorescence.^[57,58,62,129,139,140] Recently,

in a seminal work, Baker and co-workers highlighted how the literature of FCD is tainted by detrimental claims, misconceptions, and unsubstantiated predictions, which mostly arose from inadequate sample purification and characterization.^[62] Many reports have affirmed that mild hydrothermal treatments to conventional FCD precursors produce molecular fluorophores, polymers, and soft gels that, in some instances, upon drying form nanocrystals with similar FCD-like optical properties.^[60,70,129,140,141] Baker et al. showed that dialysis with an appropriate molecular weight cutoff (MWCO) membrane is the most efficient method for extracting FCD from its cocktail, containing a large number of molecular fluorophores as an impurity.^[62] However, a few reports considered membrane dialysis for sample purification, but most of them used <5 kDa MWCO membranes, which are insufficient to separate oligomeric molecular fluorophores from target FCDs. Needless to say, the very recent work by Baker and co-workers has doubted the integrity of many reports in FCD literature.^[62] Revisiting these prior reports with more scientific rigor in sample purification is highly warranted for further maturation of the carbon dot field.

In this chapter, FCD fluorescence is re-evaluated paying serious attention to sample purification. We considered that the purification protocol provided by Baker and co-workers is most efficient with some added modifications: chromatographic separation of crude FCD samples to different subsets based on their fluorescence colors under UV illumination before membrane dialysis. Our remedial study with pure FCD samples verified the veracity of many astonishing claims, where sample purifications were assuredly inadequate. Among all, the most fascinating claim on FCD fluorescence is its excitation-dependent emission, which suggests the opportunity for easy tuning of emission color without changing the particle size in various optoelectrical applications. Many reports based on ensemble measurements show that the emission peak position of FCD shifts toward the low-energy side with increasing excitation wavelength.^[19,57,59,65,72,142–144] This

phenomenon is popularly known as the red edge excitation shift (REES), frequently observed when dye molecules are scattered in an inhomogeneous medium.^[145,146] Despite several reports, and controversies, a consensus understanding of the actual origin of REES in FCD fluorescence has remained a matter of debate. Among the several claims, not always substantiated, structural heterogeneity, the distribution of emissive states, and surface energy traps are the widely discussed propositions.^[65,142–144,147,148] From these studies, it is not clear whether REES in FCD arises from ground-state heterogeneity or the electronic transitions among different emissive states within a single FCD particle. However, recent reports on one-step fluorescence bleaching and single-emission dipoles from a single FCD particle have confirmed its single-chromophoric nature.^[149,150] In contrast with the excitation-dependent emission of FCD fluorescence mostly observed in ensemble studies, recent single-molecule spectroscopic measurements revealed excitation-independent fluorescence from a single FCD particle. They further demonstrated that the excitation at different positions in ensemble measurements causes selective excitation to different optically homogeneous subsets present in the as-synthesized FCD sample. Any phenomenon that is likely to be a reflection of sample inhomogeneity is difficult to identify through an ensemble study. Nonetheless, in the present chapter, we have shown that even an ensemble measurement can efficiently establish excitation-independent emission (non-REES phenomenon) of FCD when sample purification is performed with utmost care.

3.2. Results and Discussion

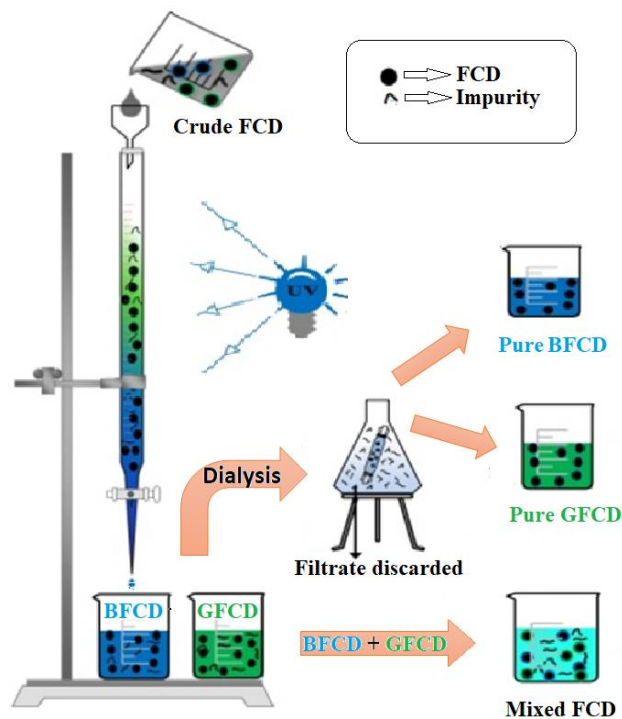
3.2.1. Synthesis of Citric acid-based Carbon dots

In this work, we synthesized FCD following an established facile one-pot hydrothermal method.^[57] Citric acid and urea were mixed thoroughly at a ~1:3 molar ratio, and this mixture was heated at ~200 °C in a hydrothermal pot for a few hours under a nitrogen gas environment. The long reaction

time and higher temperature were maintained to ensure the high degree of carbonization of the FCD core. A yellow-brown reaction residue was formed, which was cooled slowly to room temperature and subsequently dissolved in ethanol through sonication for 30 min. This crude FCD sample contained oligomeric and polymeric byproducts along with unreacted precursors. A series of purification steps were employed to ensure the efficient removal of all impurities.

3.2.2. Purification

Post-synthesis purification of FCD was performed with more scientific rigor than the prior reports, mostly using the protocol provided by Baker and co-workers with some added modifications.^[62] The ethanolic FCD solution was centrifuged for ~15 min at 10000 rpm first, and then the supernatant was collected, which is a cocktail of FCD subsets along with various fluorescent impurities. To separate the FCD subsets, a fluorescence visual silica column separation was employed, which enabled the efficient separation of crude FCD into two batches based on spectral identities: blue- and green-emitting FCD particles under UV illumination. An ethyl acetate and ethanol mixture was used as the eluent during visual column separation. The green-emitting subset (more polar) of FCD was preceded by the blue-emitting subset (less polar) within the column and reached the collecting beaker later (Figure 3.1). An extremely slow flow rate of eluent was maintained during the visual column separation to avoid cross-contamination among the two subsets. We only collected intense blue and green batches. The overlapped zone was discarded. Column-separated FCD subsets were freeze-dried and redispersed in water and subjected to further purification by membrane dialysis using ~15 kDa MWCO for at least 40 h. ~15 kDa MWCO dialysis bag ensures the complete removal of small oligomeric and polymeric impurities. All experiments were performed with dialyzed retentate to ensure collected emission from FCD only.



Scheme 3.1. Illustration of sample purification steps.

3.2.3. Characterizations and Spectral Properties

From high-resolution TEM measurements (Figure 3.1), we found that both blue-emitting FCD (BFCD) and green-emitting FCD (GFCD) exhibit an average particle size of $\sim 6\text{--}9$ nm. Powder XRD spectra of our FCD samples show a broad peak at $\sim 24^\circ$ (Figure 3.2 A), indicating an interlayer distance of ~ 0.37 nm, slightly larger than the graphite interlayer distance (~ 0.34 nm). Fourier transform infrared (FTIR) spectra of FCD samples show the presence of O–H, N–H, –COOH, C=N, C–N=, and –C=C vibrations (Figure 3.2 B). NMR spectra from the same samples indicate the presence of aliphatic protons, –CH₂ protons, –NH protons, –OH protons, ROH protons, RCOH protons, and –R₂NH protons (Figure 3.2). In NMR spectra, no well-distinguished peaks in the $\delta\sim 6\text{--}8$ region indicate the lack of aromatic ring protons. A large number of –COOH, –OH, and amine groups on the surface provide high solubility to the FCD particles in water.

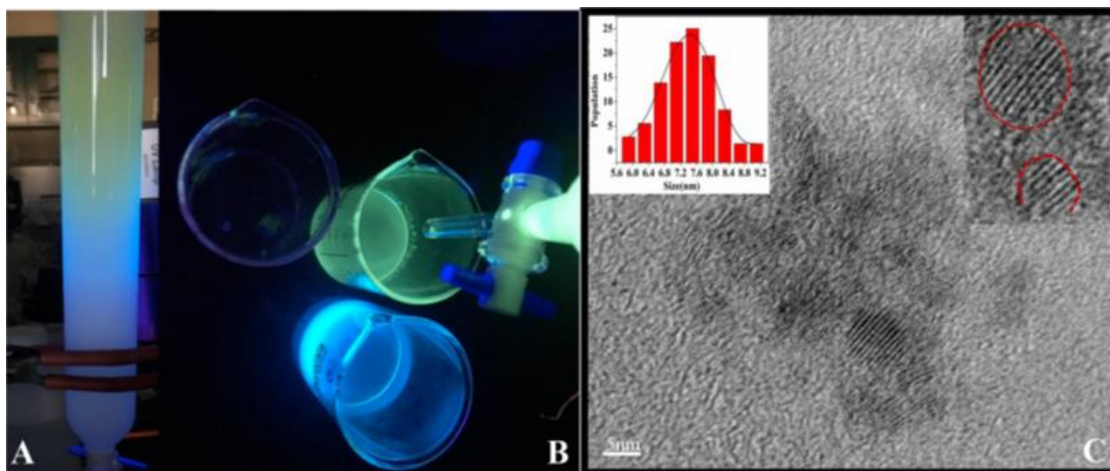


Figure 3.1. (A) Visual silica column separation of as-synthesized FCD under UV illumination (~ 365 nm). (B) Two subsets, BFCD and GFCD obtained after visual silica column separation. A third beaker containing only water was placed close to the UV lamp for comparison with the other two FCD solutions. (C) HR-TEM image of a BFCD particle and the particle size distribution. GFCD shows a similar TEM image and particle size distribution.

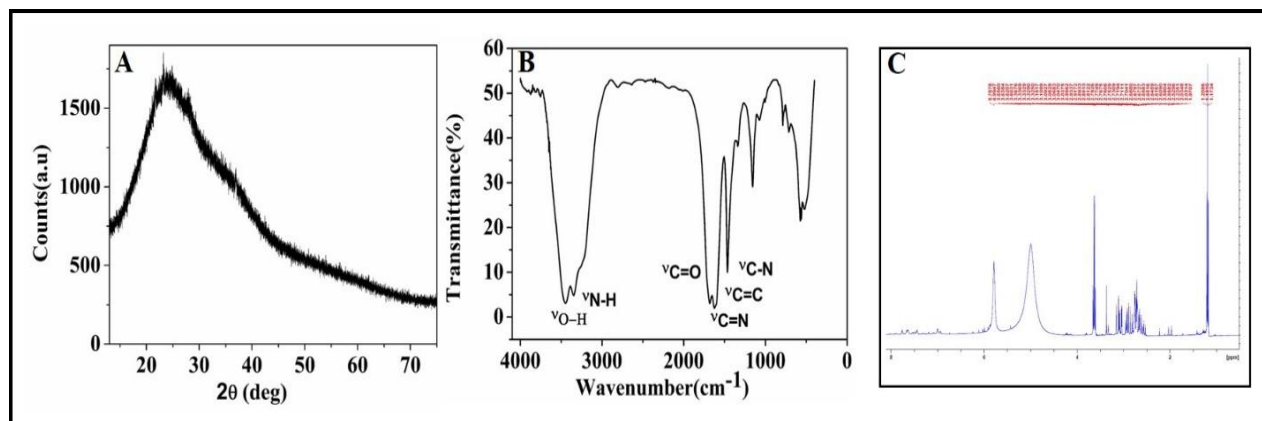


Figure 3.2. (A) PXRD spectrum of our FCD sample. Both the FCD samples (BFCD & GFCD) exhibit similar peak position. (B) FTIR spectrum indicates the presence of various groups on the surface of GFCD. C=N (1640 cm^{-1}), C-N= (1427 cm^{-1}), C=C (1600 cm^{-1}) vibrations are also detected. BFCD sample also exhibits similar peak positions. (C) ^1H NMR Spectrum of GFCD sample very similar to BFCD sample.

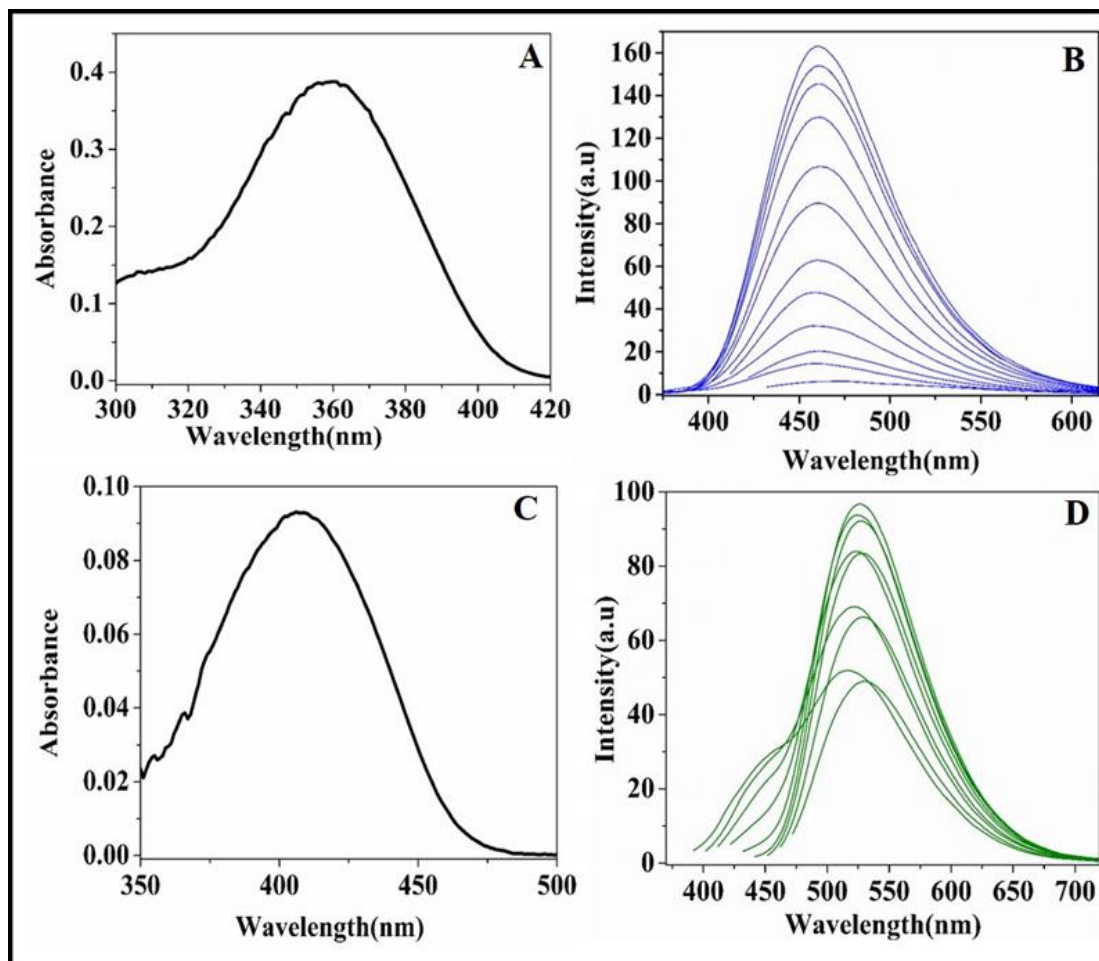


Figure 3.3. Absorption spectrum of BFC (A), GFC (C), Steady-state fluorescence spectra of BFC (B) and GFC (D) at different excitation wavelengths.

The absorption peaks of BFC and GFC in water were found to be ~ 359 nm and ~ 406 nm, respectively. Emission peak positions of BFC and GFC barely dependent on excitation wavelengths. The emission peak maxima of BFC is ~ 460 nm and GFC is ~ 528 nm (Figure 3.3). A slight REES in GFC indicates that this batch contains two closely emitting subsets; both emit at green wavelengths and are very difficult to separate further by column separation by looking at their emission colors at different excitation wavelengths. The time-resolved fluorescence lifetime measurements reveal that the average lifetimes of the FCDs are emission

wavelength independent. The average lifetimes of BFCd and GFCD are found to be ~ 9.5 ns and ~ 4.5 ns respectively (Figure 3.4).

In some instances, molecular byproducts form nanocrystals upon drying.^[60] These nanocrystals resemble FCDs in terms of their optical properties but are relatively smaller (~ 2.5 – 4.5 nm) compared to our FCD sizes (~ 6 – 9 nm). To check the possible contamination of citrazinic/succinic acid derivatives in our FCD samples, we performed a control experiment using citric acid only (without urea) as the precursor, and the same purification protocol was employed after hydrothermal treatment. Unlike the strong emission of FCD, the emission intensity of the citrazinic/succinic acid derivative retentate of the post-dialysis sample was found to be exceedingly low, much below the desired intensity level for any optical measurement. We concentrated (>10 times) the retentate by slow evaporation of $\sim 90\%$ of the water and performed spectroscopic studies of citrazinic/succinic acid derivatives. In contrast with the FCD sample, where all particles (~ 6 – 9 nm) were retained within the dialysis bag, the dialysis of citrazinic/succinic acid derivatives (~ 2 – 4.5 nm) with the same ~ 15 kDa MWCO membrane could not trap the target due to the smaller sizes of the acid derivatives.^[60] Molecular crystals of citrazinic/succinic acid derivatives with sizes of ~ 2 – 4.5 nm can be formed only after drying.^[60] In an aqueous solution, citrazinic/succinic acid derivatives remain in molecular forms with sizes less than 1 nm, and dialysis can easily separate these small molecules from FCD particles. In addition, the retentate of citrazinic/succinic acid derivatives exhibited an order of magnitude lower fluorescence quantum yield ($\phi_f \approx 0.01$ – 0.03) and an exceedingly shorter fluorescence lifetime ($\tau_{fl} \approx 0.6$ ns) compared to those ($\phi_f \approx 0.26$ – 0.53 and $\tau_{fl} \approx 4$ – 10 ns) of FCD samples (Figures 3.4 and 3.5). Although we separated FCD from citrazinic/succinic acid derivatives through visual column separation and dialysis, one should not bother much even if they remain unseparated. This is

because strong FCD emission would easily overshadow the fluorescence from citrazinic/succinic acid derivatives if both coexisted. Fittings to the time-resolved fluorescence (TRF) profiles of FCD and the citrazinic/succinic acid derivative did not reveal any similar lifetime component, which further confirmed that our purified FCD sample was completely free from citrazinic/succinic acid derivatives (Figure 3.4).

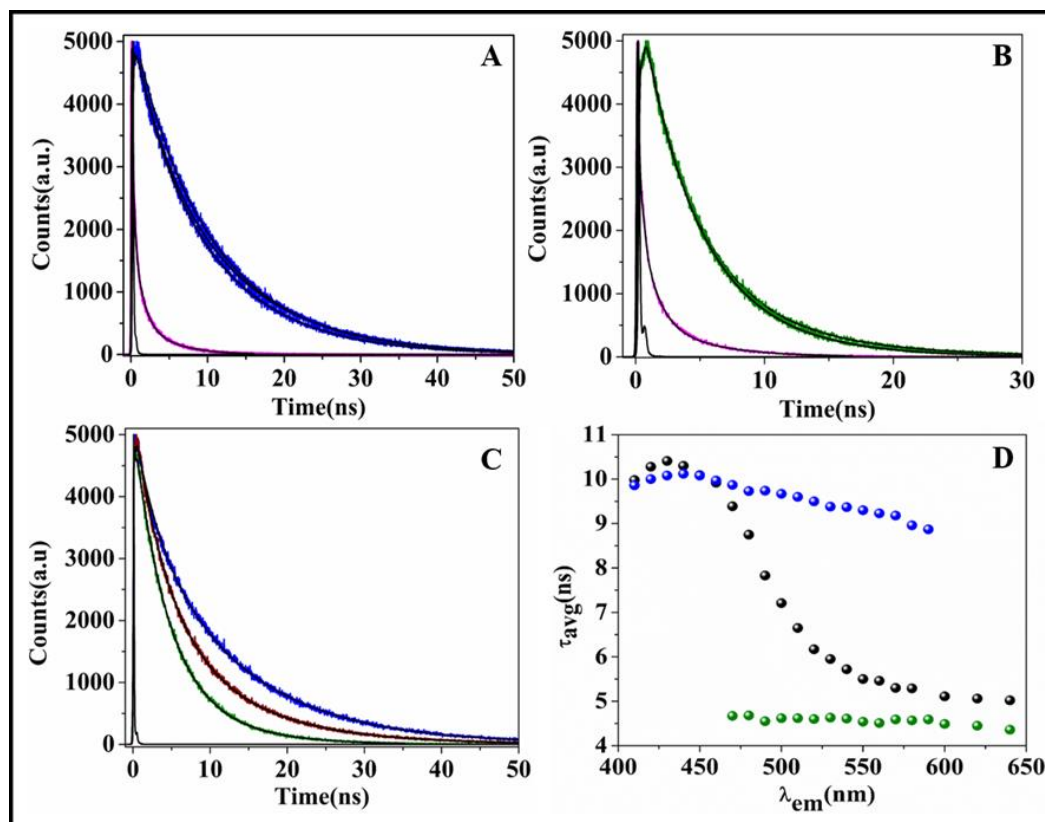


Figure 3.4. TRF of (A) BFCD ($\lambda_{ex} \approx 375$ nm), (B) GFCD ($\lambda_{ex} \approx 405$ nm) and (C) mixed FCD ($\lambda_{ex} \approx 375$ nm), at extreme blue, extreme red, and peak emission wavelengths. In (A) and (B), all three are identical. Very fast IRF (~ 80 ps) is shown by the black curve. The fast decay curves (pink) in (A) ($\lambda_{ex} \approx 375$ nm) and (B) ($\lambda_{ex} \approx 405$ nm) depict the TRF (at emission peak) of citrazinic/succinic acid derivatives, probable impurities in crude FCD. (D) Plot of the average fluorescence lifetime (τ_{avg}) as a function of the emission wavelength for all three FCD samples (BFCD, GFCD, and mixed FCD).

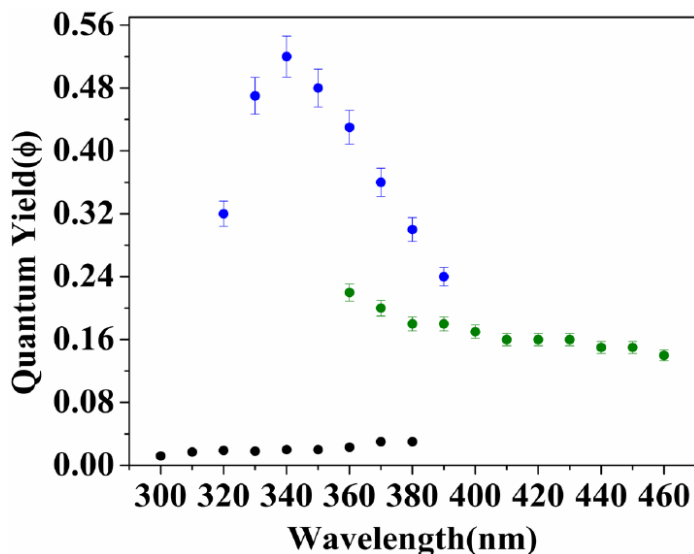


Figure 3.5. Fluorescence quantum yield (Φ_f) as a function of excitation wavelength (λ_{ex}) for citrazinic/succinic acid derivatives (black ball), GFCD (green ball) and BFCD (blue ball).

Apart from the BFCD and GFCD, we prepared another sample, where we exclude the proper sample purification step. This produced a mixture of BFCD and GFCD subsets. We shall call this sample a mixed FCD. The purpose of using the third sample was to correlate our results with previous reports of those performed experiments without proper purification of FCDs and thereby judged any phenomenon observed in their studies as intrinsic to FCD or just an artifact of an optically heterogeneous FCD sample.^[59] As expected, without proper purification, the mixed FCD shows a very broad absorption spectrum, and a large shifting (>70 nm) of the emission peak was also observed when changing the excitation position covering the whole absorption spectrum. The time-resolved fluorescence profile shows an emission wavelength-dependent average lifetime. The emission peak positions w.r.t excitation wavelength are plotted in figure 3.6. The emission wavelength-dependent fluorescence lifetimes are plotted in figure 3.4 which shows the average lifetime of BFCD and GFCD are barely dependent on emission wavelength, whereas the average lifetime of mixed FCD shortens with redshift of emission wavelengths.

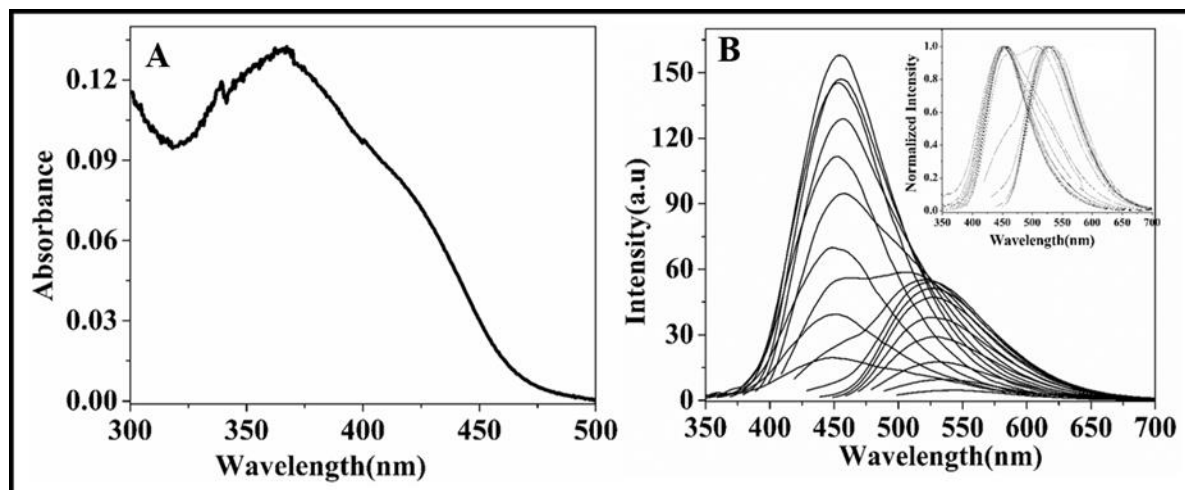


Figure 3.6. Absorption spectrum of mixed FCD (A), Steady-state fluorescence spectra of mixed FCD (B) at different excitation wavelengths. The inset of (B) shows the same spectra after normalizing with the peak intensity.

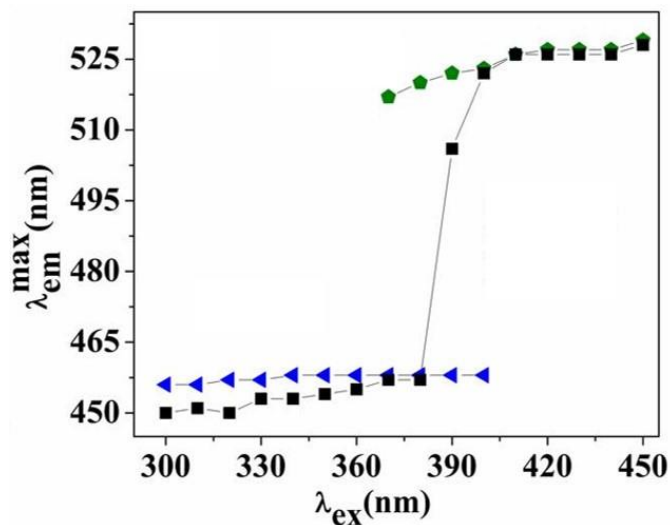


Figure 3.7. Emission peak as a function of excitation wavelength for all three samples, mixed FCD (black squares), BFCd (blue triangles) and GFCD (green pentagons).

3.2.4. Time Dependent spectral Migration and TRES, TRANES analysis

A previous study by Khan et. al. claimed that the REES in FCD fluorescence arises from a giant red edge effect caused by the slower dielectric relaxation of the water molecules around the excited

FCD dipole (i.e., slower than the fluorescence lifetime (τ_{fl}) of FCD), which violates the fundamental Kasha–Vavilov spectroscopic rule.^[59] Their notions were inadequately supported by the observed slow spectral migration (on a post-10 ns time scale) of time-resolved emission spectra (TRES) of FCD, which they corroborated due to the slow solvation dynamics of the surrounding water molecules.^[59] Their explanation not only discredited the earlier claims that held surface states to be responsible for the REES of FCD fluorescence but also invalidated the unequivocally accepted proposition, which showed bulk water as a fast solvent exhibiting sub-picosecond solvation times.^[69,147–155] All of these spectacular claims reported by Khan et al. are in accord with an earlier publication by Wu and colleagues, where they showed that slower dielectric relaxation of water (τ_{sol}) can cause excitation-dependent emission of graphene oxide (GO) by breaking Kasha's rule.^[153] In their case, the local structure of a large GO sheet retarded the solvation dynamics to a much slower time scale ($\tau_{sol} \approx 650$ ps), similar to the fluorescence lifetime (τ_{fl}) of GO that led to incomplete relaxation of the excited state of GO; the net result was excitation-dependent emission (or REES) due to a giant red edge effect.^[153] REES does not always arise from a red edge effect (i.e., incomplete solvation; $\tau_{sol} \geq \tau_{fl}$); it can also appear from ground-state spectral heterogeneity (i.e., a mixture of fluorescent molecules with different spectral signatures).^[88,154–156] Ground-state heterogeneity in GO is unlikely, as substantiated by its well-known structural uniformity, which is not true for FCD. The actual chemical structures and geometry of FCD have not been reported until now. There have been large ambiguities among the TEM images of FCD particles in different reports as well. Now the obvious question that comes to mind is, what is the origin of the time-dependent spectral migration of FCD fluorescence observed by other group if it is not slow solvation dynamics?^[59] The magnitude (\sim post- 1000 cm^{-1}) and time scale (>10 ns) of spectral migration reported by Khan et al. are unprecedentedly higher than what people generally

observed in solvation of organic dye molecules even within a very restricted environment.^[157–160] However, neither our group (cf. Figure 3.4 A,B) nor Khan et al. (Figure 3B,F of ref 59) observed any rise component in the TRF profile at red emission (Scheme 1.9, Chapter 1), which clearly rules out the notion of the sluggish solvation dynamics causing the REES. The absence of a rise component is well under our intuitive expectations; in bulk water, solvation dynamics is ultrafast (<1 ps), which remained undetected by our TCSPC setup (IRF \approx 80 ps).^[152,161] As the relaxation is complete (<1 ps) much before the FCD fluorescence starts (\sim 4–10 ns), no excitation-dependent emission due to the red edge effect can be observed in bulk water (Figure 3.3). The fluorescence lifetimes of BFCd and GFCD are found to be mostly independent of the emission wavelengths (cf. Figure 3.4 D), largely contradicting the argument of slow solvation dynamics causing REES proposed previously. Fluorescence lifetimes would have increased gradually with gradual shifting to the longer emission wavelengths if slow solvation dynamics were present.

We believe, the strong dependency of the fluorescence lifetime (τ_{fl}) of FCD on the emission wavelength is not due to slow solvation dynamics; rather, it appeared from the heterogeneity of the sample. Our mixed FCD sample showed a strong emission wavelength-dependent fluorescence lifetime (cf. Figure 3.4 D), which disappeared in BFCd and GFCD. If the emission wavelength-dependent lifetime arose due to slow solvation, it would have been also present in BFCd and GFCD. Slow solvation dynamics (or the red-edge effect) cause the formation of partially solvated energy states with sharp emission maxima. However, when their contributions are added to the actual steady-state emission spectrum, it appears much broader. This spectral broadening is known as inhomogeneous broadening.^[146] Changing the excitation wavelength would cause a change in the relative population of these emissive states. The net result would be excitation-dependent emission and large spectral migration of TRES. Excitation-dependent emission and spectral

migration can also be found from a mixture of fluorescent particles with different spectral signatures, which need to be duly verified for the FCD sample before asserting that the red edge effect causes the REES.^[59,146] Another observation can be discussed here against the slowed solvation dynamics to be the sole reason for excitation dependent emission of carbon dots. The FWHM of the mixed FCD sample is found to always be higher than the FWHM of BFCD or GFCD. The steady-state emission peak of BFCD was found to be independent of the excitation wavelength, while the emission of GFCD shifted slightly with excitation wavelength (Figures 3.3D and 3.7). This is in contrast to the mixed FCD, where large shifting (>70 nm) of the emission peak was observed when changing the excitation position (cf. Figures 3.6B and 3.7). Careful examination of figure 3.6 B reveals that shifting of the emission peak position of mixed FCD is not continuous but rather a single-step transition, from BFCD-like emission to GFCD-like emission as the excitation wavelength increases. If the excitation-dependent emission occurred due to the red edge effect, one would have observed a continuous shift of the emission peak instead of a stepwise feature because solvation dynamics produce a continuum of narrowly spaced energy states.^[158,159] A similar observation of the non-REES phenomenon of FCD fluorescence was reported earlier by Ghosh et al. using single-molecule spectroscopic measurements.^[162] However, their study showed that the emission peak and τ_{fl} of a single FCD particle were excitation-independent, but their values changed from one particle to another particle. Ground-state heterogeneity can easily mislead the ensemble measurements but not the single-molecule measurements. In the latter technique, the spectral property from a single particle is measured, and if the excitation-dependent emission were intrinsic to FCD, one would have observed the same phenomenon from a single FCD particle also.

In the next part, we will discuss how REES and time-dependent spectral migration of FCD fluorescence disappeared when we separated the as-synthesized FCD sample into two subsets (BFCD and GFCD) based on their spectral identities. As expected, both REES and spectral migrations were present in the mixed FCD sample. Our findings indicate that the REES of FCD fluorescence is neither an intrinsic property (i.e., involvement of multiple emissive sites) nor does it appear due to sluggish solvation around the FCD dipole (red edge effect); it arises only from the ground state spectral heterogeneity.

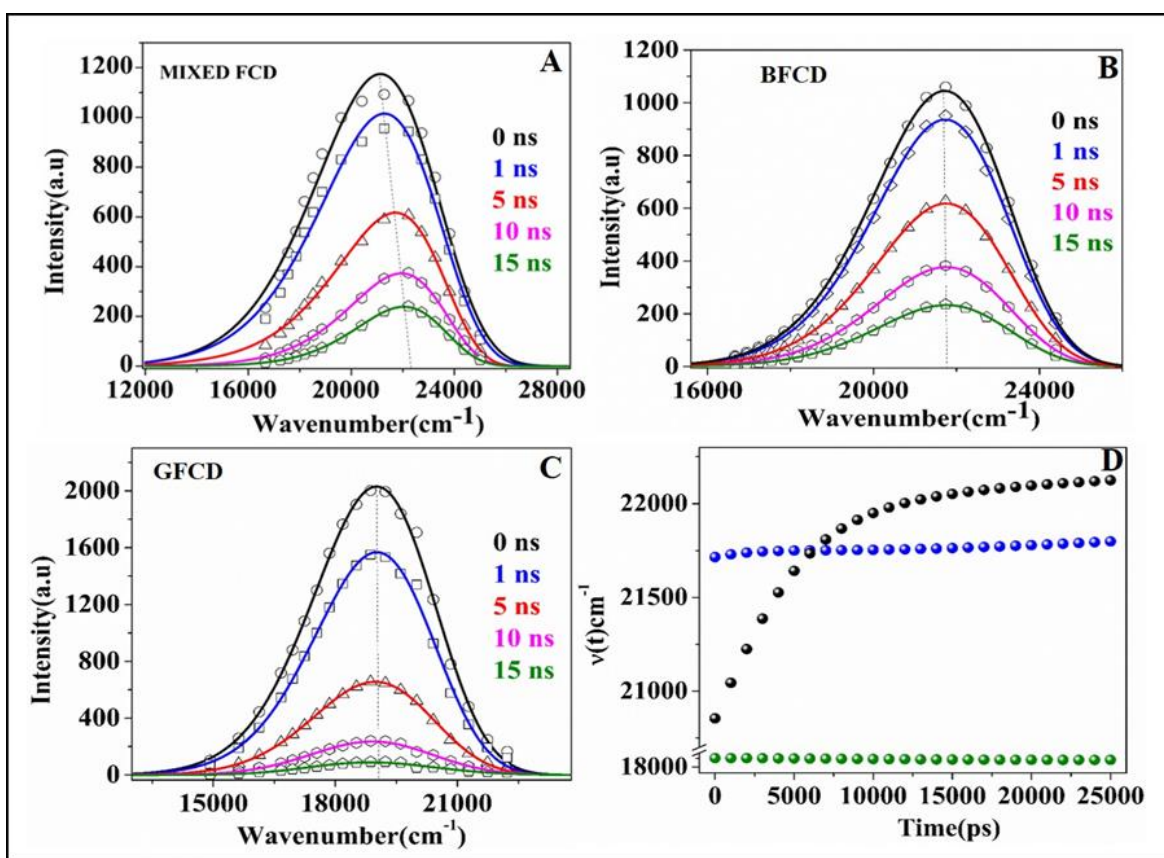


Figure 3.8. TRES of mixed FCD (A) show spectral migration toward the low-energy side with time, whereas in BFCD (B) and GFCD (C) no shift was observed. (D) Emission peak position of TRES as a function of time for all three samples.

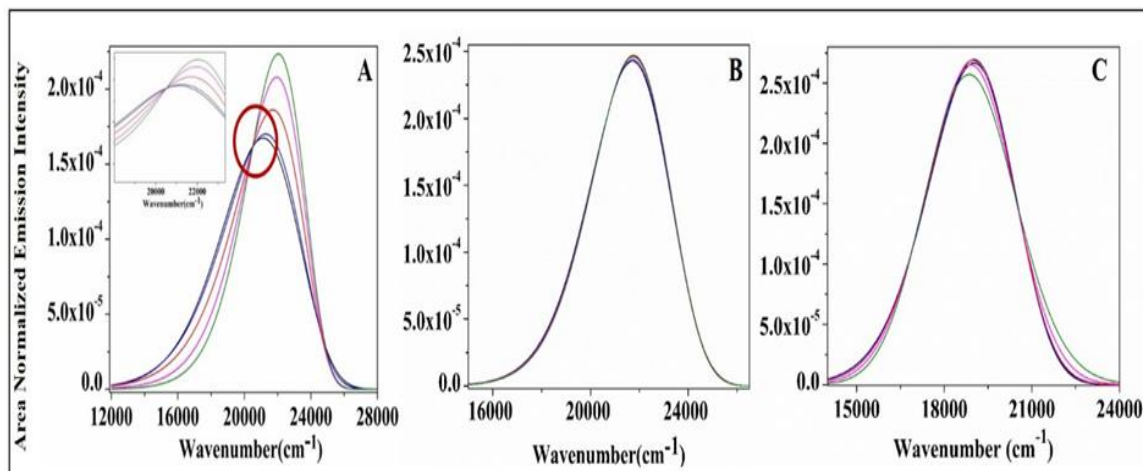
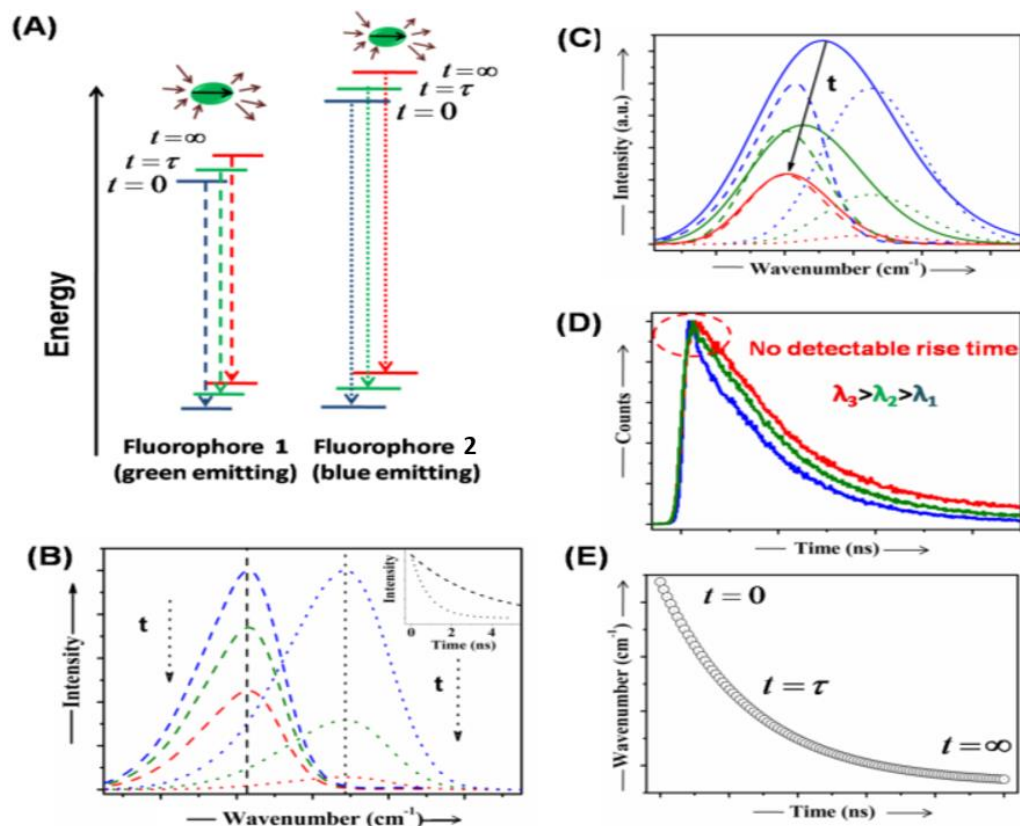


Figure 3.9. TRANES (Area Normalized TRES) of mixed FCD (A), BFCD (B) and GFCD (C). A clear iso-emissive point is obtained only in mixed FCD (A) Inset shows the zoomed version for better clarity.

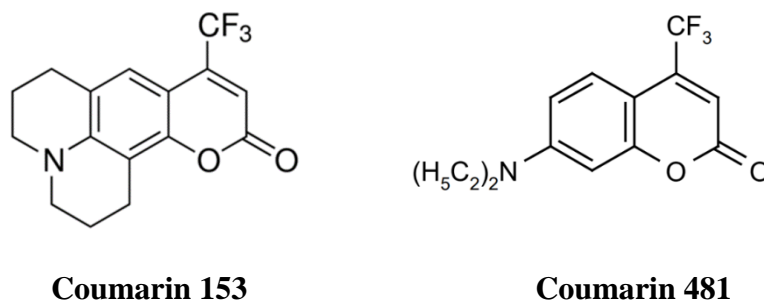
To check the validity of above explanations we generated TRES (Figure 3.8), which represent the emission spectra at different times after photoexcitation to the FCD, are constructed following the recipe of Fleming and co-workers (see the second chapter for further details).^[121] Migration of the emission energy to red wavelengths with time is frequently observed when solvation gradually stabilizes the excited-state energy of the emitting dipole (Scheme 1.9). As mentioned earlier, the ultrafast spectral migration in bulk water (~ 1 ps), cannot be observed using our TCSPC setup (IRF ~ 80 ps). However, observing a significant spectral migration (>1500 cm^{-1}) on a post-10 ns time scale from a mixed FCD sample in bulk water is indeed surprising (Figure 3.8 D). But the absence of an initial rise component in the TRF of FCD overruled the possibility of solvation dynamics. Interestingly, like excitation-dependent emission, the spectral migration also disappeared when we followed the proper purification step and obtained two spectrally homogeneous subsets (BFCD and GFCD). Our study substantially refuted the earlier notion of the red edge effect ($\tau_{\text{sol}} \gg \tau_{\text{fl}}$) causing spectral migration of FCD emission (Figure 3.8).

Chapter 1, Scheme 1.9, explains well how solvation dynamics cause the spectral migration of TRES. And when the solvation time is similar to the lifetime of the sample the REES effect is observed in steady state spectrum.^[59] Similarly, Scheme 3.2 explains how ground-state heterogeneity may also cause similar spectral migration, but in that case, a rise component in TRF cannot be observed. Correlating with our mixed FCD sample, in Scheme 3.2 we assumed that a mixed fluorophore sample consisted of two fluorophores emitting at different positions and having different lifetimes (like our mixed FCD). In contrast to our FCD samples, in Scheme 3.2, we assumed that the blue-emitting fluorophore has a shorter τ_{fl} than the green-emitting fluorophore. Qualitatively, Scheme 3.2 will correlate with our mixed FCD sample, but here, spectral migration will be in the opposite direction. Immediately after photoexcitation (i.e, at $t = 0$), both fluorophores would exhibit maximum fluorescence intensity. When their contributions are added to obtain the sum spectrum, we would observe the peak position of the sum spectrum (at $t = 0$) somewhere in between the emission peaks of the two emitting species (Scheme 3.2). At a longer time (i.e., at $t = t_1$; $0 < t_1 < \infty$), the emission intensity of the blue-emitting molecule will be lower compared to that of the green-emitting molecule due to the longer τ_{fl} of the green-emitting molecule. The combined spectrum at $t = t_1$ will be shifted toward the low-energy side as compared to the peak position of the $t = 0$ spectra. As the time passes to an even longer time t_2 ($0 < t_1 < t_2 < \infty$), the difference between the emission intensities of green- and blue-emitting fluorophores will be even higher. This will cause more shifting of the combined spectrum toward the low-energy side. In this way, ground-state heterogeneity can cause the migration of emission energy toward the longer-lifetime component with time, and one may mistakenly consider this spectral migration due to slow solvation dynamics.



Scheme 3.2. Illustration of how ground state inhomogeneity can cause spectral migration with time even in the absence of solvation dynamics. (A) Two fluorophores (blue and green-emitting) are present simultaneously, whose excited state energies do not change with time (solvation dynamics is absent). (B) TRES of the two fluorophores show the decreasing of emission intensity (without changing the emission peak) with time at different rates due to their different fluorescence lifetimes. (C) The actual time t spectrum (solid curves) of the mixed sample (blue + green fluorophore) would be the combination of time t spectra of blue (dotted curves) and green (dashed curves) emitting fluorophores. A faster diminishing rate of the blue emission (dotted curves) would cause the shifting of the overall peak position of TRES of the mixed sample towards the longer wavelengths with time, though individual peak positions do not change. (D) Fluorescence lifetime profiles of the mixed sample at different emission wavelengths. (E) The emission peak position of the mixed sample as a function of time.

To check the merit of our explanation and validation of Scheme 3.2, we performed one control experiment. We measured the migration of emission energy with the time of a mixed fluorophore containing two organic dyes: coumarin 153 (C153) and coumarin 481 (C481) in ethanol (Scheme 3.2). C153 emits at a longer wavelength (~ 525 nm) compared to C481 (~ 507 nm). The former dye also has a longer lifetime (~ 3.4 ns) than the latter one (~ 0.85 ns), exactly correlating with what we proposed in Scheme 3.2. In contrast to our FCD samples, Khan et al.^[59] observed a higher fluorescence lifetime at longer emission wavelengths though Sharma et al.^[57] and LeCroy et al.^[65] recorded the opposite (matching our results). TRF of a mixed coumarin sample did not show any rise component at the red emission wavelengths; nevertheless, strong spectral migration ($\Delta\nu > 756$ cm^{-1}) of emission was observed on the nanosecond time scale (Figure 3.11). However, spectral migration disappeared when C153 or C481 was present alone in ethanol (Figure 3.11). Several reports show that coumarin dye in a polar bulk solvent exhibits a subpicosecond solvation time.^[163–166] Therefore, it is quite natural that by using TCSPC (IRF ≈ 80 ps) we cannot observe either a subpicosecond rise time in TRF of red emission wavelengths or solvation-induced ultrafast (< 1 ps) spectral migration. Slow spectral migration on the few-ns time scale in mixed coumarin arises not from slow solvation but rather due to ground-state heterogeneity, as substantiated by not observing any spectral migration in unmixed conditions.



Scheme 3.3. Coumarin 153 and Coumarin 481

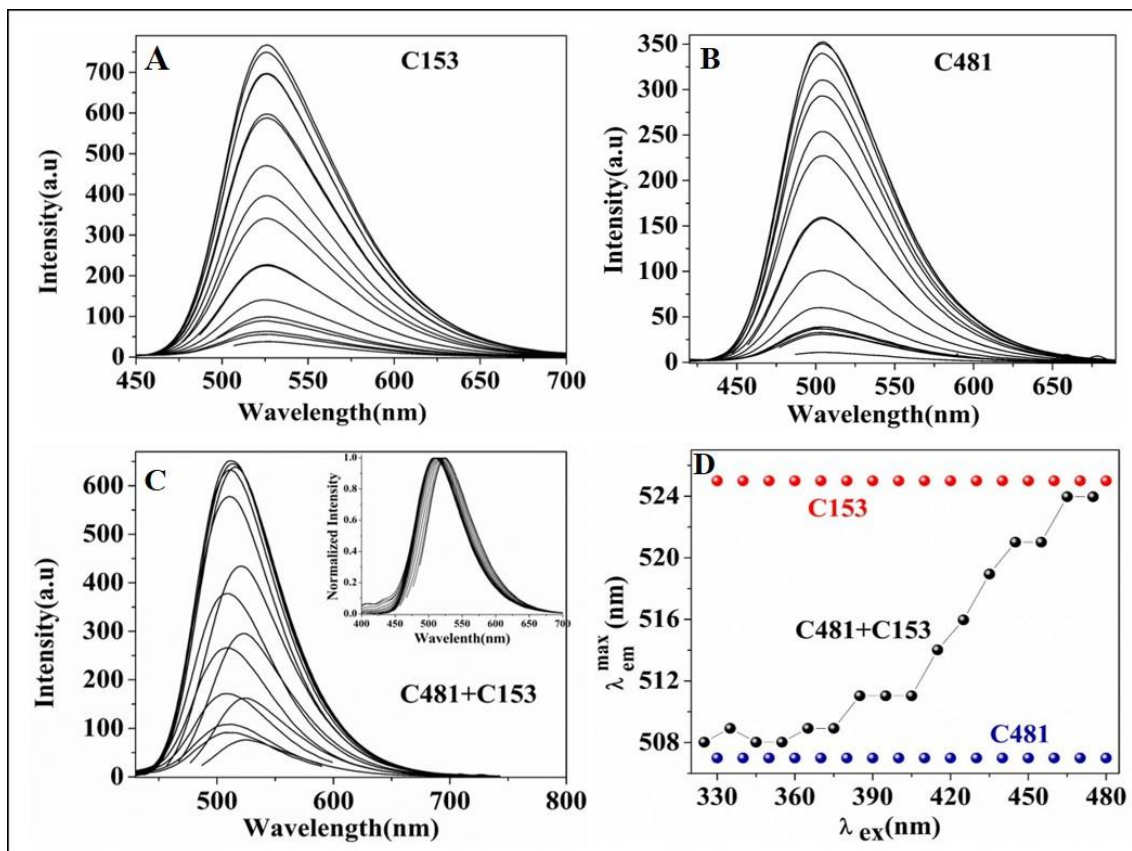


Figure 3.10. Steady state fluorescence spectra of (A) coumarin 153, (B) coumarin 481, and (C) coumarin mixture (C481 + C153), in ethanol at different excitation wavelengths. Figure (D) shows emission peak position as a function of excitation wavelength for all three samples. The inset of figure A shows the same spectra shown in figure A after normalizing with peak intensity.

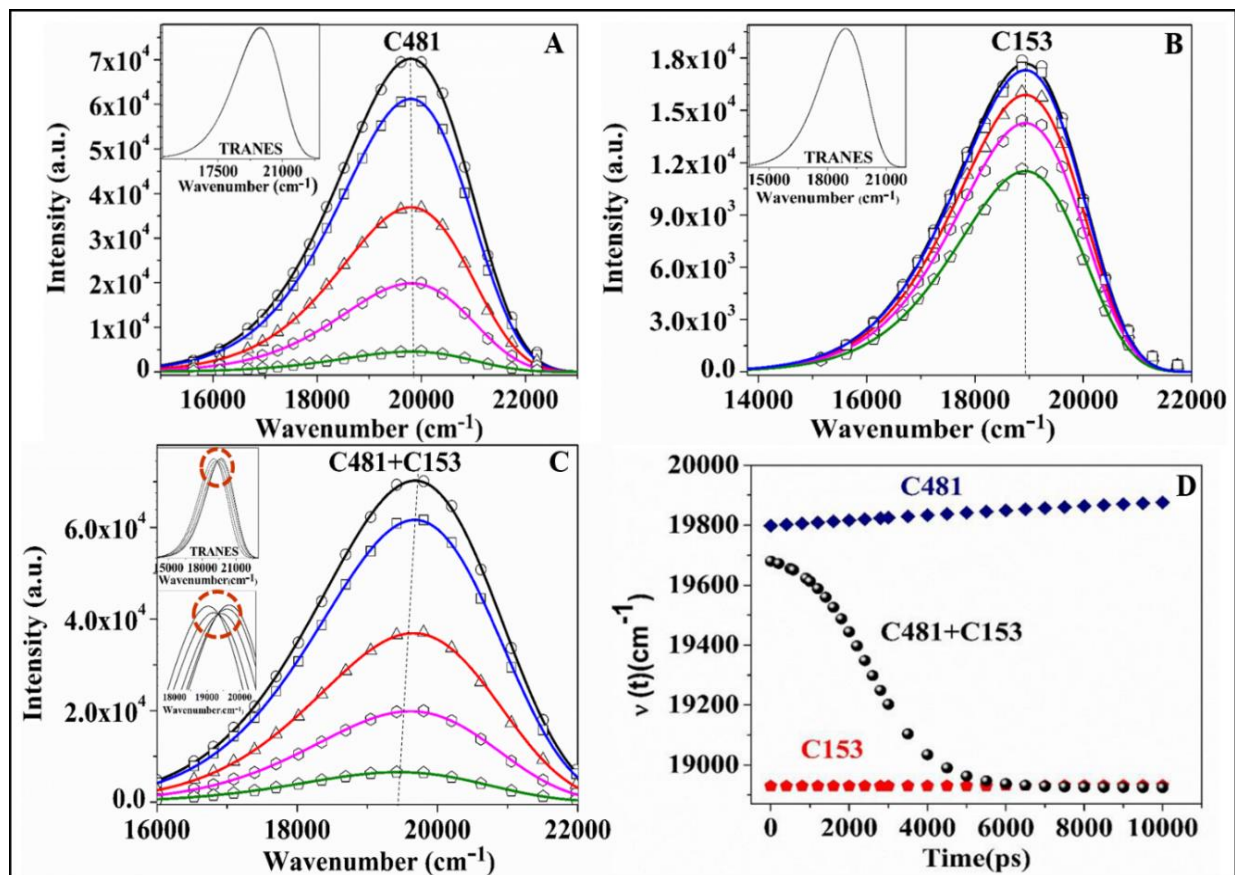


Figure 3.11. TRES of (A) C481, (B) C153, (C) C481 and C153 mixture, in ethanol at different times. Inset of C shows the same TRES after area normalization (TRANES). A clear iso-emissive point is obtained only in TRANES of C481 and C153 mixture (insets of Figure C), which is further zoomed for better clarity. (D) Time evolution of the emission peak position of TRES for all three samples.

Inadequate purification of FCD can also cause similar spectral migration and cannot be the result of slow solvation dynamics. One may use TRANES (details in chapter 2) to confirm the actual origin of spectral migration; is it due to slow solvation dynamics or ground-state heterogeneity?^[122,167] TRANES from a mixed sample of multiple emitting species should contain emission peaks for all of the fluorophores, and each peak should be connected to the next peak through an isoemissive point. In a mixture of two fluorophores with different lifetimes, the shorter-

lifetime fluorophore will go to a dark state quickly as compared to the longer-lifetime fluorophore. The intensity of TRES decreases with time due to the natural decay of the excited-state population. In this scenario, upon constructing TRANES, the dead population of the shorter-lifetime component will be converted into the living population of the longer-lifetime component as the total excited-state population does not change with time in TRANES. The presence of one isoemissive point in TRANES of dye mixture (C153 and C481) confirms the presence of two emissive species. (Figure 3.11) Observing an isoemissive point in TRANES due to solvation dynamics is unlikely as relaxation during solvation takes place following a continuum of closely spaced energy states as an unsolvated state is continuously relaxed through a solvent–solute interaction until it reaches an energetically lowest solvated state. Hence the presence of isoemissive point in TRANES of mixed FCD due to ground state heterogeneity. (Figure 3.9) As expected, the isoemissive point observed in mixed FCD disappeared when we column separated it into two batches (cf. Figure 3.9).

3.2.4. Steady state Anisotropy

To further validate our notion of a single emissive state of our column-separated FCDs, we studied excitation (and emission) steady-state anisotropy (r_{ss}) of BFCD and GFCD in highly viscous solvent glycerol. In glycerol, a negligible amount of depolarization through molecular rotation of FCD can be observed during its lifetime, which would limit the steady-state anisotropy (r_{ss}) value very close to its fundamental anisotropy (r_0) value.^[88] Figure 3.12 depicts the steady-state excitation (and emission) anisotropy values across the excitation (and emission) spectra of both FCDs (BFCD and GFCD). During excitation anisotropy measurement, emission was collected near the emission peak position (~ 460 nm for BFCD and ~ 528 nm for GFCD), and the excitation position was shifted across the excitation spectrum. On the other hand, emission anisotropy was

measured by exciting near the excitation peak (~ 375 nm for BFCD and ~ 405 nm for GFCD), and the emissions were collected across the emission spectrum. The steady-state anisotropy values for both FCDs were relatively constant ($r_{ss} \approx 0.23$ – 0.27 for BFCD and ~ 0.27 – 0.29 for GFCD) across the excitation and emission bands. Nearly the same r_{ss} values were observed for an FCD subset (BFCD or GFCD) irrespective of excitation or emission positions, which establishes the notion of a single emissive state of our purified FCD samples. A constant r_{ss} value signifies that the angle between excitation and emission dipoles is fixed irrespective of different emission or excitation positions. This is only possible when a single excited state is involved.^[88] In addition, the observation of emission position-independent fluorescence excitation spectra from aqueous BFCD and GFCD solutions further substantiates the presence of a single emissive state in our purified samples. If multiple emission states in a single FCD particle were present, one would have observed different excitation spectra from different emissive states. Many authors reported emission wavelength-dependent fluorescence excitation spectra, which we believe are due to inadequate sample purification. Our mixed FCD sample also showed emission wavelength-dependent excitation spectra but not in the pure samples.

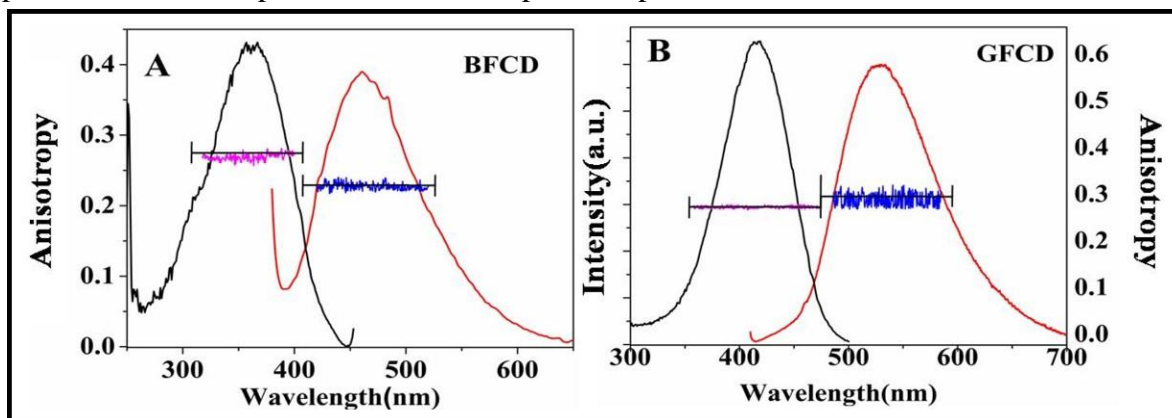


Figure 3.12. Steady-state excitation (pink horizontal line) and emission (blue horizontal line) anisotropy values across the fluorescence excitation spectrum (black) and emission spectrum (red) of BFCD (A) and GFCD (B) in glycerol.

3.3. Conclusion

In summary, we conclude that several intriguing properties of FCD fluorescence, whose origins have remained a mystery to date, mostly originated from inadequate sample purification. Through this report, we are neither contributing to the debate on the actual origin of FCD fluorescence nor proposing the chemical structure of FCD, but our work has substantiated that the actual origin of excitation-dependent emission and spectral migration of FCD fluorescence lies with its ground-state optical heterogeneity. Further, we have drawn the attention of researchers toward the urgency of sample purification with more scientific rigor. Putative molecular impurity has undoubtedly misled carbon dot literature, with detrimental claims, misconceptions, and misanalyses present. Through this work, we proposed an efficient sample purification protocol with visual column separation of crude FCD sample to different subsets and subsequently prolonged membrane dialysis. Our purified sample shows neither an excitation-dependent emission nor any spectral migration of FCD fluorescence. We also confirmed that FCD fluorescence obeys the fundamental Kasha's spectroscopic rule.

4.1. Introduction

From the discussion in chapter 1, we know GQDs are in the limelight due to a range of fascinating optical and material properties like edge effects, quantum confinements, excitation-dependent emission, low cytotoxicity, and high thermal and chemical stability.^[153,168] These remarkable properties have gradually turned GQDs into potential contenders as building blocks of light-harvesting devices, metal ion sensors, fluorescent markers, and so on.^[29,73,74] I have already discussed fluorescent carbon dots (FCD), a promising member of the carbon family in previous chapters. Despite several promises of FCDs, we preferred GQDs over FCDs for our PET study mainly because unlike FCDs, the former has well-documented structural information, larger surface area, richer spectral properties, and excellent charge mobility across the 2D π -bond network, which in turn would enable one to observe ultrafast PET when GQD is complexed with an electron donor molecule. High carrier mobility, large surface area, and compatible energy band gap have gradually turned GQDs into promising electron-accepting materials, successfully used as building blocks of organic photovoltaic (OPV) devices.^[169–173] Li et al., Gupta et al., and many other groups fabricated organic polymer (P3HT, MEHPPV etc.)/GQD-based OPV devices, which they found very efficient in power conversion compared to those having pure polymers (GQD undoped).^[169–173] In these works, GQDs are envisioned to be an excellent electron acceptor, which dissociates excitons by accepting an electron from the light-absorbing organic polymer. Organic polymers alone are not very promising light-harvesting device materials due to their short radiative

lifetime, moderate charge mobility, and lack of adequate interfaces favoring a quick charge separation. While in GQD-blended polymers, the huge surface area of GQDs helps the formation of an adequate number of p–n interfaces, which in conjunction with the excellent electron-accepting capability of GQD lead to an efficient exciton dissociation within the light-harvesting GQD-polymer composites. Despite successful integration of GQDs in photovoltaic applications, a satisfactory power conversion efficiency is not yet reached.^[169]

Through this work, we emphasized the plausible use of GQDs as light-absorbing material as well as an excellent electron scavenger, unlike its current use in OPV devices as an electron scavenger only. In contrast to the light-harvesting organic polymers, GQD possesses higher carrier mobility, longer exciton lifetime, a broader absorption profile from deep UV to the visible region, and excellent fluorescence properties. In this work, we examined the potential of GQDs as light-absorbing material and subsequently its response toward charge separation against a moderate chemical driving force. We observed that GQDs not only exhibit a long radiative excitonic recombination time (few ns), but the interfacial charge separation is also unprecedentedly fast (sub-ps) in the presence of an electron-rich organic molecule. This observation indeed adds more promises to GQDs in their device applications.^[110,169,171–173] To the best of our knowledge, the sub-picosecond (sub-ps) PET time scale observed in this study is the fastest among all reported values with similar GQD-based systems.^[110,169]

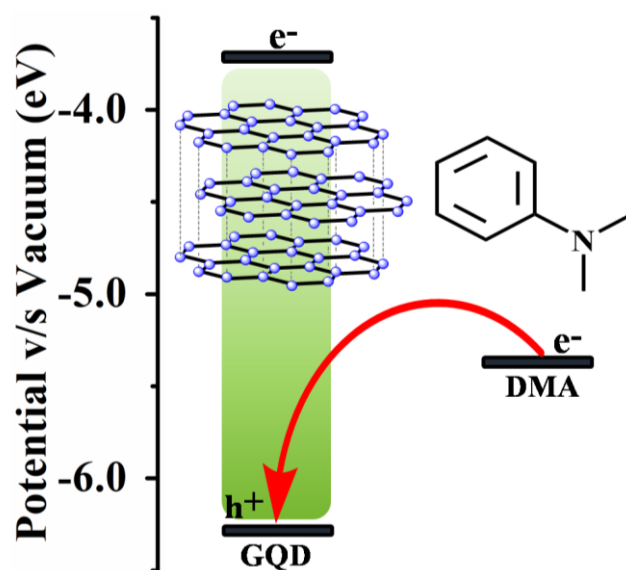
4.2. Results and Discussion

4.2.1. PET Couple Used

For our study, a highly pure aqueous Graphene quantum dots sample was purchased from Sigma-Aldrich, which was further purified by membrane dialysis. Along with GQD, we used N, N-dimethylaniline (DMA) as a hole scavenger. All the experiments were performed in Millipore

water. In our study, we selected DMA as a hole scavenger for two primary reasons: (1) Well-matched redox energy profiles of GQD and DMA (Scheme 4.1)^[110,174] (2) being nearly insoluble (<20 mM) in water, DMA is likely to form a complex with GQD in an aqueous solution which in turn would allow one to observe interfacial charge transfer kinetics, completely free from the solvent diffusion.^[111,175]

The chemical driving force ($-\Delta G_{\text{PET}} \sim 0.95$ eV) of the PET reaction was calculated from the oxidation potentials of DMA (~ 5.4 eV v/s vacuum)^[110] and the reduction potential of GQD (~ 3.7 eV v/s vacuum)^[174] respectively and the band gap energy of GQD (~ 2.65 eV) obtained from the Tauc plot. Details of ΔG_{PET} calculation and Tauc plot can be found in the second chapter.



Scheme 4.1. Energy Band Diagram of GQD-DMA Pair

4.2.2. GQD Sample Characterization and spectral Properties

HR-TEM image reveals high crystallinity, ~ 0.21 nm lattice spacing (1 0 0 plane), and an average particle size of $5.1 \text{ nm} \pm 0.6 \text{ nm}$ (Figures 4.1) of the GQD samples. Fast Fourier Transform (FFT) patterns from most of the particles show two or more sets of closely spaced 6-fold hexagonal

reflection spots, implying several graphene layers in our GQD sample.^[176,177] Further zooming the HR-TEM image to an atomic level reveals a stack of triangular layers in AAA and BBB sequences instead of a single layer of hexagonal ring pattern with ABABAB sequence, implying multiple graphene layers.^[176] Where A and B are the positions of carbon atoms in two triangular carbon sublattices. Raman spectrum shows that the I_D/I_G (disorder D band intensity/crystalline G band intensity) ratio is ~ 0.8 , signifying the high quality of our GQD sample (Figure 4.1D).

FTIR spectrum of GQD confirms the presence of $-C=C$ (aromatic 1600 cm^{-1}), $-C=N$ (1650 cm^{-1}), $-C-H$ (1460 cm^{-1} , bending), $-C-N=$ (1360 cm^{-1}), $-C-O$ (1080 cm^{-1}), $-C-N$ (1017 cm^{-1}), $=C-H$ (964 cm^{-1} , 820 cm^{-1} bending), $-OH$ (3400 cm^{-1}), and $-CH$ (3030 cm^{-1} , aromatic and 2900 cm^{-1} , alkyl) bonds (Figure 4.2 A). Polar surface groups ($-OH$, $-COOH$, etc.) enhance the solubility of GQDs in water. XRD spectrum of GQDs shows a broad peak at $\sim 23^\circ$, corresponding to an interlayer distance of $\sim 0.38\text{ nm}$ which is matching well with the reported distance between two basal planes of graphene (Figure 4.2B).

XPS spectra show the existence of broad C 1s (283 eV - 291 eV), N 1s (398 eV - 403 eV), and O 1s (530 - 535.5 eV) peaks (Figure 4.3). C 1s band is further split into four sharp bands peaked at 284.5 eV [combined peak from C-C (284.8 eV) and C=C (284 eV)], 285 eV (C-N), 286.5 eV (C=O) and 289 eV (O-C=O), respectively (Figure 4.3A). N 1s band is split into two bands (399.5 and 401 eV), representing the amide nitrogen and graphitic nitrogen, respectively (Figure 4.3B). Splitting of O 1s peak confirms the presence of C-O (533.5 eV) and C=O (532 eV) bonds, respectively (Figure 4.3C).

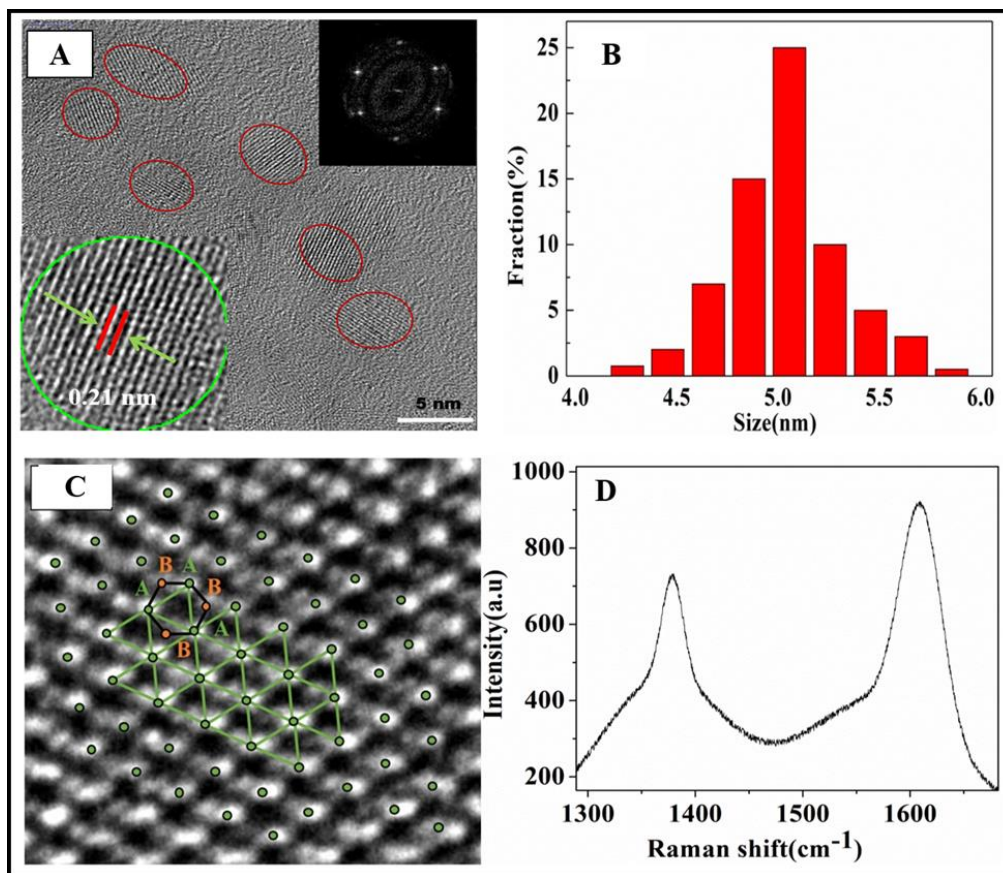


Figure 4.1. (A) HR-TEM image of GQDs. Insets show the FFT patterns and lattice spacings. (B) Size distribution of GQD particles, measured through HR-TEM. (C) Zoomed image (HR-TEM) of GQD surface to the atomic level. (D) Raman spectrum of GQDs.

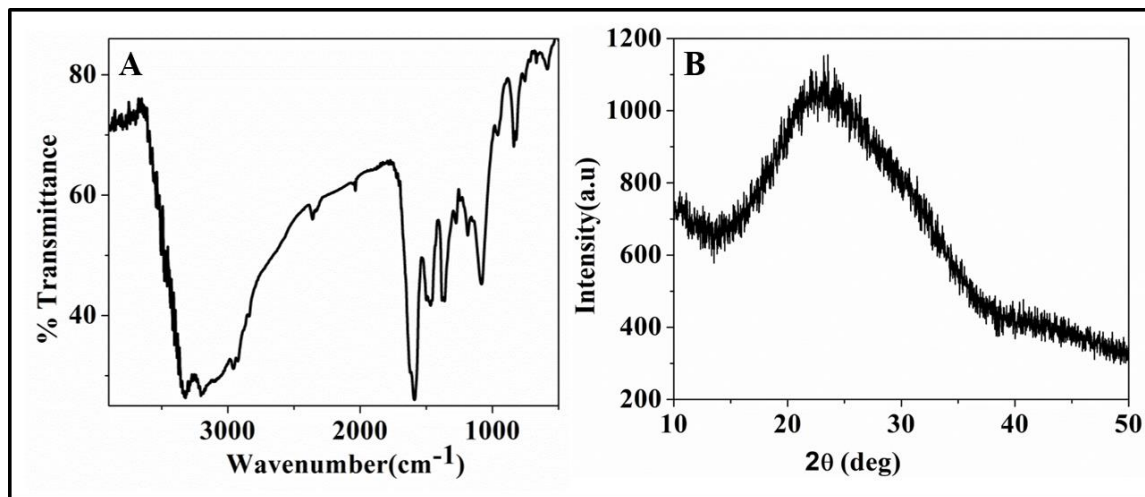


Figure 4.2. (A) FTIR spectrum of GQDs. (B) Powder XRD spectrum of GQDs.

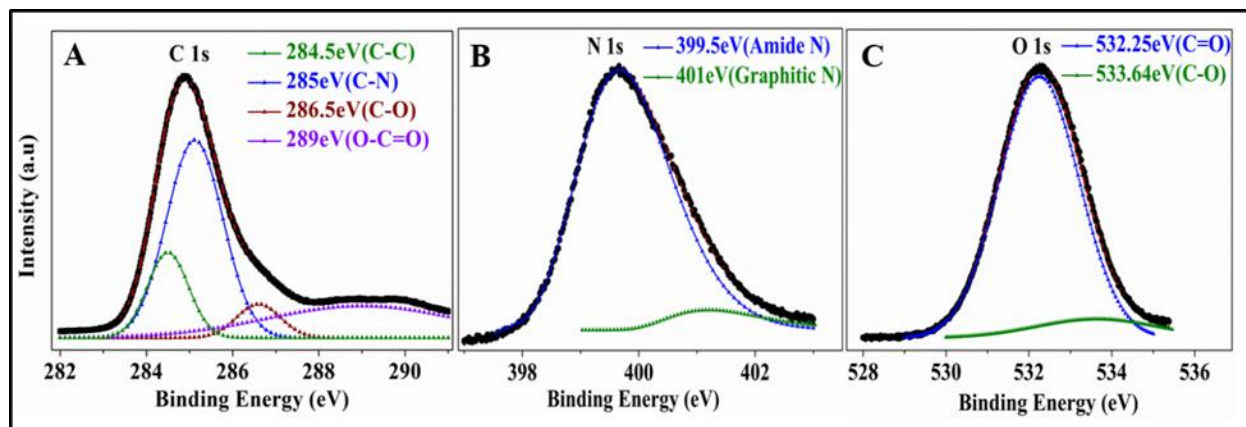


Figure 4.3. High-resolution XPS spectra (black curves) along with split curves of C 1s (A), N 1s (B), and O 1s (C), respectively.

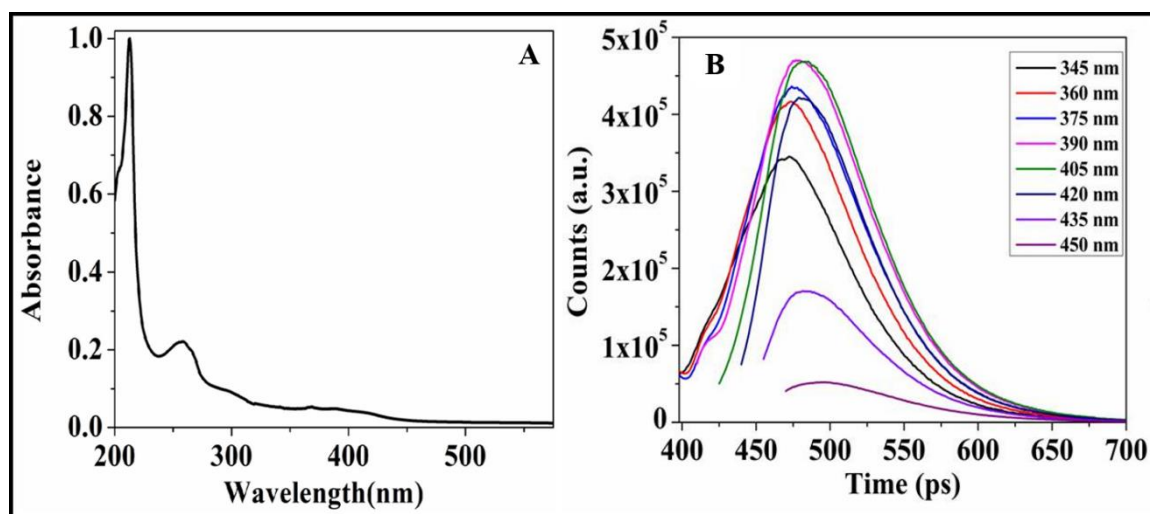


Figure 4.4. (A) Full range absorption spectrum of GQDs in water. (B) Emission spectra of GQDs in water at different excitation wavelengths. Excitation wavelengths are mentioned in the inset.

The UV–vis absorption spectrum of GQDs in water is accompanied by two well-structured bands peaked at ~ 213 nm (π – π^* transition of C=C, C=O, and C=N) and 258 nm (n – π^* transition of C=O and C=N) and a broad band in 350 to 450 nm region (Figure 4.4A). The broad band arises due to an overlap of band gap transitions with π electron transitions in partially conjugated states, typical for layered GQDs. The emission peak position of GQDs is excitation-dependent, typical for GQD/graphene oxide samples (Figure 4.4B). The GQDs are highly photoluminescent. While the

fluorescence quantum yield (Φ_f) of GQDs typically ranges from ~2% to 22%, our GQD sample shows even a higher Φ_f (~50%) in water when excited at ~405 nm.

4.2.3 Steady-State and Time-Resolved Quenching Study and Stern-Volmer (SV) plots

Analysis

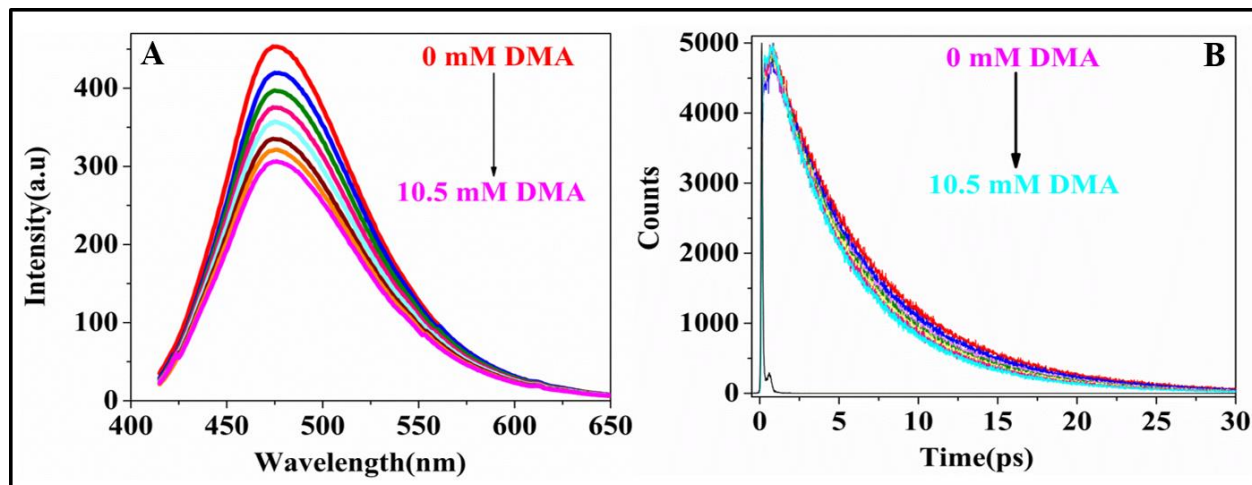


Figure 4.5. Quenching of steady state emission (A) and PL lifetime (B) of GQDs in water at 20 °C upon addition of DMA at different concentrations.

PL and fluorescence lifetime of GQDs in water quenched significantly on the addition of DMA due to a PET reaction from ground state DMA to the hole state of photoexcited GQD (Figure 4.5 and Scheme 4.1). Keeping in mind the extremely low solubility (<20 mM) of DMA in water, we used the highest DMA concentration only ~8–12 mM, much lower than its saturation concentration (~20 mM).

Steady state emissions and fluorescence lifetimes of GQDs in aqueous solution are significantly quenched by DMA (Figure 4.5). For PET analysis, time-resolved SV plots were fitted with equation,

$$\frac{\tau_0}{\tau} = 1 + k_q \tau_0 [Q] \quad (4.1)$$

Where, τ_0 , τ are the fluorescence lifetimes of GQDs in the absence and presence of Q moles/lit DMA, k_q is the bimolecular PET rate.

Steady state SV plots were fitted with equation 4.2,

$$\frac{I_0}{I} = (1 + k_q \tau_0 [Q])(1 + K[Q]) \quad (4.2)$$

I_0 and I are the steady state emission intensities of GQD in the absence and presence of Q moles/lit DMA. Values of k_q were obtained from time-resolved SV fittings and kept fixed in the steady state SV fittings. K is the association constant.

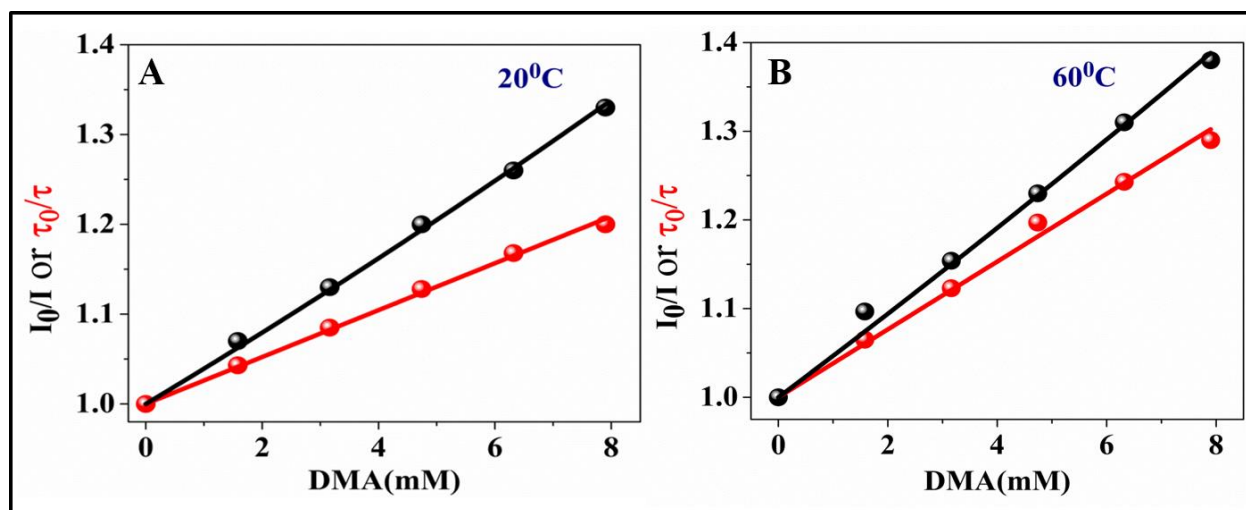


Figure 4.6. Steady-state (I_0/I) and time-resolved (τ_0/τ) Stern–Volmer (SV) plots at 20 °C (A) and 60 °C (B).

Our temperature dependence study using TCSPC (IRF ~ 80 ps) shows in all the cases (20– 60 °C) that PET rates (from 4×10^9 to $6.8 \times 10^9 \text{ M}^{-1} \text{ s}^{-1}$) approach close to the upper limit of a bimolecular diffusion-controlled process (from $6.5 \times 10^9 \text{ M}^{-1} \text{ S}^{-1}$ to $15.8 \times 10^9 \text{ M}^{-1} \text{ S}^{-1}$). This implies that the PET time scale is much faster compared to the diffusion rate of the medium (Table 4.1, Figure 4.6). At 20 °C, the lifetime SV plot shows a much lower quenching rate compared to that obtained from the steady state SV plot. However, this difference decreases with rising temperature (Figure 4.6, Table 4.1). This is a very interesting observation. In the later part of this chapter, I will explain that the actual PET time scale in a GQD-DMA complex is < 1 ps by using a femtosecond upconversion setup. Therefore, a portion of the PET kinetics (< 1 ps) other than collisional proceeds

through the GQD-DMA complex formation which escapes detection by ~ 80 ps IRF of our TCSPC, but the same is detected in the steady state quenching study. The complex formation would result in a decrease in steady state emission intensity without changing the lifetime (measured in TCSPC). Thus, a larger amount of quenching is expected in the steady state emission compared to that in the lifetime; the former technique accounts for both static (<1 ps PET in GQD-DMA complex) and collisional quenching (10–100 ns), while the latter technique accounts for only the collisional quenching (Figure 4.5). However, at elevated temperature (i.e., at 60 °C), complex formation is unlikely where only the collisional PET, unlike a <1 ps PET along with collisional PET (as in the case at 20 °C), controls the quenching process which falls well within the detection limit of our TCSPC setup. Entire PET kinetics at high temperature is equally detected through the steady state and time-resolved studies.

Temperature (°C)	K (M ⁻¹)	k _q (M ⁻¹ s ⁻¹)	k _d (M ⁻¹ s ⁻¹) of water
20	12.2	4×10 ⁹	6.5×10 ⁹
40	9.8	5.5×10 ⁹	10.6×10 ⁹
60	6.7	6.8×10 ⁹	15.8×10 ⁹

Table 4.1. Best fitted parameters of Stern-Volmer (SV) plots at different temperatures (Figure 4.6). Bimolecular diffusion-controlled rates of water, $k_d = 8 \times 10^3 RT / 3\eta$ M⁻¹s⁻¹; T is the temperature in K, R (8.3145 J mol⁻¹ K⁻¹) is the gas constant. η , the viscosity coefficient. For water $\eta = 10^{-3}$ kg m⁻¹s⁻¹ (20 °C), 0.653×10^{-3} kg m⁻¹s⁻¹ (40 °C) and 0.466×10^{-3} kg m⁻¹s⁻¹ (60 °C), respectively. [178,179]

PET can proceed through both collision and complexation mechanisms. At the millimolar range of DMA concentrations, not all GQDs would attach to a DMA molecule. A moderate value of the equilibrium constant assures there must have been a large population of free GQDs along with

GQD-DMA complexes. Binding and unbinding of GQD with a DMA molecule would cause fluctuations in the GQD emission when studied at (or near) the single-molecule level. The time scale of these fluctuations is controlled by the binding kinetics. Our FCS experiments provide mechanistic insights into the binding kinetics of GQD-DMA complex formation. Although, similar fluctuations of GQD emission are possible due to the translational diffusion of GQDs across the tiny excitation volume, the time scale of which largely differs from the μs binding kinetics and appears at the slower end of the correlation curve. Therefore a complete analysis of the FCS curve can provide not only vital information on binding kinetics but also the diffusion time scale of GQDs and thereby the particle size inhomogeneity. In the next part, we will first discuss our FCS results of binding kinetics and subsequently the sample inhomogeneity through analyzing the diffusion time distribution of GQDs and finally the PET time scale of GQD-DMA transient complexes using a femtosecond upconversion setup.

4.2.4. FCS Study of Binding Kinetics, Particle Diffusion, and Mechanism of GQD-DMA Complex Formation.

As discussed in chapter 2, we know that FCS has emerged to be the most efficient technique for studying molecular interactions, diffusions, and several other kinetics taking place within a tiny excitation volume (<1 femtoliter). The concentration of GQDs in our FCS study is used in the nanomolar (nM) range (or less) to ensure that the number of emitting molecules in the excitation volume is always ~ 1 (or less). The fewer the number of emitting molecules (GQDs) in the excitation volume, the more prominent will be the fluorescence fluctuations in the presence of DMA and thus more precise in the detection of binding kinetics. Time evolution of fluorescence fluctuations from a single GQD provides vital information on complexation and diffusion kinetics, which are difficult to obtain through ensemble studies. Time scales of the complexation processes

of interest in the FCS study must fall within a range. Slow time scale (i.e., 50– 500 μs) of translational diffusion of GQDs across the excitation volume would limit the detection of the binding time scale at the slower end, while the faster end (typically 100–500 ns) is limited by several instrumental factors like repetition rate of the excitation pulse, bin size of the correlator, instrumental dead time, signal-to-noise ratio, etc. FCS is very efficient for studying relatively fast μs kinetics since it is widely separated from the diffusion time scale. The correlation curve of nM GQDs in water in the absence of DMA is a single step decay curve, the time scale of which represents the diffusion time of GQDs across the excitation volume (Figure 4.7A). However, in the presence of DMA, the correlation curve turns into a two-step decay curve with an additional correlation at $<10 \mu\text{s}$ time regime. The inset of Figure 4.7 A, depicts the same correlation curves from the main figure but normalized at 10 μs for visualizing two processes^[180] easily: (i) correlation due to the GQD-DMA complexation kinetics ($<10 \mu\text{s}$) and (ii) diffusion kinetics of GQDs alone (in absence of DMA) or both GQDs and GQD-DMA complexes (in the presence of DMA) across the excitation volume ($>10 \mu\text{s}$). Both the processes would contribute to the correlation curve but at well-separated different time regimes. We used extremely low excitation power ($\sim 3 \text{ kW/cm}^2$) to remove triplet contribution completely from our FCS curves, otherwise, μs triplet kinetics would have overlapped with the complexation kinetics. Figure 4.8 shows that at this power FCS curves are void of triplet contribution.

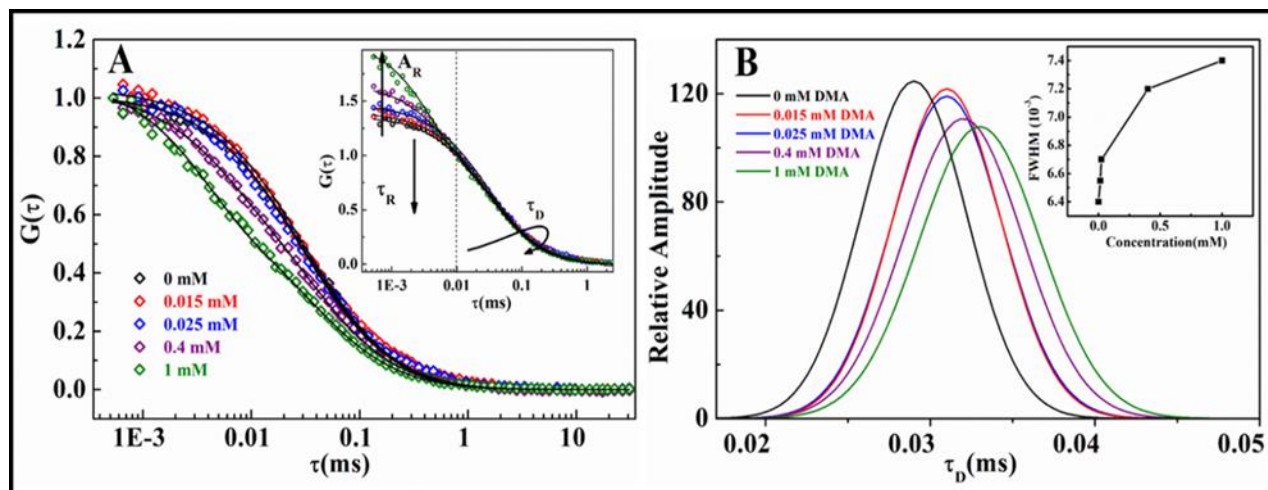


Figure 4.7. (A) FCS curves of GQDs in water at different DMA concentrations. Inset shows the same but normalized at 10 μ s. The contribution of binding reaction (A_R) appears only after the addition of DMA and increases monotonously with increasing the DMA concentration. (B) Gaussian distribution of diffusion times of GQDs at different DMA concentrations obtained from FCS curve fittings using eq 4.4. Inset shows the FWHM of the histograms as a function of DMA concentration.

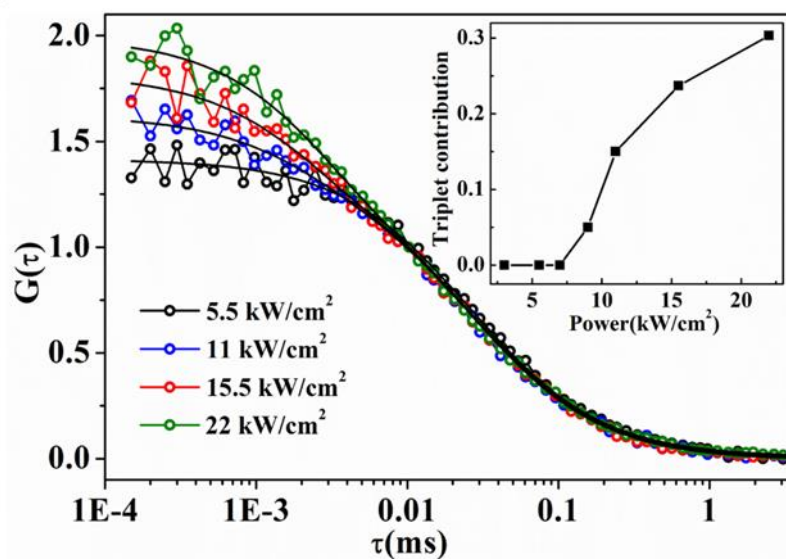
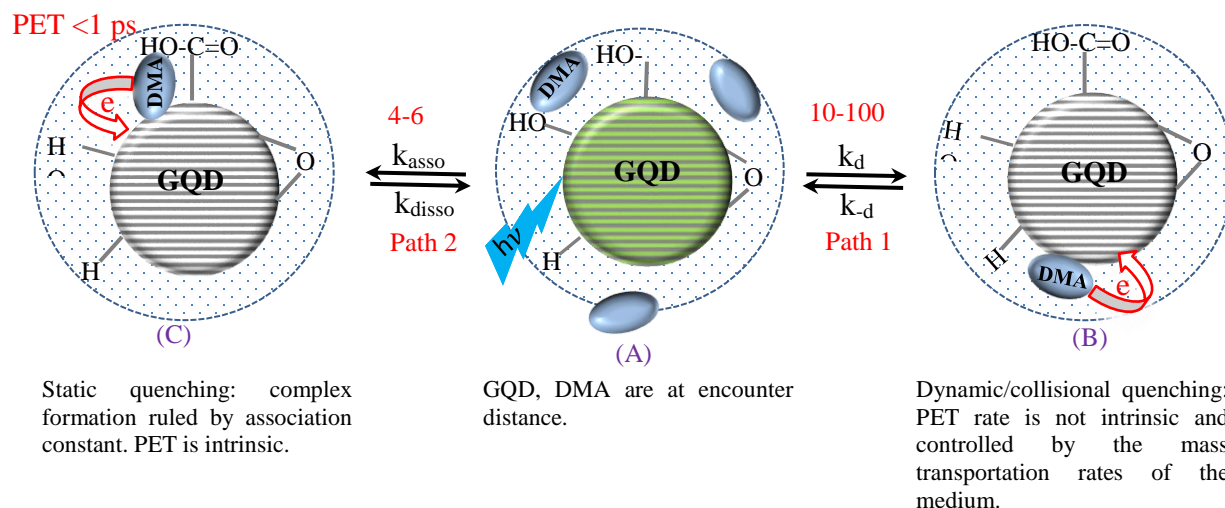


Figure 4.8. Autocorrelation curves of GQDs in water at different excitation power. Initial amplitude arises only at high excitation power (>8 kW/cm^2) due to the triplet kinetics.



Scheme 4.2. Path 1 (dynamic/collisional quenching): Collisional quenching takes place by a diffusion-controlled process, following an equilibrium ruled by k_d and k_{-d} rate constants (resulting in structure in cartoon B). Path 2 (static quenching): DMA with a favorable orientation to GQD forms a GQD-DMA static complex in the μ s timescale following an equilibrium ruled by k_{asso} and k_{disso} rate constants (resulting in structure in cartoon C).

During PET, at first DMA molecules approach the encounter distance of GQD; this is a fast process occurring in the 10s of ns time scale and is completely diffusion-controlled within the Smoluchowski limit (cartoon A of Scheme 4.2).^[178,181] For a bimolecular excited state quenching process in water, the diffusion limit for any quenching constant is $\sim 10^{10} \text{ M}^{-1} \text{ s}^{-1}$, which suggests a quenching time scale of ~ 10 to 100 ns when the quencher concentration ranges from ~ 1 to 10 mM.^{[178,181][182]} These fast diffusion-controlled rates (k_d and k_{-d} ; path 1 of Scheme 4.2) lead to the collisional quenching which escapes the temporal resolution of our FCS setup. Our FCS setup can record correlation curves from 0.5 μ s at the faster end (Figure. 4.7A). In most cases, DMA collides with a photoexcited GQD, causing an efficient collisional quenching, not detected by our FCS setup (path 1 of Scheme 4.2). However, in a few cases, the DMA molecule with favorable

geometry forms a weak GQD-DMA (1:1) static complex via hydrophobic interaction with the GQD surface and/or through the interaction with GQD head groups. The lifetime of these GQD-DMA complexes is found to be few μs and falls well within the detection limit of our FCS setup (path 2).^[180,182–187] Using our FCS setup, we can only detect the slow μs kinetics, i.e., GQD-DMA complex formation from closely placed GQD and DMA (path 2 of Scheme 4.2). This is a pseudo-first-order complexation reaction since we used DMA concentration ($\sim 0.015\text{--}1\text{ mM}$) in large excess compared to the GQD concentration ($\sim 1\text{ nM}$). The concentration of DMA ($[\text{DMA}]$) will remain constant to its initial concentration ($[\text{DMA}]_0$), despite the complex formation. Complex formation holds the donor and acceptor molecules at contact distance for a longer time ($\sim \text{few } \mu\text{s}$), during which an ultrafast PET ($< 1\text{ ps}$) from DMA to the photoexcited GQD results in modulation of GQD emission from a high-intensity state (\uparrow , free GQD) to the low-intensity state (\downarrow , quenched GQD in the GQD-DMA complex). When these intensity fluctuations are time correlated, an additional correlation due to the complexation kinetics is observed in the μs time regime of the FCS curve (Figure 4.7A, inset).^[180,183,184,188,189] In static quenching (path 2), while the intensity fluctuation of GQD is caused by an ultrafast sub-ps PET following the GQD-DMA complex formation, the time scale of intensity fluctuation in the FCS study is controlled by the slow μs complexation reaction time. This is in analogy to the collisional quenching (path 1), where the ultrafast PET time scale is masked by a relatively slow diffusion time scale (10–100 ns). However, in collisional quenching, even the slow diffusion time scale is fast enough to escape detection by our FCS setup. FCS can only detect the slow complexation kinetics (path 2). Therefore, the correlation at the μs regime, whose contribution increases with increasing DMA concentration, is due to a weak GQD-DMA transient complex formation (inset of Figure 4.7 A). In Scheme 4.2, k_d is the rate constant at which the DMA molecule collides with a GQD, and in most of the cases,

instead of a complex formation, the DMA molecule goes away (with a rate constant k_{-d}) after a collision. An ultrafast PET during collision causes the quenching. Intrinsic time scales of PET could not be detected through collisional quenching study for being their diffusion-controlled nature. Path 2 of Scheme 4.2 represents the static quenching, where k_{asso} and k_{disso} are the rates of the GQD-DMA complex formation (Cartoon C) and separation to encounter distance (Cartoon A), which occurs at a much slower time scale (4–6 μs ; path 2) when compared with that (10–100 ns; path 1) of collisional quenching. The complexation process is comfortably detected by our FCS setup. Quenching of GQD emission through PET is possible by collisional quenching (when GQD is free), as well as by static quenching (in the GQD-DMA complex). The PET rate measured by photoexciting the GQD in the GQD-DMA complex is the actual PET rate where diffusion does not play any role. If the equilibrium constant of complex formation is K ($=k_{\text{asso}}/k_{\text{disso}}$), the characteristic time of the complexation reaction is τ_R [$=(k_{\text{asso}}[\text{DMA}]_0 + k_{\text{disso}})^{-1}$, assuming pseudo first-order], and the characteristic diffusion time across the excitation volume is τ_D , then the complexation reaction coupled FCS curves can be modeled with the following equation,^[180,183,184,188]

$$G(\tau) = \frac{1}{N} \left(1 + \frac{\tau}{\tau_D}\right)^{-1} \left(1 + \frac{\tau}{\tau_D}\right)^{-1/2} [1 + A_R \exp(-\tau/\tau_R)] \quad (4.3)$$

Where, A_R [$=K[\text{DMA}]_0(1 - Q)^2/(1 + K[\text{DMA}]_0Q)^2$] is the amplitude of the complexation reaction, Q is the ratio of quantum yields of quenched state (\downarrow) to unquenched state (\uparrow), N is the average number of fluorescent molecules in the excitation volume. ω is the structural parameter of excitation volume, the value of which was obtained through calibration with a dye molecule whose diffusion coefficient is reported.^[190] However, the above equation could not fit our FCS curves satisfactorily. This is perhaps due to using a single τ_D in the above equation rather than using a set

of τ_{Ds} accounting for the size distribution of the GQD sample. By using a single τ_D value, we tacitly assumed all GQD particles have the same size (and thus the same diffusion time τ_D). Recently Sen et al. emphasized the use of a set of narrowly spaced τ_{Ds} to account for the size distribution of AOT (aerosol OT, sodium bis (2-Ethylhexyl) sulfosuccinate) microdroplets (MDs) immersed in isooctane which eventually enabled them conclusive fittings to their FCS curves with a better reduced χ^2 value when compared with that of using a single τ_D value.^[183,184] Size heterogeneity is even more drastic for our GQD sample, which suggested using a set of diffusion times (τ_{Ds}) instead of a single τ_D , covering a broad range of particle sizes. A set of τ_{Ds} , whose population follows a Gaussian distribution, are incorporated in eq 4.3 as follows,

$$G(\tau) = \frac{1}{N} \sum_{i=1}^m [a_i (f(\tau_{Di}))] \left(1 + \frac{\tau}{\tau_D}\right)^{-1} \left(1 + \frac{\tau}{\tau_D}\right)^{-1/2} [1 + A_R \exp(-\tau/\tau_R)] \quad (4.4)$$

Where,

$$a_i [f(\tau_{Di})] = \frac{B \exp\left[-2 \left\{\frac{\tau_{Di} - \tau_D}{b}\right\}^2\right]}{b\sqrt{\pi/2}}$$

In the above equation, constant B is correlated to the fraction of particles in the confocal volume having diffusion time τ_{Di} and its brightness. τ_D and b are, respectively, the peak and width of the Gaussian distribution histogram of particle diffusion times. Eq 4.4 enabled conclusive fittings to our FCS curves. Complexation reaction amplitude $A_R [=K[\text{DMA}]_0(1 - Q)^2/(1 + K[\text{DMA}]_0Q)^2]$, characteristic reaction time $\tau_R [= (k_{\text{asso}}[\text{DMA}]_0 + k_{\text{disso}})^{-1}]$, and thereby the value of association equilibrium constant K ($=k_{\text{asso}}/k_{\text{disso}}$) from the known value of Q were obtained from the fittings. During the fitting, we kept Q fixed at 0.03. Q is the quantum yield ratio of GQD fluorescence in the quenched state/ unquenched state [i.e., in neat DMA (~ 0.015)/in neat water (~ 0.50)]. Values of K and τ_R are further exploited to obtain the rates of association (k_{asso}) and dissociation (k_{disso}) of

the complexation reaction (Table 4.2). In all the cases, fittings with eq 4.4 using a set of τ_{Di} ($i = 1$ to 30) showed a reduced χ^2 value close to 1, much improved when compared with the fitting using a single diffusion time (by eq 4.3).

[DMA] (mM)	A _R	τ_R (μ s)	$k_{\text{asso}}(\text{M}^{-1}\text{s}^{-1})$	$k_{\text{disso}}(\text{s}^{-1})$	K (M^{-1})
0	0		1.16×10^8	1.66×10^5	700
0.015	0.010	6			
0.025	0.015	5.8			
0.400	0.259	4.7			
1	0.632	4			

Table 4.2. Best fitted parameters (related to the GQD-DMA complexation reaction) of FCS curves using Equation 4.4 (Figure 4.7A).

Sample inhomogeneity of GQDs is also examined by FCS by analyzing the distribution in translational diffusion times (τ_{Ds}). A broader distribution signifies a polydisperse nature of the sample, while narrow distribution indicates a monodisperse nature. FCS curves were fit satisfactorily to eq 4.4 assuming a single-modal Gaussian distribution on τ_{Di} rather than a bimodal distribution when GQD and the GQD-DMA complex coexist (Figure 4.7B). This is because bound and free forms of GQDs are quickly (in few μ s) interconverted several times during diffusion (~ 0.03 ms) of GQDs across the excitation volume, which makes it impossible to observe a bimodal distribution (accounting for GQD-DMA complexes and free GQDs). Even if the interconversions were slow, it would have been difficult to resolve two peaks in Gaussian distribution due to their slight separation in distribution peak positions. There will be a small change in size (thus diffusion time) when a large-sized GQD (~ 5.1 nm) forms a complex with a relatively small (~ 0.8 nm) DMA molecule (Table 4.2). During fittings, τ_D (distribution peak) and b (distribution width) were varied

systematically, while a set of 30 fixed diffusion times τ_{Di} ($m = 30$ in eq 4.4) were placed linearly within 0.015–0.045 ms to obtain the best distribution histogram $a_i[f(\tau_{Di})]$. By using 30 translational diffusion times, we assumed that 30 different-sized GQDs are present in the sample. With this assumption, we obtained nice fittings to the FCS curves. The histograms of diffusion times were simulated from the best-fitted parameters (Figure 4.7B, Table 4.3).

Fittings of FCS curves in early correlation show that the characteristic complexation reaction time (τ_R) shrinks from ~ 6 to ~ 4 μ s with increasing the quencher concentration from ~ 0.015 mM to ~ 1 mM, respectively (Table 4.2). The amplitude of complexation reaction (A_R) increases steadily with increasing the DMA concentration (Table 4.2, Figure 4.7A inset). There are several reports where similar μ s reaction times have been reported through FCS studies for nanoparticles and biomolecules.^[183,188,189,191] For instance, Sen et al. observed a ~ 25 μ s dimer lifetime where two AOT MDs, one loaded with ferric nitrate and the other with ammonium oxalate, were fused.^[183] Sauer et al. observed an additional μ s correlation in the FCS curve of the fluorescent dye MR121 in the presence of tryptophan which they assigned due to a MR121-tryptophan complex formation at the μ s time scale.^[189] The amplitude of complexation kinetics increases significantly with increasing the tryptophan concentration, a good agreement with our findings. Distributions of diffusion times ($a_i[f(\tau_{Di})]$ s) of GQDs at different DMA concentrations are depicted in Figure 4.7B. (Table 4.3). A relatively narrow distribution having a peak at 0.029 ms was observed in the absence of DMA. The narrow distribution of the $a_i[f(\tau_{Di})]$ histogram in the absence of DMA is well correlated with earlier observations in the HRTEM study, which showed a similar narrow distribution of particle sizes (Figure 4.1). The addition of DMA to GQD results in a little shift of the peak position of the histogram to longer τ_D (i.e., larger particle size). At the same time, fwhm broadens slightly due to the presence of different-sized particles (i.e., GQDs and GQD-DMA

complexes) (Figure 4.7B inset, Table 4.3). In summary, from the FCS study, we have observed the formation of weak GQD-DMA complexes in water with a characteristic binding time of $\sim 4\text{--}6$ μs . In the rest of this chapter, we will focus on quenching studies and subsequently accurate detection of the PET time scale of GQD-DMA complexes. The PET time scale we report here is not diffusion-controlled but rather a thermodynamically controlled intrinsic charge separation time scale.

[DMA] (mM)	B	τ_D^\dagger (ms)	b
0	0.0024	0.029	0.0064
0.015	0.0025	0.031	0.00655
0.025	0.0025	0.031	0.0067
0.4	0.0024	0.032	0.0072
1	0.0023	0.033	0.0074

Table 4.3. Best fitted parameters (pertaining to $a_i[f(\tau_{Di})]$ histogram; Figure 4.7B) of FCS curves using Equation 4.4. Here translational diffusion parameters are reported. During fitting a total of 30 fixed diffusion times (τ_{Di} ; $i=1$ to 30) were placed linearly in 0.015-0.045 ms time regime. Fitting started from 0.015 ms as the fastest diffusion time to avoid mixing of complexation reaction time (τ_R) with diffusion time.

[†]A direct correlation between diffusion time and particle size of GQD using Stokes-Einstein equation can't be obtained for plate shaped GQDs. Stoke-Einstein equation can predict diffusion time (or size) of a particle from its known size (or diffusion time) only for spherical particles.

4.2.5. Femtosecond Upconversion Study of Intrinsic Electron Transfer Kinetics of GQD-DMA Complex.

Recently Prasad et al. studied PET from aniline derivatives (including DMA) to GQDs, where they observed radical cation peaks of aniline derivatives in transient absorption measurements.^[110] Radical cation peaks confirmed that the PET was taking place from aniline derivatives to the photoexcited GQD (Scheme 4.1). However, their interesting work could not detect the intrinsic PET time scale, which seems to have escaped detection by the nanosecond time resolution of their laser flash photolysis setup. Instead, they were able to observe the diffusion-controlled rate of the medium.^[110] In the preceding section, we discussed the formation of the weak GQD-DMA complexes at room temperature. To obtain the intrinsic PET time scale which seems to be much faster compared to the diffusion-controlled processes, we used a femtosecond upconversion setup (IRF~ 0.3 ps). In the absence of DMA, femtosecond fluorescence transient of GQD ($I_t[0]$) shows an ultrafast decay (~1.5 ps) at blue emission wavelength due to the solvation dynamics which precede the long decay components (3300 and 6850 ps) due to the band edge excitonic recombination (Table 4.4). We observed that a similar ultrafast rise (~1.2 ps) component precedes the long decay components at red emission wavelengths. This fact unambiguously confirms the presence of ultrafast excited state solvation dynamics.^[161,192] Ultrafast solvation (~1 ps) of organic dye molecules in bulk water is reported by several authors.^[161,192] However, Cushing et al. reported a relatively slower solvation time (~600 ps) of graphene oxide in the aqueous medium. This is justified since the graphene oxide has a large hydrophobic surface that retards the motions of the water molecules around the surface.^[153] In the presence of the quencher ($I_t[Q]$), the ultrafast decay component at the blue emission wavelength shrinks further to <1 ps, the contribution of which increases from ~18% to ~30% with a gradual increase of DMA concentration, respectively, from

~3 to ~9 mM (Table 4.4, Figure 4.9). This fact implies the mixing of ultrafast PET (<1 ps) with an ultrafast solvation component (~1.5 ps) in the presence of DMA. To avoid the mixing, we plotted ratio curves of femtosecond transients of GQDs in the presence of the quencher to the same in the absence of the quencher (i.e., $I_t[Q]/I_t[0]$) at different DMA concentrations. The decay of these ratio curves is solely controlled by the PET kinetics, free from the solvation dynamics and excitonic recombination kinetics (inset of Figure 4.9A). $I_t[Q]/I_t[0]$ curves were fit to a multiexponential decay function which reveals that an ultrafast component (<1 ps) appears only after the addition of DMA and the contribution of which increases steadily from ~3% to ~14% with increasing the quencher concentration from ~3 to ~9 mM, respectively (Figure 4.9A inset). This ultrafast PET component, reflecting the intrinsic PET time scale of the GQD-DMA complex, precedes post-ns decay component(s) at a longer delay time due to the collisional quenching. With increasing the DMA concentration, a greater number of complexes are formed that cause more contribution of a < 1 ps PET component (Figure 4.9A inset). To further confirm that the origin of the < 1 ps component is from the interfacial PET, we recorded the femtosecond fluorescence transient of the ~9 mM DMA sample at a much elevated temperature (~70 °C), where weak GQD-DMA complexes would dissociate (Figure 4.9B). Interestingly, we found that due to the dissociation of complexes a large contribution of < 1 ps component disappeared at 70 °C when compared to that of 20 °C (Figure 4.9B). Our temperature-dependent study unambiguously confirms that the < 1 ps component is originated from the interfacial PET of GQD-DMA complexes. Since a few GQDs can form complexes, the contribution (~3%–14%) of < 1 ps component in the entire PET kinetics remains always low (Figure 4.9A inset). When we compare the later time transient (>10 ps) of 9 mM DMA sample at 70 °C with that of 20 °C, we find former decays at a much faster rate compared to that of later (Figure 4.9B inset). This is a very interesting

observation. At elevated temperature, unlike the static quenching (<1 ps) which becomes less efficient, the collisional quenching (10–100 ns) turns out to be more prominent due to the faster diffusions of GQD and DMA at elevated temperature. An efficient collisional quenching at higher temperature results in faster decay to the post-ns component(s) (Figure 4.9B). It is worth mentioning here that there is one type of PET present in the GQD-DMA redox couple, occurring at <1 ps time scale. The collisional PET rate, obtained from the lifetime quenching data using a TCSPC (Figure 4.6), is not the thermodynamically controlled intrinsic PET rate. There are two key factors which were responsible for not being able to see the actual PET kinetics from SV plots. (1) Ultrafast intrinsic PET escaped the detection by our TCSPC (~ 80 ps IRF). (2) Slow diffusion (10–100 ns) of donor and acceptors that precedes the ultrafast intrinsic PET in the overall reaction scheme shadowed the intrinsic PET. Therefore, the time-resolved SV plots are ruled by the slow diffusion time of the redox couple in water (Figure 4.6). Using a femtosecond upconversion technique (IRF ~ 0.3 ps), one can detect the ultrafast PET provided diffusion would not play any role in PET reaction. Otherwise, like TCSPC, the femtosecond upconversion setup would measure the same diffusion-controlled rates. We are fortunate that GQD forms a complex with a DMA molecule with a lifetime of 4–6 μ s, which enabled us to measure a much faster intrinsic PET time scale (<1 ps) using a femtosecond upconversion setup. In upconversion measurements, we photoexcited the GQD of the GQD-DMA complex where diffusion would not play any role in the PET reaction since DMA is already attached to GQD at the time of excitation. We strongly believe one DMA molecule is attached to a GQD despite the mM DMA concentration we used against the μ M (or nM) concentration of GQD in the upconversion (or FCS) measurement. The equilibrium constant of the GQD-DMA complex is found to be ~ 700 M^{-1} , implying a weak interaction, which is inadequate for higher-order complex formation. GQD-DMA is not a true complex in the strict

sense compared to other complexes where, unlike GQD-DMA complexes, the donor–acceptor remains attached for a longer time with a much higher value of the equilibrium constant ($\sim 10^5$ M⁻¹ or more). Even a short association time (few μ s) in our case is at least 106 and 103 times longer compared to the PET time scale (< 1 ps) and the excited state lifetime of GQDs. This enabled us to observe intrinsic PET in a GQD-DMA complex by exciting the attached GQD in a femtosecond upconversion study. Weak interaction and short association time rule out the possibility of higher-order aggregations. This notion is further substantiated by the FCS study of translational diffusion. The longer the translational diffusion time (τ_D), the larger will be the hydrodynamic radius r_h (as $r_h \propto \tau_D$). Average translational diffusion time of GQDs across the excitation volume does not change much (0.029 to 0.033 ms) as we increase the DMA concentration (0 mM to 1 mM) (Table 4.3). This fact rules out the formation of higher-order aggregates with bigger particle sizes. Higher-order aggregates if formed would have delayed the diffusion time to a greater extent. In addition, no extra peak in the absorption spectrum of GQDs representing the GQD-DMA complex formation was observed in the presence of DMA. All these facts unanimously confirm a weak one-to-one interaction between the GQD and DMA molecule causing a short-lived transient complex formation. Except the interference from collisional quenching, there are certain benefits of the solution phase PET study, like it ensures one-to-one donor–acceptor interaction when the quencher concentration is in the mM range. The one-to-one interaction would provide an accurate estimation of PET rate per quencher molecule. In the liquid phase PET study, oxygen in the air have an insignificant role in the quenching process. These are not possible in solid state PET study.

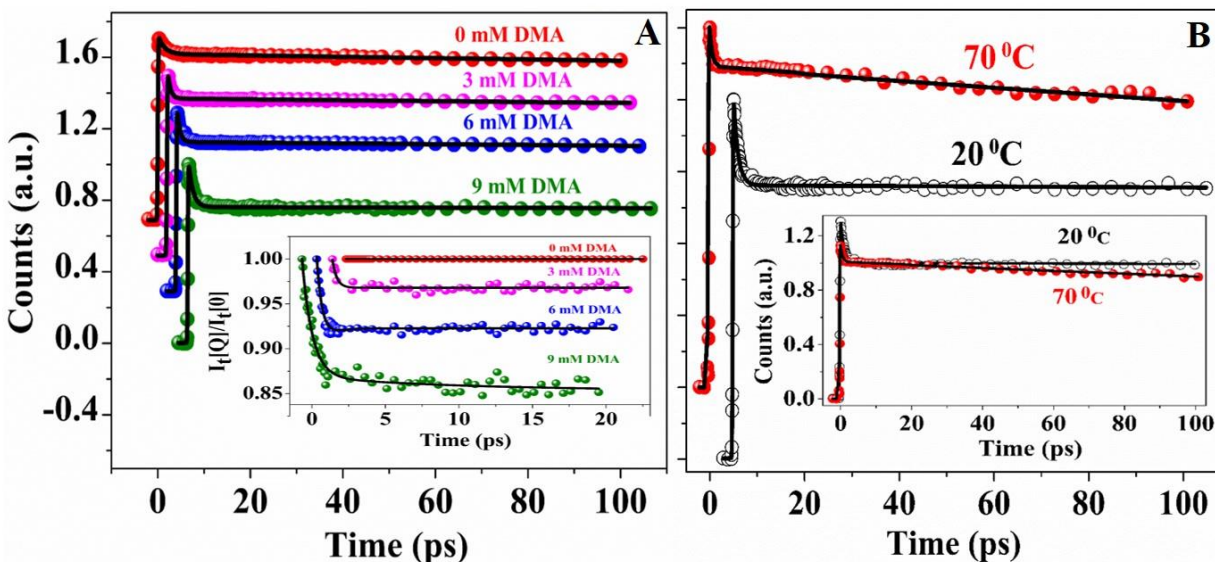


Figure 4.9. (A) Femtosecond fluorescence transients of GQDs in water at different DMA concentrations (20 °C). Inset shows the ratio curves of femtosecond transients ($I_t[Q]/I_t[0]$), decay of which is due to PET only. (B) Femtosecond transient of GQDs in the presence of 9 mM DMA at two temperatures 20 °C (black circle) and 70 °C (red ball), respectively. Large contribution of <1 ps component at 20 °C is due to an ultrafast PET of GQD-DMA complexes, which largely receded at 70 °C as most of the complexes dissociate. Interestingly, long decay components, which originate from the collisional quenching, decay at faster rates at 70 °C when compared to that at 20 °C. In the inset, we normalized the counts for both the curves at 10 ps to compare decay rates of long components visually. $\lambda_{ex} \sim 400$ nm and $\lambda_{em} \sim 470$ (little blue side of the emission peak). Solid black lines represent the fitted curves.

[DMA] (mM)	a ₁	a ₂	a ₃	τ ₁ (ps)	τ ₂ (ps)	τ ₃ (ps)
0	0.06	0.43	0.51	1.5	3300	6850
3	0.18	0.62	0.2	0.70	2950	6380
6	0.21	0.39	0.4	0.70	2350	5980
9	0.3	0.16	0.54	0.70	1300	5730

Table 4.4. Fitting parameters of femtosecond fluorescence transients ($\lambda_{\text{ex}} \sim 400$ nm and $\lambda_{\text{em}} \sim 470$ nm) of GQDs at different DMA concentrations. Since femtosecond transients were recorded only up to 100 ps, we fixed long components (post ns, τ_2 and τ_3) from TCSPC fittings.

4.3. Conclusion

In summary, we observed highly exergonic PET from an electron-rich organic molecule DMA to a photo-excited GQD. The most interesting finding of this work is the detection of <1 ps PET time scale at a GQD surface against a moderate chemical driving force ($-\Delta G^0 = 0.95$ eV). Ultrafast PET is a basic requirement for the successful utilization of the MEG process and thereby a dramatic improvement in device efficiency. To the best of our knowledge, this is the first-ever report of <1 ps PET time scale in the GQD composite. Observing an ultrafast bimolecular PET component through the solution phase study is always challenging where ultrafast kinetics are shadowed by the slow diffusion-controlled processes of the medium. However, in our study since GQD forms a moderately stable complex with DMA, solvent diffusion would not have any role in the sub-ps intrinsic PET kinetics. A noninvasive single-molecule sensitive technique FCS reveals a weak GQD-DMA complex formation with a 4–6 μs lifetime. Femtosecond upconversion study resolves a < 1 ps interfacial PET component of the GQD-DMA complex, the contribution of which largely diminishes at elevated temperature as the complex dissociates. A sub-ps component accounts for

~3%–14% of the total PET kinetics which implies only a few GQDs are engaged in the complexation reaction. A major part of the charge transfer kinetics proceeds through the collisional quenching at the post 10 ns time scale. At elevated temperature collisional quenching becomes more pronounced, causing a faster quenching rate of the longer lifetime components. Sub-ps interfacial charge transfer time scale along with rich spectral properties of GQDs would pave a new avenue with enormous possibilities of enhancing efficiencies within the next-generation devices

5.1. Introduction

In the previous chapter, I have discussed our work of highly exergonic PET from an electron-rich organic molecule DMA to a photo-excited GQD. In this chapter, I will discuss our work on temperature-dependent ultrafast interfacial charge transfer timescale and the mechanism of GQD in presence of an electron-deficient molecule. Apart from ultrafast PET timescale, GQDs bear an energy band gap compatible with most of the host materials forming thin films in device applications. Though the solution phase study undoubtedly has greater control over reaction stoichiometry, it suffers from a major disadvantage for fast PET kinetics, where PET rate levels off to the diffusion-controlled limit of the reaction medium. As in this work, the temperature-dependent TCSPC lifetime quenching study appears at the upper limit of the bimolecular diffusion-controlled rate of the medium, we obtained the diffusion-free ultrafast PET timescale of the GQD-DNT complex in aqueous methanol by employing a femtosecond upconversion technique. The ultrafast PET timescale of GQDs observed in our studies would add some potential to its ability to become an excellent candidate for light-harvesting and sensing applications.

5.2. Results and Discussion

5.2.1. Characterization of GQDs.

An aqueous GQD sample was purchased from Sigma-Aldrich. All experiments were performed within one month from the date of receipt. HR-TEM images, FFT patterns, FTIR study and Raman study showed similar properties as in the previous chapter.

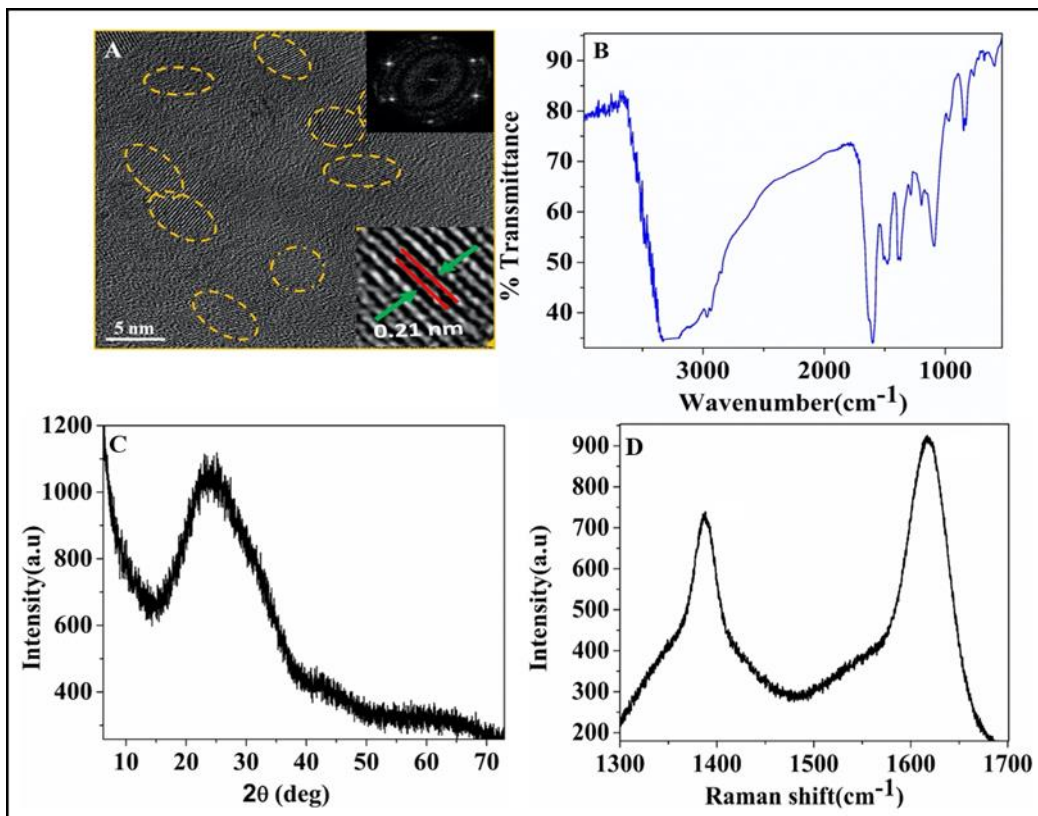


Figure 5.1. High-resolution TEM (HR-TEM) image of GQDs. Inset shows a lattice spacing of ~ 0.21 nm and the hexagonal FFT pattern. (B) Fourier transform infrared spectroscopy (FTIR) image of GQDs. (C) Powder XRD spectrum of GQDs. (D) Raman spectrum of GQDs showing the G and D bands.

5.2.2. Steady state and Time-resolved Quenching Study

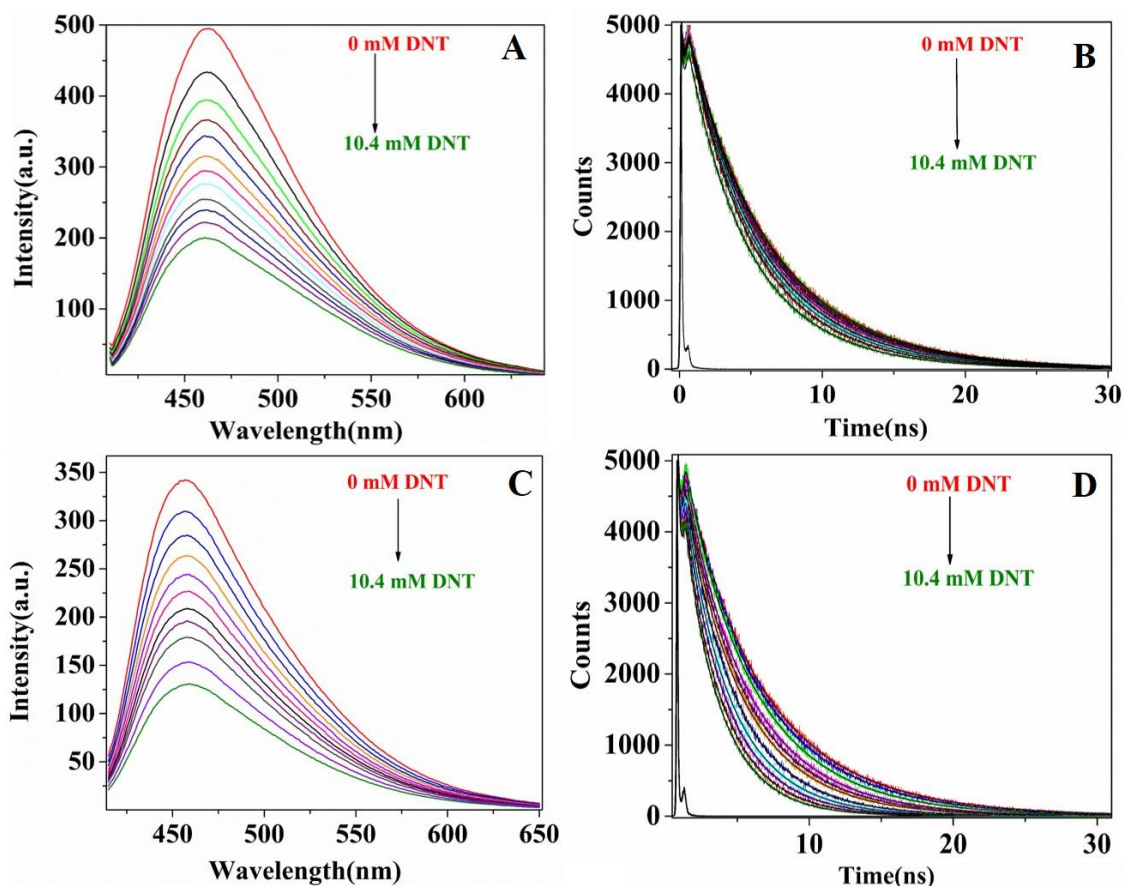
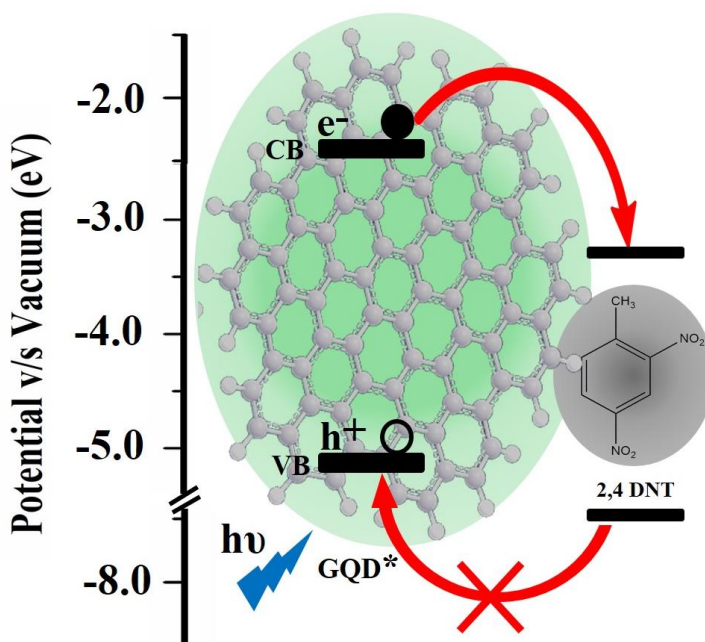


Figure 5.2. Quenching of PL (A, C), and fluorescence lifetime (B, D) of GQDs in aqueous-methanol at 20 °C (A, B) and 60 °C (C, D) in the presence of DNT at different concentrations.

The PL intensity and fluorescence lifetime of GQDs in aqueous methanol (50% by volume) are significantly quenched in the presence of DNT (Figure 5.2). While DNT is almost insoluble in pure water, it is moderately soluble in the water–methanol mixture. The solvent properties of a protic–aprotic binary solvent largely deviate from the average properties (mole fraction weighted) of the constituent solvents. However, in our case, since both methanol and water are protic and completely miscible at any ratio, their mixture would behave more like a single component solvent.

Unlike organic dye molecules, the band edge energy level of GQDs is not altered by the solvent heterogeneity, solvent local cluster formation, or synergistic effects of the binary solvent, which further confirms that the change of solvent from pure water to the water–methanol mixture would not affect the intrinsic PET rate of the GQD–DNT complex.^[193–197] Shape, FWHM, and the peak positions of absorption and emission spectra of GQDs do not change much when transferred from neat water to the water–methanol mixture, indicating neither a solvent-induced aggregation of GQDs and thereby change in their respective energy levels, nor does any structural change occur. Like PL (steady state), the fluorescence lifetime of GQDs quenches significantly in the presence of DNT. (Figure 5.2).

Among several possible pathways of quenching, PET from the high energy state conduction band (~ -2.45 eV v/s vacuum)^[174] of GQD* to the LUMO (~ -3.4 eV v/s vacuum)^[111] of DNT is the only thermodynamically favorable pathway leading to the quenching (Scheme 5.1).



Scheme 5.1. Energy levels of GQD and DNT involved in the PET reaction.

Associated chemical driving force ($-\Delta G_{\text{PET}} \sim 0.95$ eV) for the PET reaction is calculated from the energy difference between GQD-CB and DNT-LUMO as shown in the above scheme (details in chapter 2). The negative ΔG_{PET} value confirms the exergonic nature of the PET taking place from GQD* to the DNT.^[198] Other quenching mechanisms like PET from DNT-HOMO to the valence band (VB) of GQD* and FRET from the GQD* to DNT are not possible due to the following reasons: (1) we excited the sample (GQD + DNT) at ~ 405 nm, where only GQDs are excited. Since the HOMO of DNT is much lower in energy compared to that of the VB of GQD*, an electron transfer from DNT to GQD* would be thermodynamically forbidden.^[199] (Scheme 5.1) (2) FRET from GQD* to DNT can also result in quenching of GQD emission, but for that, a spectral overlapping between GQD emission with DNT absorption is essential, which is not observed here.^[200] Therefore PET from GQD* to DNT is the sole mechanism of the quenching of GQD emission. The fluorescence lifetime and PL intensity of GQDs in aqueous methanol as a function of DNT concentration are exploited in Stern–Volmer (SV) analysis to obtain the bimolecular PET rate constant (k_{PET}) and GQD–DNT binding constant (K). In the aqueous methanol, DNT is moderately soluble, which restricted us from using <12 mM as the maximum DNT concentration. The lifetime SV plot exhibits a lower quenching rate compared to that of the steady-state SV plot irrespective of the experimental temperature. However, the difference between steady-state and time-resolved quenching rates decreases with increasing the temperature (Figure 5.3).

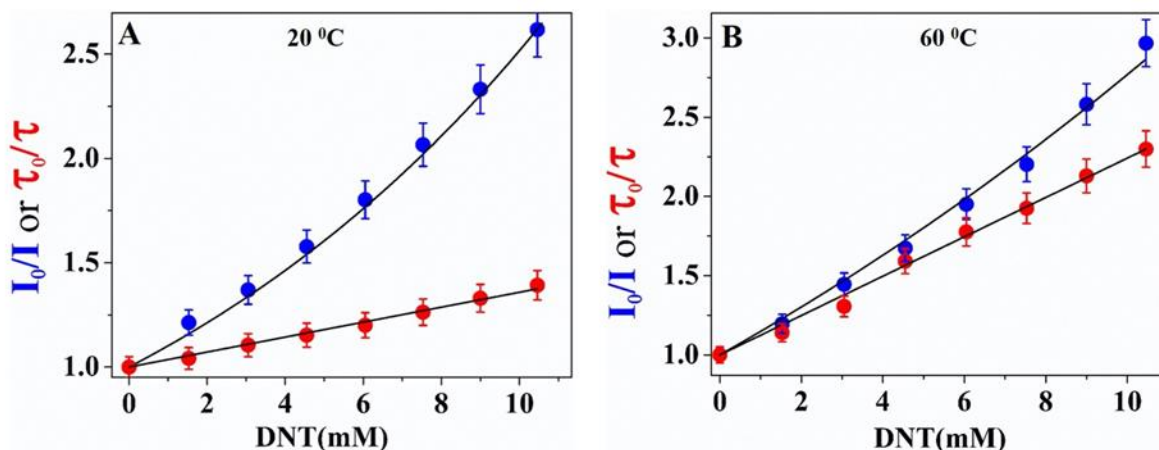


Figure 5.3. Steady-state SV plot (blue balls) and lifetime SV plot (red balls) at (A) 20 °C and (B) 60 °C, respectively.

While the lifetime SV plot is fitted solely by eq 4.1 providing the collisional PET rate (k_{PET}), the steady-state SV plot is fitted by eq 4.2 where k_{PET} is fixed from eq 4.1. Fitting to the steady-state SV plot provided us association constant (K) of the GQD–DNT complex. (details in chapter 4)

Temperature (°C)	K (M^{-1})	k_{PET} ($M^{-1} s^{-1}$)	${}^{\dagger}k_d$ ($M^{-1} s^{-1}$)
20	85	5.5×10^9	6.5×10^9
40	22	15.5×10^9	12×10^9
60	22	19.5×10^9	19×10^9

Table 5.1. Stern-Volmer fitting parameters and bimolecular diffusion-controlled rate (k_d) in aqueous methanol at different temperatures.

${}^{\dagger}k_d = 2 \times 10^3 RT (r_{GQD} + r_{DNT})^2 / 3 \eta r_{GQD} r_{DNT} M^{-1} s^{-1}$; T be the temperature (in K), R (in $JK^{-1} mol^{-1}$) be the gas constant, η (in cP) be the viscosity coefficient of methanol-water^[201], r_{GQD} (~2.55 nm) and r_{DNT} (~0.5 nm) be the radii of GQD and DNT.^[179]

Temperature	DNT (mM)	a ₁	a ₂	τ ₁ (ns)	τ ₂ (ns)
20 °C	0	0.35	0.65	4.05	6.85
	0.77	0.35	0.65	4.05	6.70
	1.53	0.35	0.65	4.00	6.50
	2.3	0.28	0.72	3.50	6.25
	3.05	0.29	0.71	3.30	6.13
	3.8	0.20	0.80	2.90	5.80
	4.55	0.25	0.75	3.00	5.80
	6.05	0.21	0.79	2.70	5.50
	7.53	0.22	0.78	2.60	5.20
	9	0.25	0.75	2.55	5.00
	10.46	0.20	0.80	2.00	4.75
40 °C	0	0.26	0.74	3.45	6.50
	0.77	0.23	0.77	3.00	6.00
	1.53	0.27	0.73	3.15	5.85
	2.3	0.26	0.74	3.00	5.50
	3.05	0.22	0.78	2.60	5.15
	3.8	0.23	0.77	2.30	4.80
	4.55	0.21	0.79	1.95	4.35
	6.05	0.20	0.80	1.80	4.00
	7.53	0.20	0.80	1.65	3.75
	9	0.20	0.80	1.20	3.45
	10.46	0.20	0.80	1.10	3.00
60 °C	0	0.26	0.74	3.20	6.35
	0.77	0.22	0.78	2.65	5.85
	1.53	0.27	0.73	2.90	5.55
	2.3	0.18	0.82	2.15	4.90
	3.05	0.27	0.73	2.60	4.80
	3.8	0.24	0.76	2.25	4.55
	4.55	0.19	0.81	1.65	3.90
	6.05	0.17	0.83	1.20	3.50
	7.53	0.18	0.82	1.10	3.20
	9	0.18	0.82	0.85	3.00
	10.46	0.17	0.83	0.75	2.75

Table 5.2. The fluorescence lifetime of GQDs at different DNT concentrations and temperatures (measured using TCSPC setup)

The fluorescence lifetime quenching of GQDs is recorded using a TCSPC setup (IRF ~ 80 ps) (Table 5.2). Lifetime SV fittings with Eq. 4.1 provided the values of $k_{\text{PET}} \sim 5.5 \times 10^9 \text{ M}^{-1} \text{ s}^{-1}$ (at 20°C), $\sim 15.5 \times 10^9 \text{ M}^{-1} \text{ s}^{-1}$ (at 40°C), and $\sim 19.5 \times 10^9 \text{ M}^{-1} \text{ s}^{-1}$ (at 60°C), respectively (Table 5.1), whereas the bimolecular diffusion-controlled rates in aqueous methanol are, $\sim 6.5 \times 10^9 \text{ M}^{-1} \text{ s}^{-1}$ (at 20°C), $\sim 12 \times 10^9 \text{ M}^{-1} \text{ s}^{-1}$ (at 40°C), and $\sim 19 \times 10^9 \text{ M}^{-1} \text{ s}^{-1}$ (at 60°C) respectively (Table 5.1). Irrespective of the temperature, the collisional PET rate appears close (or higher) to the upper limit of the diffusion-controlled rate of any bimolecular quenching process in aqueous methanol. This fact unambiguously confirms that the actual PET rate is much higher and escapes the detection by ~ 80 ps IRF of our TCSPC setup. When PET is at a diffusion-controlled limit, the PET timescale measured by TCSPC would be a mere reflection of the diffusion timescale of the GQD and quencher in the aqueous methanol rather than the intrinsic PET timescale. The diffusion-controlled PET reaction is a two-step process as discussed in previous chapter. In the first step, the GQD and DNT approach to a contact distance through a slow diffusion process, which is followed by an ultrafast (few ps) intrinsic PET reaction in the second step. The ultrafast intrinsic PET timescale of ~ 3 ps in our case is detected by the femtosecond upconversion study, to be discussed in the latter part of this chapter. The slow intrinsic PET timescale (slower than the IRF) is not the sole criterion for bimolecular liquid-phase PET kinetics to be detected by a time-resolved setup. There are two following scenarios; at least one of them should be satisfied for PET kinetics to be detected accurately by a time-resolved setup: (1) PET timescale would be much slower than the mass transportation timescale (few tens of ns or longer) of the medium. (2) Even if the intrinsic PET timescale is shorter than the mass transportation timescale of the medium, PET can still be detected provided there is a possibility of donor–acceptor complex formation. In the first scenario, the overall PET reaction is controlled by the slow timescale of PET rather than the fast diffusion,

but on a rare occasion, such an incident occurs. In scenario 2, since at the time of excitation the quencher is already attached to the fluorescent molecule, no diffusion is required for PET to occur. Thus, an intrinsic PET would be detected in both cases. However, our case is certainly not scenario 1, where PET is slower to the diffusion rate, rather the opposite. Since the diffusion rate increases with temperature, the apparent PET rate (k_{PET}) also increases in a similar manner (Table 5.1). DNT is a hydrophobic molecule, in aqueous methanol at moderate to high concentration, it would likely form a complex with GQDs through hydrophobic interactions, which is manifested by an upward curvature of the steady-state SV curve at a high DNT concentration (Figure 5.3A). Because of the propensity for dissociation of these complexes at high temperatures, the value of the binding constant (K , Table 5.1) decreases from $\sim 85 \text{ M}^{-1}$ to $\sim 22 \text{ M}^{-1}$ as the temperature is increased from $20 \text{ }^\circ\text{C}$ to $60 \text{ }^\circ\text{C}$. In the GQD– DNT complex, the ultrafast intrinsic PET timescale escapes the detection by $\sim 80 \text{ ps}$ IRF of our TCSPC setup, but the same is easily captured in the steady-state quenching study, as the complex formation would cause a decrease in GQD emission intensity. This is why the steady-state SV plot always exhibits a higher slope (or a higher quenching rate) compared to that of the lifetime SV plot. While the former accounts for both ultrafast static and slow diffusion-controlled collisional quenching, the latter accounts for only the slow collisional quenching. Low temperature ($20 \text{ }^\circ\text{C}$) favors the ultrafast static quenching through complex formation, causing a large difference in the rates derived from steady-state and lifetime SV fittings. However, at elevated temperature, the complex dissociates, leaving collisional quenching be the sole pathway of quenching that would result in a similar quenching to the steady-state and time-resolved plots as shown in Figure 5.3. At high temperature ($60 \text{ }^\circ\text{C}$), both steady-state and time-resolved SV plots report identical PET rates, which are very similar to the diffusion-controlled rate of the medium (Table 5.1).

5.2.3. Isothermal Titration Calorimetry Study of GQD–2,4-Dinitrotoluene (DNT) Complex Formation.

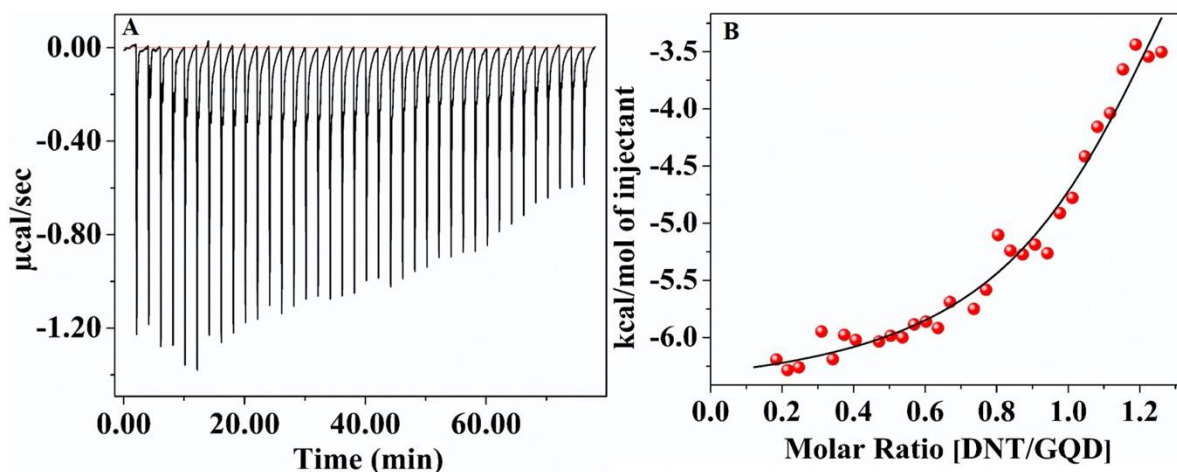


Figure 5.4. (A) Figure shows ITC raw data of exothermic binding of DNT with GQD in aqueous methanol. Each peak represents the heat release against each injection of high concentration DNT in aqueous methanol to the cell containing low concentration GQD in the same binary solvent. (B) The figure shows the binding isotherm obtained after processing the raw data and subtracting the heat of dilutions of only DNT and only GQD. The black line is the fitted curve assuming a single binding site. Binding stoichiometry is found to be ~ 1.2 , as shown by the mid-point of the fitted rise curve.

Complex formation is further substantiated by an ITC study of heat change (Figure 5.4). The ITC experiment reveals that the complexation reaction is exothermic in nature at room temperature. In the experiment, titrant DNT (~ 5 mM) in aqueous methanol is loaded in a syringe, and the titrand GQD (~ 0.5 mM) in the same solvent is placed in the sample cell. We used titrand concentration ~ 10 times lower than the titrant concentration, which is typical for ITC experiments.^[112,202] The weak solubility of DNT in the aqueous methanol restricted us from using a high DNT concentration (>5 mM) in the syringe that further limits the maximum GQD concentration to ~ 0.5

mM (i.e., ~10 times less) in the sample cell. Use of a high GQD concentration (>10 mM) would cause aggregation, which would cause not only an undesired heat change in the ITC experiment but also the spectral changes in the optical study. Therefore, low concentrations of GQD are maintained in ITC (~0.5 mM) and the optical studies (~2 μ M). However, at this low GQD concentration, the calculated C value ($C = K_a[\text{GQD}]$; assuming $K_a \sim 500 \text{ M}^{-1}$) is found to be ~2.5, which is the bare minimum value within the acceptable range of C -window (1–10,000) for the accurate determination of heat change (ΔH), association constant (K_a), and binding stoichiometry. Our assumption on the K_a value is drawn from the previous study (Chapter 4) of binding kinetics between the GQD and DMA using fluorescence correlation spectroscopy (FCS), where K_a was found to be 700 M^{-1} . Both DNT and DMA have similar sizes; both are almost insoluble in water and expected to have similar binding affinities with GQDs. Even though the quantitative estimations of the thermodynamic parameters (ΔH , K_a , etc.) through the ITC experiment may not be accurate because of the low C value, in a qualitative sense, ITC data can be used as a direct proof of GQD–DNT complex formation as manifested by the heat change when DNT and the GQD are mixed. Complex formation is indeed interesting in our case; it would provide us an opportunity to study intrinsic PET kinetics under no influence of solvent diffusion. The heat of dilution of DNT and the GQD is estimated in two control experiments, and the same is subtracted from the binding isotherm of the complexation reaction. After subtraction, a single binding site fitting model is employed, which enables a conclusive fitting to our experimental binding isotherm (Figure 5.4B). From the fitting, K is found to be $\sim 5000 \text{ M}^{-1}$ and a binding ratio (DNT to GQD) of ~ 1.2 is obtained from the mid-point of the fitted curve (Figure 5.4B). However, these values are only rough estimations. From SV analysis, we find that the static and dynamics quenching equally contribute to the overall quenching process. Through the ITC study, we find a direct proof of one-

to-one GQD–DNT complex formation. Therefore, we conclude that not all the GQDs form complexes with DNT. Free GQD population increases with increasing the temperature. Even though the quenching is ultrafast (~ 3 ps) for GQD–DNT complexes, it is slow ($>ns$) and diffusion controlled for free GQDs. TCSPC can measure only the slow timescale associated with the collisional quenching. In the next part of this chapter, I will discuss how complex formation helps one in accurate detection of diffusion-free PET kinetics using a femtosecond upconversion setup that remained undetected by a TCSPC setup.

5.2.4. Femtosecond Upconversion Studies of Intrinsic PET at Different Temperatures.

Using TCSPC with ~ 80 ps IRF, we missed the ultrafast PET kinetics. To make progress in this front, we used a femtosecond upconversion setup with a much better temporal resolution (~ 0.3 ps), which allowed us to detect the ultrafast PET component. A low association constant suggests that even at low temperature (20 °C), population of GQD–DNT complexes would remain moderate to low, while at high temperature (60 °C), almost all GQD–DNT complexes would dissociate. Nevertheless, the presence of an insignificant population of GQD–DNT complexes even at high temperature cannot be ruled out, as observed in the femtosecond upconversion study. In our previous work, using FCS, we obtained that the DMA molecule remains attached to a GQD for $4\text{--}6$ μs . DMA and DNT have similar sizes, and both are hydrophobic and almost insoluble in neat water. Therefore, a similar μs binding timescale of DNT with GQDs would be a good approximation here, which ensures the accurate detection of the ultrafast PET timescale (few ps) much before the complex dissociates (\sim few μs). We performed upconversion studies at three different temperatures at 5 °C, 25 °C, and 60 °C. The lifetime of GQDs does not change with temperature, in contrast to the “thermal quenching” phenomenon, frequently observed in perovskite and chalcogenide nanocrystals (Table 5.2).^[203] We monitored the lifetime at the

emission peak (~ 460 nm) of GQDs, while exciting the sample at ~ 405 nm (Figure 5.5). The three exponential reconvolution fit to the femtosecond transients of GQDs reveals three components with slight variations in their contributions with temperature (5 °C– 60 °C). (i) The first component is an IRF-like ultrafast decay (~ 0.3 ps), presumably be an artifact arising from the scattering of an excitation lamp. As the quencher reduces the emission intensity of GQDs, this scattering component (~ 0.3 ps) becomes more prominent within the quenched samples. Scattering could have been avoided using a higher concentration of GQDs, but that might have caused an unwanted aggregate formation. (ii) The second component is ~ 12 ps; mid-bandgap trap sites (deep traps) and/or trap sites near the exciton state (shallow traps), and/or solvation dynamics, etc. are the possible sources for this component.^[160,204,205] (iii) The slowest component (~ 5000 ps), which is fixed from TCSPC average lifetime, arises from the band-edge radiative recombination (Tables 5.1 and 5.3).^[204,205] In the presence of ~ 9 mM DNT, interfacial PET of the GQD–DNT complex shortens the ~ 12 ps component to ~ 6 ps, contribution of which reduces from $\sim 53\%$ to $\sim 34\%$ with an increase in temperature from 5 °C to 60 °C (Table 5.3). This is in the line with our intuitive expectation; at high temperature, majority of the GQD–DNT complexes dissociate, leaving PET mostly collisional (diffusion controlled). This is in contrast to the slow component, which experiences more quenching (~ 5000 ps to 2600 ps) at elevated temperature (~ 60 °C) compared to that (~ 5000 ps to 4000 ps) at reduced temperature (5 °C) (Table 5.3). This is again well under our intuitive expectation; with an increase in temperature, the mass transportation rate of the medium increases, leading to a greater amount of collisional quenching. Since the diffusion timescale is much slower ($>ns$) than the actual ultrafast PET timescale (\sim few ps), collisional quenching would result in suppression of the slow nanosecond component only. It is worth noting here that our femtosecond upconversion study reveals the actual PET timescale of the GQD–DNT

redox pair (\sim few ps), which cannot be detected using a TCSPC setup. SV analyses using the data from TCSPC report the solvent diffusion kinetics rather than PET. In order to precisely detect the PET timescale along with the contribution from a mixed process, we evaluate the femtosecond transient of GQDs in the presence of Q mM DNT [$I(t,[Q])$] after normalizing with transient of only GQDs [i.e., $I(t,[Q])/I(t)$].^[206] The decay of transients (without normalizing) in the presence of a quencher is ruled by not only the PET but also other deactivation processes (trap sites, radiative recombination, etc.) that are intrinsic to GQDs, which makes PET analysis complicated using an un-normalized transient. This is in contrast to the normalized transient, where only PET causes the decay and thereby enables the precise detection of the PET timescale (Figure 5.5C).

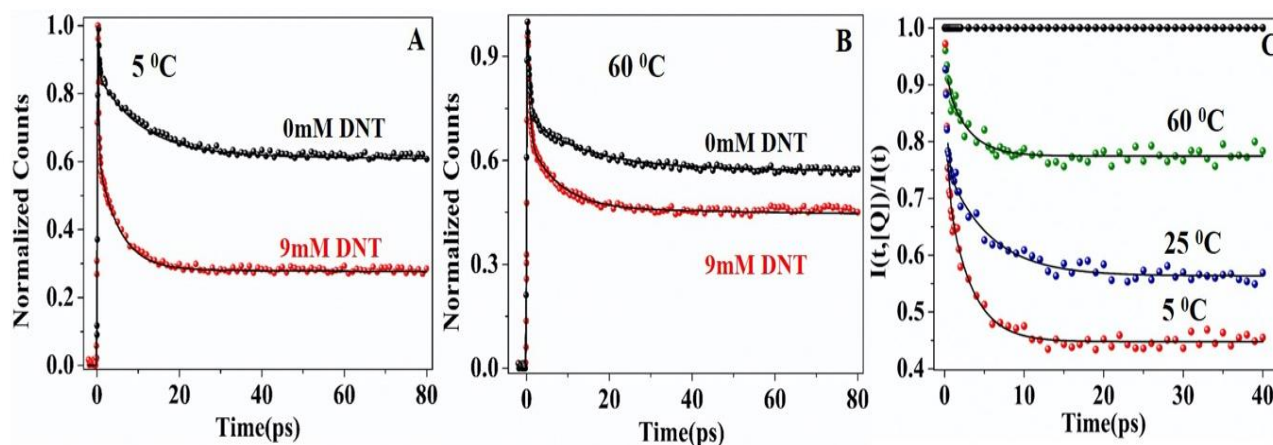


Figure 5.5 (A-B) Femtosecond transients of GQDs in aqueous methanol in the absence and presence of \sim 9 mM DNT ($\lambda_{\text{ex}} \sim 405$ nm) at 5 °C (A) and 60 °C (B), respectively. Emission was collected at the emission peak position. (C) femtosecond transients of GQDs in the absence (black balls) and presence (green, blue and red balls) of \sim 9 mM DNT after normalizing with transient of only GQDs [i.e., $I(t,[Q])/I(t)$; $Q=0$ for black balls and \sim 9 mM for others] at different temperatures. Solid lines are the exponential fitting curves. We avoided fitting to the very initial portion (< 0.6 ps) where mostly the lamp scattering contributes.

Normalized femtosecond transients $[I(t,[Q])/I(t)]$, as shown in Figure 5.5C, are fitted with a three exponential decay function. Like in femtosecond transients (without normalizing), one IRF-like ~ 0.25 ps component is observed in all the cases, which we evade by truncating the fitting window at ~ 0.6 ps to the faster end. The ultrafast component (~ 3 ps) other than IRF, whose contribution decreases from ~ 0.36 to ~ 0.16 as temperature is increased (from 5 °C to 60 °C), is assigned to be the actual PET timescale of the GQD–DNT complex (Figure 5.5C). Low contribution of the ~ 3 ps component at elevated temperature justifies well our assignment to this component; at elevated temperature, the GQD–DNT complex dissociates causing reduction in contribution of the intrinsic PET component. Here, we will not focus on the post-ns third decay component, whose precise detection is not possible from a 40 ps fitting window (Figure 5.5C). Nevertheless, the presence of the post-ns PET component is already detected in the TCSPC study, and discussed in the preceding section. This post-ns PET component is a result of collisional quenching. Because of the faster diffusion rate at elevated temperature, collisional PET becomes more efficient; thus, a greater quenching to the ns component is observed at elevated temperature (Table 5.3). The timescale of collisional quenching can be predicted from the diffusion-controlled bimolecular rate constant ($k_d \sim 6.5 \times 10^9 \text{ M}^{-1} \text{ s}^{-1}$; Table 5.1) of aqueous methanol. The typical timescale of quenching for a diffusion-controlled PET would be $(1/k_d) \sim 0.15$ ns at unit quencher concentration. Our slow PET component is also in the ns time regime, and being diffusion controlled, the timescale of this component shortens with temperature (Table 5.3).

Temperature	DNT (mM)	a ₁	a ₂	τ ₁ (ps)	τ ₂ (ps)
5 ⁰ C	0	0.27	0.73	12	5000
	9	0.53	0.47	6	4000
25 ⁰ C	0	0.23	0.77	12	5000
	9	0.48	0.52	6	4000
60 ⁰ C	0	0.22	0.78	12	5000
	9	0.34	0.66	6	2600

Table 5.3. Fitting parameters of femtosecond transients of GQDs in the absence and presence of DNT at various temperatures (Figure 5.5 A, B). A lamp-like decay component (~ 0.25 ps) is not included in the table, since it is not a real decay component. The long component (τ_2) was fixed as the average TCSPC lifetime (Table 5.2).

5.3 Conclusion

In this study, we observed the ~ 3 ps intrinsic PET timescale of the GQD–DNT complex. While at low temperature, a major portion of the PET kinetics proceeds through static quenching at elevated temperature, collisional quenching presides over the static quenching. Because of the slower timescale of collisional quenching, the TCSPC setup is ideal for accurate detection of the collisional quenching rate. We found that the collisional quenching rates appear at the upper limit of bimolecular diffusion-controlled rates irrespective of temperature; this indicates that the observed collisional PET rate is apparent, a mere reflection of the mass transportation rate of the medium. We are fortunate to have some population of GQD–DNT complexes in the reaction medium at the time of excitation, for which diffusion is not required for the PET reaction to occur. Our expectation is substantiated by the appearance of the ~ 3 ps component in the normalized GQD transients in the presence of DNT, the contribution of which decreases with an increase in temperature due to the dissociation of the complex at high temperature. It may be worth mentioning

here that while the ~ 3 ps component is derived in the presence of collisional quenching, the contribution of collisional quenching in the ~ 3 ps component is negligible. This is because the translational diffusion coefficients (D_t) of typical dye molecules (Coumarin 480, R6G, DCM, etc.) are $300\text{--}600\ \mu\text{m}^2/\text{s}$ in water, and in ~ 3 ps, molecules can travel as low as $\sim 0.06\text{--}0.08\ \text{nm}$ [$\sqrt{(4D_t\tau)}$], which is negligible compared to the sizes ($1.4\ \text{nm}\text{--}0.8\ \text{nm}$) of the dye molecules.^[190] Here, the size of GQDs is much bigger ($\sim 5.1\ \text{nm}$), and the distance traveled in ~ 3 ps would be even lesser. Therefore, during the ~ 3 ps PET reaction, diffusion cannot change the position of GQDs and DNT, and hence, the ultrafast intrinsic PET component bears a high degree of integrity by making it free from solvent diffusion. Ultrafast interfacial PET at the GQD surface is indeed interesting, endowing GQDs with an excellent material property for MEG-based photovoltaic applications where ultrafast charge separation is a prerequisite. Apart from the photovoltaic applications, an unprecedented quenching of GQD emission by DNT suggests that GQDs can be used in sensing applications for the detection of explosive nitroaromatic compounds.

6.1. Introduction

In graphite, strong “phonon-charge carrier” coupling results in a subpicosecond (subps) cooling of the hot carriers to the band edge state much before their extraction, wasting excess energy in the form of heat.^[207–212] Phonons can efficiently promote the relaxation of hot carriers in graphene since the phonon energy is quite similar to the spacings within the continuum electronic states. Similar phonon-assisted ultrafast relaxations are also observed in other bulk semiconductors (and quantum dots) of PbSe, CdSe, and perovskites.^[213–215] Exceptionally fast carrier relaxation (<1 ps) of bulk semiconductor materials makes the extraction of hot carriers challenging and fundamentally limits the efficiency of a device. This is in contrast to the semiconductor nanocrystals (NCs), where strong quantum confinement transforms the closely spaced continuum states of bulk materials into discrete energy levels in small NCs, characterized by much larger separations compared to the phonon energy. Therefore, interaction with multiple phonons would be essential for the relaxation of the above band edge states. This is a rare phenomenon due to the low probability of multiple phonon emission (i.e., phonon bottleneck).^[216–218] However, such a disparity alone in NCs cannot lead to a slower cooling than in their bulk forms because of the other competing and efficient relaxation channels in the NCs. In particular, Auger-like processes, interaction with mid bandgap surface trap states, transferring the energy of a hot electron to the hole state with larger effective mass, coupling with high-frequency vibration modes of capping

ligands, etc., are considered to be the prime relaxation channels in NCs, making cooling as fast as in their bulk forms.^[219–221] Several strategies have been considered including the synthesis of defect tolerant NCs by adding dopants, post-synthesis treatments, using higher bandgap passivating layers epitaxially grown around the NCs (i.e., heterostructures), and selecting weakly IR-active capping agents to suppress the deactivation channels that resulted in a much slower relaxation time of hot carriers in NCs.^[222–227] One of the key factors causing the low energy conversion yield of single-junction solar cells is the fast thermalization of hot carriers produced through above band edge excitation by the solar photons. In a seminal work, Guyot-Sionnest and co-workers demonstrated that the epitaxially grown heterostructure around the CdSe quantum dot (QD) suppresses the alternative relaxation channels by separating the electron spatially from the hole that significantly defers the energy transfer process, and thus, much slower cooling time (~ 1 ns) can be observed.^[227] In addition to the epitaxially grown heterostructures, eliminating trap states through surface passivation employing weakly IR absorbing capping ligands can further reduce the cooling rate. Achieving slower relaxation and subsequent extraction of these high-energy species by carefully choosing the molecular system is one of the key strategies that can significantly enhance the efficiency of a light-harvesting device. Successful extraction of hot carriers can push the efficiency of solar cell devices to $\sim 66\%$, much above the Shockley–Queisser (SQ) limiting value ($\sim 33\%$).^[228,229]

In the present work, we have reported a few ps carrier cooling time of GQDs, much slower than the subps cooling time of bulk graphene.^[207–211] Extraction of hot carriers from graphene continues to remain a challenging task for their ultrafast cooling time scale. In addition to the quantum confinement effect, many other desired material properties of GQDs, like perfectly passivated edges with hydrogen atoms, equal effective masses of electrons and holes reducing Auger-like

recombination, lower abundance of trap states as a result of well-controlled carbon chemistry, have made the cooling time of hot carriers in GQDs remarkably slow.^[207,230,231] In this work, we have also shown ultrafast hot hole extraction in a GQD composite with high efficiency by employing the femtosecond upconversion spectrometer.

6.2. Results and Discussion

6.2.1. Sample Preparation and Characterization

Graphene quantum dots dispersed in water (~1 mg/mL), N-methylaniline (NMA, purity ~99.5%), and toluene were purchased from Sigma-Aldrich. GQDs were transferred from water to toluene using the partitioning method. In brief, the aqueous solution of GQDs was mixed with the desired volume of toluene, and the solvent mixture was vortexed before settling down overnight under a nitrogen environment. The Toluene portion, clearly separated from water, was slowly taken out using a pipette. The integrity of the GQDs in toluene solution was checked by using a purification procedure, i.e., prolonged sonication followed by membrane dialysis to separate the molecular fluorophores/fluorescent oligomers, etc. (if at all present). Unlike carbon dot samples the post-dialysis retentate of our GQD sample exhibited identical absorption and emission profiles when compared to that of the crude GQD sample. Purified GQD sample with <0.3 optical density was used for further optical studies.

GQD has an average size of ~5.1 nm, a topological height of ~1.8 nm (implying ~4-5 graphene layers), mostly monodispersed, crystalline with a characteristic lattice spacing of about 0.21 nm. The presence of a large number of functional groups like O–C=O, C–O, C–N, CONH₂, etc., as detected by the FTIR study prevents GQDs from aggregating.^[232] A detailed characterization of GQD sample through HRTEM, AFM, powder XRD, and FTIR is provided in Figure 6.1. The absorption spectrum of GQDs is characterized by sharp peaks in the <365 nm region due to the

π - π^* and n - π^* transitions in organic functional groups at the GQD surface along with π - π^* transition of toluene, and broad peak at ~ 450 nm originating from bandgap transitions of GQDs involving π electrons of the conjugated states. Strong mixing of closely spaced electronic transitions, along with the vibronic coupling, has resulted in the broadening of the primary absorption peak.^[128,233] The emission peak of our GQD sample is independent of the excitation position (Figure 6.2), contrary to what is generally observed for all carbon dot samples irrespective of their synthesis procedure.

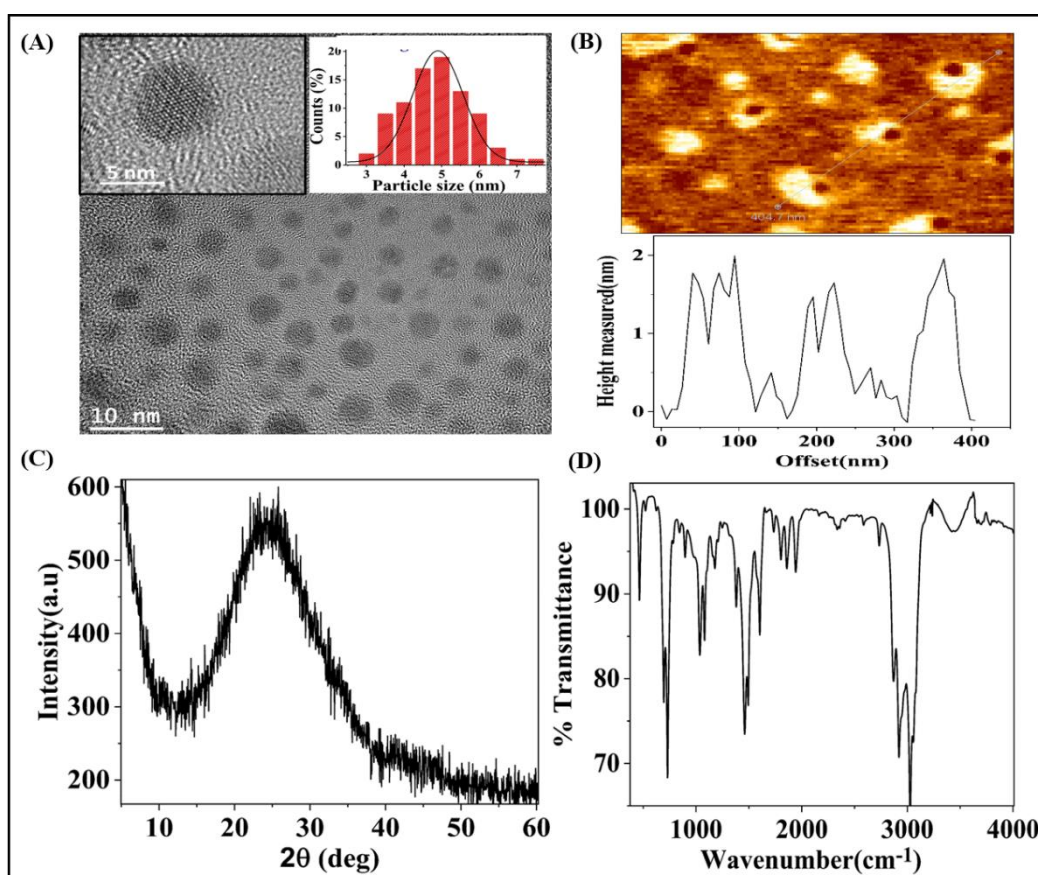


Figure 6.1. (A) Particle size distribution of GQDs obtained from the HRTEM study. (B) Topological height of the GQDs is measured to be ~ 1.8 nm from the AFM study, indicating the presence of ~ 4 -5 graphene layers. (C) Powder XRD spectrum of GQDs. (D) FTIR spectrum of GQDs shows the presence of different organic functional groups on the surface.

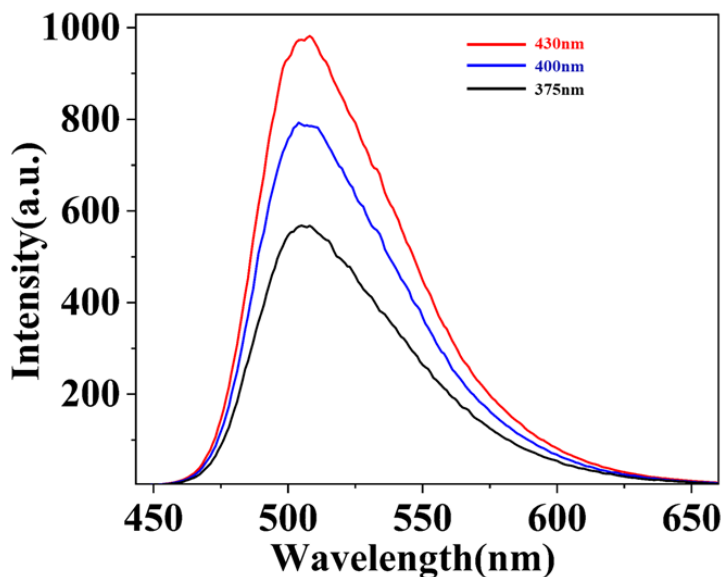


Figure 6.2. Emission spectra of GQDs in toluene at different excitation wavelengths. The excitation wavelengths are mentioned in the figure.

6.2.2. Femtosecond Upconversion Study of Hot Carrier Cooling and Extraction

To measure the cooling timescale, the colloidal GQD sample is photoexcited at two different positions: (i) much above the band edge ($\sim 1.3E_g$, $\lambda_{ex} \sim 375$ nm) and (ii) slightly above or near the band edge ($\sim 1.1E_g$, $\lambda_{ex} \sim 430$ nm), where E_g (~ 2.55 eV) is the bandgap energy of GQDs, calculated from the crossing point of the absorption and emission spectra (Figure 6.3). We used extremely low excitation power to avoid bi/ multiexciton formation. The average number of exciton per GQD per pulse ($\langle N \rangle$) was kept as low as < 0.15 , ensuring complete removal of higher-order nonlinear recombination processes including Auger and trion.^[234–238] The biexciton Auger recombination time in GQDs is just ~ 0.3 ps, this would indeed set a hurdle toward the detection of a much slower cooling time if the excitation power is high.^[234]

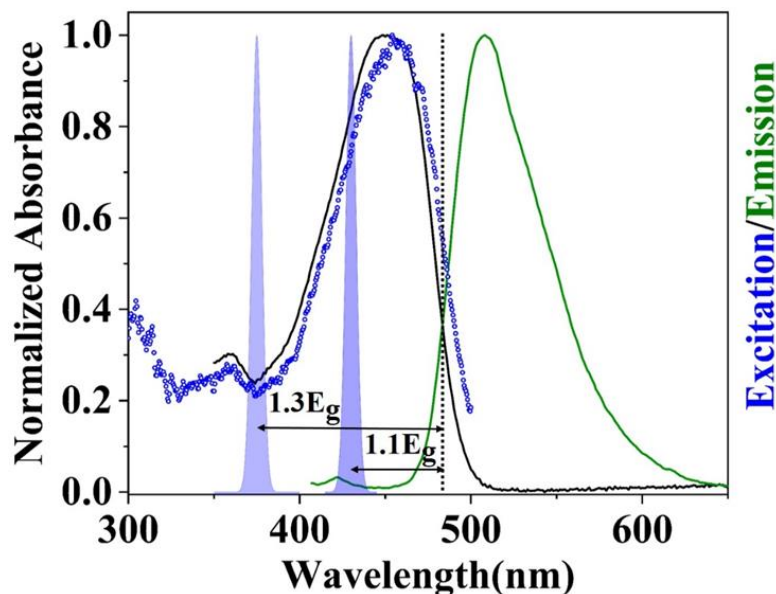


Figure 6.3. Absorption (black solid line), emission (green solid line, $\lambda_{\text{ex}} \sim 400$ nm) and excitation (blue dotted $\lambda_{\text{em}} \sim 510$ nm) spectra of colloidal GQDs dispersed in toluene. Identical absorption and excitation spectra imply the high integrity of the emission state. Above band edge (~ 375 nm) and near band edge (~ 430 nm) excitations are shown by the solid Gaussian pulses and the band edge energy is indicated by the dotted vertical black line (0-0 transition).

Figure 6.4 shows femtosecond transients of colloidal GQDs at different excitation powers. While the short-time amplitude of the transient has contributions of both single and multiple excitons (if present), the long-time amplitude (>1 ns) is solely determined by the GQDs with a single exciton. This is because a subps Auger recombination time of GQDs cannot affect the amplitude at the long delay time (i.e., ~ 2 ns).^[234] In our case, within the low fluence range (0.2×10^{15} to 1×10^{15}), the population of single exciton GQD increases gradually with a gradual increase in the fluence rate, as shown in the inset A of Figure 6.4. Interestingly, at the initial time (<1 ps) of the transient, neither an ultrafast decay at high fluence representing Auger recombination nor a superlinear dependency of amplitude on fluence can be observed. Both observations unambiguously confirm

the absence of any nonlinear recombination at our excitation power.^[237,238] In a seminal work, Sun et al. have shown that the saturation of the long-time amplitude of GQD transient can occur only at a much higher photon flux ($>3 \times 10^{15}$ photons cm^{-2} per pulse).^[234] Below this threshold, GQDs are mostly excited with a single exciton. Throughout our experiment we maintained a photon fluence rate as low as $\sim 0.2 \times 10^{15}$ photons cm^{-2} per pulse, an order of magnitude lower than the saturation fluence ($\sim 3 \times 10^{15}$), keeping in mind the onset of nonlinear processes at high fluence. At the low fluence regime ($\sim 0.2 \times 10^{15}$ to 1×10^{15}) excited state kinetics continues to remain independent of photon fluence, as substantiated by the identical natures of the normalized transients recorded at various fluence rates (inset B of Figure 6.4).

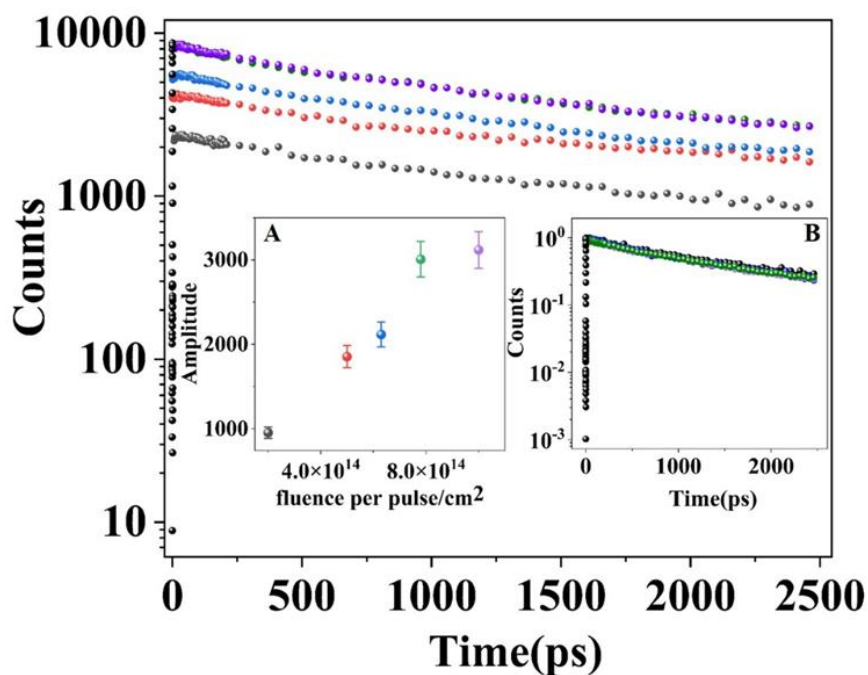


Figure 6.4. Femtosecond transients of colloidal GQDs ($\lambda_{\text{ex}} \sim 430$ nm, $\lambda_{\text{em}} \sim 505$ nm) dispersed in toluene as a function of photon fluence. We varied the fluence from 0.2×10^{15} (black curve) to $\sim 1 \times 10^{15}$ (purple curve) photons cm^{-2} per pulse. The concentration of GQDs was same for all the excitations. Inset A shows the long-time amplitude (at ~ 2 ns) of the transient as a function of photon fluence. Inset B shows the same transients as in the main figure but intensity normalized.

As discussed in chapter 1, the hot carriers are generated by exciting the sample (GQD here) with photons having energies higher than the bandgap ($h\nu > E_g$). The cooling time of hot carriers from above the band edge state to the band edge state was determined by examining the dynamic Stokes shift of time-resolved emission spectra (TRES). TRES is constructed using the spectral-reconstruction method, details of which can be found in chapter 2. For the construction of TRES, lifetime profiles were recorded at emission wavelengths separated by a regular interval of 5–10 nm, covering the entire emission spectrum, and steady state intensities of all recorded wavelengths. Figure 6.5 shows, respectively, the femtosecond transients at extreme blue, near peak, and extreme red wavelengths of the steady state emission spectrum of colloidal GQDs for both excitations, i.e., much above $\sim 1.3E_g$ ($\lambda_{ex} \sim 375$ nm) and near $\sim 1.1E_g$ ($\lambda_{ex} \sim 430$ nm) band edge states. Since the red emission ($\lambda_{em} \sim 570$ nm) mostly originates from the band edge state (“cold state”), and that evolves with time through the relaxation of the above band edge states (“hot states”), the initial time regime of the red emission transient is characterized by a few ps growth component (~ 4 – 20 ps) representing the cooling phenomenon (Figure 6.5). This is in contrast to the ultrafast initial decay components (~ 1 – 10 ps) of the transient of the blue emission (~ 465 nm) whose origin lies in the cooling of the above band edge Franck–Condon state (“hot state”) (Table 6.1, Figure 6.5). Initial ultrafast rise and decay components representing the cooling in both cases (red and blue emissions) precede the slow decay component ($>ns$) as a result of band edge recombination of cold carriers at the longer delay time of the transients (Tables 6.1 and 6.2). The similar ultrafast time scale of the decay component (at the blue emission wavelength) with that of the growth component (at the red emission wavelength) is a clear signature of relaxation of the hot carrier to the band edge state, and the characteristic relaxation time scale is indicated by the ultrafast growth or decay time (Table 6.1). This argument is further substantiated by observing a relatively slower growth

time (~ 20 ps) at the red emission with excitation above the band edge ($\lambda_{\text{ex}} \sim 375$ nm) compared to that (~ 4 ps) of the near band edge excitation ($\lambda_{\text{ex}} \sim 430$ nm) (Figure 6.5, Table 6.1). In the former case, the long trajectory of the relaxation pathway, i.e., much above the band edge to the band edge, leads to a slower time scale (Scheme 6.1). A similar observation of the excitation energy dependent cooling time in CsPbBr₃ perovskite nanocrystal (NC) has been recently reported by Samanta and co-workers.^[106] Through their pump-probe experiment, they observed carrier cooling induced bleach formation time in the perovskite NC is accelerated from ~ 800 to ~ 149 fs as the excitation is shifted from much above (~ 350 nm) to near the band edge (~ 450 nm).^[106]

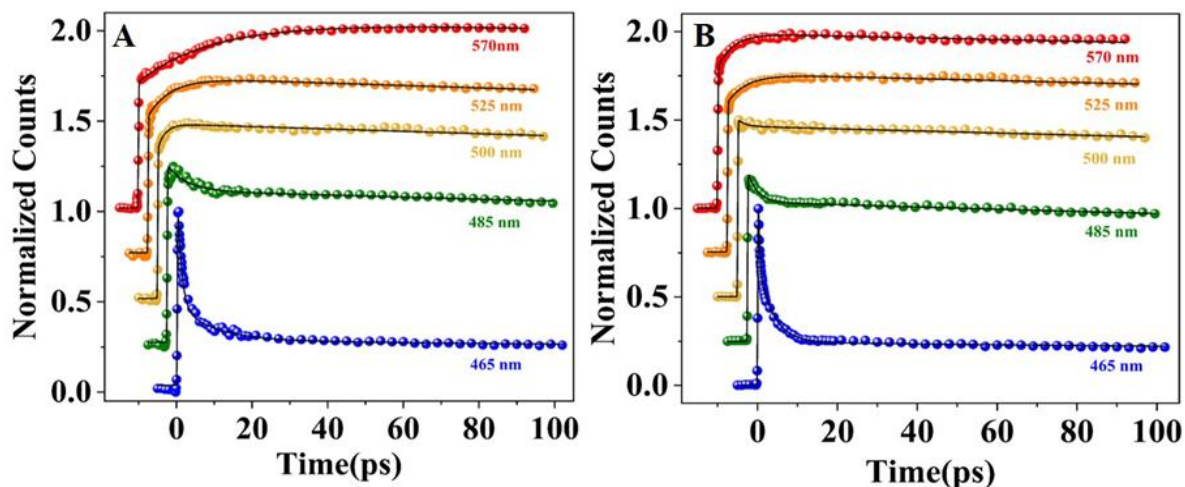


Figure 6.5. Femtosecond transients of colloidal QDs in toluene at various emission wavelengths (465 nm-570 nm) across the steady state emission spectrum at $\lambda_{\text{ex}} \sim 375$ nm (A), and 430 nm (B), respectively. We have recorded lifetimes at 12 different positions across the entire emission spectrum.

A similar kind of excited state stabilization by dipole–dipole interactions between the excited probe molecule and surrounding solvent molecules (solvation dynamics) leading to the solvated state on a picosecond time scale has been discussed in previous chapters. Putting ultrafast solvation (~ 1 ps) of a dye in the bulk solvent into perspective, a much slower (~ 650 ps) solvation time has

been reported for colloidal graphene oxide (GO) in an aqueous solution; this is indeed due to the large surface area of GO that hindered the relaxation of the solvent molecules around; as a result, a giant red edge effect or excitation dependent emission was observed for GO in aqueous solution.^[153] However, toluene being a nonpolar solvent, solvent-induced stabilization of the excited state GQD is not possible in our case, and therefore, the cooling of the hot carrier state to a thermally equilibrated band edge stage would be the sole mechanism of relaxation of the above band edge states. Several reports on the cooling of NCs (and in their bulk materials) including metal chalcogenides, perovskites, etc. showed that the trajectory of relaxation of hot carriers is initially thermalized to a quasi-equilibrium state assisted by carrier–carrier scattering and finally to a thermally equilibrated band edge state in ultrafast time scale, wherein the phonon-assisted relaxation process (i.e., carrier–phonon scattering) remains the main driving force.^[239,240]

$\lambda_{\text{ex}}(\text{nm})$	$\lambda_{\text{em}}(\text{nm})$	$\tau_1 (\mathbf{a}_1)$	$\tau_2 (\mathbf{a}_2)$	$\tau_3 (\mathbf{a}_3)$
375	465	1.1 (0.6)	9.8 (0.17)	1170 (0.23)
	505	6 (-0.17)	1356 (0.46)	2030 (0.71)
	570	20 (-0.46)	2400 (1.46)	-
430	465	3.8 (0.65)	1100 (0.35)	-
	505	2 (0.05)	1650 (0.95)	-
	570	4 (-0.39)	1900 (1.39)	-

Table 6.1. Best fitted parameters of femtosecond transients at different emission wavelengths. The longest component was fixed from its average lifetime measured at the same wavelength using TCSPC (Table 6.2.)

λ_{ex} (nm)	λ_{em} (nm)	a_1	a_2	τ_1 (ns)	τ_2 (ns)
	465	0.85	0.15	0.86	2.9
	475	0.82	0.18	0.87	2.87
	485	0.75	0.25	0.91	2.96
	495	0.63	0.37	0.92	2.99
	505	0.5	0.5	1.025	3.05
	515	0.43	0.57	0.97	3.03
	525	0.43	0.57	0.93	3.02
	535	0.4	0.6	0.98	3.04
	545	0.38	0.62	1.08	3.10
	555	0.32	0.68	1.03	3.07
	570	0.36	0.64	1.04	3.13
445	465	0.84	0.16	0.78	2.75
	475	0.84	0.16	0.79	2.77
	485	0.74	0.26	0.72	2.53
	495	0.61	0.39	0.73	2.57
	505	0.5	0.5	0.73	2.58
	515	0.44	0.56	0.72	2.56
	525	0.44	0.56	0.72	2.56
	535	0.44	0.56	0.74	2.59
	545	0.38	0.62	0.7	2.56
	555	0.38	0.62	0.73	2.59
	570	0.4	0.6	0.74	2.63

Table 6.2. Fluorescence lifetime components of GQDs in toluene at different excitation and emission wavelengths.

TRES at both excitations show a gradual shifting of the emission peak toward the low energy side with time as a result of cooling (Figure 6.6).^[241] The emission energy continues to shift until ~ 25 ps when the excitation is much above the band edge (i.e., $\lambda_{\text{ex}} \sim 375$ nm) and the same is reduced to ~ 15 ps when the excitation is near the band edge (i.e., $\lambda_{\text{ex}} \sim 430$ nm). Beyond this, no further shift in TRES can be observed. Figure 6.7 depicts the emission peak of TRES as a function of time at both excitations. The final peak position of TRES after relaxation appears at ~ 19872 cm^{-1} (ν_{∞}) at both excitations (375 and 430 nm), very close to the steady state emission peak (~ 19841 cm^{-1}) (Table 6.3). Since the few ps excited state relaxation time of our GQDs is orders of magnitude faster compared to its excited state lifetime ($> \text{ns}$), irrespective of the excitation position, the exciton is relaxed to the band edge state much before the emission starts, causing excitation independent emission popularly known as Kasha's rule. (Chapter 1)

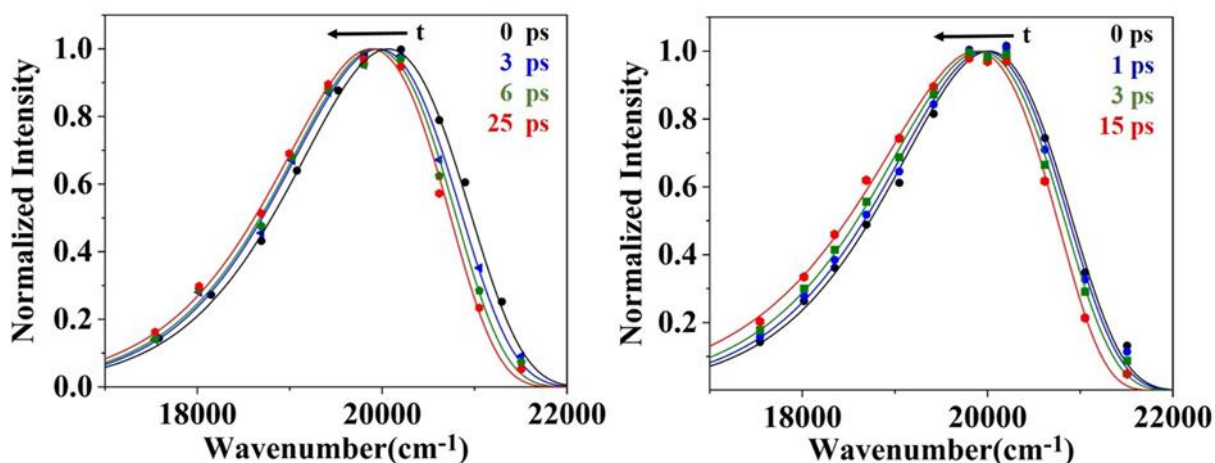


Figure 6.6. Intensity normalized time-resolved emission spectra (TRES) of colloidal GQDs in toluene at different times following the excitation at 375 nm (left figure) and 430 nm (right figure), respectively. Emission energy decreases with time as a result of the cooling of hot carriers

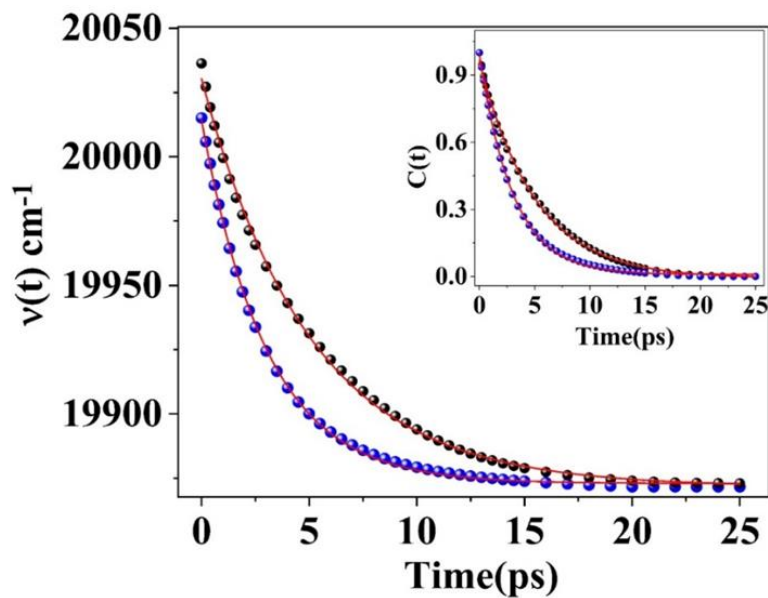


Figure 6.7. Peak position of time-resolved emission spectra (TRES) of GQDs dispersed in toluene as a function of time at $\lambda_{\text{ex}} \sim 375$ nm (black balls) and 430 nm (blue balls), respectively. Higher zero time amplitude of ~ 375 nm excitation curve compared to that of ~ 430 nm excitation curve indicating that the former excitation leading exciton to an energetically much higher state compared to the latter. Solid lines show the fittings with a single exponential decay function. Inset shows the same curves as in the main figure but normalized for comparison between their decay timescales.

λ_{ex}	ν_0 (cm^{-1})	ν_{∞} (cm^{-1})	$\Delta\nu$ (cm^{-1})	τ_{cooling} (ps)
375	20,036	19,872	164	6
430	20,015	19,872	143	3

Table 6.3. The lifetime of hot Carrier (τ_{cooling}), dynamic Stokes shift ($\Delta\nu = \nu_0 - \nu_{\infty}$) of TRES due to cooling, and peak positions of hot (ν_0) and cold (ν_{∞}) emissions of colloidal GQDs for both excitations.

Figure 6.7 shows the peak positions of TRES as a function of time $[v(t)]$ fit nicely to a single exponential decay function and the characteristic time constants representing the cooling times are collected in Table 6.3. Cooling times were found to be ~ 3 ps near the band edge excitation ($\lambda_{\text{ex}} \sim 430$ nm) and ~ 6 ps above the band edge excitation ($\lambda_{\text{ex}} \sim 375$ nm) (Figure 6.7). A slower carrier cooling time (~ 6 ps) of above band edge excitation compared to that (~ 3 ps) of the near band edge excitation is well under our intuitive expectation. The longer cooling path of the former makes the relaxation time slower. Since the ~ 375 nm excitation generates the exciton much above the band edge compared to that of ~ 430 nm excitation, zero-time TRES of the ~ 375 nm excitation are blue-shifted ($\nu_0 \sim 20036 \text{ cm}^{-1}$) compared to spectra ($\nu_0 \sim 20015 \text{ cm}^{-1}$) of ~ 430 nm excitation (Figure 6.7). Although their initial peak position defers, after relaxation, both states reach the same thermally equilibrated band edge state ($\nu_\infty \sim 19872 \text{ cm}^{-1}$).

Extraction of hot carriers much before their cooling is of prime interest among the researchers, as it enables higher efficiency of solar cell devices beyond the Shockley– Queisser (SQ) limit ($\sim 33\%$).^[228,229] Herein we studied hot carrier extraction (hole in the present case) from photoexcited GQDs by utilizing a hole scavenging molecule, N-methylaniline (NMA). Quenching of the femtosecond transient of GQDs in the presence of NMA as shown in Figure 6.8 can be a result of either hole or electron transfer or both processes. However, in our case, thermodynamic consideration of the energy states of the interacting components suggests the transfer of a hole to the NMA is the only feasible mechanism for the quenching. The initial few ps ultrafast growth components (~ 5 ps) of the femtosecond transient of GQDs at the red emission wavelength (~ 525 nm) disappear in the presence of NMA (~ 90 mM). The growth component in the absence of NMA, representing the state filling of the band edge state by hot carriers, converted to a subps decay (~ 0.8 ps) component in the presence of NMA. This is indeed due to the extraction of hot carriers

by NMA before their cooling to the band edge state. The oxidation potential of NMA (~ 5.49 eV v/s vacuum), the reduction potential of GQD (3.7 eV v/s vacuum) are obtained from literature^[110,115] and the band gap energy of GQD (~ 2.55 eV) is estimated from the cross-section of absorption and emission spectra of GQD. The value of ΔG is found to be -0.76 eV; a negative value indicating the exergonic nature of charge transfer.

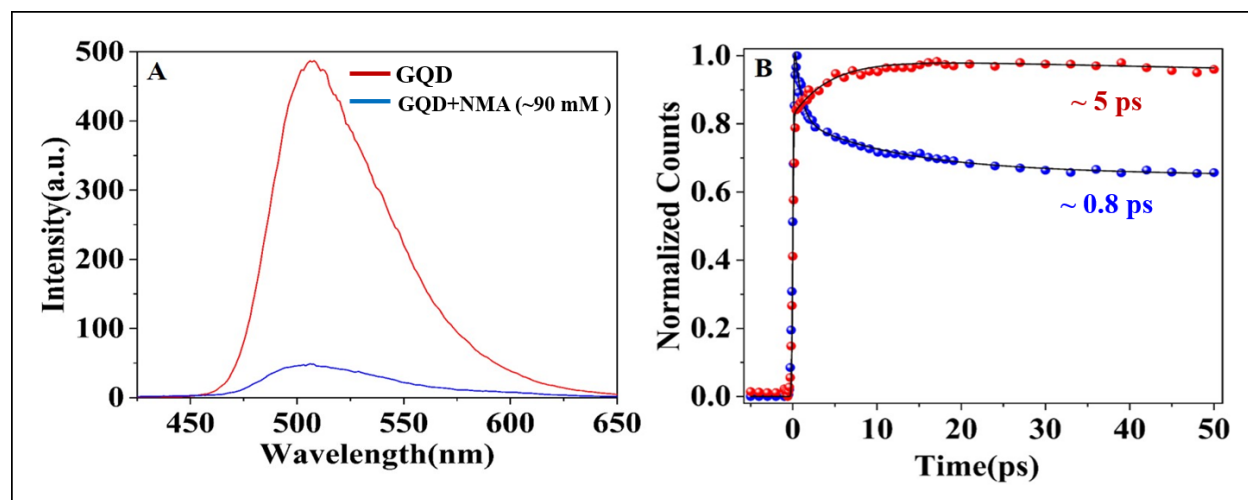
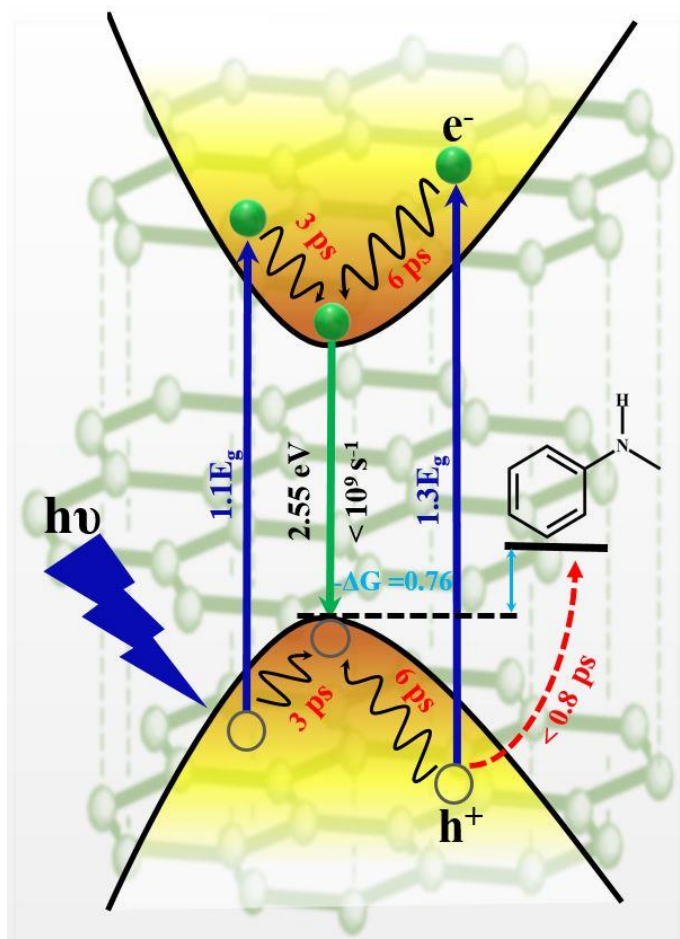


Figure 6.8. (A) steady state emission of GQD in the absence (red curve) and presence (blue curve) of ~ 90 mM NMA (B) Femtosecond transients of GQDs dispersed in toluene, in the absence (red curve) and presence (blue curve) of ~ 90 mM NMA. GQDs were excited much above the band-edge states ($\sim 1.3E_g$) and emission was collected at ~ 20 nm red from the emission peak position.

The subsps decay component (~ 0.8 ps) appears in the presence of NMA, indicating that the actual hot carrier extraction time scale is even faster than ~ 0.8 ps, and this is indeed an order of magnitude slower compared to the ~ 3 – 6 ps state-filling time by a hot carrier. The molecular system NMA was chosen for the energetic considerations of conductance and valence bands of GQDs vis a vis the LUMO and HOMO of NMA, allowing only hole transfer from photoexcited GQD to NMA (Scheme 6.1). Due to the reduced dimensionality and small size of the GQDs, a strong coupling

between electron states and hole states is obvious in electronically excited GQDs.^[207] This can be realized from the larger values of quantum size energy ($v_{Fh}/2r \approx 0.8$ eV) and electron–hole Columbic interaction energy ($-e^2/4\pi\epsilon_0 r \approx -0.4$ eV) of GQDs (compared to graphene), where r is the radius of GQD, ϵ_0 is the dielectric constant (unity for graphene), and v_F is the Fermi velocity ($\approx 10^6$ m/s in graphene), respectively.^[45,242,243] In addition, similar effective masses of the electron and hole of GQD would cause the generation of both carriers with similar energies on photoexcitation, and the relaxation kinetics cannot be observed separately for the electron and hole; rather, their evolution is correlated. In our case, thermodynamic consideration of the energy states of the interacting species suggests that only hole transfer from photoexcited GQD to NMA is possible. Growth in amplitude of only GQDs (red curve in Figure 6.8B) is proportionate to the number of carriers participating in the cooling process. By measuring the growth amplitude, one can realize the extent of carrier extraction prior to their cooling. In the presence of NMA, the growth amplitude completely disappeared, which indicates that the hot carriers' transfer efficiency is very high and completed much before their cooling. Such a high efficiency of carrier transfer is attributed to an excellent coupling of donor–acceptor electronic wave functions, rendering the faster carrier transfer time (<0.8 ps) compared to the cooling time (3–6 ps). We preferred high excitation energy ($\sim 1.3E_g$) for the hot carrier transfer study, since the high energy content carrier would have a larger spread of electronic wave function extended outside the GQD surface; as a result, high coupling would be enabled between the hot hole wave function of GQD and the HOMO of NMA.^[244] In addition to this, high energy excitation would result in a large chemical driving force for carrier extraction that would accelerate the carrier extraction kinetics. The findings of the present work discussed above are highlighted in Scheme 6.1.



Scheme 6.1. Schematic representation of carrier cooling (black spiral arrow) and hole transfer (red dotted arrow) in GQD-NMA composite. The blue up-pointed arrows indicate the near band edge excitation (left) and above band edge excitation (right), respectively. The green down pointed arrow shows the band edge emission.

6.3. Conclusion

The cooling time of the above band edge excitation ($\lambda_{\text{ex}} \sim 375$ nm) was found to be ~ 6 ps, significantly slower compared to the ~ 3 ps cooling time of the near band edge excitation ($\lambda_{\text{ex}} \sim 430$ nm), and both time scales are further remarkably slower compared to the subps cooling time of bulk graphene. In addition to this, highly efficient hot hole transfer with a faster timescale (< 0.8 ps) compared to the cooling time (3–6 ps) is observed in the GQD-NMA composite. It is worth

mentioning here that Mueller et al. observed a relatively slower (100–300 ps) lifetime of hot carriers of their GQDs in a transient absorption study.^[207] This is not surprising to us, since their GQDs were much smaller compared to our GQDs resulting in cooling of their GQDs under severe quantum confinement where fast phonon-assisted relaxation is largely retarded. However, our GQDs not only are bigger but also consist of ~4-5 graphene layers unlike the GQDs used by Mueller et al. containing mostly a single graphene layer. While Mueller et al. studied cooling under tight quantum confinement, we have studied the same but under weaker quantum confinement, and that resulted in an order of magnitude faster cooling time in our case. This is the first-ever study of carrier cooling and hot hole transfer of GQDs using a femtosecond upconversion setup. Unlike the transient absorption technique, widely used for studying the excited state kinetics of semiconductor materials which requires prior knowledge of a large number of absorption transitions by various excited state transient species which are not readily available, the fluorescence upconversion technique does not require such knowledge since only one type of transition from the band edge state to the ground electronic state contributes to the emission, and the kinetics observed using the later technique is much easier to elucidate with high accuracy.

Femtosecond Upconversion Study of Interfacial Electron Transfer from Photoexcited CsPbBr₃ Perovskite Nanocrystal To Rhodamine 6G.

7.1. Introduction

Many reports along with ones discussed in chapter 1 establish composites of perovskites have the potential to serve as building blocks of next-generation devices.^[103,245–248] Despite the several promising reports on perovskite composites in the past few years, their real potential in carrier extraction is not yet fully explored. One major obstacle toward this achievement is the undesired participation of intrinsic trap states in the carrier extraction process, making photoinduced electron transfer (PET) study in perovskite NCs challenging.^[249–251] Recent reports with metal chalcogenide QDs have shown that a judicious choice of a QD capping agent and dye molecule allows surface chemistry to complex QD with a different type of recognition dye molecules.^[112,113,252–255] Even though a large number of reports on PET are available with metal chalcogenide QDs with varying compositions, capping agent, type (core–shell, core only, etc.), and composite material/molecule, except for a few, similar studies with perovskite NCs are largely missing despite their vast photovoltaic applications. Therefore, a critical assessment of the individual constituents of an NC-composite in terms of carrier dynamics is highly warranted.

In the present work, we have designed a simple model of a NC composite (NC–r6G complex) to access the interfacial charge transfer kinetics of these novel materials (CsPbX₃). Such hybrid structures were previously used as building units in dye-sensitized solar cells. Through a rational

choice of organic acceptor molecule (r6G), we enabled moderate ΔG^0 of the PET reaction. Our goal was to achieve a fast PET time scale even at a mild ΔG^0 , since a fast charge transfer time scale would allow one to extract energy-rich species (biexciton or hot electron) much before they disappear through Auger recombination (10–200 ps) and cooling to a band edge state (<1 ps).^[220,238] Herein, with the help of a stochastic kinetic fitting model, we obtained a fast ~ 150 ps interfacial PET time scale in an NC–r6G composite. This is an interesting observation, as the obtained PET time scale is in the same order as the reported Auger recombination time scale in perovskite NCs. Our findings point toward the successful utilization of NC–r6G or similar type composites in the harvesting of high-energy species.

7.2. Results and Discussion

7.2.1. Synthesis and Characterization of CsPbBr₃ NCs.

NCs were synthesized using a reported hot injection method. In a 50 ml double-neck round bottom flask (RB) a mixture of Cs₂CO₃ (66.5 mg), octadecene (ODE, 2.5 ml), and oleic acid (OA, 0.5 ml) was heated at 120 °C under vacuum for 1 hour for complete removal of moisture. Then the mixture was transferred to N₂ atmosphere at 150 °C until all the Cs₂CO₃ reacted to form a pale yellow-coloured cesium oleate. As the cesium oleate precipitates out of ODE at room temperature, it was pre-heated to 120 °C during hot injection in the next step. In a separate reaction vessel (50 ml three-neck RB) 55 mg PbBr₂ and 5 ml ODE were dried in vacuum at 110 °C for 1 hour. Then the reaction mixture was heated under N₂ at 120 °C with the subsequent addition of dried OA and dried OLA at a 1:1 ratio (0.5 ml each). After complete dissolution of PbBr₂, the temperature of the reaction mixture was raised to 180 °C, and 0.8 ml pre-heated cesium oleate was swiftly injected into it. After 10 seconds the reaction mixture was quenched in an ice bath. The crude mixture was

then centrifuged at $\sim 12,000$ rpm for 5 minutes. The precipitate was dispersed in 0.3 ml hexane while the supernatant was discarded. The solution was again centrifuged at $\sim 12,000$ rpm for 5 minutes and the supernatant obtained was half diluted with hexane to obtain the stock solution which was then used for surface treatment. For surface treatment, 10 mg PbBr_2 and 100 μL toluene were added to the 100 μL stock solution of perovskite NCs, and the mixture was stirred for 1 hour and subsequently centrifuged at $\sim 12,000$ rpm for 5 minutes. The precipitate that contained extra salt was discarded. The rest of the stable colloidal solution of surface-treated CsPbBr_3 was collected and further diluted in toluene for optical studies.

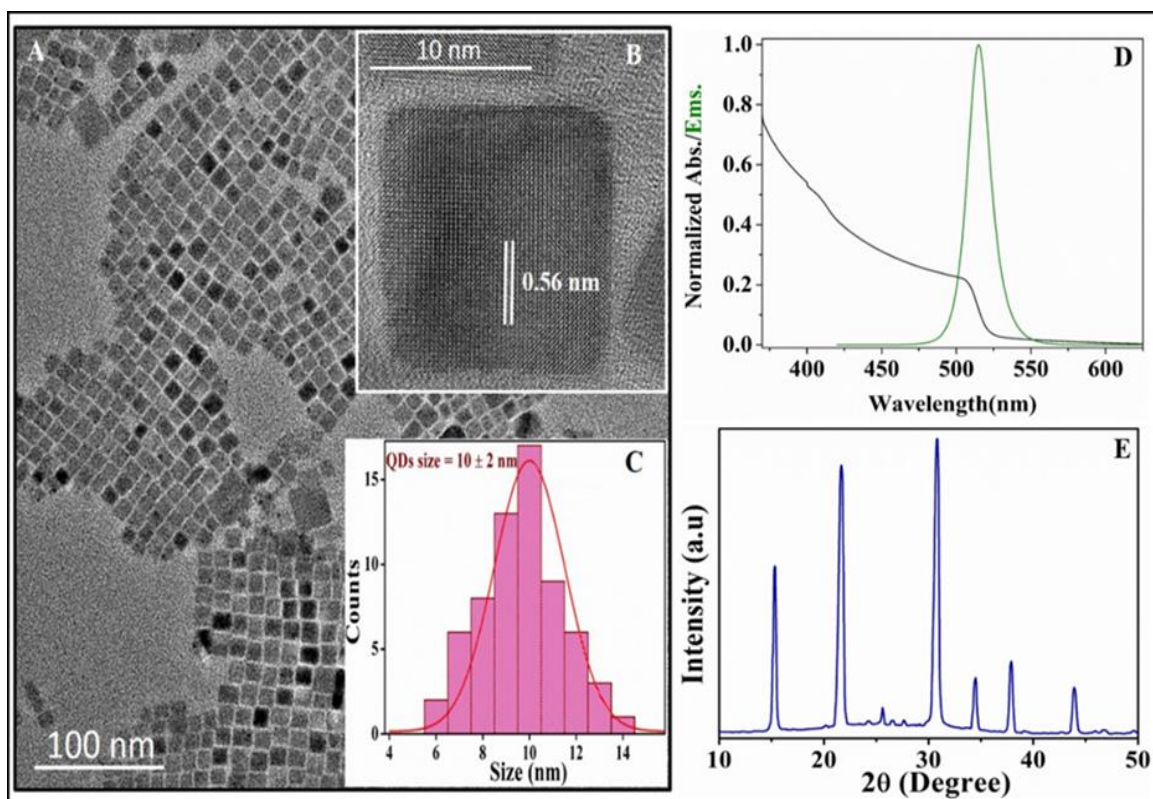


Figure 7.1. (A) TEM images of CsPbBr_3 NCs. (B) HR-TEM image of a CsPbBr_3 NC. (C) Particle size distribution of the NCs, the center of mass of which is located at 10 nm. (D) Absorption (black) and emission (green, $\lambda_{\text{ex}}=400$ nm) spectra of CsPbBr_3 NCs in toluene. (E) XRD spectrum of CsPbBr_3 NCs, which shows the cubic phase of the crystals.

The TEM image shows cubically shaped particles with a side length of 10 ± 2 nm (Figure 7.1). The first onset of the absorption spectrum and the emission peak position in toluene appear at ~ 503 and 512 nm, respectively (Figure 7.1D). These NCs are highly emissive with a PL quantum yield (ϕ_f) of ~ 75 – 80% . X-ray diffraction spectroscopy study reveals the cubic perovskite phase of these NCs (Figure 7.1E). All the structural characteristics and optical properties are consistent with previous reports.^[103,256]

7.2.2. Photoluminescence Quenching Study of NCs

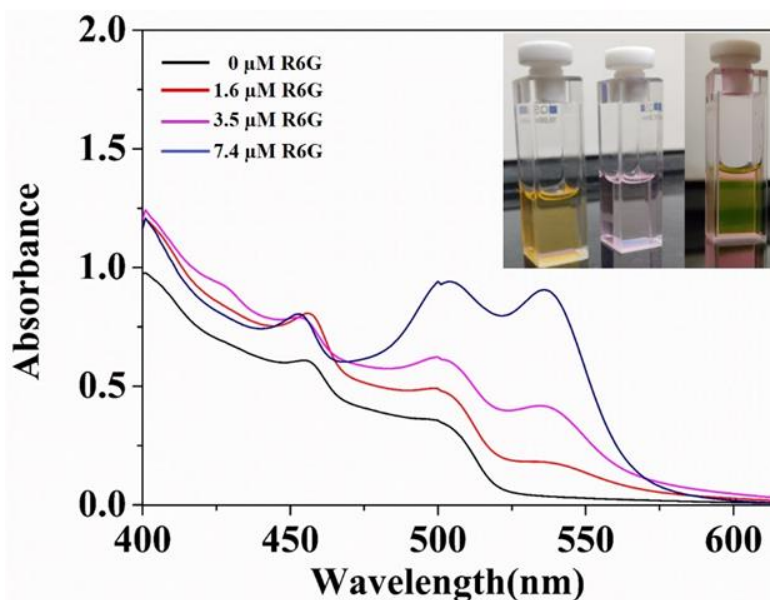


Figure 7.2. Absorption spectra of ~ 0.14 μM NCs in toluene at different r6G concentrations. Above ~ 7.4 μM r6G, the absorption spectrum does not change much. The molar extinction coefficient of NCs at the peak is $\sim 3.5 \times 10^6 \text{ M}^{-1}\text{s}^{-1}$.^[257] Inset shows cuvettes containing (i) ~ 0.14 μM NCs and ~ 7.4 μM r6G in toluene (left), (ii) saturated solution of r6G in toluene (middle) and (iii) ~ 7.4 μM r6G in water (right).

The photoluminescence quenching of colloidal CsPbBr_3 NCs in presence of r6G is studied in toluene. R6G is sparingly soluble in toluene (~ 0.4 μM), but the solubility increases to ~ 7.4 μM in

the presence of $\sim 0.14 \mu\text{M}$ NCs (r6G-to-NC ratio ~ 50), as shown in Figure 7.2. All concentrations were calculated from the absorption spectra and known values of molar extinction coefficients of NCs and r6G.^[257] Figure 7.2 (inset) shows the digital photographs of three cuvettes containing a saturated solution of r6G (~ 7.4 and $\sim 0.4 \mu\text{M}$) in toluene in the presence (strong color, left cuvette) and absence (light color, middle cuvette) of $\sim 0.14 \mu\text{M}$ NCs, and the same concentration ($\sim 7.4 \mu\text{M}$) of only r6G as in the left cuvette but in water (strong color, right cuvette) for side-by-side comparison.

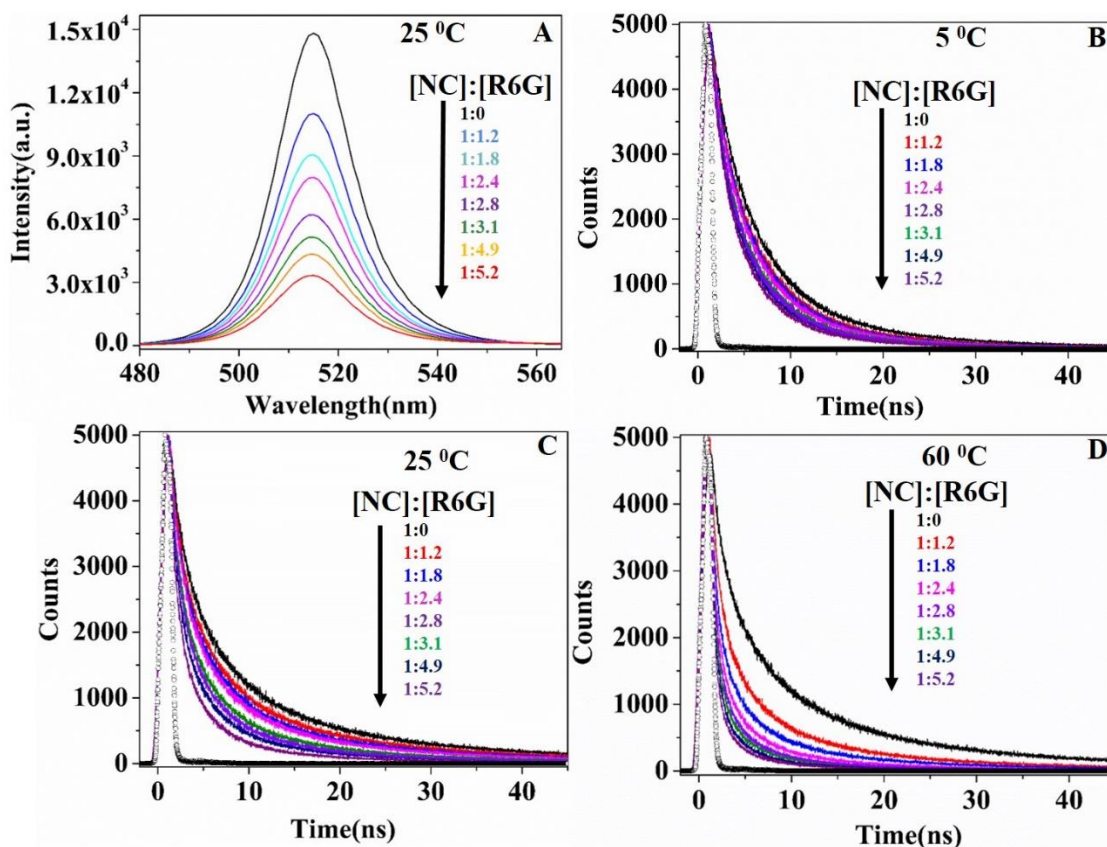
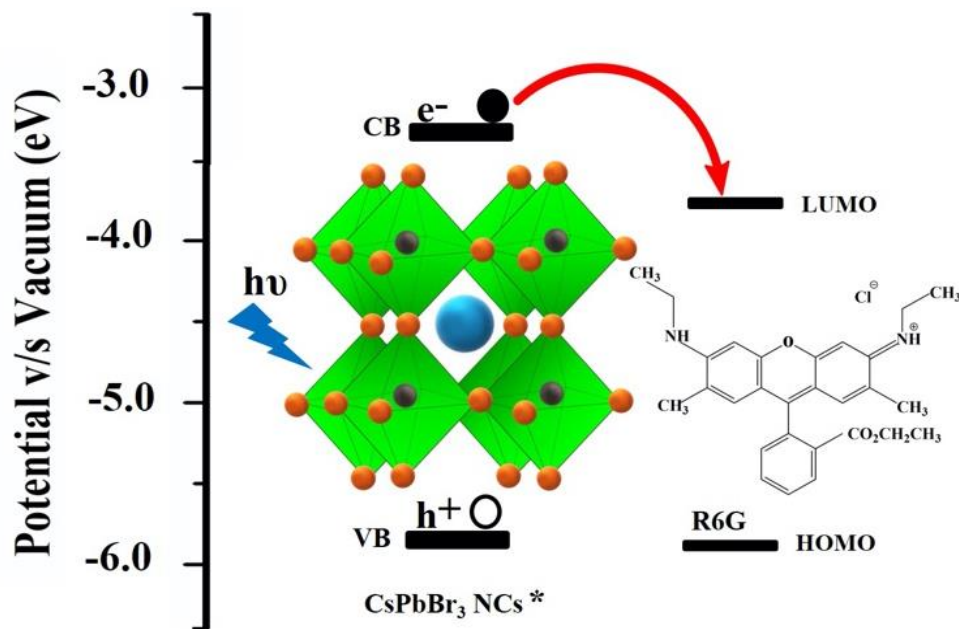


Figure 7.3. Steady-state emission (A, at 25 °C) and TCSPC recorded lifetime profiles (B–D, at 5 °C –60 °C) of NCs in toluene at various r6G concentrations. Excitation pulse (IRF ~ 0.7 ns) is shown by the dotted curves in B–D.

Addition of r6G in NC solution results in not only significant quenching of the PL of NCs but also proportionate shortening of its lifetime, implying the nonemissive nature of the complexes is involved in static quenching, NC-r6G complex is emissive and characterized with a shorter PL lifetime (Figure 7.3). The concentration of the attached r6G is calculated from the resultant absorption spectrum of r6G in the presence of $\sim 0.14 \mu\text{M}$ NCs after subtracting the absorption spectrum of pure r6G saturated in toluene. Since the absorption peak position of r6G ($\sim 535 \text{ nm}$) is far away from that ($\sim 503 \text{ nm}$) of the NCs, subtraction of the pure NC spectrum is not required for accurate estimation of the attached r6G concentration. Quite a large number of attached r6G per NC is not surprising to us, because NCs are quite big ($\sim 10 \text{ nm}$), and they have long hydrocarbon chains (Oleic acid and Oleyl amine) attached to their surface that can help to adsorb a large number of r6G molecules at NC surface. The rotational anisotropy study of r6G provides direct proof of NC-r6G complex formation. (Figure 7.6 B).

There could be two possible reasons for this quenching: (1) PET from conduction band (CB) of photoexcited NC to LUMO of r6G due to proper band alignment (Scheme 7.1)^[258–260] and/or (2) Förster resonance energy transfer (FRET) from photoexcited NC (donor) to ground state r6G (acceptor).^[200,261] Despite the good overlap of donor (NC) emission with acceptor (r6G) absorption (Figure 7.4 A), which is a prerequisite of an efficient FRET, no r6G emission (at 570 nm) was observed as a result of quenching of NCs emission (Figure 7.4 B). Therefore, quenching of NC emission in our case is attributed to PET only, even though the criteria of both PET and FRET are equally satisfied. This is possible when PET is taking place at a much faster time scale than FRET. The oxidation potential of CsPbBr₃ NC, reduction potential of r6G and the band gap energy of CsPbBr₃ NC are found to be -5.85 eV, -3.7 eV (vs vacuum) and 2.5 eV, respectively.^[262,263] The calculated value of $-\Delta G_{PET}$ is 0.35 eV. (For calculation see chapter 2)



Scheme 7.1. Band Edge and HOMO–LUMO Energy Levels of NC and r6G Participating in the PET Reaction.

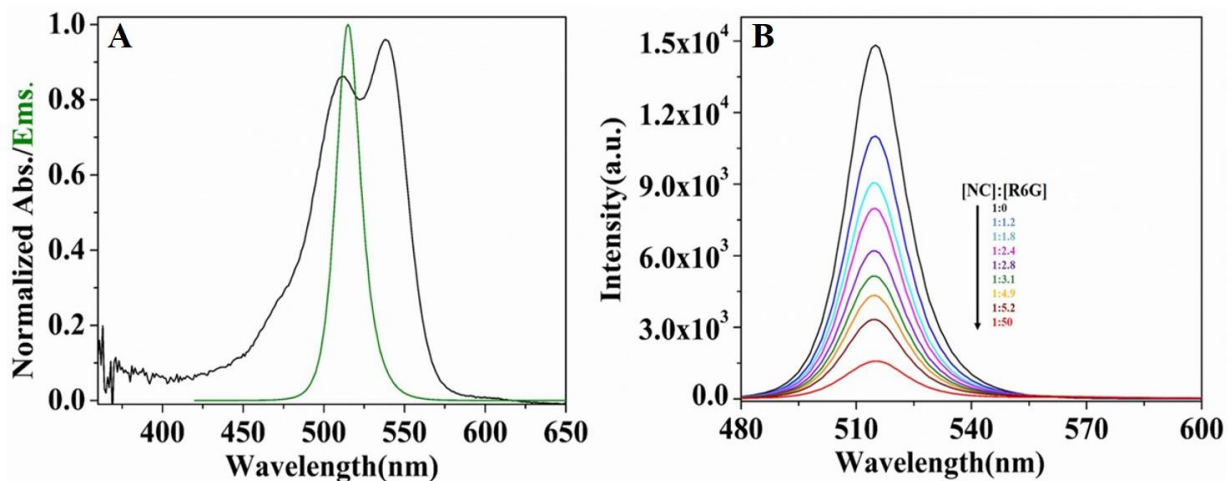


Figure 7.4. (A) Absorption spectrum of r6G in toluene (black) and emission spectrum of CsPbBr₃ NCs in toluene (green, $\lambda_{\text{ex}}=400$ nm). (B) Emission spectra of CsPbBr₃ NCs in toluene at different r6G concentrations ($\lambda_{\text{ex}}=400$ nm). The intensity of NCs is quenched upon the addition of r6G. Absence of r6G peak at 570 nm, even at the highest r6G concentration (red spectrum).

Our assignment corresponds well with a previous report on the quenching study of CdSe QD (donor) emission by rhodamine B (acceptor) by Lian and co-workers.^[253] They observed that while

PET quenches a significant fraction ($\sim 84\%$) of excitons from photoexcited CdSe QDs, only a small fraction ($\sim 16\%$) is quenched by the FRET.^[253] In our case, the FRET contribution is even smaller because of the much sharper emission spectrum of perovskite NCs that reduces the overlap integral value with the acceptor's absorption spectrum. TCSPC measured lifetime profiles are depicted in Figure 7.3 B–D at different temperatures, showing a more efficient quenching at a higher temperature, in contrast to the static quenching phenomenon (i.e., complexation-induced quenching). Since at high temperatures the complex breaks apart, a lower quenching rate or longer NC lifetime is anticipated, but just the opposite was observed (Figure 7.3 B–D). The intrinsic PET time scale in the NC–r6G complex was estimated to be ~ 150 ps using the femtosecond upconversion setup, which is much shorter than the IRF (~ 0.7 ns) of our TCSPC setup. Therefore, the quenching of the nanosecond lifetime component shown in Figure 7.3B–D undoubtedly does not influence by static quenching and is solely ruled by collisional quenching. TCSPC can measure the lifetime of the NC subpopulation that has not formed a complex with r6G at the time of excitation. It is worth mentioning here that the NC–r6G complexes cannot be detected by our TCSPC because of their lifetime (~ 150 ps) being shorter than the instrument IRF (~ 700 ps). Even in the presence of r6G, some NCs are always available in the free form that can participate in the PET through a diffusion-controlled mechanism. At an elevated temperature, the NC–r6G complex breaks apart, leading to an enhanced concentration of free r6G participating in the diffusion-controlled quenching. In addition to a highly effective quencher concentration at high temperature, the translational diffusion rate also increases with temperature, in a combined effect a drastic increase in the diffusion-controlled quenching rate is observed. The Stern–Volmer plots showed significant deviations from typical ones. (Figure 7.5) We tried to fit the Stern–Volmer plots with available fitting models but a comprehensive fitting was lacking in every case. A linear fit to the

lifetime Stern-Volmer Plot is associated with not only an unacceptable chi-square value but also a bimolecular quenching constant with an abnormally high value ($K_a \sim 10^4 \text{M}^{-1}\text{s}^{-1}$).

Temperature	[NC]:[r6G]	a ₁	a ₂	τ ₁ (ns)	τ ₂ (ns)	τ _{avg} (ns)
5 °C	1 : 0	0.80	0.20	3.25	8.47	4.29
	1 : 1.2	0.82	0.18	2.54	7.19	3.38
	1 : 1.8	0.82	0.18	2.51	6.91	3.30
	1 : 2.4	0.83	0.17	2.49	6.75	3.21
	1 : 2.8	0.88	0.12	2.15	6.25	2.64
	1 : 3.1	0.89	0.11	2.11	6.18	2.55
	1 : 4.9	0.90	0.10	2.05	6.01	2.45
	1 : 5.2	0.91	0.09	1.93	5.73	2.27
25 °C	1 : 0	0.89	0.11	2.43	11.30	3.40
	1 : 1.2	0.93	0.07	2.13	10.16	2.69
	1 : 1.8	0.94	0.06	2.07	9.61	2.52
	1 : 2.4	0.95	0.05	1.94	9.13	2.30
	1 : 2.8	0.96	0.04	1.79	8.25	2.05
	1 : 3.1	0.97	0.03	1.69	7.59	1.87
	1 : 4.9	0.98	0.02	1.57	7.21	1.68
	1 : 5.2	0.99	0.01	1.39	6.24	1.44
60 °C	1 : 0	0.90	0.10	2.18	11.18	3.08
	1 : 1.2	0.97	0.03	1.61	8.77	1.83
	1 : 1.8	0.99	0.01	1.45	7.98	1.52
	1 : 2.4	0.993	0.007	1.26	6.71	1.30
	1 : 2.8	0.997	0.003	1.13	5.811	1.14
	1 : 3.1	0.5	0.5	1.11	1.11	1.11
	1 : 4.9	0.5	0.5	0.91	0.91	0.91
	1 : 5.2	0.5	0.5	0.87	0.87	0.87

Table 7.1. Tail fitting parameters of TCSPC measured fluorescence transients of CsPbBr₃ NCs at different NC-to-r6G ratios and temperatures.

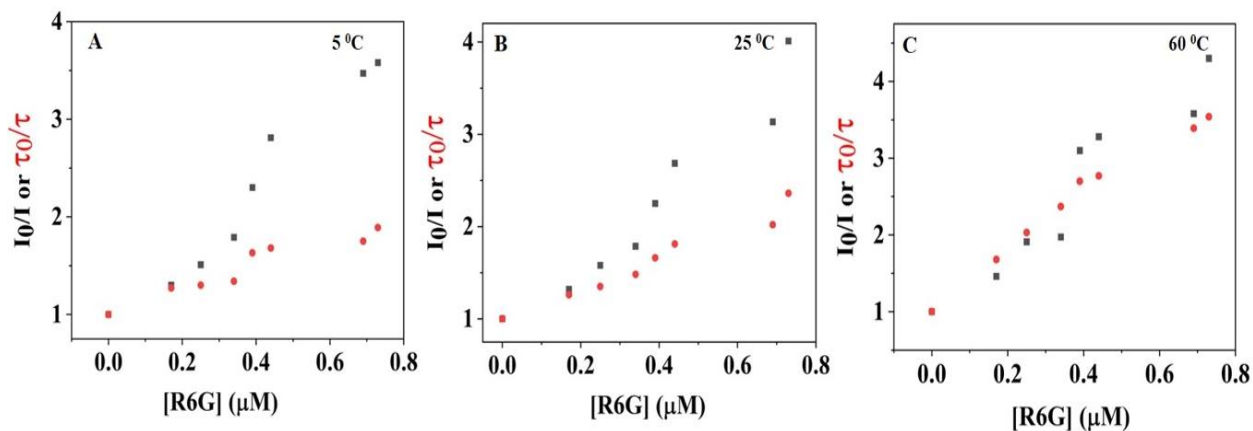


Figure 7.5. Time-resolved (TCSPC) and steady-state Stern-Volmer plots at different temperatures.

The temperature-dependent trend of quenching at a later time regime (obtained from TCSPC) switches at the initial time regime studied using a femtosecond upconversion setup will be discussed in the latter part of this chapter. Unlike the diffusion-controlled nature of the later time quenching, quenching at the initial time regime (<100 ps) is attributed to the NC-r6G complex formation. As the complex breaks apart at high temperatures, the quenching rate decreases. In this chapter, we only focus on the initial time regime of PET kinetics due to its intrinsic nature. I will provide a comprehensive understanding of intrinsic PET with help of a femtosecond upconversion study.

7.2.3. Rotational Anisotropy Study

The rotational anisotropy study of r6G provides direct proof of NC-r6G complex formation.^[264–267] Since r6G is sparingly soluble in toluene, one cannot measure the rotational anisotropy of r6G in toluene using a femtosecond upconversion setup. Utilizing our upconversion setup with the second harmonic of the Ti-sapphire laser, we can only excite the sample anywhere between 375 and 430 nm. Even the longest excitation (~ 430 nm) of femtosecond upconversion is far from the absorption peak (~ 535 nm) of r6G. The molar extinction coefficients of r6G remain significantly

low across the excitation window (375–430 nm) of our femtosecond upconversion setup (Figure 7.6A). One may consider using a high concentration of r6G in an anisotropy study, but this is not possible in toluene. Luckily, we found one readily available solvent, methanol, which is iso-viscous with toluene where r6G is highly soluble. Given the fact that the rotation diffusion time of a dipole primarily depends on the solvent viscosity, one may expect similar rotational diffusion times from iso-viscous solvents. We studied the rotational anisotropy decay of a high concentration of r6G in methanol, and because of their (toluene and methanol) similar viscosities, we assumed the rotational diffusion time scale obtained in methanol would be identical to that in toluene. Since the solubility of r6G in toluene is greatly enhanced in the presence of NCs, switching the solvent is not necessary when NCs are present. The rotational time scale of r6G in methanol was found to be ~ 120 ps, in excellent agreement with the previous report.^[268]

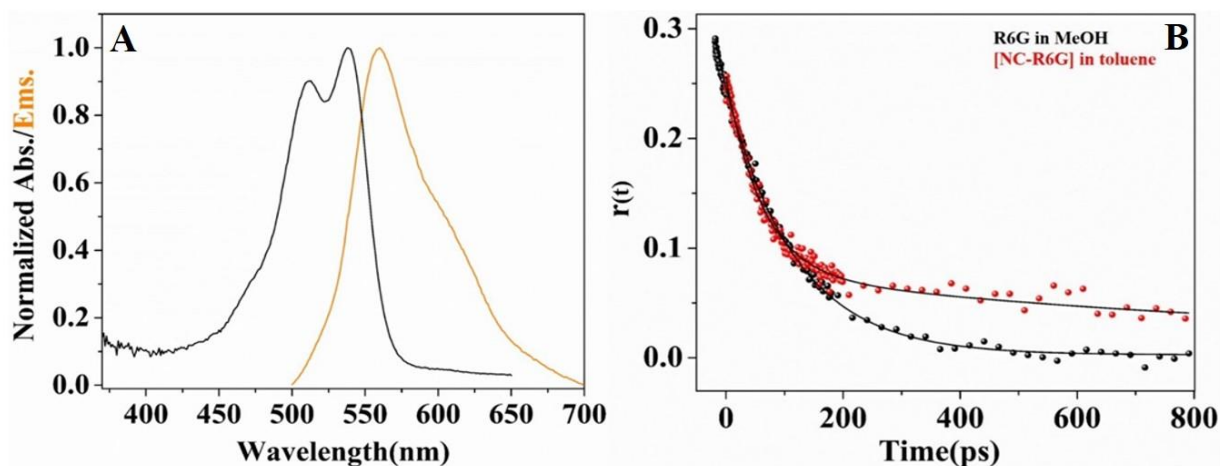


Figure 7.6. (A) Absorption (black) and emission (orange, $\lambda_{\text{ex}}=490$ nm) spectra of r6G in toluene. (B) Rotational anisotropy decay of r6G in methanol (black balls) and toluene in the presence of NCs (red balls). Samples were excited at 430 nm, while the emissions were collected at emission peak positions of r6G in free (without NCs) and bound (with NCs) forms.

Figure 7.6 (B) shows rotational correlation time of r6G gets slower in the presence of NCs, a clear manifestation of NC–r6G complex formation. Unlike the monoexponential decay (~ 120 ps) of anisotropy of only r6G in methanol, bound r6G (in NC solution) exhibits biexponential decay (~ 60 ps and >1 ns) with an additional slow component (>1 ns, 27%) originating from the overall rotation of the NC–r6G complex. The origin of the fast component (~ 60 ps, $\sim 73\%$) in NC solution cannot be attributed to the rotation of free r6G present in toluene at an exceedingly low concentration, since the rotational time scale of free r6G is twice as slow (~ 120 ps) than the ~ 60 ps component. For a moment, even if we assume the ~ 60 ps component was due to the rotation of free r6G, then a large contribution ($\sim 73\%$) of this component is not commensurate with the fact that only ~ 0.4 μM r6G remains free, while ~ 7.4 μM is in the bound form. The origin of the ~ 60 ps rotational component is most likely from a wobbling type motion in a cone of the attached r6G molecule as described by the “wobbling-in-cone model.”^[269–271]

This model nicely explains the biexponential anisotropy decay of dye molecules attached to a micelle. Unlike the only molecular rotation (time scale $\tau_M \sim 4\pi\eta r_h^3/3KT$) causing depolarization of dye molecule in the pure solvent, for a micelle-bound dye, depolarization is caused by two additional motions other than the rotation of dye along with the micelle (time scale τ_M). First, the wobbling-like motion of the dye in a cone (time scale τ_w), and second, the translational motion of dye on the micelle surface (time scale τ_t). If the attached r6G molecule in our case exhibits a similar wobbling-like motion causing biexponential decay of anisotropy (τ_{slow} and τ_{fast}), then the translational motion (τ_t) and overall rotation (τ_M) would then describe the slow component of anisotropy as $1/\tau_{\text{slow}} = 1/\tau_t + 1/\tau_M$, while wobbling (τ_w) along with other two motions (τ_M and τ_t) would define the first component as $1/\tau_{\text{fast}} = 1/\tau_t + 1/\tau_M + 1/\tau_w$. In most of the cases in micelles, $\tau_M \gg \tau_t \gg \tau_w$ (i.e., $\tau_{\text{fast}} \sim \tau_w$). In our case, if we assume NC is structurally similar to micelle, then

the origin of the ~ 60 ps rotational component would likely be a result of a wobbling type motion of the attached r6G molecules.^[269,272]

7.2.4. Femtosecond Upconversion Study of Quenching at Different Temperatures.

Since we intend to record the intrinsic PET of an NC-r6G complex, the quenching study at the initial time regime (<100 ps) is crucial. As discussed before initial time kinetic is largely free from solvent diffusion parameters, even for a collisional quenching. This is because the root-mean-square distance ($\sqrt{\Delta x^2}$) traveled by r6G ($D_r \sim 535 \times 10^{-10} \text{m}^2/\text{s}$ in toluene) during 100 ps (τ) is just ~ 3.2 nm [$\sqrt{(2D_r\tau)}$], which is even shorter than the size of an NC (~ 10 nm).^[190,273–275] Therefore, only those r6G molecules present immediately adjacent to the NCs (<3.2 nm) at the time of excitation will contribute to the quenching studied in the first ~ 100 ps acquisition time window. Since donor-acceptor are already at (or near) contact distance, diffusion is not required for the PET reaction. Figure 7.7 depicts the femtosecond transients of NCs at different NC-to-r6G mole ratios at room temperature and elevated temperature. Femtosecond PL transients are fit to a stochastic model originally proposed by Tachiya, shown by the solid lines in Figure 7.7. Several groups have already used this model to realize the stoichiometry of interaction between donor and acceptor molecules. Such information enables the expression of the PET rate against a single quencher molecule.^[255,276–278]

The lifetime of high Φ_f NCs is mostly governed by the band edge radiative recombination (rate constant k_0) with some contribution from m_t (mean number per NC) trap states participating in the quenching through a nonradiative pathway (rate constant k_t per trap state). The proposed stochastic model assumes these independent trap states (m_t per NC) are distributed within the NCs following the Poisson statistic (Equation 7.1).^[255,276–278]

$$\Phi(n) = (m_t^n/n!) \exp(-m_t) \quad (7.1)$$

where $\Phi(n)$ is the probability function describing the number of occurrences of NC bearing n defect states and the center of mass of this distribution is located at $n = m_t$. Based on the concept of Poisson distribution of the trap states, and following Tachiya's derivation, one can eventually reach eq 7.2, which provided us with conclusive fittings to the NC transients (Figure 7.7).^[278]

$$I(t) = I(0) \exp[-k_0 t - m_t \{1 - \exp(-k_t t)\}] \quad (7.2)$$

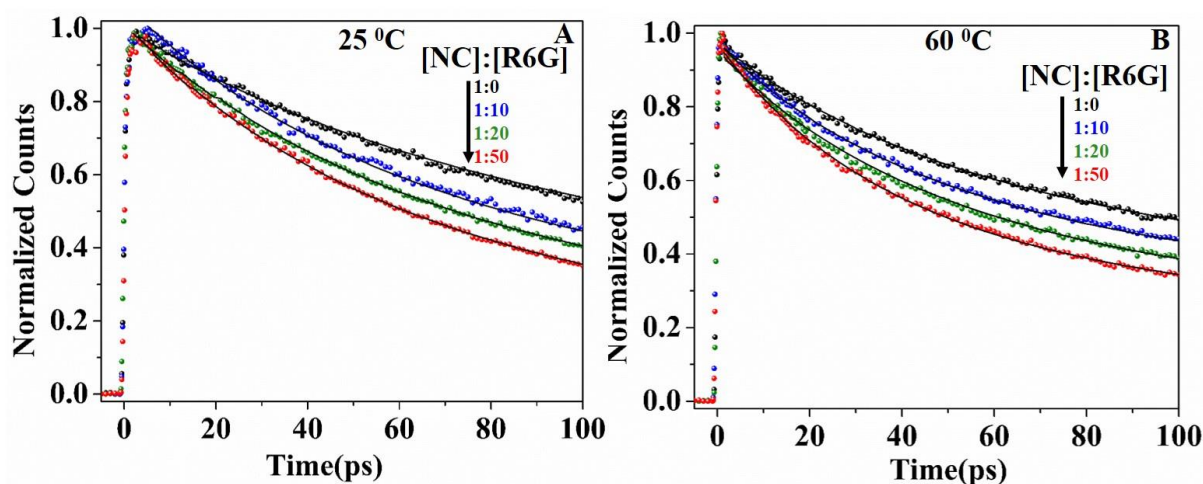


Figure 7.7. Femtosecond transients of NCs in toluene at different NC-to-r6G ratios at 25 °C (A) and 60 °C (B), respectively. Transients are fit to a stochastic kinetic model, best fitted curves are shown by the black solid lines. We fitted the transients after a few picoseconds following the excitation to avoid any interference from the excitation pulse.

In the presence of r6G, if we assume the adsorption of r6G molecules at the NC surface also follows a similar Poisson statistic (as in trap-state distribution), an additional Poisson term describing the r6G-induced quenching has to be incorporated in eq 7.2 while fitting the transients of NCs in the presence of r6G (Equation 7.3).

$$I(t) = I(0) \exp[-k_0 t - m_t \{1 - \exp(-k_t t)\} - m_q \{1 - \exp(-k_q t)\}] \quad (7.3)$$

In the above equation, m_q is the mean number of quencher molecules attached to an NC and k_q is the PET rate constant per quencher molecule. $k_0 + m_t k_t + m_q k_q$ is the excited-state depopulation rate constant of the NCs in the presence of quencher, and $m_q k_q$ is the rate constant of PET due to m_q attached r6G molecules. While eq 7.2 provided a satisfactory fitting to the femtosecond transient of NCs without a quencher, eq 7.3 provided fittings in the presence of the quencher. Conclusive fittings reveal even though the mean number of trap states associated with an NC (~ 1.2) does not change with temperature, the trap-induced quenching time scale ($1/k_t$) gets shorter from 145 to 127 ps with an increase in temperature from 5 to 60 °C, respectively (Figure 7.8, Tables 7.1 and 7.2). Quenching of emission at high temperature is common in NCs, caused by the thermally activated trapping of carriers and/or phonon-assisted nonradiative recombination.^[279–281] The low population of the defect states (~ 1.2 per NC) resulted in a high fluorescence quantum yield ($\sim 75\text{--}80\%$) of our NCs. Using a femtosecond upconversion setup, we studied PET kinetics with a gradual increase in r6G-to-NC ratio from ~ 10 to ~ 50 , above which r6G settles down at the bottom. Despite the large r6G-to-NC ratios we used, the actual mean number of r6G molecule (m_q) participating in the PET reaction per NC always remains low ($\sim 0.3\text{--}1$) even at the highest concentration ratio (r6G-to-NC ~ 50) and lowest temperature (~ 5 °C). In every case, irrespective of temperature and r6G concentration, the PET time scale ($1/k_q \sim 150$ ps) per quencher molecule remains the same. Our observed PET time scale is consistent with other reports on bimolecular electron/hole transfer from perovskite NC to an organic molecule. For instance, Samanta and co-workers observed ~ 120 and ~ 170 ps hole transfer time scales from photoexcited CsPbBr₃ and CsPbI₃ NCs to 1-ampinopyrene.^[103] In a seminal work, Lian and co-workers reported a ~ 65 ps PET time scale (half-life) of the CsPbBr₃ NC-benzoquinone pair.^[247] The most interesting observation of our temperature dependence study is that the mean number of r6G molecules per

NC participating in PET reaction (m_q) for a fixed bulk r6G-to- NC ratio does not change much with temperature (Table 7.2). For example, at the highest r6G concentration (r6G-to-NC ~ 50), $m_q \sim 0.98$ at 5 °C, and it remains almost the same ($m_q \sim 0.87$) at elevated temperature (~ 60 °C). An m_q value lower than 1 at low r6G-to-NC concentration ratios implies that many of the NC-r6G complexes do not participate in the PET reaction. Even for the participating complexes, only one (or a few in a rare case) from a large number of attached r6G molecules deeply buried within the capping layer of NC, participates in the PET reaction. Since at elevated temperature mostly the r6G molecules residing at the solvent-capping layer interface and/ or planted at shallow depths from the surface are detached, there is little or no change of m_q with the increase in temperature (Table 7.2).

Temperature	[NC]:[r6G]	m_t	m_q	$\tau_0=1/k_0$ (ps)	$\tau_t =1/k_t$ (ps)	$\tau_q=1/k_q$ (ps)
5 °C	1:0	1.2	0	9000	145	150
	1:10		0.3			
	1:20		0.47			
	1:50		0.98			
25 °C	1:0	1.2	0	9000	130	150
	1:10		0.32			
	1:20		0.46			
	1:50		0.93			
60 °C	1:0	1.2	0	9000	127	150
	1:10		0.32			
	1:20		0.45			
	1:50		0.87			

Table 7.2. Fitting parameters of femtosecond transients of NCs using Stochastic Kinetic Model at different NC-to-r6G ratios and temperatures.

The PET kinetics recorded through similar bimolecular quenching studies are often found to be apparent mainly for two reasons: (i) Bimolecular PET rate of freely diffusing donor and acceptor molecules normally levels off to the diffusion-controlled limit. In such a case, the observed PET rate would reflect the mass transportation rate of the medium. (ii) The actual donor–acceptor stoichiometry of a PET reaction may largely deviate from their bulk concentration ratio, leading to an inaccurate estimation of the PET rate. In our study, we overcame both by using a femtosecond upconversion setup which enabled us to record the early time PET kinetic (<100 ps) where the effect of diffusion is negligible. In addition, we used an analytical fitting model that reveals the mean number of r6G participating in the PET reaction (~ 0.3 – 1) in an NC is much lower compared to the number of attached r6G (~ 10 – 50 per NC). Even though the PET time scale of NC–r6G complex is relatively slow (~ 150 ps), we preferred to use a femtosecond upconversion setup, using this technique one can able to measure the kinetics immediately after excitation (<1 ps). This would allow one to realize diffusion-free PET kinetics.

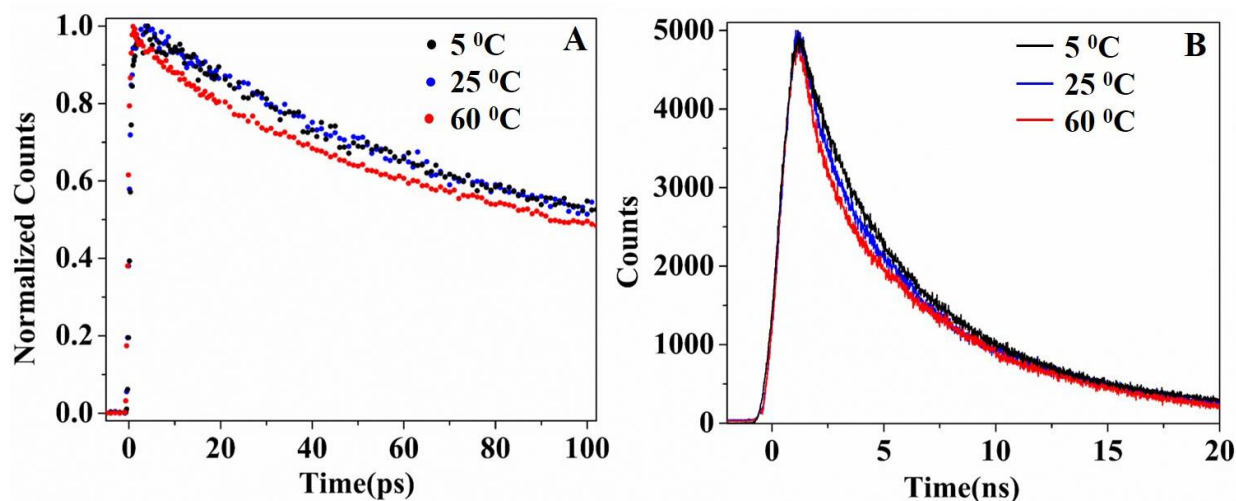


Figure 7.8. Respectively, Femtosecond and TCSPC transients (A and B) of CsPbBr₃ NCs in toluene at three different temperatures 5 °C (black), 25 °C (blue) and 60 °C (red).

7.3. Conclusion

In this work, we have recorded ~150 ps interfacial intrinsic PET timescale of NC-r6G complex. The fitting of femtosecond transients with a stochastic kinetics model reveals that despite the high fluorescence quantum yield (ϕ_f ~75-80%) of our NCs, they are not entirely defect-free. The presence of a small defect population (~1.2 per NC) was identified through our analysis. These intrinsic quencher sites are assigned to shallow mid-band gap trapped states by several reports, and cannot be removed entirely through surface treatments. Trap states efficiently quench the excited state NCs (in ~127-145 ps timescale) through a nonradiative band-edge recombination pathway. The most interesting observation of this work is the participation of a few r6G molecules (~0.3-1) per NC in the PET reaction, despite a large number (~10-50) of attached r6G molecules. The temperature dependence study reveals that only the deeply buried r6G molecules within the surface capping layer of NCs participate in the PET reaction. Since their locations are deep inside the capping layer, an increase in temperature cannot separate them from the NC. Through this work, we have highlighted the urgency of femtosecond study in obtaining diffusion-free PET kinetics. In addition to this, early time kinetics recorded in this work provides an accurate donor-acceptor stoichiometry. The findings of this work will help researchers to realize the actual potentials of perovskite NC-organic molecule composites in various photovoltaic and optoelectronic applications.

Summary and Future Prospects

Photophysical processes in nanostructured semiconductor materials are studied in this thesis to understand the nature, carrier dynamics and charge transfer processes of the materials for their widespread applications. Excitation-dependent emission nature of carbon dots samples, ultrafast hot carrier relaxation in GQDs, and ultrafast charge transfer dynamics in GQD/inorganic halide perovskite NCs- molecular composites are explored with the help of time-resolved fluorescence techniques in this thesis. The techniques range from ensemble methods (fluorescence upconversion, TCSPC) to single-molecule methods (fluorescence correlation spectroscopy).

The present work provides beneficial new information regarding the urgency of FCD sample purification with more scientific rigor, ultrafast carrier dynamics of GQD-molecular composites where GQD can be used as both electron donor and acceptor, slow carrier cooling time scale GQD in comparison to the bulk graphene and designing of simplest NC composite model to access the interfacial charge transfer kinetics.

The key findings of this thesis are,

- i. The actual origin of excitation-dependent emission and spectral migration of FCD fluorescence lies with its ground-state optical heterogeneity. Several intriguing properties of FCD fluorescence, whose origins have remained a mystery to date, mostly originated from inadequate sample purification.
- ii. Highly exergonic PET from an electron-rich organic molecule DMA to a photo-excited GQD is observed. <1 ps PET time scale in a GQD-DMA complex is confirmed by upconversion technique whereas the single molecule sensitive FCS method confirms the 4-6 μ s timescale of complexation.

-
-
- iii. At low temperature, a major portion of the PET (from GQD to electron deficient DNT) kinetics proceeds through static quenching but at elevated temperature, collisional quenching presides over the static quenching. Ultrafast (~ 3 ps) intrinsic PET timescale of the GQD–DNT complex is observed by employing a femtosecond upconversion technique.
 - iv. By employing a femtosecond upconversion spectrometer, highly efficient hot hole transfer with a faster timescale (< 0.8 ps) compared to the carrier cooling time (3–6 ps) of GQD is observed in the GQD-NMA composite.
 - v. ~ 150 ps interfacial intrinsic PET timescale of NC-r6G complex is observed by employing a femtosecond upconversion spectrometer. The fitting of femtosecond transients with a stochastic kinetics model reveals the participation of a few r6G molecules ($\sim 0.3-1$) per NC in the PET reaction, despite a large number ($\sim 10-50$) of attached r6G molecules. The temperature dependence study reveals that only the deeply buried r6G molecules within the surface capping layer of NCs participate in the PET reaction.

The findings of this research will aid the scientific community in the development of next-generation photovoltaic devices, as well as the fluorescence quenching in these materials can be used for additional sensing applications.

References

- [1] Y. Fu, M. Willander, in (Eds.: Y. Fu, M. Willander), Springer US, Boston, MA, **1999**, pp. 1–30.
- [2] M. G. Bawendi, M. L. Steigerwald, L. E. Brus, *Annu. Rev. Phys. Chem.* **1990**, *41*, 477–496.
- [3] T. Takagahara, K. Takeda, *Phys. Rev. B* **1992**, *46*, 15578–15581.
- [4] J. Li, J. Z. Zhang, *Coord. Chem. Rev.* **2009**, *253*, 3015–3041.
- [5] Y. M. Sung, T.-G. Kim, D.-J. Yun, M. Lim, D.-S. Ko, C. Jung, N. Won, S. Park, W. S. Jeon, H. S. Lee, J.-H. Kim, S. Jun, S. Sul, S. Hwang, *Small* **2021**, *17*, 2102792.
- [6] Z. Li, J. Wei, F. Wang, Y. Tang, A. Li, Y. Guo, P. Huang, S. Brovelli, H. Shen, H. Li, *Adv. Energy Mater.* **2021**, *11*, 2101693.
- [7] N. N. Ledentsov, *Semicond. Sci. Technol.* **2011**, *26*, DOI 10.1088/0268-1242/26/1/014001.
- [8] M. A. Cotta, *ACS Appl. Nano Mater.* **2020**, *3*, 4920–4924.
- [9] A. P. Litvin, I. V. Martynenko, F. Purcell-Milton, A. V. Baranov, A. V. Fedorov, Y. K. Gun'Ko, *J. Mater. Chem. A* **2017**, *5*, 13252–13275.
- [10] Y. Zhang, G. Wu, F. Liu, C. Ding, Z. Zou, Q. Shen, *Chem. Soc. Rev.* **2020**, *49*, 49–84.
- [11] J. Siegert, S. Marcinkevičius, Q. X. Zhao, *Phys. Rev. B - Condens. Matter Mater. Phys.* **2005**, *72*, 1–7.
- [12] L. Duan, L. Hu, X. Guan, C. H. Lin, D. Chu, S. Huang, X. Liu, J. Yuan, T. Wu, *Adv. Energy Mater.* **2021**, *11*, 1–23.
- [13] L. M. Nikolenko, V. F. Razumov, *Russ. Chem. Rev.* **2013**, *82*, 429–448.

-
- [14] P. V. Kamat, *J. Phys. Chem. Lett.* **2013**, *4*, 908–918.
- [15] G. H. Carey, A. L. Abdelhady, Z. Ning, S. M. Thon, O. M. Bakr, E. H. Sargent, *Chem. Rev.* **2015**, *115*, 12732–12763.
- [16] Z. Pan, I. Mora-sero, Q. Shen, H. Zhang, Y. Li, K. Zhao, J. Wang, X. Zhong, J. Bisquert, *J. Am. Chem. Soc.* **2014**, *136*, 9203–9210.
- [17] D. V. Pandi, V. Saraswathi, N. Muthukumarasamy, S. Agilan, P. Balraju, D. Velauthapillai, *Opt. Mater. (Amst)*. **2021**, *112*, 110774.
- [18] A. Andruszkiewicz, X. Zhang, M. B. Johansson, L. Yuan, E. M. J. Johansson, *Nanoscale* **2021**, *13*, 6234–6240.
- [19] I. V. Martynenko, A. P. Litvin, F. Purcell-Milton, A. V. Baranov, A. V. Fedorov, Y. K. Gun'Ko, *J. Mater. Chem. B* **2017**, *5*, 6701–6727.
- [20] T. Jamieson, R. Bakhshi, D. Petrova, R. Pocock, M. Imani, A. M. Seifalian, *Biomaterials* **2007**, *28*, 4717–4732.
- [21] C. T. Matea, T. Mocan, F. Tabaran, T. Pop, O. Mosteanu, C. Puia, C. Iancu, L. Mocan, *Int. J. Nanomedicine* **2017**, *12*, 5421–5431.
- [22] F. Erogbogbo, K. Yong, I. Roy, G. Xu, P. N. Prasad, M. T. Swihart, *ACS Nano* **2008**, *2*, 873–878.
- [23] M. Howarth, W. Liu, S. Puthenveetil, Y. Zheng, L. F. Marshall, M. M. Schmidt, K. D. Wittrup, M. G. Bawendi, A. Y. Ting, *Nat. Methods* **2008**, *5*, 397–399.
- [24] W. Cai, D. W. Shin, K. Chen, O. Gheysens, Q. Cao, S. X. Wang, S. S. Gambhir, X. Chen,
-

-
- Nano Lett.* **2006**, *6*, 669–676.
- [25] L. Ye, K. T. Yong, L. Liu, I. Roy, R. Hu, J. Zhu, H. Cai, W. C. Law, J. Liu, K. Wang, J. Liu, Y. Liu, Y. Hu, X. Zhang, M. T. Swihart, P. N. Prasad, *Nat. Nanotechnol.* **2012**, *7*, 453–458.
- [26] S. Zhu, Y. Song, J. Shao, X. Zhao, B. Yang, *Angew. Chemie - Int. Ed.* **2015**, *54*, 14626–14637.
- [27] J. Liu, R. Li, B. Yang, *ACS Cent. Sci.* **2020**, *6*, 2179–2195.
- [28] F. Yuan, S. Li, Z. Fan, X. Meng, L. Fan, S. Yang, *Nano Today* **2016**, *11*, 565–586.
- [29] X. Li, M. Rui, J. Song, Z. Shen, H. Zeng, *Adv. Funct. Mater.* **2015**, *25*, 4929–4947.
- [30] J. Peng, W. Gao, B. K. Gupta, Z. Liu, R. Romero-Aburto, L. Ge, L. Song, L. B. Alemany, X. Zhan, G. Gao, S. A. Vithayathil, B. A. Kaiparettu, A. A. Marti, T. Hayashi, J. J. Zhu, P. M. Ajayan, *Nano Lett.* **2012**, *12*, 844–849.
- [31] G. U. Siddiqui, J. Ali, K. H. Choi, Y. Jang, K. Lee, *J. Lumin.* **2016**, *169*, 342–347.
- [32] J. Ali, G. U. D. Siddiqui, Y. J. Yang, K. T. Lee, K. Um, K. H. Choi, *RSC Adv.* **2016**, *6*, 5068–5078.
- [33] M. F. Bertino, R. R. Gadipalli, L. A. Martin, L. E. Rich, A. Yamilov, B. R. Heckman, N. Leventis, S. Guha, J. Katsoudas, R. Divan, D. C. Mancini, *Nanotechnology* **2007**, *18*, DOI 10.1088/0957-4484/18/31/315603.
- [34] S. R. M. Santiago, T. N. Lin, C. H. Chang, Y. A. Wong, C. A. J. Lin, C. T. Yuan, J. L. Shen, *Phys. Chem. Chem. Phys.* **2017**, *19*, 22395–22400.
-

-
- [35] F. J. Chao-Mujica, L. Garcia-Hernández, S. Camacho-López, M. Camacho-López, M. A. Camacho-López, D. Reyes Contreras, A. Pérez-Rodríguez, J. P. Peña-Caravaca, A. Páez-Rodríguez, J. G. Darías-Gonzalez, L. Hernandez-Tabares, O. Arias de Fuentes, E. Prokhorov, N. Torres-Figueroa, E. Reguera, L. F. Desdin-García, *J. Appl. Phys.* **2021**, *129*, DOI 10.1063/5.0040322.
- [36] M. He, X. Guo, J. Huang, H. Shen, Q. Zeng, L. Wang, *Carbon N. Y.* **2018**, *140*, 508–520.
- [37] D. V Talapin, S. Haubold, A. L. Rogach, A. Kornowski, M. Haase, H. Weller, *J. Phys. Chem. B* **2001**, *105*, 2260–2263.
- [38] F. Zhang, S. Huang, P. Wang, X. Chen, S. Zhao, Y. Dong, H. Zhong, *Chem. Mater.* **2017**, *29*, 3793–3799.
- [39] Y. Wang, X. Chang, N. Jing, Y. Zhang, *Anal. Methods* **2018**, *10*, 2775–2784.
- [40] W. Kwon, S. W. Rhee, *Chem. Commun.* **2012**, *48*, 5256–5258.
- [41] A. Talib, S. Pandey, M. Thakur, H. F. Wu, *Mater. Sci. Eng. C* **2015**, *48*, 700–703.
- [42] C. De Mello Donegá, P. Liljeroth, D. Vanmaekelbergh, *Small* **2005**, *1*, 1152–1162.
- [43] X. T. Zheng, A. Ananthanarayanan, K. Q. Luo, P. Chen, *Small* **2015**, *11*, 1620–1636.
- [44] X. Xu, R. Ray, Y. Gu, H. J. Ploehn, L. Gearheart, K. Raker, W. A. Scrivens, *J. Am. Chem. Soc.* **2004**, *126*, 12736–12737.
- [45] L. A. Ponomarenko, F. Schedin, M. I. Katsnelson, R. Yang, E. W. Hill, K. S. Novoselov, A. K. Geim, *Science (80-.)*. **2008**, *320*, 356–358.
- [46] X. Li, S. Zhang, S. A. Kulinich, Y. Liu, H. Zeng, *Sci. Rep.* **2014**, *4*, 1–8.

-
- [47] F. Liu, M. H. Jang, H. D. Ha, J. H. Kim, Y. H. Cho, T. S. Seo, *Adv. Mater.* **2013**, *25*, 3657–3662.
- [48] M. Zhao, *Appl. Sci.* **2018**, *8*, DOI 10.3390/app8081303.
- [49] D. Pan, J. Zhang, Z. Li, M. Wu, *Adv. Mater.* **2010**, *22*, 734–738.
- [50] T. Fan, W. Zeng, W. Tang, C. Yuan, S. Tong, K. Cai, Y. Liu, W. Huang, Y. Min, A. J. Epstein, *Nanoscale Res. Lett.* **2015**, *10*, DOI 10.1186/s11671-015-0783-9.
- [51] J. Tang, J. Zhang, Y. Zhang, Y. Xiao, Y. Shi, Y. Chen, L. Ding, W. Xu, *Nanoscale Res. Lett.* **2019**, *14*, 241.
- [52] S. Wang, I. S. Cole, D. Zhao, Q. Li, *Nanoscale* **2016**, *8*, 7449–7458.
- [53] S. N. Baker, G. A. Baker, *Angew. Chemie - Int. Ed.* **2010**, *49*, 6726–6744.
- [54] L. Liang, X. Peng, F. Sun, Z. Kong, J. W. Shen, *Nanoscale Adv.* **2021**, *3*, 904–917.
- [55] T. A. Tabish, C. J. Scotton, D. C. J Ferguson, L. Lin, A. Van Der Veen, S. Lowry, M. Ali, F. Jabeen, P. G. Winyard, S. Zhang, *Nanomedicine* **2018**, *13*, 1923–1937.
- [56] P. Zhao, L. Zhu, *Chem. Commun.* **2018**, *54*, 5401–5406.
- [57] A. Sharma, T. Gadly, A. Gupta, A. Ballal, S. K. Ghosh, M. Kumbhakar, *J. Phys. Chem. Lett.* **2016**, *7*, 3695–3702.
- [58] A. Sharma, T. Gadly, S. Neogy, S. K. Ghosh, M. Kumbhakar, *J. Phys. Chem. Lett.* **2017**, *8*, 1044–1052.
- [59] S. Khan, A. Gupta, N. C. Verma, C. K. Nandi, *Nano Lett.* **2015**, *15*, 8300–8305.

-
- [60] S. Khan, A. Sharma, S. Ghoshal, S. Jain, M. K. Hazra, C. K. Nandi, *Chem. Sci.* **2017**, *9*, 175–180.
- [61] K. Mishra, S. Koley, S. Ghosh, *J. Phys. Chem. Lett.* **2019**, *10*, 335–345.
- [62] J. B. Essner, J. A. Kist, L. Polo-Parada, G. A. Baker, *Chem. Mater.* **2018**, *30*, 1878–1887.
- [63] L. Xiao, H. Sun, *Nanoscale Horizons* **2018**, *3*, 565–597.
- [64] S. Yang, J. Sun, X. Li, W. Zhou, Z. Wang, P. He, G. Ding, X. Xie, Z. Kang, M. Jiang, *J. Mater. Chem. A* **2014**, *2*, 8660–8667.
- [65] G. E. LeCroy, F. Messina, A. Sciortino, C. E. Bunker, P. Wang, K. A. S. Fernando, Y.-P. Sun, *J. Phys. Chem. C* **2017**, *121*, 28180–28186.
- [66] H. Ding, S.-B. Yu, J.-S. Wei, H.-M. Xiong, *ACS Nano* **2016**, *10*, 484–491.
- [67] F. Yuan, Z. Wang, X. Li, Y. Li, Z. Tan, L. Fan, S. Yang, *Adv. Mater.* **2017**, *29*, DOI 10.1002/adma.201604436.
- [68] H. Li, X. He, Z. Kang, H. Huang, Y. Liu, J. Liu, S. Lian, C. H. A. Tsang, X. Yang, S. T. Lee, *Angew. Chemie - Int. Ed.* **2010**, *49*, 4430–4434.
- [69] F. Ehrat, S. Bhattacharyya, J. Schneider, A. Löf, R. Wyrwich, A. L. Rogach, J. K. Stolarczyk, A. S. Urban, J. Feldmann, *Nano Lett.* **2017**, *17*, 7710–7716.
- [70] M. J. Krysmann, A. Kelarakis, P. Dallas, E. P. Giannelis, *J. Am. Chem. Soc.* **2012**, *134*, 747–750.
- [71] Y. Du, S. Guo, *Nanoscale* **2016**, *8*, 2532–2543.
- [72] L. Cao, X. Wang, M. J. Meziani, F. Lu, H. Wang, P. G. Luo, Y. Lin, B. A. Harruff, L. M.

-
- Veca, D. Murray, S.-Y. Xie, Y.-P. Sun, *J. Am. Chem. Soc.* **2007**, *129*, 11318–11319.
- [73] M. Li, T. Chen, J. J. Gooding, J. Liu, *ACS Sensors* **2019**, *4*, 1732–1748.
- [74] S. Campuzano, P. Yáñez-Sedeño, J. M. Pingarrón, *Nanomaterials* **2019**, *9*, DOI 10.3390/nano9040634.
- [75] M. Dutta, S. Sarkar, T. Ghosh, D. Basak, *J. Phys. Chem. C* **2012**, *116*, 20127–20131.
- [76] J. Briscoe, A. Marinovic, M. Sevilla, S. Dunn, M. Titirici, *Angew. Chemie - Int. Ed.* **2015**, *54*, 4463–4468.
- [77] C. Zhu, D. Chao, J. Sun, I. M. Bacho, Z. Fan, C. F. Ng, X. Xia, H. Huang, H. Zhang, Z. X. Shen, G. Ding, H. J. Fan, *Optoelectron. Devices Integr. OEDI 2015* **2015**, 1–3.
- [78] A. Kojima, K. Teshima, Y. Shirai, T. Miyasaka, *J. Am. Chem. Soc.* **2009**, *131*, 6050–6051.
- [79] X. He, Y. Qiu, S. Yang, *Adv. Mater.* **2017**, *29*, 1–27.
- [80] J. Shamsi, A. S. Urban, M. Imran, L. De Trizio, L. Manna, *Chem. Rev.* **2019**, *119*, 3296–3348.
- [81] J. S. Manser, J. A. Christians, P. V. Kamat, *Chem. Rev.* **2016**, *116*, 12956–13008.
- [82] L. Protesescu, S. Yakunin, M. I. Bodnarchuk, F. Krieg, R. Caputo, C. H. Hendon, R. X. Yang, A. Walsh, M. V. Kovalenko, *Nano Lett.* **2015**, *15*, 3692–3696.
- [83] A. Dey, J. Ye, A. De, E. Debroye, S. K. Ha, E. Bladt, A. S. Kshirsagar, Z. Wang, J. Yin, Y. Wang, L. N. Quan, F. Yan, M. Gao, X. Li, J. Shamsi, T. Debnath, M. Cao, M. A. Scheel, S. Kumar, J. A. Steele, M. Gerhard, L. Chouhan, K. Xu, X. G. Wu, Y. Li, Y. Zhang, A. Dutta, C. Han, I. Vincon, A. L. Rogach, A. Nag, A. Samanta, B. A. Korgel, C. J. Shih, D. R.
-

-
- Gamelin, D. H. Son, H. Zeng, H. Zhong, H. Sun, H. V. Demir, I. G. Scheblykin, I. Mora-Seró, J. K. Stolarczyk, J. Z. Zhang, J. Feldmann, J. Hofkens, J. M. Luther, J. Pérez-Prieto, L. Li, L. Manna, M. I. Bodnarchuk, M. V. Kovalenko, M. B. J. Roeffaers, N. Pradhan, O. F. Mohammed, O. M. Bakr, P. Yang, P. Müller-Buschbaum, P. V. Kamat, Q. Bao, Q. Zhang, R. Krahne, R. E. Galian, S. D. Stranks, S. Bals, V. Biju, W. A. Tisdale, Y. Yan, R. L. Z. Hoye, L. Polavarapu, *ACS Nano* **2021**, *15*, 10775–10981.
- [84] J. Song, J. Li, X. Li, L. Xu, Y. Dong, H. Zeng, *Adv. Mater.* **2015**, *27*, 7162–7167.
- [85] H. Zhu, Y. Fu, F. Meng, X. Wu, Z. Gong, Q. Ding, M. V. Gustafsson, M. T. Trinh, S. Jin, X. Y. Zhu, *Nat. Mater.* **2015**, *14*, 636–642.
- [86] Y. F. Xu, M. Z. Yang, B. X. Chen, X. D. Wang, H. Y. Chen, D. Bin Kuang, C. Y. Su, *J. Am. Chem. Soc.* **2017**, *139*, 5660–5663.
- [87] S. Ahmad, C. George, D. J. Beesley, J. J. Baumberg, M. De Volder, *Nano Lett.* **2018**, *18*, 1856–1862.
- [88] J. R. Lakowicz, *Principle of Fluorescence Spectroscopy*, Springer Science And Business Media, **2013**.
- [89] B. Valeur, *Molecular Fluorescence Principles and Applications*, Wiley-VCH Verlag GmbH, **2001**.
- [90] W. Sun, M. Li, J. Fan, X. Peng, *Acc. Chem. Res.* **2019**, *52*, 2818–2831.
- [91] T. Gunnlaugsson, H. D. P. Ali, M. Glynn, P. E. Kruger, G. M. Hussey, F. M. Pfeffer, C. M. G. dos Santos, J. Tierney, *J. Fluoresc.* **2005**, *15*, 287–299.

-
- [92] H. Park, H. Il Kim, G. H. Moon, W. Choi, *Energy Environ. Sci.* **2016**, *9*, 411–433.
- [93] S. Krishnamurthy, P. V. Kamat, *ChemPhysChem* **2014**, *15*, 2129–2135.
- [94] A. Pal, S. Srivastava, P. Saini, S. Raina, P. P. Ingole, R. Gupta, S. Sapra, *J. Phys. Chem. C* **2015**, *119*, 22690–22699.
- [95] S. Chakrabarty, H. Kaur, T. Pal, S. Kar, S. Ghosh, S. Ghosh, *RSC Adv.* **2014**, *4*, 35531–35540.
- [96] K. E. Knowles, M. Malicki, E. A. Weiss, *J. Am. Chem. Soc.* **2012**, *134*, 12470–12473.
- [97] A. J. Nozik, *Renew. Energy* **2001**, *52*, 193–231.
- [98] I. Ahmed, L. Shi, H. Pasanen, P. Vivo, P. Maity, M. Hatamvand, Y. Zhan, *Light Sci. Appl.* **2021**, *10*, DOI 10.1038/s41377-021-00609-3.
- [99] S. S. Lim, D. Giovanni, Q. Zhang, A. Solanki, N. F. Jamaludin, J. Wei, M. Lim, N. Mathews, S. Mhaisalkar, M. S. Pshenichnikov, T. C. Sum, **2019**, *3*, 1–7.
- [100] G. Ghosh, K. Marjit, S. Ghosh, A. Ghosh, R. Ahammed, A. de Sarkar, A. Patra, *J. Phys. Chem. C* **2021**, *125*, 5859–5869.
- [101] Z. Zhang, W. Liu, Q. S. Ma, W. Zhang, C. Wang, R. Pu, C. W. Ju, R. Li, *J. Phys. Chem. C* **2021**, *125*, 9296–9302.
- [102] I. J. Chen, S. Limpert, W. Metaferia, C. Thelander, L. Samuelson, F. Capasso, A. M. Burke, H. Linke, *Nano Lett.* **2020**, *20*, 4064–4072.
- [103] A. De, N. Mondal, A. Samanta, *J. Phys. Chem. C* **2018**, *122*, 13617–13623.
- [104] N. Mondal, A. De, A. Samanta, *Nanoscale* **2018**, *10*, 639–645.
-

-
- [105] N. Mondal, A. De, S. Das, S. Paul, A. Samanta, *Nanoscale* **2019**, *11*, 9796–9818.
- [106] A. De, S. Das, A. Samanta, *ACS Energy Lett.* **2020**, *5*, 2246–2252.
- [107] P. V. Kamat, *Acc. Chem. Res.* **2012**, *45*, 1906–1915.
- [108] K. Tvrdy, P. A. Frantsuzov, P. V. Kamat, *Proc. Natl. Acad. Sci. U. S. A.* **2011**, *108*, 29–34.
- [109] J. Chakkamalayath, G. V. Hartland, P. V. Kamat, *J. Phys. Chem. C* **2021**, *125*, 17881–17889.
- [110] T. Ghosh, S. Chatterjee, E. Prasad, *J. Phys. Chem. A* **2015**, *119*, 11783–11790.
- [111] S. Koley, M. R. Panda, S. Ghosh, *J. Phys. Chem. C* **2016**, *120*, 13456–13465.
- [112] K. Bharadwaj, H. Choudhary, S. Hazra, S. Ghosh, *Chem. - An Asian J.* **2019**, *14*, 4207–4216.
- [113] K. Bharadwaj, H. Choudhary, S. Hazra, S. Ghosh, *ChemPhysChem* **2020**, *21*, 415–422.
- [114] K. Mishra, D. Acharjee, A. Das, S. Ghosh, *J. Phys. Chem. B* **2021**, *125*, 11017–11025.
- [115] K. Mishra, A. Das, S. Ghosh, *J. Phys. Chem. C* **2020**, *124*, 24115–24125.
- [116] K. Mishra, A. Das, S. Ghosh, *J. Phys. Chem. C* **2021**, *125*, 9638–9645.
- [117] K. Mishra, D. Acharjee, A. Das, S. Ghosh, *J. Phys. Chem. Lett.* **2022**, *13*, 606–613.
- [118] W. Becker, *Advanced Time-Correlated Single Photon Counting Techniques*, **2005**.
- [119] A. Benda, M. Hof, M. Wahl, M. Patting, R. Erdmann, P. Kapusta, *Rev. Sci. Instrum.* **2005**, *76*, DOI 10.1063/1.1866814.
- [120] H. Chosrowjan, S. Taniguchi, F. Tanaka, *FEBS J.* **2015**, *282*, 3003–3015.

-
- [121] M. Maroncelli, G. R. Fleming, *J. Chem. Phys.* **1987**, *86*, 6221–6239.
- [122] A. S. R. Koti, M. M. G. Krishna, N. Periasamy, *J. Phys. Chem. A* **2001**, *105*, 1767–1771.
- [123] D. Magde, E. L. Elson, W. W. Webb, *Biopolymers* **1974**, *13*, 29–61.
- [124] A. Van Orden, J. Jung, *Biopolymers* **2007**, *89*, 1–16.
- [125] T. Wohland, S. Maiti, R. Machan, *An Introduction to Fluorescence Correlation Spectroscopy*, **2020**.
- [126] A. Gupta, J. Sankaran, T. Wohland, *Phys. Sci. Rev.* **2019**, *4*, DOI doi:10.1515/psr-2017-0104.
- [127] J. Tauc, *Chem. Commun.* **1968**, *3*, 37–46.
- [128] C. Zhu, S. Yang, G. Wang, R. Mo, P. He, J. Sun, Z. Di, N. Yuan, J. Ding, G. Ding, X. Xie, *J. Mater. Chem. C* **2015**, *3*, 8810–8816.
- [129] M. Righetto, A. Privitera, I. Fortunati, D. Mosconi, M. Zerbetto, M. L. Curri, M. Corricelli, A. Moretto, S. Agnoli, L. Franco, R. Bozio, C. Ferrante, *J. Phys. Chem. Lett.* **2017**, *8*, 2236–2242.
- [130] S. Y. Lim, W. Shen, Z. Gao, *Chem. Soc. Rev.* **2015**, *44*, 362–381.
- [131] A. Das, D. Roy, M. Mandal, C. Jaiswal, M. Ta, P. K. Mandal, *J. Phys. Chem. Lett.* **2018**, *9*, 5092–5099.
- [132] S. Karthik, B. Saha, S. K. Ghosh, N. D. Pradeep Singh, *Chem. Commun.* **2013**, *49*, 10471–10473.
- [133] D. Tan, S. Zhou, J. Qiu, *ACS Nano* **2012**, *6*, 6530–6531.

-
- [134] X. Zhai, P. Zhang, C. Liu, T. Bai, W. Li, L. Dai, W. Liu, *Chem. Commun.* **2012**, 48, 7955–7957.
- [135] M. Li, S. X. A. Zhang, *Chem. Mater.* **2014**, 26, 6084.
- [136] S. Zhu, Q. Meng, L. Wang, J. Zhang, Y. Song, H. Jin, K. Zhang, H. Sun, H. Wang, B. Yang, *Angew. Chemie - Int. Ed.* **2013**, 52, 3953–3957.
- [137] L. Wang, S. J. Zhu, H. Y. Wang, S. N. Qu, Y. L. Zhang, J. H. Zhang, Q. D. Chen, H. L. Xu, W. Han, B. Yang, H. B. Sun, *ACS Nano* **2014**, 8, 2541–2547.
- [138] S. Zhu, J. Zhang, S. Tang, C. Qiao, L. Wang, H. Wang, X. Liu, B. Li, Y. Li, W. Yu, X. Wang, H. Sun, B. Yang, *Adv. Funct. Mater.* **2012**, 22, 4732–4740.
- [139] A. M. Chizhik, S. Stein, M. O. Dekaliuk, C. Battle, W. Li, A. Huss, M. Platen, I. A. T. Schaap, I. Gregor, A. P. Demchenko, C. F. Schmidt, J. Enderlein, A. I. Chizhik, *Nano Lett.* **2016**, 16, 237–242.
- [140] J. P. Kim, Z. Xie, M. Creer, Z. Liu, J. Yang, *Chem. Sci.* **2017**, 8, 550–558.
- [141] W. Kasprzyk, S. Bednarz, P. Zmudzki, M. Galica, D. Bogdał, *RSC Adv.* **2015**, 5, 34795–34799.
- [142] D. Pan, J. Zhang, Z. Li, C. Wu, X. Yan, M. Wu, *Chem. Commun.* **2010**, 46, 3681–3683.
- [143] X. Wang, L. Cao, F. Lu, M. J. Meziani, H. Li, G. Qi, B. Zhou, B. A. Harruff, F. Kermarrec, Y. P. Sun, *Chem. Commun.* **2009**, 3774–3776.
- [144] L. Li, G. Wu, G. Yang, J. Peng, J. Zhao, J. J. Zhu, *Nanoscale* **2013**, 5, 4015–4039.
- [145] A. Chattopadhyay, S. Haldar, *Acc. Chem. Res.* **2014**, 47, 12–19.
-

-
- [146] J. R. Lakowicz, S. Keating-Nakamoto, *Biochemistry* **1984**, *23*, 3013–3021.
- [147] M. O. Dekaliuk, O. Viagin, Y. V. Malyukin, A. P. Demchenko, *Phys. Chem. Chem. Phys.* **2014**, *16*, 16075–16084.
- [148] X. Wen, P. Yu, Y. R. Toh, X. Hao, J. Tang, *Adv. Opt. Mater.* **2013**, *1*, 173–178.
- [149] S. K. Das, Y. Liu, S. Yeom, D. Y. Kim, C. I. Richards, *Nano Lett.* **2014**, *14*, 620–625.
- [150] A. P. Demchenko, M. O. Dekaliuk, *Nanoscale* **2016**, *8*, 14057–14069.
- [151] W. Jarzęba, G. C. Walker, A. E. Johnson, M. A. Kahlow, P. F. Barbara, *J. Phys. Chem.* **1988**, *92*, 7039–7041.
- [152] B. Bagchi, *Annu. Reports Prog. Chem. - Sect. C* **2003**, *99*, 127–175.
- [153] S. K. Cushing, M. Li, F. Huang, N. Wu, *ACS Nano* **2014**, *8*, 1002–1013.
- [154] A. Samanta, *J. Phys. Chem. B* **2006**, *110*, 13704–13716.
- [155] A. Demchenko, *Springer Int. Publ. Switzerland*, **2016**.
- [156] P. Sen, S. Ghosh, K. Sahu, S. K. Mondal, D. Roy, K. Bhattacharyya, *J. Chem. Phys.* **2006**, *124*, DOI 10.1063/1.2197495.
- [157] A. Samanta, *J. Phys. Chem. Lett.* **2010**, *1*, 1557–1562.
- [158] N. Nandi, K. Bhattacharyya, B. Bagchi, *Chem. Rev.* **2000**, *100*, 2013–2045.
- [159] K. Bhattacharyya, *Acc. Chem. Res.* **2003**, *36*, 95–101.
- [160] X. X. Zhang, M. Liang, J. Hunger, R. Buchner, M. Maroncelli, *J. Phys. Chem. B* **2013**, *117*, 15356–15368.
-

-
- [161] R. Jimenez, G. R. Fleming, P. V. Kumar, M. Maroncelli, *Nature* **1994**, *369*, 471–473.
- [162] S. Ghosh, A. M. Chizhik, N. Karedla, M. O. Dekaliuk, I. Gregor, H. Schuhmann, M. Seibt, K. Bodensiek, I. A. T. Schaap, O. Schulz, A. P. Demchenko, J. Enderlein, A. I. Chizhik, *Nano Lett.* **2014**, *14*, 5656–5661.
- [163] S. J. Rosenthal, R. Jimenez, G. R. Fleming, P. V. Kumar, M. Maroncelli, *J. Mol. Liq.* **1994**, *60*, 25–56.
- [164] B. Bagchi, B. Jana, *Chem. Soc. Rev.* **2010**, *39*, 1936–1954.
- [165] S. Roy, B. Bagchi, *J. Chem. Phys.* **1993**, *99*, 9938–9943.
- [166] M. Glasbeek, H. Zhang, *Chem. Rev.* **2004**, *104*, 1929–1954.
- [167] N. Dhenadhayalan, K. C. Lin, R. Suresh, P. Ramamurthy, *J. Phys. Chem. C* **2016**, *120*, 1252–1261.
- [168] V. Georgakilas, J. A. Perman, J. Tucek, R. Zboril, *Chem. Rev.* **2015**, *115*, 4744–4822.
- [169] J. Shen, Y. Zhu, X. Yang, C. Li, *Chem. Commun.* **2012**, *48*, 3686–3699.
- [170] Y. Li, Y. Hu, Y. Zhao, G. Shi, L. Deng, Y. Hou, L. Qu, *Adv. Mater.* **2011**, *23*, 776–780.
- [171] S. Rawalekar, S. Kaniyankandy, S. Verma, H. N. Ghosh, *J. Phys. Chem. C* **2010**, *114*, 1460–1466.
- [172] V. Gupta, N. Chaudhary, R. Srivastava, G. D. Sharma, R. Bhardwaj, S. Chand, *J. Am. Chem. Soc.* **2011**, *133*, 9960–9963.
- [173] D. Yu, Y. Yang, M. Durstock, J. B. Baek, L. Dai, *ACS Nano* **2010**, *4*, 5633–5640.

-
- [174] X. Yan, B. Li, X. Cui, Q. Wei, K. Tajima, L. S. Li, *J. Phys. Chem. Lett.* **2011**, *2*, 1119–1124.
- [175] A. Rosspeintner, E. Vauthey, *Phys. Chem. Chem. Phys.* **2014**, *16*, 25741–25754.
- [176] G. S. Kumar, U. Thupakula, P. K. Sarkar, S. Acharya, *RSC Adv.* **2015**, *5*, 27711–27716.
- [177] L. Tang, R. Ji, X. Li, G. Bai, C. P. Liu, J. Hao, J. Lin, H. Jiang, K. S. Teng, Z. Yang, S. P. Lau, *ACS Nano* **2014**, *8*, 6312–6320.
- [178] M. Montalti, A. Credi, L. Prodi, M. T. Gandolfi, *Handbook of Photochemistry, 3rd Edition*, CRC Press, **2006**.
- [179] J. I. Steinfeld, J. S. Francisco, W. L. Hase, **1998**.
- [180] P. Schwille, E. Haustein, *Fluorescence Correlation Spectroscopy. An Introduction to Its Concepts and Applications*, **2002**.
- [181] S. Jazani, I. Sgouralis, O. M. Shafraz, M. Levitus, S. Sivasankar, S. Pressé, *Nat. Commun.* **2019**, *10*, DOI 10.1038/s41467-019-11574-2.
- [182] D. R. Larson, D. Zenklusen, B. Wu, J. A. Chao, R. H. Singer, *Science (80-.)*. **2011**, *332*, 475–478.
- [183] S. Sharma, N. Pal, P. K. Chowdhury, S. Sen, A. K. Ganguli, *J. Am. Chem. Soc.* **2012**, *134*, 19677–19684.
- [184] N. Pal, S. D. Verma, M. K. Singh, S. Sen, *Anal. Chem.* **2011**, *83*, 7736–7744.
- [185] E. L. Elson, *Biophys. J.* **2011**, *101*, 2855–2870.
- [186] K. Chattopadhyay, S. Saffarian, E. L. Elson, C. Frieden, *Biophys. J.* **2005**, *88*, 1413–1422.
-

-
- [187] S. Koley, M. R. Panda, K. Bharadwaj, S. Ghosh, *Langmuir* **2018**, *34*, 817–825.
- [188] W. Al-Soufi, B. Reija, M. Novo, S. Felekyan, R. Kühnemuth, C. A. M. Seidel, *J. Am. Chem. Soc.* **2005**, *127*, 8775–8784.
- [189] S. Doose, H. Neuweiler, M. Sauer, *ChemPhysChem* **2005**, *6*, 2277–2285.
- [190] S. Ghosh, U. Mandal, A. Adhikari, K. Bhattacharyya, *Chem. - An Asian J.* **2009**, *4*, 948–954.
- [191] T. Otsu, K. Ishii, T. Tahara, *Nat. Commun.* **2015**, *6*, 1–9.
- [192] N. Nandi, S. Roy, B. Bagchi, *J. Chem. Phys.* **1995**, *102*, 1390–1397.
- [193] S. Gupta, S. Rafiq, P. Sen, *J. Phys. Chem. B* **2015**, *119*, 3135–3141.
- [194] D. Chakrabarty, A. Chakraborty, D. Seth, N. Sarkar, *J. Phys. Chem. A* **2005**, *109*, 1764–1769.
- [195] T. Pradhan, P. Ghoshal, R. Biswas, *J. Chem. Sci.* **2008**, *120*, 275–287.
- [196] R. Halder, B. Jana, *J. Phys. Chem. B* **2020**, *124*, 8023–8031.
- [197] A. S. Jalilov, *ACS Omega* **2020**, *5*, 20409–20416.
- [198] M. Saladin, M. Maroncelli, *J. Phys. Chem. B* **2020**, *124*, DOI 10.1021/acs.jpcc.0c06839.
- [199] L. Mosca, R. S. Khnayzer, M. S. Lazorski, E. O. Danilov, F. N. Castellano, P. Anzenbacher, *Chem. - A Eur. J.* **2014**, *21*, 4056–4064.
- [200] K. Bharadwaj, S. Koley, S. Jana, S. Ghosh, *Chem. - An Asian J.* **2018**, *13*, 3296–3303.
- [201] S. Z. Mikhail, W. R. Kimel, *J. Chem. Eng. Data* **1961**, *6*, 533–537.
-

-
- [202] S. Koley, S. Ghosh, *Phys. Chem. Chem. Phys.* **2016**, *18*, 24830–24834.
- [203] X. Cai, J. E. Martin, L. E. Shea-Rohwer, K. Gong, D. F. Kelley, *J. Phys. Chem. C* **2013**, *117*, 7902–7913.
- [204] S. Seth, T. Ahmed, A. De, A. Samanta, *ACS Energy Lett.* **2019**, *4*, 1610–1618.
- [205] A. De, S. Das, N. Mondal, A. Samanta, *ACS Mater. Lett.* **2019**, *1*, 116–122.
- [206] L. Song, R. C. Dorfman, S. F. Swallen, M. D. Fayer, *J. Phys. Chem.* **1991**, *95*, 3454–3457.
- [207] M. L. Mueller, X. Yan, B. Dragnea, L. S. Li, *Nano Lett.* **2011**, *11*, 56–60.
- [208] T. Kampfrath, L. Perfetti, F. Schapper, C. Frischkorn, M. Wolf, *Phys. Rev. Lett.* **2005**, *95*, 26–29.
- [209] M. Breusing, C. Ropers, T. Elsaesser, *Phys. Rev. Lett.* **2009**, *102*, 1–4.
- [210] J. Yan, Y. Zhang, P. Kim, A. Pinczuk, *Phys. Rev. Lett.* **2007**, *98*, 1–4.
- [211] B. Gao, G. Hartland, T. Fang, M. Kelly, D. Jena, H. Xing, L. Huang, *Nano Lett.* **2011**, *11*, 3184–3189.
- [212] K. J. Williams, C. A. Nelson, X. Yan, L. S. Li, X. Zhu, *ACS Nano* **2013**, *7*, 1388–1394.
- [213] A. Honarfar, H. Mourad, W. Lin, A. Polukeev, A. Rahaman, M. Abdellah, P. Chábera, G. Pankratova, L. Gorton, K. Zheng, T. Pullerits, *ACS Appl. Energy Mater.* **2020**, *3*, 12525–12531.
- [214] Y. Gao, E. Talgorn, M. Aerts, M. T. Trinh, J. M. Schins, A. J. Houtepen, L. D. A. Siebbeles, *Nano Lett.* **2011**, *11*, 5471–5476.

-
- [215] J. Fu, Q. Xu, G. Han, B. Wu, C. H. A. Huan, M. L. Leek, T. C. Sum, *Nat. Commun.* **2017**, *8*, DOI 10.1038/s41467-017-01360-3.
- [216] J. Urayama, T. B. Norris, J. Singh, P. Bhattacharya, *Phys. Rev. Lett.* **2001**, *86*, 4930–4933.
- [217] L. Wang, Z. Chen, G. Liang, Y. Li, R. Lai, T. Ding, K. Wu, *Nat. Commun.* **2019**, *10*, 1–8.
- [218] Y. Yang, D. P. Ostrowski, R. M. France, K. Zhu, J. Van De Lagemaat, J. M. Luther, M. C. Beard, *Nat. Photonics* **2016**, *10*, 53–59.
- [219] T. Winzer, E. Malić, *Phys. Rev. B - Condens. Matter Mater. Phys.* **2012**, *85*, 1–5.
- [220] C. Melnychuk, P. Guyot-Sionnest, *Chem. Rev.* **2021**, *121*, 2325–2372.
- [221] L. W. Wang, M. Califano, A. Zunger, A. Franceschetti, *Phys. Rev. Lett.* **2003**, *91*, 1–4.
- [222] L. Dai, Z. Deng, F. Auras, H. Goodwin, Z. Zhang, J. C. Walmsley, P. D. Bristowe, F. Deschler, N. C. Greenham, *Nat. Photonics* **2021**, *15*, 696–702.
- [223] Q. Shen, T. S. Ripolles, J. Even, Y. Ogomi, K. Nishinaka, T. Izuishi, N. Nakazawa, Y. Zhang, C. Ding, F. Liu, T. Toyoda, K. Yoshino, T. Minemoto, K. Katayama, S. Hayase, *Appl. Phys. Lett.* **2017**, *111*, DOI 10.1063/1.4991993.
- [224] F. Wang, N. A. Melosh, *Nano Lett.* **2011**, *11*, 5426–5430.
- [225] J. Yin, P. Maity, R. Naphade, B. Cheng, J. H. He, O. M. Bakr, J. L. Brédas, O. F. Mohammed, *ACS Nano* **2019**, *13*, 12621–12629.
- [226] F. C. M. Spoor, S. Tomić, A. J. Houtepen, L. D. A. Siebbeles, *ACS Nano* **2017**, *11*, 6286–6294.
- [227] A. Pandey, P. Guyot-Sionnest, *Science (80-.)*. **2008**, *322*, 929–32.
-

-
- [228] S. Rühle, *Sol. Energy* **2016**, *130*, 139–147.
- [229] S. Kahmann, M. A. Loi, *J. Mater. Chem. C* **2019**, *7*, 2471–2486.
- [230] a K. Geim, *Prospects* **2009**, *324*, 1–8.
- [231] J. C. W. Song, M. S. Rudner, C. M. Marcus, L. S. Levitov, *Nano Lett.* **2011**, *11*, 4688–4692.
- [232] V. Țucureanu, A. Matei, A. M. Avram, *Crit. Rev. Anal. Chem.* **2016**, *46*, 502–520.
- [233] M. Li, S. K. Cushing, X. Zhou, S. Guo, N. Wu, *J. Mater. Chem.* **2012**, *22*, 23374–23379.
- [234] C. Sun, F. Figge, J. A. McGuire, Q. Li, L. S. Li, *Phys. Rev. Lett.* **2014**, *113*, 3–7.
- [235] J. Chen, M. E. Messing, K. Zheng, T. Pullerits, *J. Am. Chem. Soc.* **2019**, *141*, 3532–3540.
- [236] A. De, N. Mondal, A. Samanta, *Nanoscale* **2017**, *9*, 16722–16727.
- [237] N. S. Makarov, S. Guo, O. Isaienko, W. Liu, I. Robel, V. I. Klimov, *Nano Lett.* **2016**, *16*, 2349–2362.
- [238] G. E. Eperon, E. Jedlicka, D. S. Ginger, *J. Phys. Chem. Lett.* **2018**, *9*, 104–109.
- [239] J. M. Richter, F. Branchi, F. Valduga De Almeida Camargo, B. Zhao, R. H. Friend, G. Cerullo, F. Deschler, *Nat. Commun.* **2017**, *8*, 1–7.
- [240] T. R. Hopper, A. Gorodetsky, A. Jeong, F. Krieg, M. I. Bodnarchuk, M. Maimaris, M. Chaplain, T. J. Macdonald, X. Huang, R. Lovrincic, M. V. Kovalenko, A. A. Bakulin, *Nano Lett.* **2020**, *20*, 2271–2278.
- [241] J. A. Gardecki, M. Maroncelli, *J. Phys. Chem. A* **1999**, *103*, 1187–1197.
- [242] L. Brus, *Nano Lett.* **2010**, *10*, 363–365.
-

-
- [243] V. I. Klimov, *Annu. Rev. Phys. Chem.* **2007**, *58*, 635–673.
- [244] G. Grimaldi, R. W. Crisp, S. Ten Brinck, F. Zapata, M. Van Ouwendorp, N. Renaud, N. Kirkwood, W. H. Evers, S. Kinge, I. Infante, L. D. A. Siebbeles, A. J. Houtepen, *Nat. Commun.* **2018**, *9*, 1–10.
- [245] L. Zhao, Y. L. Lin, H. Kim, N. C. Giebink, B. P. Rand, *ACS Energy Lett.* **2018**, *3*, 2708–2712.
- [246] R. Quintero-Bermudez, A. H. Proppe, A. Mahata, P. Todorović, S. O. Kelley, F. De Angelis, E. H. Sargent, *J. Am. Chem. Soc.* **2019**, *141*, 13459–13467.
- [247] K. Wu, G. Liang, Q. Shang, Y. Ren, D. Kong, T. Lian, *J. Am. Chem. Soc.* **2015**, *137*, 12792–12795.
- [248] S. Mandal, L. George, N. V. Tkachenko, *Nanoscale* **2019**, *11*, 862–869.
- [249] D. B. Khadka, Y. Shirai, M. Yanagida, K. Miyano, *J. Mater. Chem. C* **2017**, *6*, 162–170.
- [250] J. Yuan, L. Zhang, C. Bi, M. Wang, J. Tian, *Sol. RRL* **2018**, *2*, 1–6.
- [251] S. Ye, H. Rao, Z. Zhao, L. Zhang, H. Bao, W. Sun, Y. Li, F. Gu, J. Wang, Z. Liu, Z. Bian, C. Huang, *J. Am. Chem. Soc.* **2017**, *139*, 7504–7512.
- [252] S. Kaniyankandy, S. Rawalekar, H. N. Ghosh, *J. Phys. Chem. C* **2012**, *116*, 16271–16275.
- [253] A. Boulesbaa, Z. Huang, D. Wu, T. Lian, *J. Phys. Chem. C* **2010**, *114*, 962–969.
- [254] A. Boulesbaa, A. Issac, D. Stockwell, Z. Huang, J. Huang, J. Guo, T. Lian, *J. Am. Chem. Soc.* **2007**, *129*, 15132–15133.
- [255] S. Sadhu, M. Tachiya, A. Patra, *J. Phys. Chem. C* **2009**, *113*, 19488–19492.

-
- [256] M. I. Bodnarchuk, S. C. Boehme, S. Ten Brinck, C. Bernasconi, Y. Shynkarenko, F. Krieg, R. Widmer, B. Aeschlimann, D. Günther, M. V. Kovalenko, I. Infante, *ACS Energy Lett.* **2019**, *4*, 63–74.
- [257] V. K. Ravi, A. Swarnkar, R. Chakraborty, A. Nag, *Nanotechnology* **2016**, *27*, DOI 10.1088/0957-4484/27/32/325708.
- [258] T. K. Mukherjee, P. P. Mishra, A. Datta, *Chem. Phys. Lett.* **2005**, *407*, 119–123.
- [259] M. Kumbhakar, S. Nath, T. Mukherjee, H. Pal, *J. Chem. Phys.* **2005**, *123*, DOI 10.1063/1.1953579.
- [260] S. D. Choudhury, M. Kumbhakar, S. Nath, S. K. Sarkar, T. Mukherjee, H. Pal, *J. Phys. Chem. B* **2007**, *111*, 8842–8853.
- [261] M. Chakraborty, T. Ahmed, M. Sarkar, *Langmuir* **2019**, *35*, 16172–16184.
- [262] V. K. Ravi, G. B. Markad, A. Nag, **2016**, *3*, DOI 10.1021/acsenerylett.6b00337.
- [263] S. U. M. Park, A. J. Bard, **1977**, *77*, 137–152.
- [264] J. E. Thomaz, C. M. Lawler, M. D. Fayer, *J. Phys. Chem. B* **2017**, *121*, 4544–4553.
- [265] A. Adhikari, S. Dey, D. K. Das, U. Mandal, S. Ghosh, K. Bhattacharyya, *J. Phys. Chem. B* **2008**, *112*, 6350–6357.
- [266] P. Toele, H. Zhang, M. Glasbeek, *J. Phys. Chem. A* **2002**, *106*, 3651–3658.
- [267] P. Setua, C. Ghatak, V. G. Rao, S. K. Das, N. Sarkar, *J. Phys. Chem. B* **2012**, *116*, 3704–3712.
- [268] C. Porter, P. Sadkowski, C. J. Tredwell, *Chem. Phys. Lett.* **1977**, *49*, 3–7.
-

-
- [269] S. Sen, D. Sukul, P. Dutta, K. Bhattacharyya, *J. Phys. Chem. A* **2001**, *105*, 7495–7500.
- [270] S. Koley, S. Ghosh, *J. Phys. Chem. B* **2017**, *121*, 1930–1940.
- [271] H. S. Tan, I. R. Piletic, M. D. Fayer, *J. Chem. Phys.* **2005**, *122*, DOI 10.1063/1.1883605.
- [272] K. Sahu, S. K. Mondal, S. Ghosh, D. Roy, K. Bhattacharyya, *J. Chem. Phys.* **2006**, *124*, DOI 10.1063/1.2178782.
- [273] P.-O. Gendron, F. Avaltroni, K. J. Wilkinson, *J. Fluoresc.* **2008**, *18*, 1093.
- [274] G. Majer, K. Zick, *J. Chem. Phys.* **2015**, *142*, 6–11.
- [275] A. Rosspeintner, G. Angulo, E. Vauthey, *J. Am. Chem. Soc.* **2014**, *136*, 2026–2032.
- [276] S. Kundu, S. Sadhu, R. Bera, B. Paramanik, A. Patra, *J. Phys. Chem. C* **2013**, *117*, 23987–23995.
- [277] P. Kumar, T. Pascher, M. Tachiya, S. K. Pal, *J. Photochem. Photobiol. A Chem.* **2015**, *296*, 35–39.
- [278] M. Tachiya, *J. Chem. Phys.* **1982**, *76*, 340–348.
- [279] F. Palazon, F. Di Stasio, S. Lauciello, R. Krahne, M. Prato, L. Manna, *J. Mater. Chem. C* **2016**, *4*, 9179–9182.
- [280] B. Conings, J. Drijkoningen, N. Gauquelin, A. Babayigit, J. D’Haen, L. D’Olieslaeger, A. Ethirajan, J. Verbeeck, J. Manca, E. Mosconi, F. De Angelis, H. G. Boyen, *Adv. Energy Mater.* **2015**, *5*, 1–8.
- [281] M. Liu, Q. Wan, H. Wang, F. Carulli, X. Sun, W. Zheng, L. Kong, Q. Zhang, C. Zhang, Q. Zhang, S. Brovelli, L. Li, *Nat. Photonics* **2021**, *15*, 379–385.
-